Titre: Title:	Controlled Functionalization of Surfaces Through Syngas Photo-Initiated Chemical Vapor Depostion
Auteur: Author:	Donya Farhanian
Date:	2017
Type:	Mémoire ou thèse / Dissertation or Thesis
Référence: Citation:	Farhanian, D. (2017). Controlled Functionalization of Surfaces Through Syngas Photo-Initiated Chemical Vapor Depostion [Thèse de doctorat, École Polytechnique de Montréal]. PolyPublie. https://publications.polymtl.ca/2706/

URL de PolyPublie: PolyPublie URL:	https://publications.polymtl.ca/2706/
Directeurs de recherche: Advisors:	Gregory De Crescenzo, & Jason Robert Tavares
Programme: Program:	Génie chimique

UNIVERSITÉ DE MONTRÉAL

CONTROLLED FUNCTIONALIZATION OF SURFACES THROUGH SYNGAS
PHOTO-INITIATED CHEMICAL VAPOR DEPOSITION

DONYA FARHANIAN

DÉPARTEMENT DE GÉNIE CHIMIQUE

ÉCOLE POLYTECHNIQUE DE MONTRÉAL

THÈSE PRÉSENTÉE EN VUE DE L'OBTENTION

DU DIPLÔME DE PHILOSOPHIAE DOCTOR

(GÉNIE CHIMIQUE)

JUILLET 2017

UNIVERSITÉ DE MONTRÉAL

ÉCOLE POLYTECHNIQUE DE MONTRÉAL

Cette thèse intitulée:

CONTROLLED FUNCTIONALIZATION OF SURFACES THROUGH SYNGAS
PHOTO-INITIATED CHEMICAL VAPOR DEPOSITION

présentée par : FARHANIAN Donya

en vue de l'obtention du diplôme de : Philosophiae Doctor

a été dûment acceptée par le jury d'examen constitué de :

M. LEGROS Robert, Ph. D., président

M. TAVARES Jason-Robert, Ph. D., membre et directeur de recherche

M. DE CRESCENZO Gregory, Ph. D., membre et codirecteur de recherche

M. HARVEY Jean-Philippe, Ph. D., membre.

M. GIRARD-LAURIAULT Pierre-Luc, Ph. D., membre externe

DEDICATION

To my mother who I lost during this journey and always taught me to face my fears.

To my lovely family who love me no matter what.

To my wonderful love of life Walid.

ACKNOWLEDGEMENT

First and foremost, I would like to thank my supervisors, Prof. Jason R. Tavares and Prof. Gregory De Crescenzo for giving me the opportunity to work under their supervision, and for their continuous support throughout all the challenges I faced during this research. Their solid knowledge in the field of surface modification, positive attitude, prompt responses, good advices, and dedication to their students motivated me to carry out this research successfully.

I would like to immensely thank to Dr. Josianne Lefebvre who put a lot of time and effort in teaching me how to work with XPS machine and interpret my results and helped me with TOF-SIMS measurements. I would like to thank Dr. Hossein Monajati from École de technologie supérieure (ETS), Mr. C. Clement (Université de Montréal) and Prof. C. Pellerin and Dr. X. Wang from the Chemistry Department of Université de Montréal for their kind help during SEM, profilometry and FTIR measurement. Furthermore, I would like to thank Mr. Jean-Philippe Masse and Ms. Nicole Macdonald from the Centre for Characterization and Microscopy of Materials (CM^2) of École Polytechnique de Montréal.

Special thanks are directed to the present and past members, doctors and doctors to be, internship students of the photochemical surface engineering laboratory (PhotoSEL) for their fruitful discussions and comments, Dr. Faezeh Sabri, Dr. Evelyne Kasparek, Ms. MeiQi Xu, Ms. Bahareh Zakeri, Ms. Vickie Labonte, Ms. Ariane Berard, Mr. Christopher A.D. Dion, Mr. Wendell Raphael, Dr. Hamed Nasri, Dr. Ehsan Hosseininasab, Dr. David Brassard, Dr. Charles Bruel, Dr. Quentin Beuguel. A special thanks goes to Mr. Wendell Raphael for his help on French abstract translation. Thank you for your supports, encouragements and the times we enjoyed together inside and outside the lab!

RÉSUMÉ

Les techniques de modification de surface ont gagné beaucoup d'intérêt en raison de leur capacité à adapter, sans altérer la majeure partie d'un matériau, les propriétés de sa surface. Cependant, il existe un besoin pour de nouveaux précurseurs ainsi que pour des procédés peu coûteux et industriellement évolutifs.

Bien que de nombreuses méthodes aient été exploitées pour la modification de surface de nanoparticules (NP), la plupart souffrent de la complexité de la préparation (par exemple la technique sol-gel), du matériel coûteux et des conditions de fonctionnement coûteuses et prohibitives (basse pression et/ou haute température, pour la déposition en phase vapeur par plasma ou thermiquement activée - CVD -). Ce projet de recherche abordera ces limites en étudiant une approche de fonctionnalisation plus pertinente du point de vue technique, c'est-à-dire la CVD photo-initiée (PICVD). Cette technique est supérieure en raison de la conception simple du réacteur, sa facilité d'utilisation et de contrôle, son évolutivité, sa polyvalence, son abordabilité et sa faible empreinte écologique. En plus de traiter les problèmes de traitement énumérés ci-dessus, l'efficacité énergétique de cette méthode est plus élevée que les méthodes CVD traditionnelles puisque la longueur d'onde utilisée pour l'irradiation des précurseurs est choisie pour cibler des liaisons moléculaires spécifiques.

D'autre part, les déchets industriels deviennent un véritable défi pour le monde d'aujourd'hui. La production mondiale de gaz de synthèse a été enregistrée à 116 000.0 MW thermiques (MWth) en 2014 et devrait atteindre 213 100 MWth d'ici 2020, avec un taux de croissance annuel composé de 9,5% entre 2015 et 2020. Compte tenu de la production massive de syngas en tant que sous-produits de plusieurs procédés, la mise en oeuvre pratique de ce composé pour le revêtement fonctionnel pourrait avoir un impact profond dans l'environnement, ainsi que dans les industries de revêtement et de dépôt.

Pour surmonter ces problèmes, nous avons examiné la synthèse de Fischer-Tropsch. Dans ce procédé, des catalyseurs sont utilisés pour transformer du syngaz en hydrocarbures. Les catalyseurs se désactivent pendant ce processus en raison de la formation d'espèces de carbone légèrement polymérisées. Cet encrassement de surface peut être réimaginé comme de l'ingénierie de surface. Ceci nous a incités à considérer le gaz de synthèse comme un précurseur réactif alternatif dans le PICVD.

Cette présente thèse analyse le PICVD en trois parties distinctes:

(1) La faisabilité et l'applicabilité du PICVD par gaz de synthèse via des lampes UVC à partir d'une étude de cas en gestion des déchets.

(2) Les cinétiques et les mécanismes de réaction du PICVD ainsi que les paramètres opérationnels optimaux permettant un contrôle sur la chimie, l'épaisseur et la morphologie du film déposé.

(3) Détermination du potentiel de mise à l'échelle du PICVD par l'encapsulation fonctionnelle de nanoparticules magnétiques d'oxyde de fer dans un réacteur à lit fluidisé assisté par jet dans l'objectif de son industrialisation qui permettra de diminuer de l'écart entre le revêtement de nanoparticules à grande échelle et à petite échelle.

Dans la première section, nous développons une méthodologie permettant d'extraire des nanoparticules fonctionnelles encapsulées peu coûteuses provenant de cendres volantes issues de déchets municipaux. En plus de démontrer les bénéfices apportés à l'environnement grâce à l'application économique de deux flux de déchets, soit les cendres volantes municipales et la production mondiale de gaz de synthèse, notre approche illustre la possibilité de production de matériels de valeur à faible coût.

Dans la deuxième partie de cette thèse, nous présentons de quelles façons les paramètres opérationnels, c'est-à-dire le temps de résidence, la durée du traitement ainsi que le ratio gazeux, affectent l'épaisseur, la morphologie et la densité de groupes fonctionnels d'intérêts. Nous proposons ensuite une cinétique et un mécanisme de réaction pour le PICVD pas gaz de synthèse via des lampes UVC, ceci n'ayant jamais été fait auparavant.

Finalement, dans la troisième partie de ce travail, nous diminuons l'écart entre le revêtement de surface de nanoparticules à petite échelle et les applications industrielles à grande échelle, permettant ainsi la synthèse de grandes quantités de nanoparticules multifonctionnelles encapsulées avec une technique à faible consommation d'énergie et consommant un déchet gazeux (syngaz) à température ambiante et pression atmosphérique. Ceci représente une étape considérable vers le développement durable.

Les recherches présentées dans cette thèse sont donc multidisciplinaires et originales sur plusieurs aspects:

- Dans le domaine de l'environnement, elle aide à résoudre le problème de déchet en les réutilisant à l'aide d'un procédé à faible consommation d'énergie.

- Dans le domaine du matériau, elle apporte une solution potentielle au problème d'agglomération des nanoparticules ainsi qu'au développement de nanocatalyseurs et de membranes de séparation.

- Dans le domaine des biomatériaux, elle permet de produire des nanoparticules encapsulées fonctionnelles, ayant des applications en imagerie et dans la délivrance de médicaments lors de traitement thérapeutique contre le cancer, en grandes quantités à partir d'une technique économique.

ABSTRACT

Surface modification techniques have gained a lot of interest due to their ability to tailor surface properties without altering the bulk of the material. However, there is a need for new precursors as well as cheap, industrially scalable processes.

Although many methods have been exploited for surface modifications, most are suffering from complexity of preparation (e.g., sol-gel technique), expensive equipment and expensive and prohibitive operating conditions (low pressure and / or high temperature, for plasma or thermally-activated chemical vapor deposition - CVD -). Thus, this research project will address these limitations by studying a more technically relevant functionalization approach, i.e., photo-initiated CVD (PICVD). This technique has superiority due to its simple reactor design, ease of use and control, scalability, versatility, affordability and low environmental footprint. In addition to addressing the treatment problems listed above, the energy efficiency of this method is higher than traditional CVD methods since the wavelength used for precursor irradiation is selected to target specific molecular bonds.

On the other hand, industrial waste is becoming a real challenge for today's world. The global syngas production was recorded at 116,600.0 MW thermal (MWth) in 2014 and is projected to reach 213,100.0 MWth by 2020, at a compound annual growth rate of 9.5% between 2015 and 2020. Given the massive scale production of syngas as by-products of several processes, the practical implementation of this compound for functional coating may have a profound impact on the environment, as well as on the coating and deposition industries.

To overcome these issues, we investigated Fischer−Tropsch synthesis. In this process, catalysts are used to transform syngas into hydrocarbons. Catalysts deactivate during this process because of the formation of lightly polymerized carbon species. This surface fouling can be reimagined as surface engineering; this triggered us to consider syngas as an alternative reactive precursor in PICVD.

In this thesis, we investigated three distinct aspects of the PICVD process:

(1) Feasibility and applicability of syngas PICVD via UVC lamps through a waste management case study.

(2) Kinetics and mechanism of the process while looking at the effective operational parameters in order to have control over the chemistry, film thickness as well as morphology of the deposited film.

(3) Scalability of the process through functional encapsulation of magnetic iron oxide nanoparticles in jet-assisted fluidized bed reactor towards industrialization and fulfilling the gap between large-scale and small-scale nanoparticle coating.

In the first section, we have developed a methodology to extract cheap functional encapsulated nanoparticles from municipal fly ash waste stream. Our proposed approach, not only benefits the environment through economic application of two waste streams: municipal fly ash and global syngas production but also help the low cost production of valuable materials.

In a second part of this research thesis, we showed how the operational parameters, e.g. residence time, treatment duration as well as gas ratio, affect the thickness, morphology and density of functional groups of interest, we proposed a kinetics and mechanism for syngas PICVD process via UVC lamps which has never been done before.

The third part of this thesis work bridged the gap between small-scale nanoparticle surface coating and large-scale industrial applications, allowing the synthesis of large quantities of encapsulated multifunctional nanoparticles with an energy-saving technique that consumed gas waste (syngas) at ambient temperature and at atmospheric pressure, a considerable step towards sustainability development.

The research presented in this thesis is thus multidisciplinary and original on several aspects:

- in the field of environment, help to address the waste stream problems by reusing them for a valuable industries under low energy consumption process.

- in the field of material, potentially address the problem of agglomeration of nanoparticles and the development of nanocatalysts and separating membrane.

- in the field of biomaterials, produce functional encapsulated nanoparticles in large quantities with economic technique which have great application in imaging and drug delivery for therapeutic application in cancer treatment.

TABLE OF CONTENTS

LIST OF TABLES

LIST OF FIGURES

LIST OF ABBREVIATIONS

ABF	Agglomerate Bubbling Fluidization
ACS	Absorption Cross Section
AFM	Atomic Force Microscope
ALD	Atomic Layer Deposition
AP	Anionic Polymerization
APTEOS	3-Amino Propyl Tri Eth Oxy Silane
APTS	p-Amino Phenyl Ttrimethoxy Silane
APF	Agglomerate Particulate Fluidization
ATR-FTIR	Attenuated total reflectance - Fourier Transform Infrared Spectroscopy
BE	Binding Energy
BP	Benzo Phenone
CA	Acyano Acrylate
CFI	Canadian Foundation for Innovation
CI	Confidence Interval
CM^2	Centre for Characterization and Microscopy of Materials
CP	Cationic Polymerization
CRC	Canada Research Chairs
CVD	Chemical Vapour Deposition
DDT	Diphenyl Di Thieno
DUV	Deep Ultra Violet
DPS	Dialkyl Phenacyl Sulfonium
DRIFTS	Diffuse Reflectance Infrared Fourier Transform Spectroscopy
EDS	Energy Dispersive X-ray Spectroscopy
EIC	Extracted Ion Chromatograms
ETS	École de Technologie Supérieure
EUV	Extreme UV
FBRs	Fluidized Bed Reactors
FB-PICVD	Fluidized Bed Photo-Initiated Chemical Vapor Deposition
FESEM	Field Emission Scanning Electron Microscopy
FRQNT	Fonds de Recherche du Québec en Nature et Technologies

FRP	Free Radical Polymerization
FTIR	Fourier Transform Infrared Spectroscopy
FT	Fischer–Tropsch
FTS	Fischer–Tropsch Synthesis
FUV	Far Ultra Violet
FWHM	Full Width at Half Maximum
GC-MS	Gas Chromatography-Mass Spectrometry
HEMA	Hydroxy Ethyl Meth Acrylate
HRTEM	High-Resolution Transmission Electron Microscopy
HTFT	High Temperature Fischer–Tropsch
ICDD	International Centre for Diffraction Data
ICP-AES	Inductively Coupled Plasma Atomic Emission Spectroscopy
IPC	Iron Penta Carbonyl
ITX	Isopropyl Thio Xanthone
JCPDS	Joint Committee on Powder Diffraction Standards
LCVD	Laser Chemical Vapor Deposition
LED	Light Emitting Diodes
LP	Low-Pressure
LPD	Liquid Phase Deposition
LTFT	Low Temperature Fischer–Tropsch
MAA	Methyl Acrylic Acid
MIONPs	Magnetic Iron Oxide Nanoparticles
MMA	Methyl Meth Acrylate
MP	Medium Pressure
MPDM	Methylmethacrylate Phenyl Di Methyl
MPDMS	Methylmethacrylate Phenyl Di Methyl Silyl
MPTES	Mercapto Propyl Tri Ethoxy Silane
MRI	Magnetic Resonance Imaging
MSW	Municipal Solid Waste
MTMS	Methyl Tri Methoxy Silane
NP	Nano Particle

NSERC	Natural Sciences and Engineering Research Council of Canada
PACVD	Photo-Assisted CVD
PECVD	Plasma-Enhanced Chemical Vapour Deposition
PEG	Poly Ethylene Glycol
PEO	Poly Ethylene Oxide
PFM	Penta Fluorophenyl Methacrylate
PhotoSEL	Photochemical Surface Engineering Laboratory
PICVD	Photo-Initiated Chemical Vapor Deposition
PIs	Photo-Initiators
PMTMS	Poly Methyl Tri Methoxy Silane
PMMA	Poly Methyl Meth Acrylate
PTTMSS	Propylmethacrylate Tris-Tri Methyl Siloxy Silyl
PSs	Photo-Sensitizers
PTFE	Poly Tetra Fluoro Ethylene
PVD	Physical Vapour Deposition
PVDF	Poly Vinyli Dene Fluoride
RS	Reactive Species
SAED	Selected Area Electron Diffraction
SCM	Supplementary Cementitious Material
SEM	Scanning Electron Microscope
SF	Sensitivity Factors
SPR	Surface Plasmon Resonance
TACVD	Thermally Activated Chemical Vapour Deposition
TEM	Transmission electron microscopy
TFE	Tetra Fluoro Ethlene
TGA	Thermal Gravimetric Analysis
TMPTA	Tri Methylol Propane Tri Acrylate
TOF-SIMS	Time-Of-Flight Secondary Ion Mass Spectrometry
TPGDA	Tri Propylene Glycol Di Acrylate
QDs	Quantum dots
UCNPs	Upconverting Nano Particles

UV	Ultra Violet
VUV	Vacuum UV
VW	Volmer-Weber
XPS	X-Ray Photoelectron Spectroscopy
XRD	X-Ray Diffraction

LIST OF APPENDICES

CHAPTER 1:   INTRODUCTION

Engineering and modification of surfaces is a multidisciplinary field. It intends to add new properties to the surface of materials in order to expand their serviceability. Today's concept of surface thin film deposition has been widely recognized as the most promising field for the preparation of different tailored materials with selective binding and functionalities in catalyst, food packaging, biochip sensors, gas detectors, etc. industries. The next decades will entail further commercialization of this field and integration of this concept into a variety of manufacturing lines. Techniques for fabrication of functionalized polymeric-based surfaces have been predominantly based on wet chemistry, but other new methods such as plasma and chemical vapour deposition are growing quite fast. Wet chemistry techniques suffer from a processing point of view; they often involve toxic or environmentally unfriendly solvents, complex preparation methods and challenges for the removal of solvents from the main desired product. Plasma and thermal chemical vapour deposition (CVD) circumvent these flaws, but up until now still require complex and expensive equipment as well as prohibitive operating conditions (low pressure and / or high temperature)[1-5]. These drawbacks limit scale-up to very high added value applications, and subsequently inhibit commercialization.

Photo-initiated chemical vapour deposition (PICVD) under atmospheric pressure using UV-sensitive precursors is a technique that can circumvent the drawbacks of traditional thermal or plasma CVD. It benefits from a simple reactor design, ease of use and control, scalability, versatility, affordability and low environmental footprint. In addition, its energy efficiency is higher than traditional CVD methods since the wavelength used for excitation of precursors is selected to target specific molecular bonds. Little attention has been devoted to this promising technique using ubiquitous germicidal UV lamps (UVC light mainly emitted at a wavelength of 253.7 nm) [6, 7]. Thus far, vacuum UV (VUV) lamps have been exploited mainly for surface thin film deposition due to the high energy they provide for chemical bond breakage[8-17].

This prior focus on VUV is due to the fact that most organic compounds absorb selectively in the VUV range – this highlights the need to use new precursors compatible with UVC, all the while respecting the desire to keep the overall approach low-cost. Given the massive scale production of syngas (combination of CO and H_2) as a product of several processes, the practical implementation of this gas mixture for functional coating could have a profound impact on both the coating and

deposition industries, not to mention an environmental impact given that syngas is often produced through the gasification of waste. Thus, we looked to the well-established Fischer−Tropsch synthesis literature to apply this precursor for thin film deposition. In the Fischer−Tropsch process, syngas is used in the presence of catalysts to produce hydrocarbons. Catalysts deactivate over time due to the formation of lightly polymerized carbon species on their surface. This surface fouling can be reimagined as surface engineering and triggered us to consider syngas as an alternative reactive precursor in PICVD.

With syngas, PICVD provides a convenient and versatile route for the encapsulation and/or fabrication of chemically functionalized surfaces at both nano and micro scales. Beyond the formation of a coating, PICVD allows for surface functionalization (i.e. addition of specific chemical groups), which is required to make surfaces bioactive or appropriate for a variety of applications, such as biosensor chips, gas detectors, catalysis, membranes, artificial organs and implants[18, 19]. Most studies on polymeric thin film deposition have concentrated on maximizing the thickness of the deposited film or functionalities, losing focus for the desired application. Take for example the case of nanoparticles (NPs). Their high surface-to-volume ratio make them interesting for a wide variety of industries, including applications in drug delivery, in vivo imaging, sensor technology, cotton and cloths technology even food packaging, to name only a few. However, due to their inherently high surface energy, NPs tend to agglomerate in an effort to lower their energy state[20], but this compromises their surface-driven properties. Maintaining their small-scale size is a key parameter to sustain optical and magnetic properties. For example, the light emission of quantum dots is size-tunable [21-24] and in the later coated magnetic iron oxide nanoparticles [25-28] using resonance imaging detection machines for in vivo bioimaging application are examples. In the case of magnetic iron oxide nanoparticles, by increasing the size of coating the magnetic effect of these particles decreases which jeopardizes their application [29-32]. Coating and encapsulation of NPs can limit agglomeration by changing their surface charge while providing a platform for their functionalization. However, the production of functionalized encapsulated nanoparticles is still very slow due to the expensive/complex synthesis and treatment techniques.

Based on the information provided in the literature, and despite the studies on VUV-PICVD, there are very few studies with UVC lamps in the PICVD field. There is a need for new precursors and

with that comes a need to understand their deposition kinetics, to control film thickness and improve functionality with respect to the desired application.

Thus, the main objective of this project is to investigate and develop syngas PICVD for thin film deposition on micro and nano surfaces, towards the development of organic coatings with functional groups available for various applications.

The first part of this work is a proof-of-concept case study to investigate the applicability of syngas PICVD for extraction and treatment of nanoparticles from municipal solid waste ash. The second part of this work focuses on the chemistry and kinetics of thin film deposition on flat surfaces via syngas PICVD to investigate the effect of operational parameters such as residence time, treatment duration and gas ratio on the structure, morphology, and properties of the film. These findings lead to a proposed mechanism for thin film deposition, taking into account the individual effects of each precursor, as well as the role of a contaminant as photo-catalyst in the process. The third part of this work leverages both the proof-of-concept work on nanoparticles and the new knowledge gained on the chemistry and kinetics to encapsulate nanoparticles on a large-scale in a jet-assisted fluidized bed syngas PICVD system.

This dissertation comprises seven chapters and is structured around three articles that have been submitted to scientific journals:

- ➢ Chapter 1 provides an extensive literature review including a discussion on the five main topics of interest: (1) Surface modification techniques; (2) Photo-initiated chemical vapor deposition basics; (3) Nanoparticles and their fluidization; (4) Syngas and fly ash production; and (5) Fundamentals of Fisher-Tropsch reactions.

- ➢ Chapter 2 reiterates the main objective and formulates the specific objectives of this work, along with the organization of the articles.

- ➢ Chapter 3, 4, and 5 report the three articles containing the main results of this study.

- ➢ Chapter 6 presents a general discussion with respect to the results obtained.

- ➢ Chapter 7 concludes the work, summarizing the original contributions and proposing some recommendations for future work.

CHAPTER 2:   LITERATURE REVIEW

To provide the required baseline for this project and allow a clear understanding of its novelty, this section reviews the pertinent literature, divided into five main sections: (1) Surface modification techniques; (2) Photo-initiated chemical vapor deposition basics; (3) Nanoparticles and their fluidization; (4) Syngas and fly ash production; and (5) Fundamentals of Fisher-Tropsch reactions. The second part is intended to be extended and submitted as a literature review article. This section included contributions from an internship student Ms. MeiQi Xu as well as my colleagues Mr. Hamed Nasri and Mr. Ehsan Hoseininasab.

2.1 Surface Modification Techniques

Surface engineering is an interdisciplinary research field that connects physical, chemical, and optical properties of materials and has major relevance for several industrial sectors such as tool machining, automotive, aeronautics, plastic manufacturing, biotechnology, electronic, food packaging, sport accessories, etc. (Figure 2-1). Surface engineering exploits appropriate technologies to achieve desired surface properties, and involves compromises between design aspects and expenses. Inherently, this field deals with changing the physical (shape, texture, etc.) or chemical surface properties (corrosion, chemical stability, adhesion, etc.) [33, 34].

Figure 2-1: Some sectors of surface engineering [33, 34].

Various techniques have been exploited for surface modification by introducing different precursors for either surface coating or surface functionalization, including:

- Liquid phase deposition (LPD);

- Atomic layer deposition (ALD);

- Physical vapour deposition (PVD);

- Chemical vapour deposition (CVD);

2.1.1 Wet chemical or liquid phase deposition (LPD)

In this process, the precursor solutions start as single-phase solutions or liquids and then undergo the sol-gel transition to become a two-phase system of solid and solvent-filled pores. This two-phase system is an alcogel, which is an oxide polymer that compacts in solvents. This irreversible process treats the surface by applying a prepared oxide or non-oxide precursor liquid solution to a substrate by draining, spinning or dipping. This method is capable of coating the inner and outer surfaces of porous three-dimensional complex geometries at the same time [35, 36]. The time duration of the sol-gel transition depends on the chemical properties of the initial solution. Moreover, based on the desired functionality reactive precursors with subsequent functional groups participate in the reaction. For instance, in the case of –OH grafting, dextran and in the case of –COOH grafting polyacrylic acid are among popular grafting precursors. This technique is easy to run in any laboratory and it can be performed under normal conditions. In comparison to other deposition processes, the sol-gel method is quite inexpensive in terms of equipment because it does not require a vacuum or any special equipment. However, it involves toxic solvents and produces many chemical wastes, which need to be extracted from the modified surface. As a result, this makes it unsuitable for large industrial scale applications [37, 38].

In the case of metal oxide deposition, we have liquid phase deposition in which crystalline metal oxide thin films are created from liquid solutions at low temperatures. The liquid solution used is a metal fluoride complex that slowly hydrolyzes after the addition of aluminum metal or boric acid [1]. These compounds are the fluoride scavengers. This means that they destabilize the fluorine complex and cause precipitation of the oxide. These films are usually produced from highly acidic aqueous solutions rather than basic solutions [2, 39-41]. In general, LPD can be used to deposit any metal oxide that forms stable fluoride complexes [2]. The main advantages of using this

deposition method is that sophisticated equipment and a large energy supplies are not needed [1]; the process is relatively simple and able to perform at low temperatures [42]. Despite these advantages, LPD is a wet chemistry or sol-gel technique which needs long solution preparation and involves slow deposition rates [2, 39-41].

2.1.2 Atomic layer deposition (ALD)

Atomic layer deposition or atomic layer epitaxy is used to produce epitaxial films and solid molecular films on solid substrates. In this process, monatomic layers can be developed in sequence. These reaction sequences are performed under controlled effective conditions (deposition rate, temperature, pressure, etc.) so that the surface reaction fully saturates to construct the monatomic layer. This allows the film to be coated uniformly onto complex geometries. The surface coverage by the film is determined by the quantity of the absorbed reactants. The saturation density of the precursor and the saturation mechanism will be influenced by the monatomic layer reformation that occurs in the sequence. This sequence also allows a greater range of reactants to be used [5, 43-50]. Moreover, the deposited film thickness can be adjusted and controlled precisely in the ALD process. It is possible to scale up this process to large surfaces and still be able to produce good quality films with good reproducibility and uniformity [5]. The main disadvantages of ALD are (1) the needs for high purity substrates to reach the desired products, (2) expensive reactor and processing conditions due to the need for high purity treatment system and working under high temperature for vaporization of precursors, (3) slow deposition rates and (4) needs for volatile precursors. This technique is not applicable for biological substrates being sensitive to heat or substrates that have fragile structure and large impurities. Moreover, it is mostly used for deposition of semiconductors [5, 43-50]. A schematic of an ALD reactor for nanoparticle coating is presented in Figure 2-2.
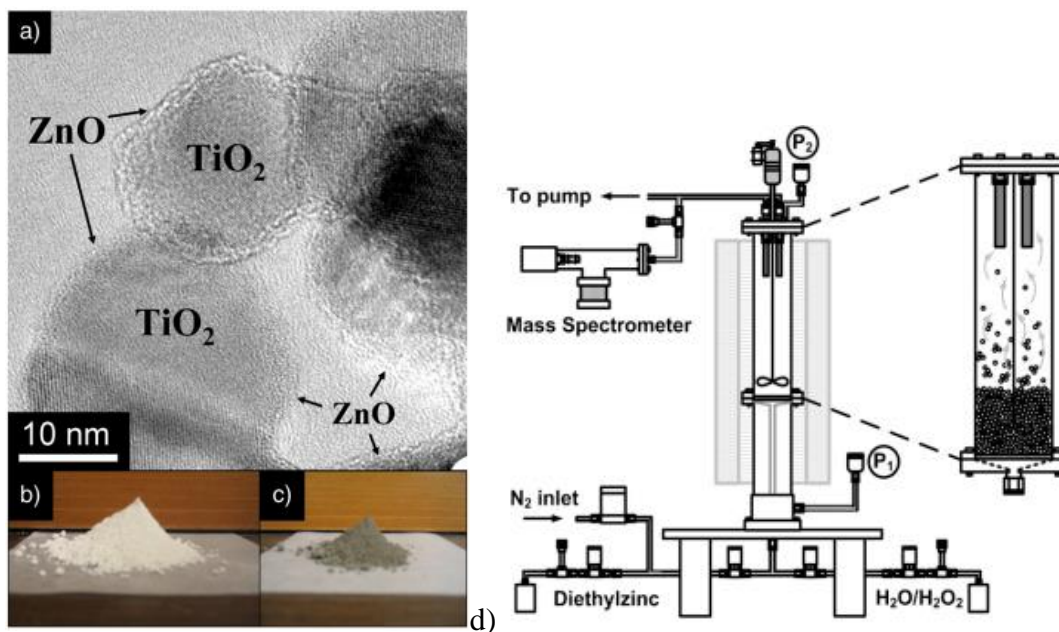
Figure 2-2: ZnO ALD deposition: a) HRTEM image of ZnO-coated TiO_2 nanoparticles; b) white color uncoated TiO_2 powder; c) gray color ZnO coated-TiO_2 powder at 177 °C process; d) schematic of the fluidized bed reactor [51].

2.1.3 Physical vapour deposition (PVD)

Physical vapour deposition uses pure gasified sources of materials through evaporation. Evaporation of materials is done using high power resistive heating, laser ablation, etc. Solid thin films are formed as a result of condensation of gasified materials on the surface without any chemical reactions. For PVD, either high temperature or high vacuum pressure or both are necessary. This is the main drawback of the process leading to high energy consumption. On the other hand, most of the designs need cooling water system to dissipate large heat loads. Most coatings produced via this process have good impact strength and stability for high temperature environment as well as excellent abrasion resistance and durability [52-54].

2.1.4 Chemical vapour deposition (CVD)

Chemical vapour deposition involves chemical reactions of gaseous reactants that occur in an activated environment, using sources such as heat, light or plasma. This lead to the formation of solid thin films or powders on the surface of substrates [5, 55, 56]. This chemical system presents

many advantages, such relatively low deposition rates (allowing for better control), and can exploit a wide range of precursors. In addition, CVD has the capability to create dense and pure materials. It can produce uniform coating on complex geometries with good reproducibility and it has the capability to easily control and adjust the deposition rate [5, 57]. The surface morphology, the orientation, thickness, adhesion, purity and the crystal structure of the resulting product can be controlled by adjusting the process parameters [19]. However, CVD also has a few disadvantages. The first difficulty is when one deposits multi-component materials onto a surface (multi-source precursors); this is because different precursors have different vaporization rates. Another disadvantage is that the cost of fabrication will increase when sophisticated reactors and vacuum systems are needed. Also, there may be safety and chemical hazard issues due to the usage of gas precursors [19].

2.1.4.1 Thermally activated chemical vapour deposition (TACVD)

This CVD process involves thermal energy, such as infrared radiation and resistive heating, to activate chemical reactions and produce a solid film. This process tends to exploit inorganic chemical precursors in a hot wall or cold wall reactor, with heating or cooling cycles [5, 20, 57]. This chemical process becomes limited because of the small range of possible monomers that can be decomposed [20]. Further, it is not applicable when heat-sensitive substrates are used.

2.1.4.2 Plasma-enhanced chemical vapour deposition (PECVD)

A plasma is a partially ionized gas composed of electrons, ions and electronically excited species [4, 5, 58-61]. At low temperatures, plasma-enhanced chemical vapour deposition applies electron and ion bombardment to initiate film deposition. Typically, high-voltage electrical power is applied to the system (at low pressure) to break down the gas and produce a luminous discharge. The free electrons found in the gas reactants are initially excited, but the ions are relatively heavier so they stay unaffected [19]. The low-pressure gas collides inelastically with the high-energy electrons to produce chemically active free radicals, ions and excited neutrals. These species react at lower temperatures. They can undergo chemical reactions at the surface of the substrate, leading to thin film formation [4, 62-65]. PECVD disadvantages include the requirement for vacuum systems and a sophisticated reactor design to generate and contain the discharge plasma [5]. This will lead to an increase in fabrication and operation cost. Also, PECVD depositions lack high purity because of the unreacted precursors and by-products that have not completely desorbed and remained in

the deposited film. PECVD cannot be performed at low frequencies because they incite unwanted compressive stresses on the films that can be damaging and lead to cracking [5]. Another disadvantage is that PECVD has low efficiency because large amounts of energy is wasted on low energy electrons. PECVD also leads to unstructured coatings with low cross-linking due to chemical reactions happening too rapidly (though this can be in part mitigated through pulsing) [20]. Moreover, PECVD deals with drifting and scratching/ and breaking the bulk of substrates (surface etching) and thus deposited film may penetrates into the bulk itself instead of just depositing on the outmost top surface layer of the substrate. PECVD drastically depends on the reactor configuration and all operational parameters should be revisited in case of any change in reactor configuration, affecting the reproducibility of the samples following scale changes [5, 66, 67]. Compared to TACVD, PECVD can take place at relatively low temperatures [4, 5]. This process can decrease deposition temperatures while having the capability of producing high quality films at tolerable deposition rates and it involves wide range of surface chemistries. This will be convenient and favourable when temperature sensitive substrates are used. Another advantage is that the microstructure and the deposition temperature can be separately controlled in PECVD. This process can be applied for surface modification of different geometries in a few seconds [5, 66, 67].

2.1.4.3   Photo-initiated chemical vapour deposition (PICVD)

PICVD process is a chain reaction initiated using photons as an energy source for polymerization of multifunctional monomers, oligomers, reactants and even polymers. Different terminologies have been applied for PICVD in the literature such as photo-assisted CVD (PACVD), photo-CVD, photopolymerization, and photo-induced CVD [20]. In this process, light is absorbed by the photosensitive reactive species, forming intermediates, such as free radicals, cations and anions, which carry out further reactions and result in polymerization. In this process, light absorption of the photo-reactive molecules and light emission from the source should overlap in order to produce intermediate molecules [68]. PICVD is regarded as an evolutionary dry technique for film deposition. It has several advantages: it is an efficient, environment friendly and potentially economical technique for surface modification due to its solvent free nature, low energy consumption and highly controlled selective deposition. Scale-up of PICVD may be readily feasible due to above-mentioned advantages along with possibility of surface treatment at

atmospheric pressure and temperature in one-step. Moreover, PICVD does not need pre- or post-treatment, and it can be applied to complex geometries [14, 69]. PICVD process can result in both photo-thermal and photochemical process depending on the photon energy. If the photon energy first converts to heat, film growth will be due to the photothermal process. (This process is often called laser chemical vapor deposition (LCVD)). In this process, precursor gases are transparent to the wavelength of the irradiation source. In a photochemical process, not only the precursors but also the substrate itself may absorb the photon energy in the form of heat and both may have effect in the film growth [19]. Given its potential, this technique is discussed in greater detail in the following section. PICVD needs either a photo-sensitive precursors or contributory photosensitive reagents to initiate the chain reaction. Moreover, most explorations of this approach have involved the use of expensive UV lamps with limited treatment area. Given the limited number of photo-sensitive compounds, expensive UV lamps, special windows for reactor design and small area treatment, PICVD process has not yet been scaled up [14, 69].

2.2 Photo-Initiated Chemical Vapor Deposition Technique: Basics and Fundamentals

Various parameters can affect a PICVD process, including:

(1) The wavelength and irradiance of light sources as well as the irradiation rate;

(2) The type, number and the amount of precursor used for coating;

(3) The type, number and amount of photoinitiators or photosensitizers;

(4) The operational parameters such as temperature and pressure, etc;

(5) The type, number and amounts of reactive reagents for functionalization.

2.2.1 Light source

In PICVD processing, the emission spectrum and number of available incident photons are crucial factors affecting deposition [70]. By wisely selecting the wavelength of the light source, the absorption of light by compounds will be maximized. Further, depending on the compound's absorption properties, different wavelengths may bring different excitation pathways and thus, different mechanisms. This leads to judicious consumption of energy and controlled

polymerization and functionalization towards selective reactions. The required energy for PICVD processing comes from photons, which are part of electromagnetic spectrum. Common optical radiation sources include (1) Infrared light irradiation, (2) Visible light irradiation (3) Ultraviolet light irradiation (4) Vacuum Ultraviolet light irradiation (5) Extreme UV (EUV) [71]. Figures 2-3 and 2-4 summarize light source classification and some common sources for PICVD.
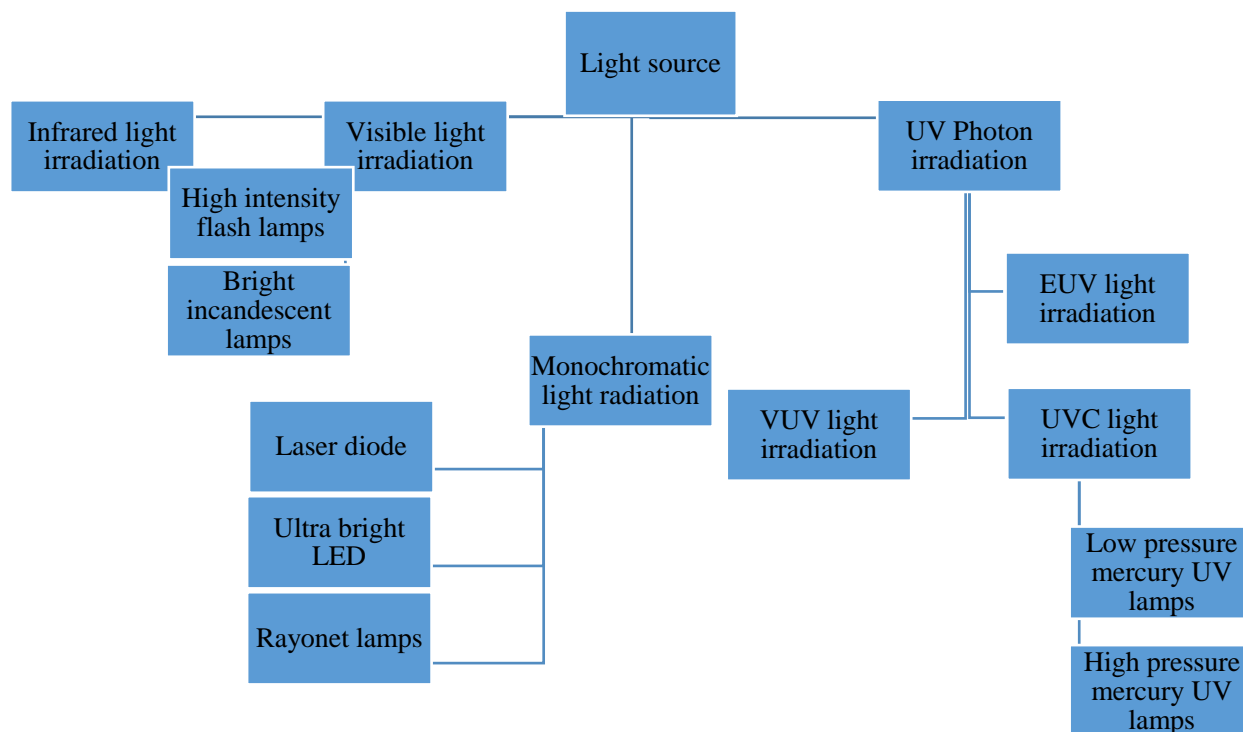
Figure 2-3: Light source classification
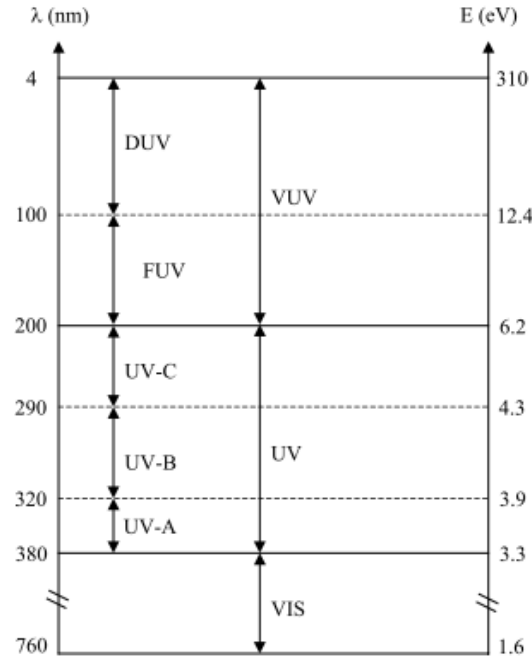
Figure 2-4: Photon wavelength and corresponding energy level for different types of light source [71, 72].

Focusing more specifically on UV (wavelength range), several different configurations are possible based on the wavelength of interest. Two classes of UV lamps have extensively been used in PICVD process; they are discussed in detail in this section.

2.2.1.1 Ultraviolet lamps

UV lamps consist of mercury and mercury amalgam with indium and gallium in order to control mercury vapor pressure, when the electric current passes through the electrodes of the lamps, mercury vapor will heat up and due to electron transmission, ultraviolet or visible light will emit. Based on the wavelength, UV lamps can be classified in UVC (100-280 nm), UVB (280-320 nm), and UVA (320-400 nm). Various types of UV lamps are currently used in surface engineering field including medium pressure (MP) UV lamps with UVC/UVB wavelength, low-pressure (LP) UV lamps with narrow UVC wavelength, microwave UV lamps and Light emitting diodes (LED) [73, 74]. UV LED lamps have some advantages over other UV lamps, in these lamps, no toxic mercury metal has been used and it has smaller dimensions compared to the UV lamps. These lamps consist of p-n junction semiconductor that emit irradiation due to diversity of semiconductor materials as

well as excess (negative or n-type) and shortage of electrons (positive or p-type). Most of UV LED lamps consists of GaN, AlGaN as semiconductor materials. These lamps produce wide range of wavelength and irradiance [73, 74]. VUV lights are another subsection of UV lamps like krypton lamps, deuterium lamps. VUV radiation refers to the wavelength domain between 112 and 200 nm with only two subdivisions: far ultraviolet (FUV) and deep ultraviolet (DUV) [72].

2.2.1.2 Excimers lamps

Excimer lamps are mercury free lamps using pure or mixed rare or halogen gases. These types of lamps have much lower efficiency (about 8%) compared to LP and MP Mercury lamps. Both Microwave UV lamps (which work by microwave power) and the exterior lamps are made of glasses with neither openings nor electrodes [73]. Excimer lamps are common light sources for surface coating. Generally, excimers can be classified under two main groups [12]: pure or mixed (1) rare and (2) halogen gases. Rare or halogen gases either as a pure or mixed produce different emission spectrum. Table 2-1 shows different excimer lamps and their corresponding peak wavelength [75].

Table 2-1: Pure and mixed gas excimer lamps with their respective peak wavelength [75].

Pure gas excimer	He_2*	Ne_2*	Ar_2*	Kr_2*	Xe_2*	F_2*	Cl_2*	Br_2*	I_2*
Wavelength (nm)	74	83	126	146	172	157	259	289	342

Mixed gas excimer	ArCl*	ArF*	KrCl*	KrF*	XeI*	XeBr*	XeCl*	XeF*
Wavelength (nm)	175	193	222	248	253	282	308	354

Photon flux (φ) is a parameter to compare the efficacy of the UV lamps. It is defined as the number of photons per second per unit area (Equation 2-1, Figure 2-5). The photon flux is related to the number of generated electrons due to excitation for light generation and thus the produced current.

However, it does not give information about wavelength and subsequently the energy of photons [76].

$$\varphi = \frac{number\ of\ photons}{sec.unit\ area} \qquad\qquad \text{Equation 2-1}$$
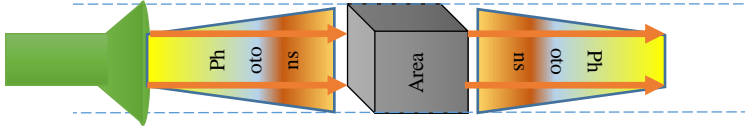
Figure 2-5: Photon flux representing the number of photons per second per unit area.

To determine the power density for a wavelength in units of W/m², the energy of the single photons (Joules) must be multiplied by the photon flux (Equation 2-2, Figure 2-6). Considering that the photon flux is the number of photons striking a surface in a given time, multiplying this parameter to the energy of the photons gives power density which is the energy striking a surface per unit time. Power density is expressed in W/m² and also called irradiance in most of the cases [76].

$$H\left(\frac{W}{m^2}\right) = \varphi \times \frac{hc}{\lambda}\ (using\ SI\ units) \qquad\qquad \text{Equation 2-2}$$

Where H: power density in units of W/m²; (φ): photon flux in Joules; h: Planck's constant in J·s; λ: wavelength in m; and c: speed of light in m/s.
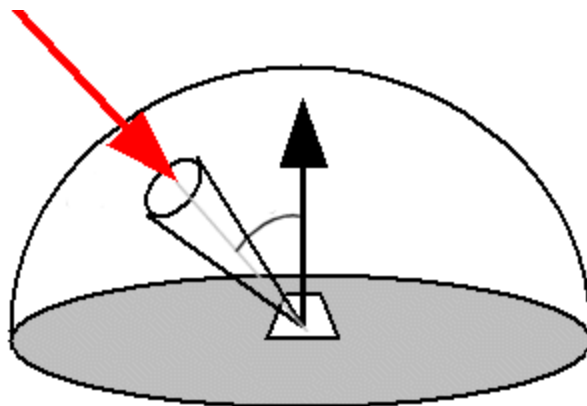
Figure 2-6: Representative figure of power density showing the energy striking a surface per unit time [77] (Image credit, MIT).

Photon fluxes vary according to the type of lamp. The delivered flux in Hg arc lamps, doped Hg lamps and electrodeless Hg lamps are high, typically > 1–2 W/cm². LEDs emitting at 365 or 395 nm can emit several W/cm² photon flux (up to 24 W/cm²). Hg-Xe, Xe lamps, halogen lamps, fluorescent bulbs and white or blue LED bulbs generally emit less than 10 mW/cm², while diode lasers emit in the range of 10–100 mW/cm² [70].

Low pressure Hg lamps (i.e. UVC lamps) emit light mainly at 253.7 nm (with a secondary peak at 185 nm). They are one of the most efficient lamps for thin film deposition since 60% of the electrical input converts to light, with 85% of the emission at 253.7 nm [73] . The irradiance (power density) of these lamps is low (0.002–0.004 W/m^2) while it can be improved by increasing the number of lamps or decreasing the distance of light source from the surface [73]. Very few studies focused on using UVC lamps for surface coating and particle encapsulation [78, 79].

Power density of excimers varies based on the type and amounts of excimer gases [75]. Numerous studies exploited Xe_2^* excimer lamps either in silanization or organic coating [80, 81] due to their high photon energy. Moreover, they are used for micro-patterning of UV curable polymers [82] and even deposition of nitrogen rich films [83, 84].

2.2.2 Window materials

Various materials absorb UV radiation at different wavelength. In order to supply light to a reaction chamber, specific window materials must be used, as a function of the desired wavelength (Figure 2-7).

Window Materials	Thickness (mm)
LiF	1.95
MgF$_2$	1
CaF$_2$	0.25
Sapphire	0.32
BaF$_2$	1.95
Suprasil (Enhanced UV transmission quartz)	10
Quartz	2
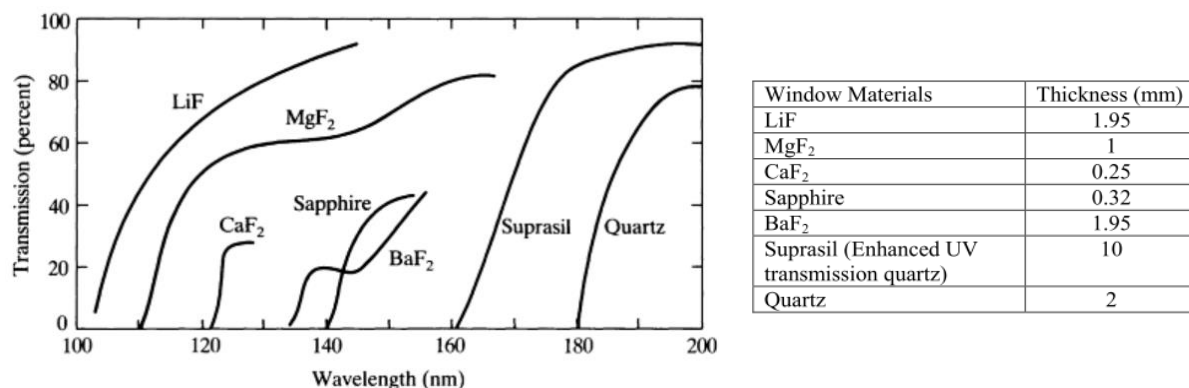
Figure 2-7: VUV transmission for readily available window materials in the market [19].

The need for specialized window materials, especially in cases where transmission below 170 nm is required (as in the case of VUV) results in high cost of the treatment process and deposition and limits the substrate size (~1 cm^2) [16, 17, 85] (considering that for these process, the price of window materials ranges from $200 (e.g. BaF$_2$ Disk with 13 mm diameter and 2 mm costs 224 USD and more for larger sizes) [86]. To partially circumvent the substrate size limitation, Wertheimer's group exploited a conveyor as a mobile substrate holder, which allowed them to deposit polymeric thin film on a flexible ribbon (1 cm wide by 24 cm long) [17].

2.2.3 Precursor selection

Precursor selection is another important factor in PICVD as it can directly determine the properties of the coating. Precursor selection will be affected by:

(1) the required bulk properties of the desired coating;

(2) the applied light source for chemical reactions;

(3) the reactor type and configuration;

(4) the desired application of the final coated surface;

Normally, organic compounds consist of polyatomic molecules with various bond energies. Chemical bond dissociation occurs when the incident energy of irradiated photons exceeds the bond energy. UV absorption by the compound and irradiated incident energy should be greater than this bond energy to result in primary or complete bond cleavage. Therefore, the required energy for bond cleavage is a pertinent parameter to select the appropriate light source [87]. Various types of UV lamps emit photons with 4.88-15 eV (253.7-82.6 nm or 112.54 -346 kcal/mol) energy which are capable of breaking most chemical bounds between carbon, hydrogen, oxygen and halogens [12, 71]. Table 2-2 shows the bond energy of common chemical bonds, with the corresponding wavelength required for their breakdown (assuming the molecule absorbs at that wavelength).

Table 2-2: Required energy and corresponding wavelength for common chemical bond cleavage (adapted from [88]).

Bond	Energy (eV)	Wavelength λ (nm)
C≡C	8.7	142.5
C=C	6.9	179
C-C	3.7	336
C-Br	1.9-3.0	408-636
C-Cl	2.6-3.7	332-477
C≡O	11.1	111.6
C=O	8.3	149.4
C-O	3.5-4.3	286-357
O-O	1.5	817
O-H	3.7-5	249-336
C-H	4.1-4.9	286-301

Molecular structure, viscosity, functionality, absorption peak and number of reactive entities per molecule affect precursor reactivity, the reaction pathways and the structure of the final product (linear or cross-linked polymerization) [14].

Precursor should either absorb UV light, or have functional reactivity to the radical/excited species or anions/cations produced from photoinitiators (PIs)/photosensitisers (PSs) upon UV exposure (see section 2.2.4). If a precursor has unsaturated groups, it can also react with other chemical reagents in PICVD system (instead of directly with the desired substrate) [89]. The absorption cross section (ACS) and absorption coefficient are two known definition in the photochemistry of materials. These two terms are related to the ability of a compound to absorb specific wavelengths and, thus, exciting and producing reactive species under that radiation. ACS spectra for most compounds can be found in the literature [90-92], with the HITRAN database and Max-Planck Institute for Chemistry in Germany being the most popular references for organic compounds [93]. Based on ACS and the information from Table 2-2, one could speculate if the photochemical reaction can occur at a given wavelength [94].

Many of the monomers discussed herein applied in the liquid phase; however, the scientific principles are fully transferable to gas phase studies. Many researchers have studied photopolymerized systems involving acrylate compounds, because these have high reactivity, greater than methacryllic, allyl and vinyl groups (in order of increasing reactivity: vinyl group < allyl group < methacrylic group < acrylic group) [89]. Another type of monomers worth mentioning are monoacrylates that include a carbamate or oxazolidone. These monomers are extremely reactive due to the high propagation rate and low termination rate; they are able to increase the photopolymerization rate extensively. It was also observed the polymers generated this way are insoluble in water [95] . Acrylate-based monomer and its derivatives can be often polymerized without PIs [14, 96, 97], due to their poly-functionality and self-initiating reaction structure.

Monomers with more than one reactive group render termination steps less effectively. These monomers are capable of producing thicker and more cross-linked polymers compared to uni-functional monomers (which lead to the generation of linear polymers) [96]. Silicone acrylates have the highest reactivity of PI-free coating systems, but are very sensitive to the presence of oxygen in the reactive environment, requiring inertization [14].

Allen et al. have classified monomers into two main groups based on their functionalities. Generation I have either one or two functionalities and normally have low viscosity. They are used as diluent monomers and include compounds such as methyl methacrylate and styrene. This group however has strong odor and toxicity and therefore their application has decreased. Generation II are called prepolymers and have more than two functionalities. Examples include glycerol propoxylate triacrylate and urethane acrylates [89] .

Vinyl groups are also well-known reactive functional groups for free radical polymerization (FRP: see section 1.2.5) [96]. Blyth and Hoffmann were able to polymerize styrene under sunlight to produce glass like material. Later on, Berthelot and Gaudecheon utilized UV light to polymerize ethylene [68]. Vinyl ethers are extremely versatile. By varying the composition and choosing the correct photo-initiators and co-polymers, polymers with specific properties can be generated. The rates of polymerization for vinyl ethers differ as well due to the nucleophilicity of different functional groups on those monomers [95]. In general, the polymers formed from vinyl-based monomers possess low elongation, toughness, impact resistance and tend to be glassy and brittle [98].

Liu's group has explored the usage of multifunctional thiols and enes: two diene monomers with phosphor groups including 1-methacryl-allyl ethoxyethyl-diphenyl phosphate and bis-(1-methyl methacryl)-methyl-diphenyl phosphate as well as oxygen containing trithiol: N,N-bis(ethyl 3-mercaptopropionate)-3-mercapto-propionamide, for photopolymerization under 365 nm UV light to reduce the oxygen inhibition effect and to produce hard coating with high flexibility [98].

Montero et al. (2008) from Prof. Gleason's group [99] applied PICVD for the copolymerization of vaporized pentafluorophenyl-methacrylate (PFM) with hydroxyethyl methacrylate (HEMA) onto silicon substrates. (Figure 2-8). Both deposition rate and functionalization were the focus of this study. They either introduced the two monomers simultaneously (constant HEMA flow rate), varying the PFM flow in order to tailor functionalization via amine groups (O,O-bis (2-aminoethyl) polyethylene (PEG-diamine)), or used graded copolymerization, whereby they introduced PFM into the reactor after 90 nm of HEMA film had been deposited, in order to confine the functionalization with PFM in the near surface region (~20 nm).
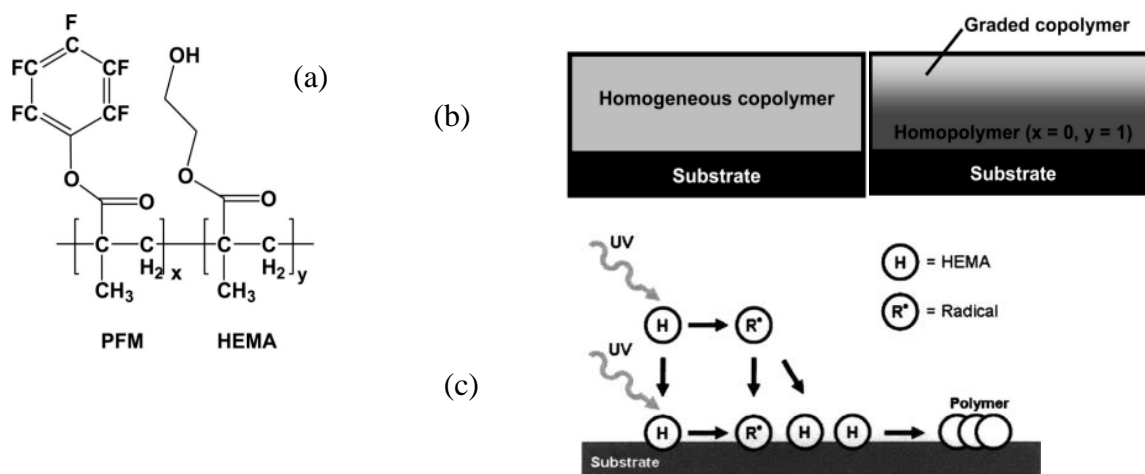
Figure 2-8: Schematic of the (a) chemical composition (b) physical structure of the homogeneous and graded copolymer films and (c) reaction mechanism [99].

2.2.4 Photoinitiators (PIs) and photosensitizers (PSs)

Since most monomers lack the ability to generate sufficient active species, photoinitiators (PIs) and photosensitizers (PSs) are often used in the polymerization process to increase the number of reactive species, radicals, anions or cations. The most important characteristics of PIs are the ability to absorb the wavelength/energy from the light source and the production of a sufficient number of active species for initiation. In the case of PICVD, which is a gas-phase process, it is important for PIs to have high vapor pressure so that even if liquid PIs are injected into the reactor, they are able to vaporize or atomize within seconds to react with gas molecules [69, 89, 100, 101]. Despite the fact that many of the monomers discussed herein applied in the liquid phase; the scientific principles are fully transferable to gas phase studies.

In cases where PIs fail to absorb the energy provided by the UV light or are unable to generate enough reactive species to initiate polymerization, PSs can be added to enhance the rate of polymerization. PSs are capable of acting as electron and hydrogen donors in interaction with excitable molecules. Thus, the PSs absorb the UV radiation and transfer energy to PIs or non UV-sensitive compounds in order to activate them [96, 102]. These compounds can have great effect on the final product by leading the reaction through their radicals and active molecules. They have the potential to accelerate film deposition in low-energy irradiation. Thereby, PIs and PSs determine and control conversion, and speed of reaction as well as molecular weight of final

polymeric film [14, 69, 97]. The main difference between PIs and PSs is that although PIs are consumed in the reaction PSs are not. In the case of PIs, by-products are formed while reactions with PSs are safe from extra by-products [20].

Hong and coworkers have explored using benzophenone (BP) in combination with isopropylthioxanthone (ITX) as PIs. They discovered that ITX acted as a PS to improve the efficiency of polymerization and final hydrophilicity of the film. It was also hypothesized that ITX can form an excited-state complex while transferring energy or electrons to BP and hence generate more reactive species [103]. Another thiophene derivative, 3,2-diphenyldithieno [3,2-b-2,3-d] thiophene DDT, can act as a PS along with a diphenyliodonium hexafluorophosphate PI for photopolymerization of acrylic monomers, specially tri methylol propane triacrylate (TMPTA) [71]. Common PS belong to the alcohol, ether, amine or thiol families. Tertiary amines with their high efficiency and relatively low cost are among the most common PSs [96].

Some monomers are very stable and need very short wavelength irradiation (refer to section 2.2.3 on precursor selection). On the other hand, high-energy irradiation may cause cross-linking and branching. In this case, PIs and PSs can allow initial radical production for backbone breakdown. Another great advantage of photoinitiated polymerization is that the coating generated can be thermally degraded into copolymers that can be dissolved without damaging the substrate. Although PIs expedite the reaction, they may cause instability, discoloration and unpleasant odor in the final product due to their reactive nature. A major drawback of these compounds is the aging of the final formulation due to migration or rearrangements of remaining molecules of PIs [14, 104]. During functionalization and encapsulation of surfaces, some of the active functionalities decay over time, which is called "aging"[35]. Structural retention and integrity are other crucial features of polymeric films that closely correspond to the stability of functional groups [69]. Macromolecular PIs are the best choice for avoiding decomposition of final formulation due to either their stable reactive compounds or internal bonding with the product. PIs are classified into three main groups based on the initiation process [95, 104-107]:

(1) Photo-cleavage radical PIs: PIs with aromatic carbonyl compounds participate in reactions via C-C bond cleavage upon UV exposure. This group is among the most effective due to production of two radicals. Most of PIs in this category are based on benzoyl functionality, given its high reactivity [95, 104-107].

(2) Hydrogen abstraction radical PIs: Some aromatic ketones are first excited to their singlet state and then triplet state upon UV irradiation. In this state, they tend to perform hydrogen abstraction reaction from H-donor molecules and produce surface radicals [89, 104]. Benzophenone and its derivatives (benzils, camphorquinone, terephthalophenonese and xanthones) are among the most common PIs of this group due to their high reactivity and effectiveness, and incapability of proceeding chain reaction without H-donor molecules [95, 103-107]. The efficiency of polymerization can also be increased through addition of tertiary amine as co-initiator to hydrogen abstraction PI system, especially for carbonyl and thioxanthane initiators [104]. Radicals such as α-amino alkyl, formed through the hydrogen abstraction process, have great reactivity with unsaturated monomers. Another advantage of tertiary amines is that they can reduce the oxygen quenching effect through a peroxidation process. Oxidation can also be prevented by adding thiol and phosphate compounds to react with oxygen or use oxygen insensitive monomers [89].

(3) Cationic PIs: Protonic acids are powerful cationic PIs that produce radicals in the presence of H donor molecules upon UV exposure. Cationic PIs initiate polymerization through the production of Lewis or Brønsted acids and are mainly used in the polymerization of epoxy and vinyl ether monomers. During the formation of protonic acid, radicals can also be produced, which can be used to polymerize acrylate monomers. Hence, these PIs can be used on their own or mixed with radical PIs (forming a "hybrid initiator"), to polymerize acrylate and epoxy systems [89, 95, 104]. Despite the lower capacity of cationic PIs, their main advantage over the previous PIs is that they are used extensively due to their insensitivity to the atmospheric oxygen and quenching processes. Also, their effectiveness continues post polymerization in the absence of a light source [95].

2.2.5 Polymerization mechanism

Based on generated photo-reactive intermediates, PICVD can be classified into three main polymerization mechanisms: (1) Free Radical Polymerization (FRP), (2) Cationic Polymerization (CP) and (3) Anionic Polymerization (AP), or a combination thereof [70]. However, the free radical mechanism is the most common [68, 96, 104, 108].

FRP consists of three steps: Initiation, Propagation and Termination (Table 2-3). In the first stage, the reactive species (RS) are raised to an electronically excited state (by promotion of an electron to higher energy orbital), generating radicals (R•). RS can be monomers, PI or PS compounds. Through collision of these radicals with monomers, chain initiating radicals RM1• are produced.

Then, propagation will continue by successive additions of other monomers, intermediates and oligomers. The chain increments result in either linear or cross-linked polymers [68, 96, 108]. Spatial radical formation leads to cross-linked polymers that are denser than linear varieties. Eventually, macromolecules, radicals, RS and monomers collide and radical coupling or disproportionation takes place and polymerization growth stops [68].

Table 2-3: Mechanism of free radical polymerization [68, 96, 108].

$RS \rightarrow RS^* (hv) \rightarrow R\bullet$	Initiation Stage
$R\bullet + M1 \rightarrow RM1\bullet$ $RM_n\bullet + M \rightarrow RM_{n+1}\bullet$	Propagation Stage
Coupling: $R1M_n\bullet + R2M_m\bullet \rightarrow R1M_{n+m}R2$ Disproportionation: $R1M_n\bullet + R2M_m\bullet \rightarrow R1M_n + R2M_m$	Termination Stage

The same procedure takes place in cationic and anionic polymerization, except that in those cases, cationic and anionic species initiate the polymerization [68, 96, 104, 108]. PIs tend to play an important role in cationic and anionic polymerization, with dialkylphenacyl sulfonium salt (DPS) photoinitiators being the most common for cationic polymerization. On the other hand, solutions of ethyl acyanoacrylate (abbreviated CA) containing $trans\text{-}Cr(NH_3)_2(NCS)_4-$ causes rapid anionic polymerization under visible light irradiation [68].

2.2.6 Impact of operational parameters

Surface functionalities and coating thickness are dictated by operational parameters, including the light source, monomer and environmental conditions.

2.2.6.1 Emission spectrum and wavelength

When the first layers of deposition are produced, penetration of UV lamps into the organic coating layer and the intensity gradient within the coating layers strongly affect the reaction conversion. This leads to thicker coating for less UV absorbent monomers in that wavelength [14]. For instance,

aliphatic acrylates have lower extinction coefficients compared to the aromatic acrylates at 222 nm. This conduct deeper penetration of UVC radiation in these monomers and formation of thicker photopolymerized layers [109].

2.2.6.2 Light intensity

In general, increasing light intensity can increase the rate of polymerization because of the excess heat generated. The heat can increase the mobility of monomers and thus conversion. However, for multiacrylate monomers, as the light intensity reaches a certain limit, the rate of polymerization will remain constant. Reactive species are still being generated, but the diffusion of the monomer limits the rate of polymerization [95]. The Beer-Lambert law is one of the first laws that is applied on PICVD processes [110]. In this law (Equation 2-3), the number of gas molecules, N, intensity of the optical source, I, and absorption cross section (ACS) of that gas media, σ plays role.

$$I_t = I_i\, e^{-N\sigma L} \hspace{4cm} \text{Equation 2-3}$$

Where I_i and I_t are the optical intensities (W.cm^{-2}) incident upon and transmitted by the gaseous medium, respectively. σ is the ACS (generally expressed in cm^2) for the gas precursors at that wavelength. In cases where molecules of gas absorb more than one photon, we will have following reaction for photo dissociation of precursors:

precursors + nhν → products
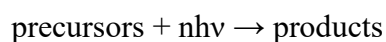
Therefore, rate of reaction is defined by Equation 2-4:

$$R = \sigma^n \left(\frac{I}{h\nu}\right)^n \hspace{4cm} \text{Equation 2-4}$$

Where I is the transmitted optical intensity (in W.cm^{-2}) and n is expressed in units of cm^{2n}-(s)$^{n-1}$ [i.e., cm^2 for n = 1, cm^4-s for n = 2, cm^6-s^2 for n = 3]. For n>1, it is a nonlinear equation. This is typically the case of high intensity processes like photochemistry via laser, and mostly with polyatomic molecules [110]. However, this equation (Equation 2-4) only applies when the gas-molecules have the ability to absorb the photon from the optical source. The absorption cross-section is a function of the wavelength of the light source. In systems using PIs, the chain reaction

is controlled by the initiation rate of the PI. This initiation rate is governed by following equation [95]:

$$r_i = \emptyset_i I_i [1 - exp(-A)]$$ Equation 2-5

In which r_i is the rate of initiation; Φ_i the quantum yield of initiating species; I_i: incident light intensity and A: light absorbance of PIs.

Based on Equations 2-4 and 2-5, the reaction rate is directly increased by increasing the light intensity of the UV lamps, which in turn affects the extent of polymerization. Intensification of light from 0.25 mW/cm^2 to 24 mW/cm^2 during photopolymerization of methacrylic acid and tri(ethyleneglycol) dimethacrylate mixture (100/1 mol) in the presence of Irgacure 651 as PI, lead to a polymerization rate increase from 2.0×10^{-3} s^{-1} to 1.2×10^{-2} s^{-1}, which in turn lead to a 20% increase in monomer conversion [96].

Furthermore, light intensity affects the linear and cross-linked structure of polymeric films. He et al. investigated this effect on the photopolymerization of methyl acrylic acid (MAA) hydrogels with tri(ethylene glycol) dimethacrylate under a wide range of UV irradiance (2.0–24 mW/cm^2). They observed that greater light intensity causes fast gelation and thus a less cross-linked structure. Indeed, monomers cured with low light intensity have more time and greater chance for spatial radical formation, leading to more compact and cross-linked structures [91].

2.2.6.3 Oxygen content

Oxygen is one of the great radical scavengers due to its electronegativity. In addition, oxygen molecules absorb UV radiation (in < 240 nm wavelength). In other words, PICVD can be inhibited because radicals are either consumed through scavenging, or their formation is suppressed through decreased light intensity. Experimental results with oxygen in the presence of acrylate monomers showed that below 1000 ppm oxygen content in the reactive environment, there is no great impact on photopolymerization kinetics due to radical scavenging [14]. Traditionally, several additives have been added to reduce effect of oxygen content by either consuming oxygen (e.g. metallic copper or ascorbic acid) or producing extra radicals (e.g. H_2O_2, which decomposes to OH radicals) [96]. Oxygen can also have an important impact on effectiveness of PIs and PSs and constrains the mobility of active species. If the ambient oxygen content is high, it is more likely that the radicals will be quenched by oxygen and thus the initiation rate will reduce [69, 89, 100, 101].

The effect of oxygen concentration without any added photosensitizing agent on the photopolymerization of Tetrafluoroethlene (TFE) was studied at 2537 Å and 1849 Å. The experiment conducted at near atmospheric pressure (800 mm Hg) and at near room temperature (30 °C). However, the gas temperature, due to the direct UV lamp irradiation, was in the range of 50 °C to 60 °C. The results showed at concentration of oxygen up to about 20 ppm that the oxygen initiated the photopolymerization of TFE towards producing polytetrafluoroethylene (PTFE). However, at higher concentrations, oxygen acted as an inhibitor, i.e. formation of PTFE was inhibited until most of the oxygen had been consumed. At this point, homopolymerization of the olefin occurs along with an auto-acceleration. Moreover, the photolysis of TFE, with or without oxygen, was studied in the presence of excess of N_2O and N_2. Similarly, in case of low partial pressure, oxygen was nearly completely consumed to give tetrafluoroethylene oxide and carbonyl fluoride as the primary products of the reaction in a 1:1 molar ratio; however, when the molar ratio of oxygen: TFE was greater than 1:6 the formation of PTFE was inhibited while poly (oxydifluoromethylene) was formed. The production rate of poly (oxydifluoromethylene) and other oxygen containing volatile products reached to a maximum, and at higher oxygen concentrations the production rate of poly (oxydifluoromethylene) was constant. The same experiments with lower partial pressure of TFE monomer resulted in formation of smaller amounts of tetrafluoroethylene oxide and perfluorocyclopropane compared to carbonyl fluoride and poly (oxydifluoromethylene). This study shows that oxygen even can affect the mechanism of photopolymerization and end products in some cases.

2.2.6.4 Temperature

The thermal decomposition of the precursors in the gas phase and/or substrate surface occurs based on two different mechanisms:

1) photo-thermal or pyrolytic mechanism, in which raising the temperature of the substrate causes thermal decomposition of the precursor in the gas phase and/or on the substrate surface.

2) photolytic mechanism, in which photoreaction of precursor occurs in the gas phase followed by decomposition of the intermediate products on the surface [5].

In the photo-thermal mechanism, light sources (such as pulsed lasers) provide a localized surface heating without increasing the temperature of the bulk substrate. The temperature is sufficiently high to initiate the thermal reaction, but not to cause thermal damage to the substrate.

The substrate temperature plays an important role on film deposition too. Increasing the substrate temperature can promote surface reactions, but can also lead to desorption of both precursors and products [20]. For instance, Tsao and Ehrlich [111] have shown that slight heating from 23°C to 28°C in UV photopolymerization of methyl methacrylate (MMA) on silicon (Si) may reduce the coverage of deposited film by a factor of three, reflecting weak Van der Waals bonding for adsorbed layers. Also, the results reported by Hsieh and Zellers [112] confirmed this behavior for polymerization of MMA, (trimethylsilyl)methylmethacrylate (MTMS), (phenyldimethylsilyl)methylmethacrylate (MPDM), and ((tris-trimethylsiloxy)silyl) propylmethacrylate (PTTMSS, 20% difunctional siloxane) on substrate of silicon, glass, and synthetic quartz ([113]). They observed that the deposition rate is inversely related with substrate temperature in the range of 5°C to 35°C, and that at certain monomer pressure, there was no measureable film formation above a critical temperature of substrate. The maximum temperature at which polymer films can be formed on the surface depends on the partial pressure and type of monomer. For instance, for MMA, MTMS, and PMTMS the critical temperature was 30°C, 15°C, and 10°C, respectively. However, in the photolytic mechanism, light sources at wavelengths $\leq$ 250 nm (in the UV spectrum) lead to the non-thermal formation of radicals from gas precursors. Therefore, deposition can occur at lower temperature compared to the photo-thermal mechanism, and remarkably lower than the other types of CVD techniques. This is one of the main advantages of this method compared to the other CVD techniques. According to the photoreaction rate (Equation 2-6), the temperature of the gas phase including vapor precursor, PSs or PIs affect the process through reaction rate. As Equation 2-6 shows an increase of temperature leads to an increase of the photopolymerization reaction rate.

$$R_a = (I_i/hv)\Phi . exp(-\sigma(\lambda)pl/kT) \hspace{4cm} \text{Equation 2-6}$$

Where:

R_a: rate of reaction; I_i: incident UV intensity (W); $h\upsilon$: photon energy (J); Φ: photochemical quantum efficiency(dimensionless); $\sigma(\lambda)$: absorption cross section (m^2); p: partial pressure (Pa); l: optical path length (m); k: Boltzmann's constant ($J.K^{-1}$); T: vapor temperature (K).

Scherzer et al. [114] investigated the kinetic profiles of photopolymerization of tripropylene glycol diacrylate (TPGDA) with 0.1% 2benzyl-2-dimethylamino-1-(4-morpholinophenyl) butane-1 as photoinitiator. They found out that by increasing the temperature, the reaction rate increased after 35% conversion. They claimed increasing the temperature lead to the enhancement of the segmental mobility in the network and this makes more residual double bonds accessible for polymerization. Tryson et al. [115] also found that the temperature affects the photopolymerization rate only at higher conversion rates, but no effect was observed at lower conversions. On the contrary, Broer et al. [116] and Lecamp et al. [101] indicated that there is a maximum reaction rate occurring at a specific temperature between the glass transition temperature and the thermal polymerization temperature of the reactants, followed by decreasing the reaction rate at higher temperatures. They showed there is an Arrhenius-like behavior at lower temperatures. Also, the reaction rate decreases because of various reasons such as: (1) evaporation of monomer or photoinitiator (which decreases the mobility and diffusion of reactants), (2) thermal degradation of the photoinitiator, (3) thermally initiated dark reaction, (4) interference of thermal polymerization on photocalorim and (5) shrinkage of the sample or coating. Scherzer et al. [114] clearly showed that these phenomena do not have a significant effect on the photopolymerization of some monomers under determined irradiation conditions and in a specific temperature range (25–100 °C).

2.2.6.5   Monomer structure, volatility, viscosity and ratio

The molecular structure of the monomers greatly affects the initiation mechanism. The polymerization rate is controlled by three main parameters [95]:

(1) Chemical structure of the monomer: the amount and reactivity of functional groups.

(2) Concentration of the monomer.

(3) Viscosity of the monomer; in the case of liquid monomers.

Monomers with self-initiating structures like brominated aromatic acrylates do not need PIs to initiate and promote the reaction [117]. Polymers produced by catalyst- or PI-free polymerization

are of interest for medical applications since they have less impurity and do not have the disadvantages of ageing in PI-assisted systems.

Several studies showed that the structure of deposited film mainly affected by the structure of the monomer and photolysis parameters, and photons selectively react with first triple-bonded sites, then double-bonded sites [118-123].

Density of functional groups formed on the surface, as well as polymeric film growth can be controlled by changing the composition and flow rate of monomers in the incoming feed gas. Previously we mentioned that Montero et al. (2009) [99] worked on photopolymerization of pentafluorophenyl-methacrylate (PFM) with hydroxyethyl methacrylate (HEMA) onto silicon substrates (see section 2.2.3). In this study, they changed the molar composition of PFM in the gas stream from 0% to 71%, and they found that film composition was different from the gas composition. They related this aspect to the difference in volatility and reactivity of the participating monomers in the reaction [99, 124]. Tsao and Ehrlich [111] investigated both monomer surface coverage and polymerization rate as functions of partial pressure of monomer in a series of separate experiments. The partial pressure of the monomer is a crucial parameter that can highly affect the polymer growth rate. The monomer pressure in the gas phase determines the number of collision of gas phase molecules with the surface, which then continuously refills the surface with fresh adsorbed monomer and allows the polymerization reaction to continue. Furthermore, the greater the number of molecules in the gas phase, the higher the probability of breaking the monomer bonds and formation of free radicals. Several studies investigated the effect of monomer pressure on the polymerization rate. The mercury-sensitized photolysis of tetrafluoroethylene (TFE) with UV light of 253.7 nm was first studied by Atkinson [125]. During the reaction, the pressure falls and a white solid powder, polytetrafluoroethylene $(CF_2)_n$, is formed, with perfluorocyclopropane as a secondary product. To study the mechanism of this reaction, several studies have been performed [126-128].

The polymerization reaction could be carried out at sub-atmospheric, atmospheric or super-atmospheric pressures, and at temperatures between about 10 °C and 150 °C, preferably about 25 to 80 °C. They showed the produced polymers have physical properties identical to polytetrafluoroethylene produced by known wet chemistry approaches, e.g. by polymerization in aqueous suspension or emulsion using heat and/or peroxygen catalysts. The rate of change in

pressure of TFE is a measure of the rate of formation of polymer. Experimental data showed that increasing the partial pressure of nitrous oxide (N_2O) at approximately constant partial pressure of C_2F_4 strongly affected the reaction time: the addition of 6.5% of N_2O may double the reaction rate. Previously, Heicklen and Knight [129] had showed photosensitized decomposition of N_2O upon mercury lamp exposure caused production of oxygen atoms in the presence of TFE and oxygen. This lead to acceleration of polymerization reaction.

For the first time, Tsao and Ehrlich [111] showed that the rate of photopolymerization of MMA was a function of the reaction kinetics of surface-adsorbed monomer and hence depends upon the partial pressure of monomer and substrate temperature. They showed, at pressure beyond 10 Torr, multilayer adsorption begins at the surface and dramatically enhanced by increasing the pressure. They have not shown any graph, but they claimed that slight warming reduces the coverage greatly, e.g. at 29 Torr the surface coverage will decrease by a factor around 3 due to temperature increase from 23°C to 29 °C. Hsieh et al. [112] studied the controlled growth of poly methyl methacrylate (PMMA) film on the surface of different substrate used as microanalytical system in the absence of photoinitiator. Their results with different monomers including methyl methacrylate (MMA), (trimethylsilyl) methylmethacrylate (MTMS), and (phenyldimethylsilyl) methylmethacrylate (MPDMS) on untreated glass substrate were in agreement with the earlier results reported by Tsao and Ehrlich. Deposition rate varied directly with the partial pressure of MMA monomer in the pressure range from 15 to 80 Torr. However, the growth rates were consistently lower for MTMS and MPDMS monomers compared to MMA due to the low vapor pressure of these monomers. More recently, Gleason's group have synthesized an ultrafine swellable film of hydrogel poly(hydroxyethyl methacrylate) (pHEMA) using PICVD process by varying partial pressure of monomer (HEMA) while the residence time was kept constant [6]. By analyzing the films produced at different monomer partial pressures, they demonstrated that the swelling properties can change considerably. Comparing these results with another set of experiments at different gas flow rates (different gas residence times), they suggested that polymerization occurs on the surface rather than in the vapor phase, and the surface chemistry is the dominant initiation mechanism for film formation.

2.2.6.6 PIs and PSs concentration

PIs concentration plays key role in the depth of curing, the structure of final products, as well as the reaction mechanism and polymerization kinetics [95, 103-107]. These are directly affected by the light absorbance and therefore initiation rate based on Equation 2-7:

$$A = \varepsilon\, I\, [PI]$$ Equation 2-7

In which A is Light absorbance; l: sample thickness; ε: absorptivity of PI and [PI]: concentration of PI. This is extensively discussed in section 2.2.4.

2.2.6.7 Reactor design

There are four main components in PICVD reactors: (1) gas precursor media, (2) optical source, (3) substrate (4) deposited layer or coated film and (5) Exhaust system (Figure 2-9). Although all PICVD reactors consists of these components, there are different configurations associated to these elements [19].
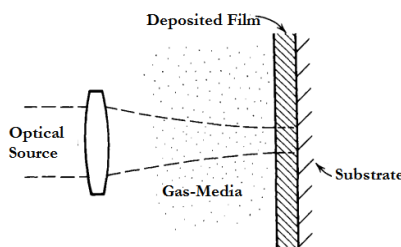
Figure 2-9: Basics of PICVD reactors [19].

Optical beam irradiation to the substrate can be either perpendicular or parallel. Based on this, there are four photo-beam delivery models onto the substrates (Figure 2-10).

(a) Spot focus

(b) Projection

(c) Line focus
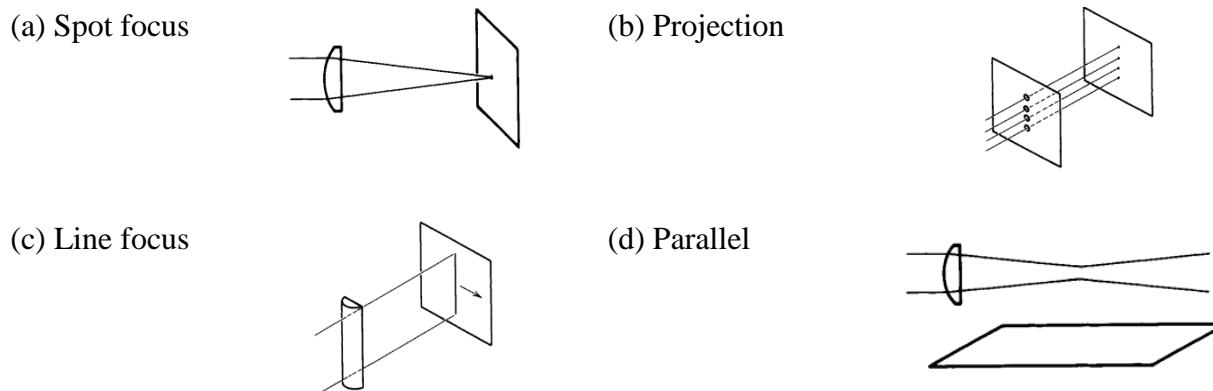
(d) Parallel

Figure 2-10: Most common optical delivery of beam to the substrate: (a) Spot focus, (b) Projection, (c) Line focus, (d) Parallel: (a) and (b) mostly used for small features and spatially selective deposition while (c) and (d) are applied for large-area deposition techniques [19].

The simplest mode is spot focus, which centralizes the beam at one point. Projection mode is common in the case of patterned deposition using a mask to pattern the optical source. Both spot focus and projection modes are optimal when selective, small area deposition is desirable. Both line focus and parallel modes are applied for large area deposition. Contrary to (a), (b) and (c), in parallel mode (d), the beam is not irradiating the substrate directly; therefore, photochemical reactions occur in the gas phase and produces reactive species that migrate and react with the surface (or with each other to finally deposit onto the substrate). In this configuration, the chance of thermal decomposition or secondary changes of coated substrate decreases [19]. Figure 2-11 shows some of the common PICVD reactors used in the literature.
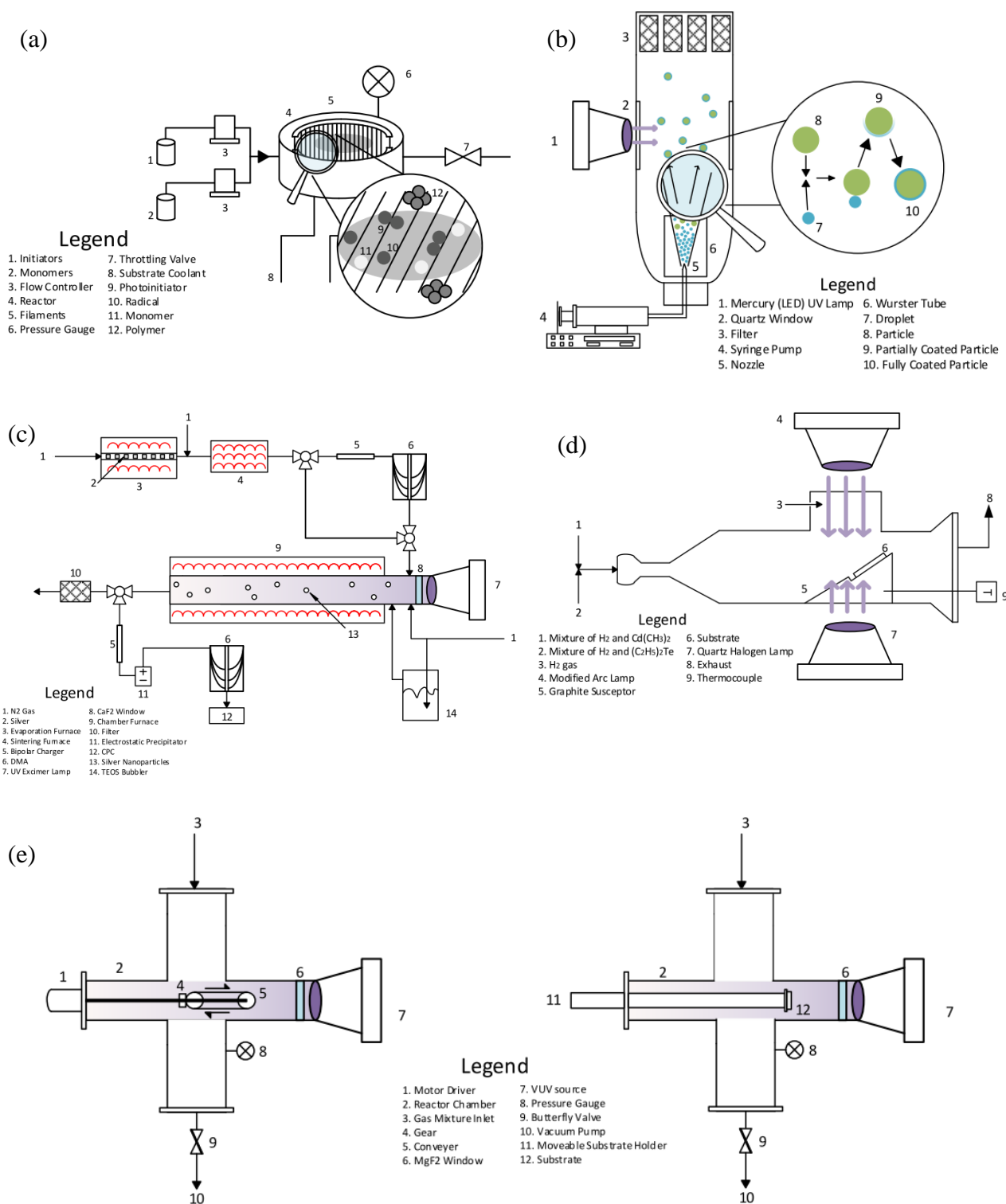
Figure 2-11: Summary of popular PICVD reactor designs in literatures: (a)[124, 130, 131];(b)[132]; (c)[133, 134]; (d)[19]; (e)[13, 15-17].

2.2.7 Functional moieties

Surface functionalization is a unique implementable method to tune surface properties based on the desired application. Generally, there are two paths to add functionality to the surface. First strategy is based on introducing functionality in one step and second method requires bifunctional reactive agents. In this second method, one functionality couples to the surface, while the other is responsible for functionality growth (Figure 2-12) [135]. Surface treatment can be done by using either the polyfunctional polymeric monomers or secondary surface treatment using dendrimers reagents after the coating with a layer of polymers which does not have all required functionalities [35, 136]. Usually, surface functionalization is achieved by selecting monomers containing desired functional groups. Sometime, initial coating of the surface with organic polymers does not have all the required functionality, therefore secondary treatment is required. Selected polymers need to undergo surface treatment for additional functionalization, which is called "grafting". This is either due to the inert nature of the selected polymers (polymers does not have required functional groups) or need for multifunctional moieties [35, 136].
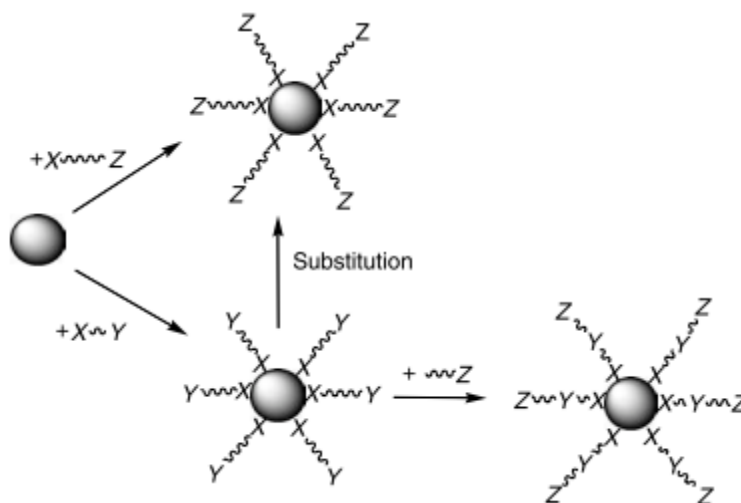
Figure 2-12: Two strategies for functionalization: Method 1 (top): Ligands with the Z functionality react directly with the surface; Method 2 (bottom): A ligand with a Y functionality interact directly with the surface and then extra functionality (Z) will add to the matrix [135].

Functional groups can be attached to the polymeric surface by covalent or non-covalent bonds. Each of these attachments have their benefits and limitations. Covalent immobilization leads to strong, stable attachments of functional groups to the polymeric surface. In contrast, non-covalent conjugations with easy disassociation are appropriate for drug delivery. In such a system, linkages release from surface and dissipate in the environment [35]. In some cases, one functional group has an intermediary role to conjugate secondary functional groups in the surface. Most bioactive compounds are linked to the main surface by intermediary functions [97]. Perusal of literature review demonstrates that multifunctional surfaces open new avenue in different fields such as biomedical imaging and drug delivery.

2.2.7.1 Amines and ammonium ions functionality

Nitrogenated, N-rich, or aminated surfaces are surfaces of special interest for bio-applications. These surfaces improve cell adhesion and affect cellular processes [16, 137]. Protonated amine groups, which possess a positive charge, can attract negatively charged biomolecules. NH_3 is among the common precursors to anchor amine ligands to the polymers, especially using PICVD process [136].

2.2.7.2 Carboxyl functionality

Carboxyl functionality mainly comes from carboxylic acid dendrimers. This functionality, like amine groups, facilitates anchoring of proteins and other bioactive groups to the surface. Moreover, it is one of the functionalities that can make the surface more hydrophilic due to its –COOH groups [138-142]. The weak structure of carboxylic acids make them good candidates for adding carboxyl functionality to the deposited films. A series of these acids, such as acetic, oxalic, malonic, succinic, etc., have been exploited for this purpose [138]. Figure 2-13 shows some common –COOH and $–NH_2$ groups exploited for functionalization of surfaces (specifically, nanoparticles).
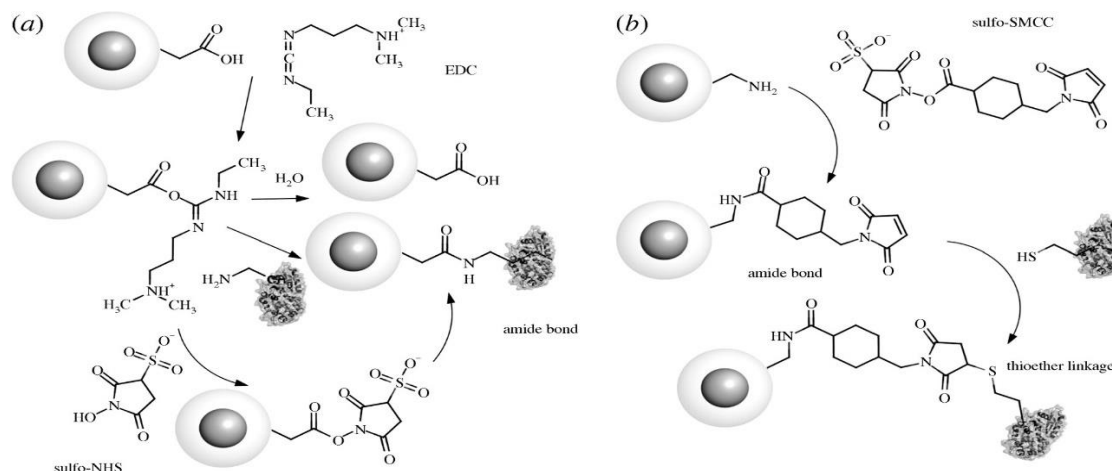
Figure 2-13: (a) Common conjugation with carboxylic acid functionalities: this functionality can react further either with primary amino group and form stable amide bond or with NHS or sulpho-NHS. (b) Particles with primary amino groups can be reacted with active ester compounds to form amide bonds [143].

2.2.7.3 Thiols and disulfide functionality

Organosulfur compounds are common agents for adding sulfhydryl and disulfide functionality to the surface (Figure 2-14). These ligands have a high affinity and interaction with metal surfaces, particularly noble metals [143-149]. In addition, they can be oxidized to sulfate or sulfonate groups [144]. Thiols or thiolate groups exchanges thiol–thiol functionality with other molecules in their surrounding environment [135]. However, partial desorption of thiolated species is a concern that compromises the stability of the ligand and the organic film, accelerating aging [145].
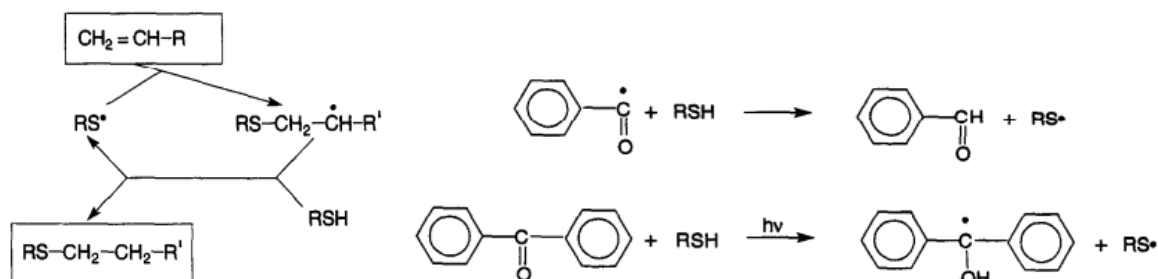
Figure 2-14: Thiol functionalization in a PICVD process [104].

2.2.7.4   Phosphine functionality

Phosphine functionalities are among the weakest ligands that can be replaced by other existing ligands in the surrounding environment. Thiol ligands with their stable structure easily replace this functionality. Polyphosphine ligands can produce more stable ligands compared to phosphine. Thus, di- or triphosphine compounds such as bis(diphenylphosphino)- decane or bis(diphenylphosphinoethyl)phenylphosphine are exploited in order to have firmly stable functionality (applied in palladium nanoparticles) [150]. P–OH, P–OR (R: alkyl) or P–O⁻ containing precursors are responsible for formation of phosphines functionality [135].

2.2.7.5   Hydroxyl functionality

Surfaces with hydroxyl functionality provide wettability characteristic, which is one of the most desired properties for treated surfaces. Materials with high amount of -OH groups are called hydrophilic (or superhydrophilic) (Figure 2-15). These materials have water contact angles below 5°. This property can be added to polymeric films by using oxygen-containing monomers [151, 152]. Some neutral hydrophilic polymers include polyacrylamide and poly(ethylene oxide) (PEO), phospholipids, dextran, and others [152]. Beyond –OH, hydrophilic property can be attributed to the presence of groups such as –CONH–, –CONH$_2$, –COOH, –SO$_3$H and POOH [140, 152]. By increasing the polarity of surface molecules or chemical groups with electric dipole or multipole moment, wettability and hydrophilic properties of the surfaces increase [152].
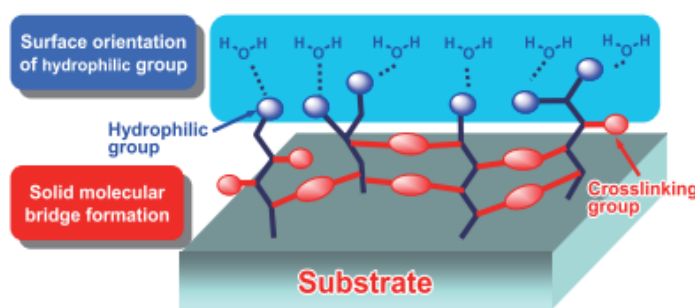
Figure 2-15: Hydrophilic surface[153].

2.2.7.6   Silane functionality

Silanes are among popular functionalities due to their potential for bearing several subsequent functionalities such as amino, cyano, carboxylic acid, epoxy groups, etc. Numerous commercial silane agents are applied in literature for functionalization. HCl or alcohol by-products are formed when using chloro- or alkoxysilanes that may damage the main substrate surface [135]. This functionality makes it possible to have binding reactions between metals, polymers and biomolecules such as peptides, proteins, nucleic acids, enzymes. The 3-aminopropyltriethoxysilane (APTEOS), p-aminophenyltrimethoxysilane (APTS) and mercaptopropyltriethoxysilane (MPTES) agents are often exploited to add amino and sulphydryl groups, respectively. Other silanes like tetraethoxysilane (TEOS), $(CH_3CH_2-O)_3-Si-(CH_2)_3-NH-COO$-estrone, are applied for shell coating of NPs, especially magnetic nanoparticles [154].

2.3   Nanoparticles And Their Fluidization

2.3.1   Nanoparticle description and importance

Nanoparticles (NPs) are particles with at least one spatial dimension smaller than 100 nm [155]. A wide range of NPs exists, and they are available in various shapes such as spheres, nanotubes, nanohorns and nanocages. They can be synthesized from silicon, iron oxide, liposomes, micelles, dendrimers organic compounds, gold, carbon, semiconductors and many other materials [154, 156]. The properties of NPs are surface-driven and can be different from their large-scale counterparts. This has resulted in numerous research endeavors and the anticipated applications of these materials are large. However, most of the NPs are inorganic and they do not possess suitable surface properties for specific applications. They may (1) oxidize easily due to exposure to air or oxidizing environment compromising their dispersion (such as oxidized silver nanoparticles, in which the partial oxidation affects the particle size as well as aggregation in media with a high electrolyte content, resulting in a loss of antibacterial activities [157], (2) have high surface energy and a strong tendency for agglomeration [135, 158], (3) may release toxic compounds or are toxic in nature [24, 159-164], (4) undergo biodegradation [165, 166]. Thereupon, it may be necessary to modify their surfaces in order to extend their physical and chemical properties and render them compatible with other environments and matrices [154]. The most common ways to do this are encapsulation and chemical grafting. The encapsulation of NPs avoids particles agglomeration,

particles oxidation and even add new properties [135]. Figure 2-16 shows some of the NPs used in biological applications, their shape and conjugated groups.
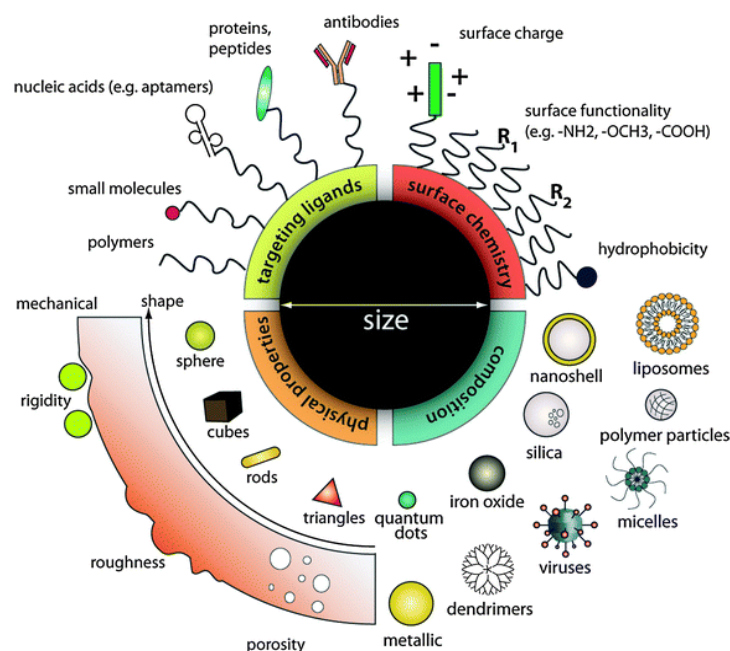
Figure 2-16: Different types of NPs and their design for intracellular applications [156].

Given the very wide field of nanomaterials, this review will focus on NPs target towards drug delivery and imaging applications, more specifically NPs with optical and magnetic properties, such as quantum dots, upconverting nanoparticles and magnetic nanoparticles.

2.3.2 Quantum dots

Quantum dots (QDs) NPs are spherical or near spherical fluorophores semiconductor nanocrystals which have different optical and electronic properties due to their size. If electricity or light is applied to QDs, they emit light of specific frequencies and these frequencies can be precisely tuned by changing their size, shape and material, giving rise to many applications [24, 159-164]. They consist of a core from periodic groups III/V (ZnO, ZnS, CdS, CdSe, or CdTe, etc.) or II/VI (GaN, GaP, GaAs, InP, or InAs, etc.) and a shell composed of materials such as ZnS, PbS, etc. (Figure 2-17) [24, 159-164]. The core on its own has a low quantum yield, which is why a high band-gap semiconductor shell is required to increase quantum yield. This also prevents oxidation of the core. Several techniques can be exploited for QD synthesis, summarized in Table 2-4. Varying the amount of precursor and the crystal growth time leads to different core sizes, and subsequently

emission of light at different wavelengths (Figure 2-17). QDs have a longer fluorescence lifetime (10-40 ns) than organic fluorophores (nanoseconds). These properties make QDs useful as multispectral (multi-color) imaging agents.

Table 2-4: Common QD synthesis methods [160].

Method of QD preparation	Structure	Core precursors	Stabilizing agent	Conditions
Hydrothermal	CdTe	Cadmium(II) chloride, tellurium powder, sodium borohydride	Glutathione, thioglycolic acid (TGA)	Reaction at 140 °C (autoclave), pH 9–10
Growth on a template	CdSe	Cadmium(II) sulfate, selenium powder, sodium sulfite	–	Synthesis in aqueous environment on a carboxyl group functionalized single wall carbon nanotubes template
Precipitation	Eu, Er-doped ZnO	Zinc nitrate, europium(III) nitrate, erbium(III) nitrate	–	Precipitation in water solution after ammonium bicarbonate addition
Ultrasound-assisted	Mn-doped ZnS	Zinc acetate, manganese(II) acetate sodium sulfide	Adenosine triphosphate (ATP)	Aqueous solution, room temperature, argon flow, ultrasonication (1 kW, 30 min.)
Microwave assisted	CdSe-TeS	Cadmium(II) chloride, tellurium powder, selenium powder, sodium borohydride, mercaptopropionic acid	Mercaptopropionic acid (MPA)	Synthesis in aqueous medium (pH 9.0, 140 °C, inert gas). Microwave irradiation: 200 W
Solvothermal	CdSe	Cadmium(II) oxide, selenium powder	Trioctylphosphine (TOP)	Reaction in water-free solution (1-octadecene, oleic acid, oleylamine) at 150 °C (1 h) under nitrogen flow
Photochemical	CdTe	Cadmium(II) chloride, tellurium powder, sodium borohydride	Thioglycolic acid (TGA)	Aqueous synthesis (pH 11.2) at 30 °C, light source: Xe lamp (150 mW/cm^2)
Electrochemical	CdSe	Cadmium(II) sulfate, selenium (as cathode)	Thioglycolic acid (TGA)	Firstly electrochemical synthesis of hydrogen selenide (phosphoric acid electrolyte) in inert gas flow. Nucleation of CdSe nanocrystals promoted by H$_2$Se saturation and their growth at 100 °C
Aerosol-gel synthesis	ZnO	Tetraethoxysilane (TEOS), zinc nitrate	Siliceous matrices	TEOS hydrolysis (60 °C, 4–12 h) in acidic solution (Zn^{2+}, HCl and water). Atomization of obtained suspension, drying (diffusion dryer) and pyrolysis at 300–600 °C (tube furnace)
Laser ablation	SiC	Polycrystalline silicon carbide	–	Laser ablation (800 nm) in water. Laser power: 115–500 mW, irradiation time: 2–3 h
Electron beam irradiation	SnSe	Tin(II) chloride, sodium selenite	Cetyltrimethylammonium bromide (CTAB)	Synthesis in water solution by electron beam irradiation (350 kGy, 20 min.)
γ-Irradiation route	Mn-doped ZnS	Zinc acetate, manganese(II) acetate, sodium sulfite	Chitosan, thioglycolic acid (TGA)	Aqueous synthesis at room temperature under ambient pressure. Radiation condition: 1.1×10^{15} Bq, dose 5–30 kGy/h
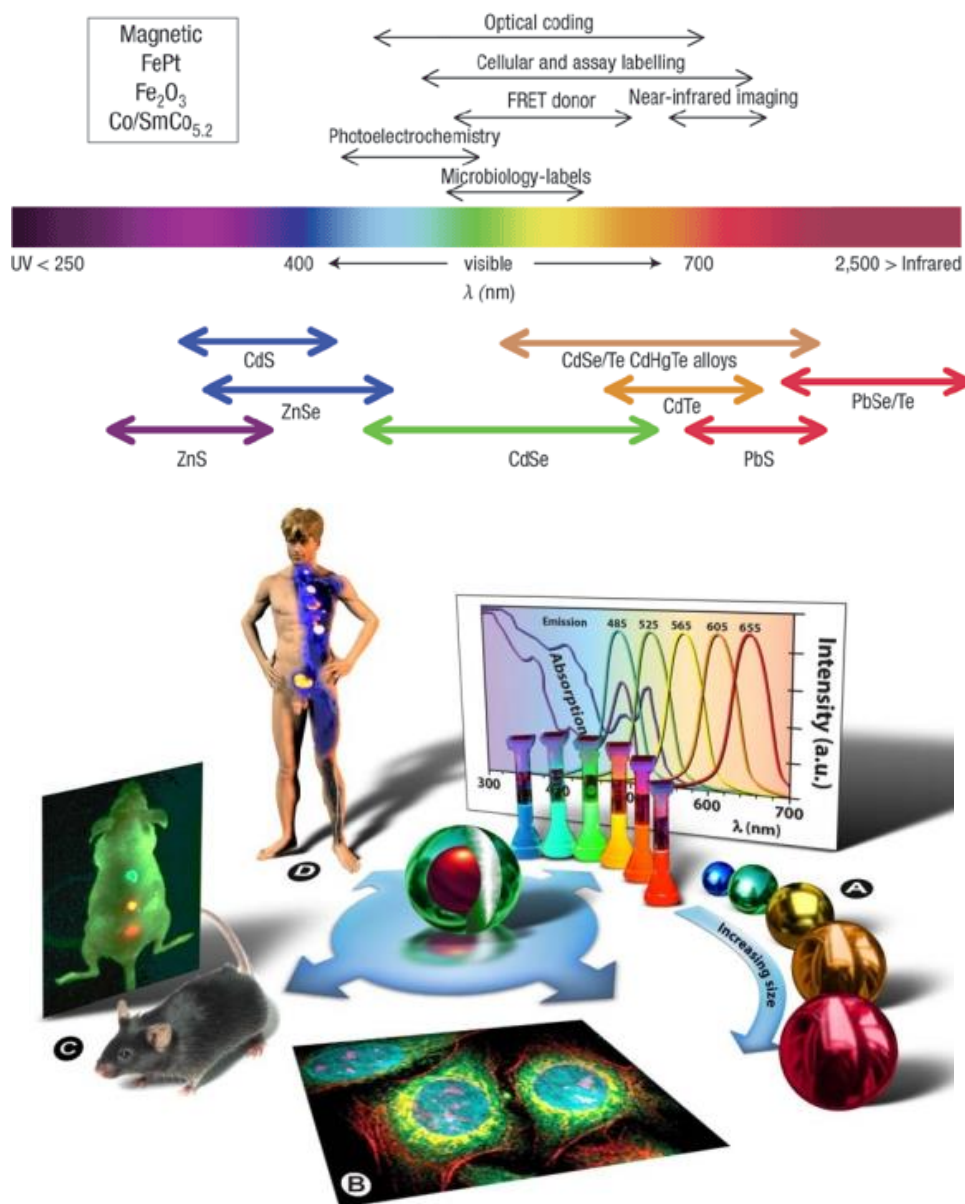
Figure 2-17: QD as a multi-color diagnostic imaging tools [162, 167].

QDs can be used to improve diagnostic methods in cancer and tumor therapy, map the human genome and complete gene sequences, etc [162, 167]. In order to make the QDs appropriate agents for bio imaging, their surface should be modified using polymeric thin films and functional ligands. Figure 2-18 shows some of the ligands and polymers that have been used for this purpose.

SHELL
ZnS, ZnSe, ZnO, PbS, CdS, CdSe, ZnTe

DOPING IONS
Mn^{2+}, Er^{3+}, Eu^{3+}, Ag^+, Cu^{2+}, Cd^{2+}

CORE
Chalcogenides
CdS, CdSe, CdTe, PbS, PbSe, PbTe, ZnS, ZnSe, ZnO
Nitrogen family
InP, InAs, GaN, GaP, GaAs
Others
CuCl, SiC, Bi_2O_3, carbon, silicon

STABILIZING LAYER
Hydrophilic
TGA, 3-MPA, CTAB, chitosan, gemini-surfactants
Hydrophobic
TOP, TOPO

LIGANDS
Vitamins, drugs, polypeptides, proteins, cellular growth factors

Abbreviations:
CTAB: cetyltrimethylammonium bromide
EDBEA: (ethylenedioxy)-bis-ethylamine
MPA: 3-mercaptopropionic acid
Ni-NTA: Ni^{2+}-nitrilotriacetic acid complex
PEG: poly(ethylene glycol)
TGA: thioglycolic acid
TOP: trioctylphospine
TOPO: trioctylphosphine oxide

LINKERS
PEG, Ni-NTA complex, EDBEA, antibodies, biotin-streptavidin complex

Figure 2-18: Some of the ligands and polymers exploited in functional modification of QDs [160].

Despite this potential, image processing and image analysis techniques need to improve to allow sufficient color resolution for simultaneous detection of multispectral QD signals and several studies have been devoted to the cytotoxicity of QDs [164, 167, 168]. To overcome this drawback, the core should be encapsulated with a ZnS shell or other capping material known to reduce toxicity [164, 167, 168]. Recently, new non-toxic QDs with I-III-VI2 structure such as $AgInS_2$, $CuInS_2$ and ZnS-$AgInS_2$ have been developed and showed better control of band-gap energies [169].

2.3.3 Upconverting nanoparticles

Upconverting NPs (UCNPs) convert long wavelength radiation (such as infrared or near infrared) into shorter wavelength (such as visible irradiation). UCNPs are doped-hosts with transition metal

ions with 3d, 4d, 5d orbitals such as Ti^{2+}, Ni^{2+}, Mo^{3+}, Re^{4+}, or Os^{4+} [170]. Dopant provides luminescent characteristics. The host material's crystal lattice provides spaces for this transition by determining suitable distance between dopant ions, and coordinate number of dopants. The efficiency of UCNPs depends on host-dopant ion interactions, the host matrix, the dopant ions and their concentrations. Like QDs, UCNPs have a shell to protect the luminescent from oxidation and its release to the environment. Trifluoroacetate and oleate are two main precursors used in the synthesis of UCNPs [170, 171].

Several dopants can be mixed into a single host to provide multicolor emission. Nann's group demonstrated this phenomena using colloidal mixtures of $NaYbF_4$:Er^3 (emission band in green), $NaYbF_4$:Ho^{3+} (emission band in red) and $NaYbF_4$:Tm^{3+}, $NaYF_4$:Yb^{3+} (emission band in blue and IR) [172]. Common hosts for UCNPs can be classified into two main groups: oxide material (such as phosphates, zirconates, vanadates, silicates, titanates, molybdates, hydroxides and oxysulfides) and fluorides. Hexagonal $NaYF_4$ (β-$NAYF_4$) is the most efficient for both green and blue UCNPs. These type of NPs are another candidate agents for optical imaging [170, 171, 173, 174]. Figure 2-19 shows modified UCNPs used for in vivo multicolor imaging of a mouse.
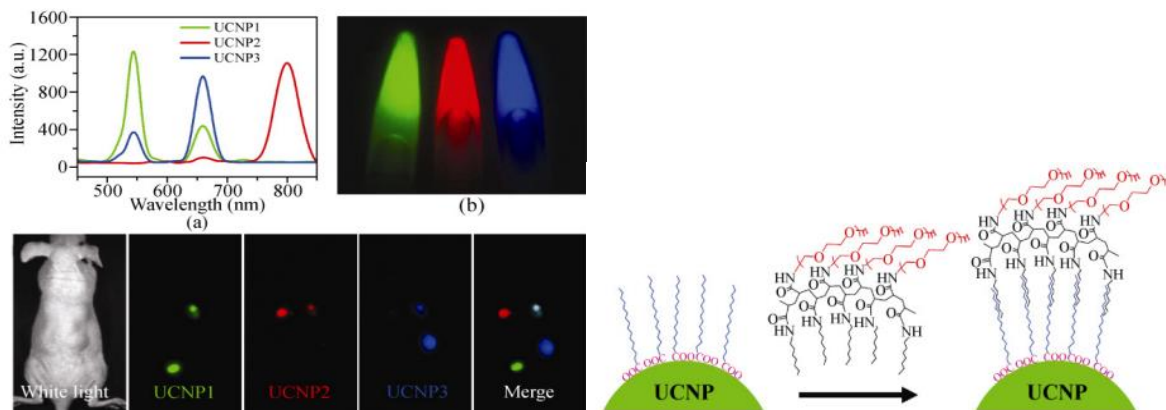
Figure 2-19: UCNPs for in vivo multicolor images of a mouse[172].

Hydrophobic UCNPs have great interest for biological applications. Hu et al. (2008) [175] prepared hydrophobic and amphiphilic LaF_3:Yb^{3+},$Er^{3+}$and LaF_3:Yb^{3+},Ho^{3+} with an average particle size of 15 nm in an oleic acid solution. However, the encapsulation of UCNPs with polymers and ligands causes photon relaxation, decreasing the luminescent, though this can be overcome by using an

active or luminescent shell. Yb^{3+} and Er^{3+} dopants are used to provide active shells (and potentially add tunable multicolor fluorescence properties) [176, 177].

2.3.4 Magnetic iron oxide nanoparticles (MIONPs)

MIONPs can be spread inside the human body using a magnetic field and made to accumulate in a targeted area [30, 32, 178-182]. A wide range of iron oxides have been exploited as MIONPs: Fe_3O_4 (magnetite), α-Fe_2O_3 (hematite, weakly ferromagnetic or antiferromagnetic), γ-Fe_2O_3 (maghemite, ferromagnetic), FeO (wüstite, antiferromagnetic), and finally ε-Fe_2O_3 and β-Fe_2O_3. Magnetite and maghemite are the commonly retained for biological application due to their biocompatibility [30, 32, 178-182]. Other metals such as Co, Mg, Mn as well as alloys like $CoPt_3$, FePt, etc. can be incorporated in the MIONPs synthesis processes[181]. The size, shape and composition of these NPs greatly depends on the type of salt used for synthesis such as chlorides, sulfates, nitrates, etc. Popular methods for the synthesis of MIONPs include co-precipitation, thermal decomposition and/or reduction, micelle synthesis, hydrothermal synthesis, and laser pyrolysis techniques [30, 32, 178-182]. One of the common MIONPs production techniques is based on organic phase thermal decomposition of Fe(acetylacetonate) or iron pentacarbonyl $Fe(CO)_5$, followed by oxidation [29, 31]. In this process, $Fe(CO)_5$ reacts with oleic acid at 100 °C. Then, produced NPs are oxidized using trimethylamine oxide as a mild oxidant to form monodispersed γ-Fe_2O_3 nanocrystallites. Particle size can be varied from 4 to 16 nm by controlling the experimental parameters [29, 31]. The other popular method for the production of size-controlled MIONPs is based on high temperature (265 °C) reaction of Fe(acetylacetonate) in phenyl ether in the presence of alcohol, oleic acid, and oleylamine. Seed-mediated growth methods can be applied subsequently to synthesize larger (up to 20 nm) monodispersed magnetite NPs dispersed into nonpolar solvents using smaller magnetite NPs as seeds. Then Fe_3O_4 nanoparticles can be transformed easily into γ-Fe_2O_3 NPs by annealing in the presence of oxygen at high temperature (250 °C) [29, 31]. Surface modification of these NPs is essential due to their great tendency for agglomeration, further highlighting the need for polymeric coating with desired functional groups to have hybrid inorganic/organic properties, etc. MIONPs imaging and functionalization are depicted in Figure 2-20.
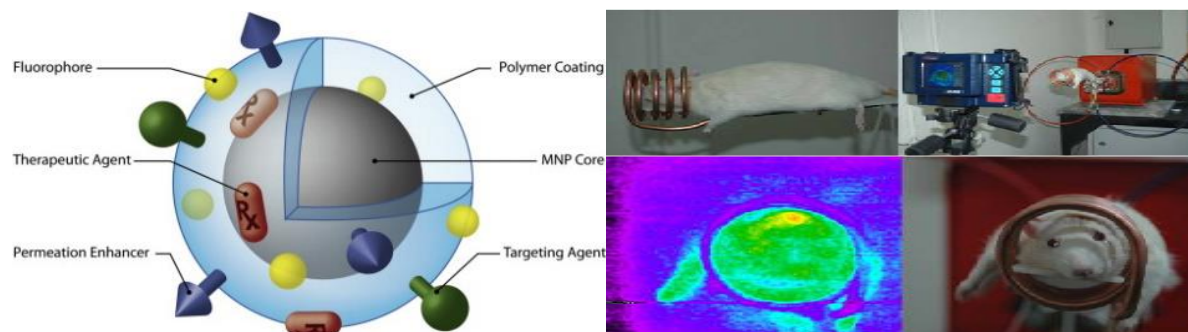
Figure 2-20: MNPs as an imaging agent [31, 183].

NPs needs to be encapsulated as mentioned previously to overcome their agglomeration and add new properties to their bulk. As for flat surfaces, surface modification techniques can be applied for this modification. Considering (1) the separation challenge of NPs from solvents due to their small size and (2) the possibility of encapsulating small quantities of NPs via wet chemistry processes, gas phase modification methods are appealing. On the other hand, gas-phase treatment of NPs requires fluidization of solid phase NPs in the gas phase to overcome their agglomeration while exposing NPs to reactive gases. Fluidization is basically flotation of solid phase particles in the fluid phase (liquid or gas). In this process, static solid-like behavior converts to a dynamic fluid-like state [184, 185]. This way, the amount of treated particles would be much higher than with wet processes (gram instead of milligram) and treated particles would be easily separated from the gas stream.

2.3.5 Fluidization of nanoparticles

Fluidized bed reactors are among the most popular reactors for the functional encapsulation of nanoparticles. These reactors consist of two main phases: solid and fluid (liquid or gas) streams. By introducing the gas flow into a solid bed made of particles, particles move upward and produce empty spaces between particles. When the gas velocity is low, aerodynamic drag on each particle is also low, which causes the bed to remain in a fixed state. The aerodynamic drag force then counteract the gravitational force when the gas velocity increases and results in bed expansion (increase in the volume of the bed) [184-189].

By further increasing gas velocity, particles reach to a critical value in which the upward drag force equals the downward gravitational force. This causes particle suspension/flotation in the gas

stream. At this point, the particles have fluidic behavior and the bed is completely fluidized. This velocity is called the minimum fluidization velocity (U_{mf}). Fluidic behavior of particles continues up until the particles escape the bed. The velocity up to which the particles have such a fluidic behavior is called U_c or complete fluidization velocity. Between U_{mf} and U_c, particles maintain their fluidization and behave as a fluid and the volume of the bed gradually increases. Particles with lower density than the density of the bed start floating on the surface of the bed and bobbling up and down, while particles with a higher density stick to the bottom of the bed. This causes channeling in the bed and allows the particles to be transported like a fluid [184-189].

Further increase of gas velocity leads to decrease in bulk density of the bed. Thus, particle fluidization becomes more violent until the particles no longer form a bed. The velocity at which the particles start to have turbulent behavior is called U_t. In this state, particles start to escape the bed [184-189].

Generally, particles are classified by the Geldart scale into four groups based on their size, density and density of the fluidization medium: Geldart A, aeratable; Geldart B, sand-like; Geldart C, cohesive; and Geldart D, spoutable. On the basis of their physical properties, NPs fall under the Geldart group C (<30 μm) (Figure 2-21) [187, 190]. Geldart C particles are very cohesive and can rarely be fluidized without assistance. This is due to their inter-particle forces, which are often greater than those fluid can exert on the particle. This high inter-particle force comes from their very small particle size, strong electrostatic charges or from the presence in the bed of very wet or sticky material. As a result of such forces, particle mixing and heat transfer between a surface and the bed is poorer compared to the Geldart A and B particles [187, 190, 191].
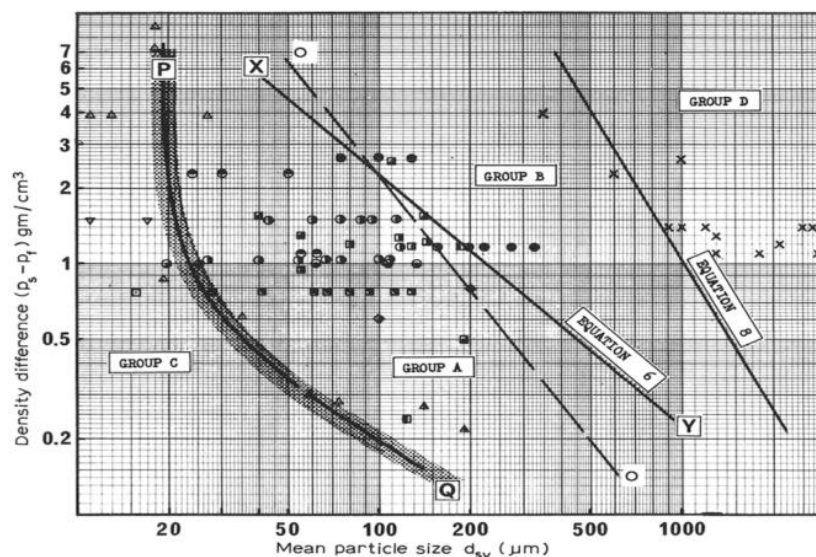
Figure 2-21: Geldart classification of particles (ρ_f and ρ_s are gas and solid particle density, respectively, and dsv is the particle size)[190].

The inter-particle forces lead to the formation of agglomerates of different shapes and sizes. In this state, the particle bonds may be permanent or not. Table 2-5 shows some of the common forms of NP agglomerates.

Table 2-5: Agglomeration kinetic growth models in a 2D embedding space (D_f is their mass fractal dimension of their 3D analogs) [189].

Based on the agglomeration of particles, two type of fluidization are possible: (1) Agglomerate Particulate Fluidization (APF), and (2) Agglomerate Bubbling Fluidization (ABF). The difference between these two types is summarized in Table 2-6.

Table 2-6: Specifications of APF and ABF of NPs [187].

	APF	ABF
Primary particle size	Nanoparticles	Micro, Submicron, Nanoparticles
Agglomerates	Loose, multi-stage, light in weight	Dense, single-stage, heavy in weight
Bulk density	Low (< 100 kg/m^3)	High (> 100 kg/m^3)
Fluidization characteristics	1. Low minimum fluidization velocity 2. Bubbleless 3. Bed expansion ratio is high 4. Agglomerates are uniformly distributed in the bed 5. Fluidized bed homogeneously expands, and the bed density decreases with increasing gas velocity 6. Negligible elutriation	1. High minimum fluidization velocity 2. With bubbles 3. Bed expansion ratio is low 4. Large agglomerates are at the bottom of the bed, with small ones at the top 5. Bed expansion ratio and emulsion phase density do not change much with increasing gas velocity 6. Considerable elutriation

Different types of assistance methods have been used to overcome agglomeration of NPs in a fluidized bed. Those include magnetic fields, vibration, microjets, rotating and centrifugal, stirring, sound-assisted fluidization, electro-fluidization and impactor-assisted fluidization [187, 189, 192]. Table 2-7 summarizes assisted fluidization techniques, their advantages and limitations.

The minimum fluidization velocity (U_{mf}) and turbulent velocity (U_t) are dependent on shape, size, and density of the particles as well as gas density. Fluidized bed reactors should be operated at a velocity between these two limits in order to have fluidization while preventing elutriation of NPs from the reactor. Experimental approaches to determine the U_{mf} of given particles is based on investigation of the fluidization regime by measuring the pressure difference between the entrance and exhaust of the fluidized bed chamber as a function of the gas flow rate (Figure 2-22).

Table 2-7: Summary of assisted fluidization methods, advantages and limitations [187].

Method	Advantageous	Limits
Acoustic wave	Channeling and slugging are eliminated. Minimum fluidization velocity decreases. Agglomerate size decreases. Elutriation rate decreases.	It is energy intensive. Decrease in elutriation loss is not appreciable. Operation outside the optimal ranges of SPL and f_s, not only won't improve the fluidization quality, but also deteriorates it. Operating problem with the presence of sound with high SPL. Mixing of different nanoparticles could be achieved up to microscale.
Vibro-fluidization	Channeling and slugging are eliminated. Bed pressure drop increases. Minimum fluidization velocity decreases. Agglomerate size decreases. Elutriation rate decreases.	It is energy intensive. Decrease in elutriation loss is not appreciable. Bubbles would arise at high vibration intensity. Processing of as-received fine/ultrafine particles by this approach is not feasible. Mixing of different nanoparticles could be achieved up to microscale.
Magnetically assisted fluidization	Fluidization of completely defluidized bed would be feasible. Minimum fluidization velocity decreases. Size of bubbles in bubbling fluidization regime of some micron size fine particles decreases. Elutriation rate decreases.	It is energy intensive. Decrease in elutriation loss is not appreciable. when large and dense magnets are used: The magnets mostly present at the bed bottom and the magnetic aid cannot transmit effectively in the whole bed. when ferro-magnetic particles with size and density similar/close to those of bed material are used: The magnets act as foreign particles and acceptance of these particles in the process is the main question.
Electrofluidization	Bed expansion increases in the case of nonuniform alternating electric field along the bed height. Elutriation rate decreases.	Bed expansion decreases and highly heterogeneous fluidized bed appears in the case of horizontal electric field.
The use of a centrifugal fluidized bed	Minimum fluidization velocity decreases. Agglomerate size decreases, smaller than those attainable by assisting the bed with acoustic, magnetic and electric fields, and mechanical vibration. Elutriation rate decreases.	Bed expansion decreases. Mixing of different nanoparticles could be achieved up to microscale. Powerful compressor is needed to supply the required fluidizing medium. Attrition is a harmful problem for this type of fluidized beds.
The use of a tapered fluidized bed	Simultaneously fluidizes large agglomerates at the bed bottom and small agglomerates at the top of the bed. Elutriation of small agglomerates is hindered.	Not reported.
Additional of foreign particles	There is no need to change the column design or obtain additional equipment. Elutriation rate decreases. Makes circulating fluidization mode of ultrafine particle agglomerates possible.	Acceptance of the presence of foreign particles in the process is under the question.
The use of micro-jet as secondary flow	Channeling is hindered. Bed pressure drop increases. Minimum fluidization velocity decreases. Bed expansion increases, much higher than those obtained by other techniques. Agglomerate size decreases. The fluidization characteristics of ABF powders change into APF ones. Mixing of different nanoparticles could be achieved up to nanoscale. It is easy to scale-up.	Not reported.

Figure 2-22: Various regimes of a particle bed at different gas velocities (U_{mf}: minimum fluidization velocity, U_{cf}: complete fluidization velocity) [185].

Many researchers have exploited fluidized bed reactors (FBRs) for the encapsulation of NPs [46, 48, 193-197]. Esmaeili et al. applied FBR for the encapsulation of zirconia and aluminum NPs (43.7 nm) via in situ polymerization using polyvinylidene fluoride (PVDF) as a reactive coating monomer and supercritical carbon dioxide as a fluidizing medium [198]. Feng et al. applied FBR (FBR supplied by the Wusterizing company) with photo-initiated cationic polymerization on potassium chloride (KCl) particles (40-200 mesh: 0.420 mm- 0.074 mm) [132]. However, there is no research reporting the use of a fluidized bed reactor for the encapsulation of NPs by PICVD technique.

2.4 Syngas And Fly Ash Production

Gasification is an important industrial process for waste management. A gasifier is basically a high temperature reactor (900-1600 °C) in which a mainly carbon-based feed stream (coming from crude oil, organic waste streams, coal, biomass, natural gas, etc) is partially oxidized. The feed stream dictates the type of gasifier used – possible configurations include fluidized beds, slurry reactors and plasma gasifiers, among others. In this process, the carbon-containing feed reacts with an oxygen source (e.g. air, water) in substoichiometric conditions. The main products are raw syngas as well as soot, ash and slag (Figure 2-23). Depending on the feed source and operating

conditions, some catalysts can be employed to increase selectivity, conversion and and reaction rate. Common catalysts include Fe_2O_3, $MgCO_3$, $CaCO_3$, Na_2CO_3, K_2CO_3 or $CsCO_3$, etc.[199-203].
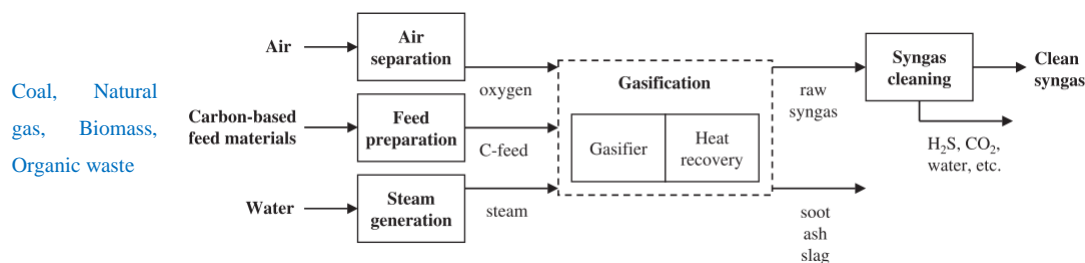
Figure 2-23: Schematic of synthesis gas generation process[199].

The raw syngas contains impurities, mainly in the form of CO_2, H_2O, H_2S, NH_3, etc. Once cleaned, it can be used as a fuel or as a feed source for Fisher-Tropsch processing (hydrocarbon production) [200, 201].

Among the secondary products formed through gasification (as well as other thermal processing approaches, such as incineration), ash comprises the inorganic materials (such as Cu, Pb, Zn, As, Cd, Cr, Hg, Ni, Fe). The amounts of these materials are different based on the feed source. Ash can be classified as heavier "bottom ash", typically found at the bottom of the reaction environment, and finer "fly ash" that is carried with the gas stream and must be separated as part of gas cleaning steps. Various techniques are employing for fly ash removal, such as sieving, magnetic separation or chemical washing and carbonation. Ash components are present in the oxide or organometallic form, in a wide range of sizes and compositions [204-208].

2.5 Fundamentals OF Fisher-Tropsch Processing

Based on the ratio of CO: H_2, reaction temperature (high or low temperature) as well as catalyst type, a series of hydrocarbons can be generated from syngas through the Fisher-Tropsch (FT) process. Table 2-8 summarizes some of these products.

Table 2-8: Hydrocarbon products from FT process [199].

FT syncrude property	HTFT	LTFT
Carbon number range	C_1–C_{30}	C_1–C_{120}
Main product	C_2–C_{10} alkenes	waxes
Normal product phases[a]		
gases (C_1-C_4)	20–25%	5–10%
oil	20–25%	15–20%
wax	0%	20–25%
aqueous organics	~5%	1–2%
water	45–50%[b]	50–55%[b]
Organic compound classes[a]		
alkanes (paraffins)	20–30%	major product (>70%)
cycloalkanes (naphthenes)	<1%	<1%
alkenes (olefins)	major product (>50%)	15–20%
aromatics	1–5%	<1%
oxygenates	10–15%	~5%

[a]All percentages are on a mass basis.
[b]Closed gas loop, ie, no net water gas shift conversion.

High-temperature FT processes (HTFT) uses iron-based catalysts to produce gasoline and linear low molecular mass olefins at 300-350 °C. Low-temperature FT processes (LTFT) either use iron or cobalt catalysts to produce high molecular mass linear waxes at 200-240 °C [199, 209].

In these processes, CO polymerization happens on the surface of the catalysts. In parallel, water-gas shift and secondary conversion of primary FT products also occur [209]. Figures 2-24 and 2-25 show reaction network resulting in the formation of some products.
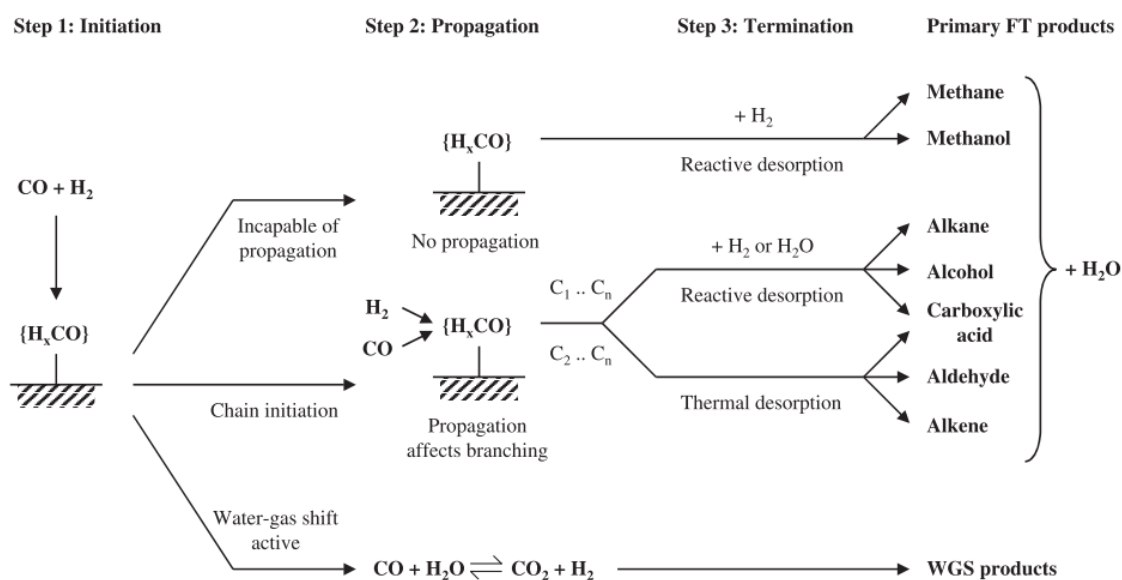
Figure 2-24: Syngas reaction network[95, 199].
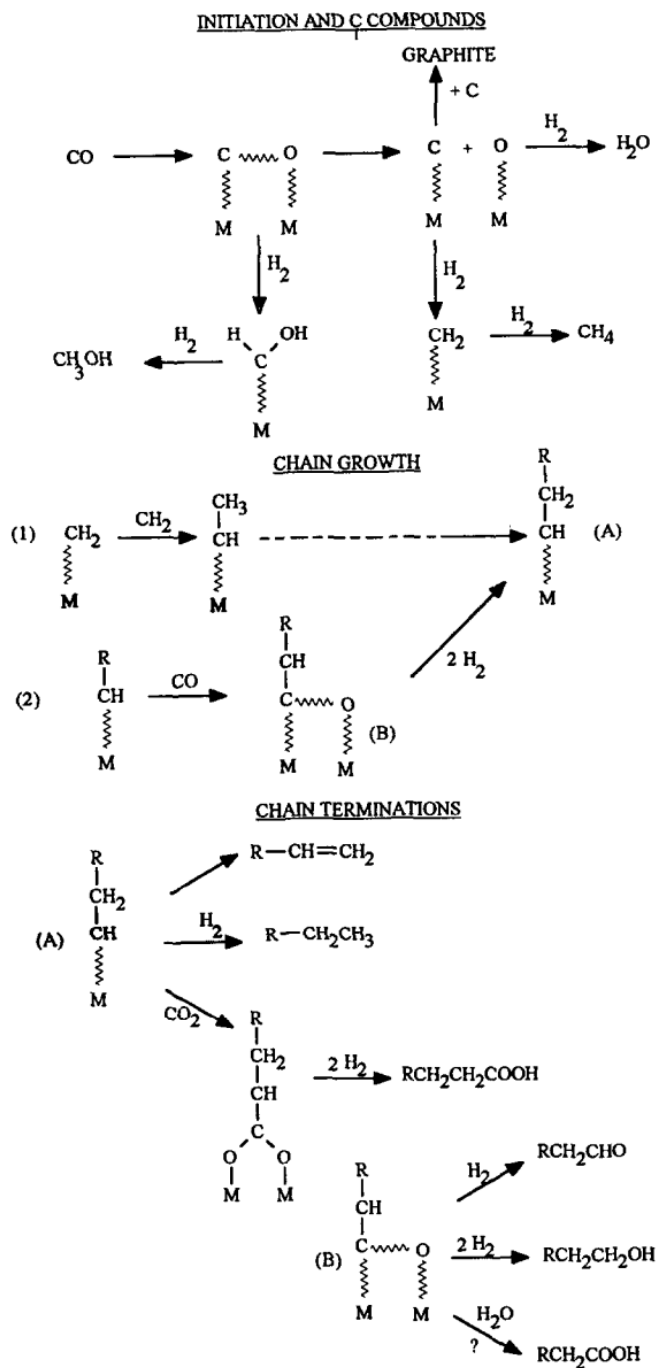
Figure 2-25: Mechanism of the FT reaction[209].

Initiation: In the first step, "initiation" happens due to the adsorption of CO on FT catalysts. This step has the most important role in the reaction pathway and final products; it is mainly dependent

on the catalyst. To become active chain initiators, CO molecules should be bounded, dissociated, and partially hydrogenated on the catalyst surface [209-211].

Propagation: Chain growth can take place on the catalyst surface by addition of CO molecules to another chain initiator or to an already growing chain. In other words, growth happens by either (1) hydrogenation of CO-derived intermediate molecules or (2) attachment of two active carbons from the growing chain that are attached to the catalyst. Branching only happens when the retention of oxygen on more than one carbon is impossible [209-211].

Termination: FT product selectivity happens in this step, affecting not only the carbon number distribution, but also the functional groups associated with the product. This mostly depends on the nature of the catalyst and the operating conditions. Thermal desorption and reactive desorption are two competing processes for termination. Thermal desorption is influenced by bond weakness between the catalyst and the surface intermediate. Due to thermal desorption, weak bonds break down while strong bonds remain in the catalyst surface and results in formation of longer chain intermediates, and therefore unsaturated products either with an alkene (olefin) or an aldehyde functionality. Reactive desorption, on the other hand, deals with product desorption and bond breakage between the catalyst and the surface intermediate. Products based on desorption are mainly formed by hydrogenation, resulting in the formation of products with alkane (paraffin), and alcohol or even carboxylic acids functionalities [209-211]. Moreover, it was found that by increasing the ratio of water partial pressure to H_2 partial pressure the ratio of carboxylic acid to alcohol selectivity increases too[199].

2.5.1 Fisher-Tropsch catalysts

Several catalysts have been applied for FT process and this is an area of active research [87, 94, 209-219]. FT catalysts are basically CO polymerization and hydrogenation catalysts. FT catalytic reactions cannot be explained unless the structure and reactivity of the carbon monoxide are studied. The CO molecule contains 14 electrons in total: six contributed by carbon and eight by oxygen with a :C:::O: structure (only the valence electrons are depicted). CO molecules dissociate readily over certain transition metals and this is a necessary condition for Fischer-Tropsch catalytic reactions. In this process, occupation of CO 2π (antibonding) orbital and bonding of the dissociated carbon and oxygen atoms to transition metal catalysts takes place. Metal-CO complexes involve both σ and π bonding. These transition metals form strong bonds with compounds (CO, ethylene)

that contain π-electron systems or have orbitals of suitable energy and symmetry to form dπ-bonds [209]. Multiple metal-carbon bonds can form due to the overlap of metal-COπ bonds and metal dπ orbitals with empty antibonding CO orbitals (Figure 2-26). FT catalysts include Fe, Co, Ni, Mo, Ru, Rh, W, and other platinum group noble metals. The most active and popular metals for FT synthesis are Fe, Co, Ni, Ru and Os, with Re and Rh. In practice, only Fe and Co are industrially employed due to their best performance for cost.
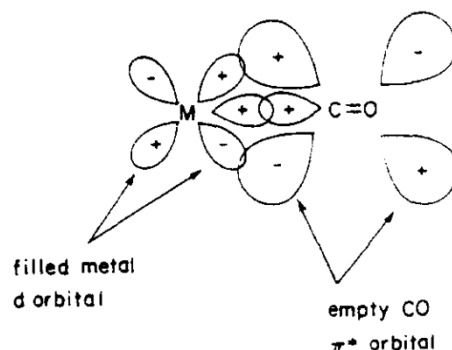
Figure 2-26: Molecular orbital representation of a CO-transition metal bond [209].

Dissociation of CO molecules should happen on metal catalysts to make FT reactions possible. In some catalysts (e.g. Pd, Pt and Cu), dissociative adsorption of CO is the main route, while in others associative adsorption is most likely (rhodium is probably the best example). In certain type of catalysts, CO is adsorbed both ways. Figure 2-27 clarifies catalysts and conditions for these reactions.
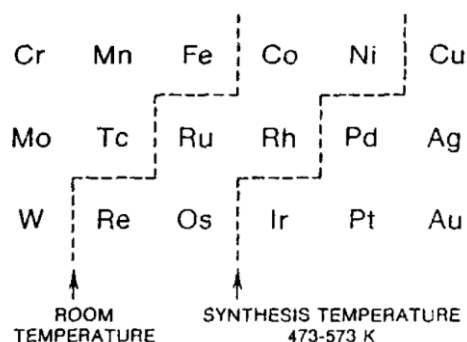
Figure 2-27: Metals that adsorb CO dissociatively and non-dissociatively at ambient temperature and Fischer- Tropsch reaction temperatures [209].

In Figure 2-27 the dotted line separates three groups of catalysts: (1) catalysts near the left dotted line (Cr, MO, etc.) dissociatively chemisorb CO at room temperature; (2) by increasing the temperature, the line is shifted to the right and shows catalysts like nickel and copper, rhodium and palladium, and osmium and iridium, which operate at 200-300 °C for the FT reactions; (3) catalysts to the right of this dotted line (Cu, Pd, Ir,…) are useful for methanol synthesis. At higher temperatures, the line would be shifted even more to the right and CO can dissociatively chemisorb even on copper and palladium.

Syngas has reducing characteristic; thus in the presence of catalysts like Fe, Co and Ni, there is a high possibility of reducing these metal-based oxygen carriers to form metal carbonyls [220-222]. Metal carbonyls form at high pressures, but at temperatures too low for FT synthesis [209]. Although the reduced catalyst is mainly in the form of Fe metal, part of that is converted to a mixture of iron oxide and iron carbide phases, the latter of which are very active for FT catalysis [199]. During FT processing, even primary FT products can readsorb on the catalyst, resulting in formation of secondary products (intermediates capable of chain initiation).

Promoters are another components in the catalyst formulation which have a specific functions, common promoters can be classified into three main groups[199]:

(1) K_2O: Alkali promoters are used to increase the probability of chain growth by suppressing reactive desorption on the catalyst. They also have great impact on selectivity of the catalysts. Potassium is the most effective alkali promoter.

(2) Cu: Copper is a reducing promoter that facilitates catalyst reduction during catalyst preparation and formation of iron oxide/hydroxide phases. It increases the chance of active site formation, but does not participate in FT catalysis itself.

(3) SiO_2: Silica is a structural promoter that causes large surface area and pore volume formation, while not participating in FT catalysis.

Under HTFT, catalysts need additional mechanical strength compared to the LTFT synthesis; thus, chemical promoters (like K_2O) and structural promoters that are difficult to reduce (metal oxides like MgO and Al_2O_3) are employed. In LTFT synthesis, supported cobalt FT catalysts are most often employed [199].

2.5.2 Fisher-Tropsch products

A wide range of hydrocarbons and oxygenated compounds are produced in FT processes. The major groups of products include hydrocarbons such as paraffins and olefins, and chief oxygenated products are primary alcohols. In saturated hydrocarbons, straight-chain paraffins, along with some 2-methyl branched paraffins are dominant products and terminal olefins are among the most common olefins. Main reaction routes for generation of such products are presented in Equations 2-8 to 2-13.

Paraffins $$nCO + (2n + 1)H_2 \rightarrow C_nH_{2n+1} + nH_2O$$ Equation 2-8

Olefins $$nCO + 2nH_2 \rightarrow C_nH_{2n} + nH_2O$$ Equation 2-9

Alcohols $$nCO + 2nH_2 \rightarrow C_nH_{2n+1}OH + (n - 1)H_2O$$ Equation 2-10

Water gas shift $$CO + H_2O \rightarrow CO_2 + H_2$$ Equation 2-11

Boudouard reaction $$2CO \rightarrow C + CO_2$$ Equation 2-12

Coke deposition $$H_2 + CO \rightarrow C + H_2O$$ Equation 2-13
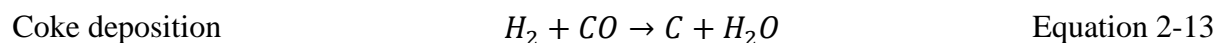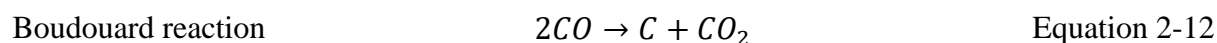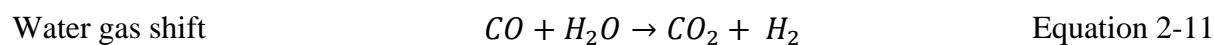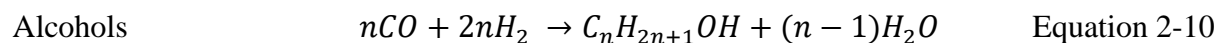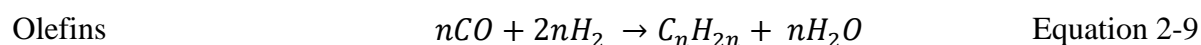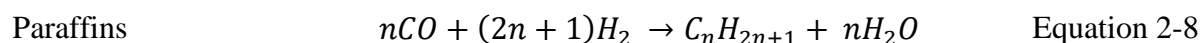
Figure 2-28 shows some of the commercials, near commercials and potential products of FT-process.
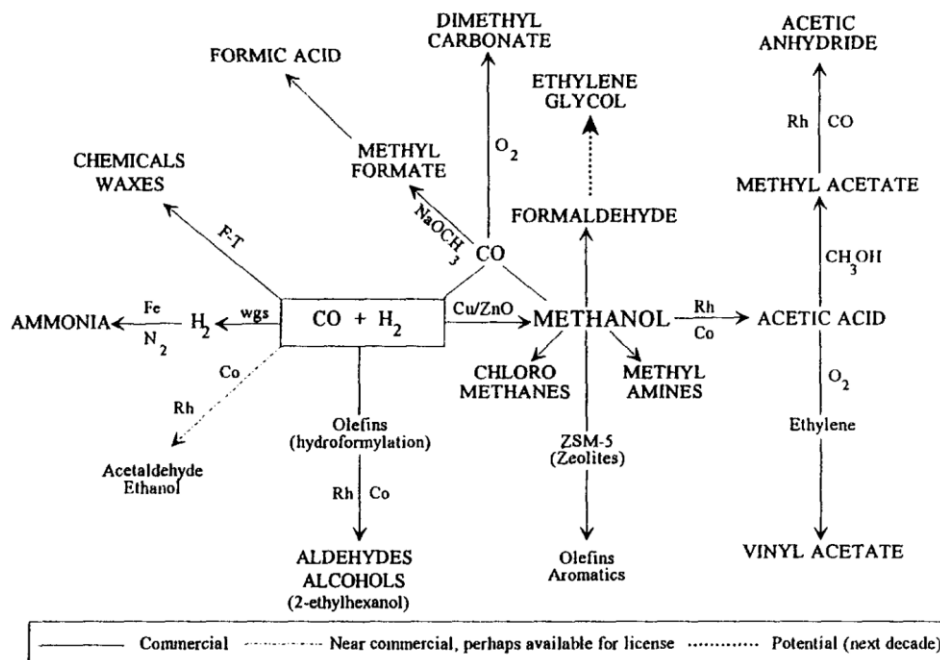
Figure 2-28: Commercials, near commercials and potential products of syngas reactions[209].

2.5.3 Fisher-Tropsch catalysts poisoning

Catalysts poisoning or deactivation is one of the major concerns in heterogeneous reactions, especially in FT processes [199, 209, 211]. The most important type of deactivation happens due to coke deposition, and metal catalysts are particularly sensitive to sulfur poisoning [209, 222]. Other impurities such as iron carbonyls or electro-negative elements, such as chlorides and bromides, are also FT catalyst poisons. Co-LTFT catalysts are also sensitive to ammonia, as it reduces Co's activity. However, it does not effect Fe-FT catalysts and can be used to yield amines containing compounds [199, 223-225]. The extent of deactivation in FT catalysts depends on the operating conditions and syngas composition, through three main deactivation pathways [199, 209, 226]:

(1) Deposition (coke formation or poisoning): Heavy polymerized materials produced during FT synthesis can cause fouling of the catalysts. This is especially prevalent in Co-LTFT catalysts. In the case of HTFT processing, deposits are more carbonaceous in nature and over long operation the amount of carbon deposited could be even higher than the amount of iron catalyst itself. This type of deactivation is not permanent and can be removed by

hydrogenation or washing with a light hydrocarbon liquid; however, this can lead to a decrease of mechanical strength and thus increase loss by attrition.

(2) Oxidation: If the water partial pressure is sufficiently high, oxidation of active sites may happen. Fe-LTFT catalysts are particularly sensitive to this.

(3) Sintering: sintering is a minor deactivation pathway leading to the loss of active sites in catalysts. However, this deactivation pathway can become important in the case of small size particle catalysts as it will lead to the formation of larger particles (limiting available surface area).

Figure 2-29 summarizes different pathways of catalysts deactivation.
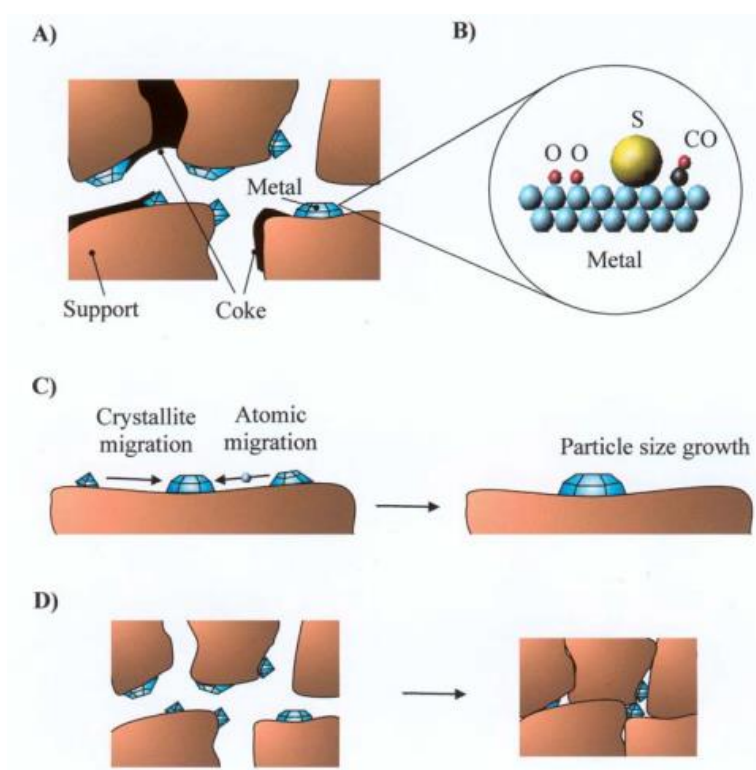
Figure 2-29: Catalyst deactivation mechanisms: A) Coke formation, B) Poisoning, C) Sintering of the active metal particles, and D) Sintering and solid-solid phase transitions and encapsulation of active metal particles [226].

CHAPTER 3: OBJECTIVES AND ORGANIZATION OF THE ARTICLES

Based on the literature review, we realized that although numerous methods have been exploited for surface modification and thin film deposition, these methods suffer from multi stage preparation (sol-gel), expensive equipment and in some cases working under vacuum (thermally activated and plasma chemical vapor deposition (CVD)). Grounded in these problems, this research attempts to extend the industrial-centered approach for thin film deposition using Photo-initiated chemical vapor deposition (PICVD). Further expanding upon this concept, we will investigate a novel precursor – syngas, which is the waste product of several industries and has the demonstrated potential to produce several chemicals and functional groups. Applying this compound as a precursor can therefore not only bring versatility, but also resolve environmental issues. Moreover, little attention has been devoted to application of UVC lamps for surface coating. Thus, this research focused on photo-initiated chemical vapor deposition of syngas in the present of UVC lamps for surface treatment and particle coating in order to propose an innovative approach using waste gas for the production of polymeric coating for various industries.

3.1 Objectives

3.1.1 General objective

The main objective of this research is to synthesis and fabricate multifunctional thin polymeric films on micro and nano surfaces using syngas photo initiated chemical vapor deposition stimulated by UVC lamps.

3.1.2 Specific objectives

To achieve the above-mentioned objective, the following specific objectives are outlined:

(1) Demonstrate syngas PICVD works on NPs using a specific case study.

(2) Understand the kinetics and chemistry using a simplified substrate geometry.

(3) Scale-up the technology for industrial NP treatment.

3.2 Organization Of The Articles

To satisfy the above mentioned objectives, results of this research is presented in three main scientific journal articles. Chapters 3 to 5 give the main results of this thesis and corresponding scientific findings. The following is a brief description of each chapter and the link between them:

Chapter 3 describes the first article of this thesis entitled: "Combined Extraction and Functionalization of Low-Cost Nanoparticles from Municipal Solid Waste Fly Ash through PICVD". In this article, we make the proof of concept of PICVD process through extraction of low-cost, low-grade nanoparticles from the massive scale production of fly ash from municipal solid waste (MSW) incineration process. We propose a methodology in which CO/H_2 are used as precursors, along with H_2O_2 as a photoinitiator to accelerate the kinetics of reaction. These were injected to a semi plug flow reactor to treat ash powders. Then, treated ash was dispersed in a polar solvent (e.g. water) to separate larger particulates through suspension and extract lighter nanoparticles remaining in the supernatant. This paper was published in the *Journal of Environmental Chemical Engineering, 2014, Vol. 2*. My colleague W. Raphael helped me to perform experiments associated to this article and my other colleague C.A. Dorval Dion assisted in writing the introduction section of the article. I was responsible for the experimental analysis, interpretation of the experimental results and writing the article.

Chapter 4 presents the second article of this study entitled: "Kinetics, Chemistry, and Morphology of Syngas Photo-initiated Chemical Vapor Deposition". In this article, flat silicon wafer was used as a simplified substrate geometry for thin film deposition via syngas PICVD process. Critical density of deposited functional groups on the surfaces were identified via XPS and TOF-SIMS to understand the chemistry and kinetics of deposition leading to the proposal of a reaction mechanism. Moreover, the effect of operational parameters e.g., residence time, treatment duration as well as gas ratio on the extent of functionality, film thickness as well as morphology of the deposited film were extensively discussed. This paper was published in *Langmuir, 2017, Vol.33*.

Chapter 5 is the third article of this research entitled: "Large Scale Encapsulation of Magnetic Iron Oxide Nanoparticles via Syngas PICVD". In this section, encapsulation of magnetic iron oxide nanoparticle in jet-assisted fluidized bed syngas PICVD reactor was studied to investigate the possibility of process scale-up. TEM analysis indicated presence of organic coating with 1.5-10 nm thickness. TGA and XPS high resolution confirmed the presence of coating and deconvolution of C1s spectra indicated same chemical composition as our last article. Moreover, UV/Vis absorption showed more tendency of particles for dispersion in non-polar solvents like n-dodecen. This manuscript has been submitted to *Nanoscale*.

CHAPTER 4:   ARTICLE 1: COMBINED EXTRACTION AND FUNCTIONALIZATION OF LOW-COST NANOPARTICLES FROM MUNICIPAL SOLID WASTE FLY ASH THROUGH PICVD

D. Farhanian, C.A. Dorval Dion, W. Raphael, G. De Crescenzo, J.R. Tavares

Department of Chemical Engineering, École Polytechnique de Montréal, P.O. Box 6079, Station Centre-Ville, Montreal, Quebec, H3C 3A7, Canada

KEYWORDS:
PICVD; Nanoparticles; Functionalization; Surface functionalization; MSW fly ash

Abstract

While nanoparticles have been the focus of intensive research for several years as a result of their remarkable surface-driven properties, they remain, for the most part, stuck in the lab. This unfortunate fact can be explained by three main reasons: (1) most studies have not dealt with the scalability and cost issues related to the use of nanomaterials on an industrial scale; (2) a great deal of focus has been applied to "outlier" results that promise far more than can be delivered; and (3) very little attention has been given to surface engineering. We propose to curtail the significant cost issue by extracting low-cost, low-grade nanoparticles that are appropriate for several applications from a ubiquitous and abundant feed stock: fly ash from municipal solid waste (MSW) incineration. The novel technique we apply is capable of both extraction and functionalization of the nanoparticles present in this undervalued waste stream using photo-initiated chemical vapor deposition (PICVD). By setting functionalization conditions to favor hydrophilic surface properties, the treated ash can readily be dispersed in a polar solvent such as water: larger particulates then settle out of suspension, while the lighter nanoparticles remain in the supernatant and are ready for use. While it is true that this method yields low-grade nanoparticles (polydisperse and multi-composite), these can be used in a variety of applications where composition is less crucial, such as increasing the thermal conductivity of composites and nanofluids.

4.1 Introduction

Even if nanoparticles are omnipresent in research laboratories, the cost of these advanced materials remains a limiting factor to their widespread implementation. While the usage of expensive, pure and spherical nanoparticles made from exotic materials can be justified for some high-end applications like drug carriers and microelectronics, some more modest applications call for cheaper sources of nanoparticles [1, 2]. In the hope of finding cheaper alternatives, attention has recently been paid to unconventional sources of ultrafine powders, such as ash from the incineration of municipal solid waste (MSW), coal, cane or oil shale [1, 3-8]. Indeed, several studies focused on the type and level of nanoparticles present in the ash residues [1, 9-11]. Such interest is mainly justified because the accumulation of large quantities of ash is becoming a serious environmental problem [5, 12-16]. Both MSW and fly ash are considered as renewable resources due to their valuable materials content [3, 13, 15, 17, 18]. They also constitute an important debate

due to their toxicity, causing important cardiopulmonary diseases at low concentrations [16, 18-20].

The interesting aspect of using fly ash is that it does not really have any value on the market, since it is currently disposed of in landfills or used in cements [5, 18]. However, valorization through use as a cement additive or filler is not applicable in the case of MSW fly ash. Indeed, many jurisdictions do not allow its use because of its potential hazardous materials content. For jurisdictions where it is permitted for use as a supplementary cementitious material (SCM), additional long-term durability testing is underway [21–24]. Furthermore, it must be taken into account that if fly ash is affordable, it is far from being usable as is for many reasons: (1) the substances are not pure, (2) the chemical composition is variable (particularly if sourced from MSW) and (3) the particle size distribution is wide and variable. The use of fly ash also restrains the selection of materials available; indeed, it often contain minerals such as illite, kaolinite, chlorite, calcite, alumina and quartz; in other words, metals are present in oxydized form [6, 16, 18]. Indeed, the composition can vary according to the source of the ash, but typical compositions are silica (49-64 % wt), alumina (14-30 % wt), iron oxide (6-23 % wt) and CaO (1-7 % wt) [1, 5, 6, 12, 13]. That means that the intended end-use must either encourage the use of such minerals and derivatives, or not be sensitive to the nature of the material at all. An example of the former would be any usage that is suited to silica (SiO_2), which can be used as an additive to cement [3, 4] or rubber matrices [13, 25] to improve their mechanical properties, or as an adsorbent and catalyst support due to its physical chemistry properties [11, 19]. On the other hand, MSW fly ash contains some valuable materials including As, Al, B, Ba, Cd, Cr, Cu, Hg, Mn, Mo, Ni, Pb, Sb, Se, Zn, in oxidized or ionic salt form [26, 27]. In cases where composition is not a problem, these nanomaterials can be used in order to increase the overall thermal conductivity of the composites [28– 30] and nano fluids [31–33]. For applications more sensitive to particle size distribution or chemical composition, the nano- materials can be further treated before use, through size segregation [2,32,34] or chemical treatment [2,29,30,35].

Recently, several studies focused on implementation of nano- particles as a filler in production of composite using in situ polymerization techniques [29, 30]. However, there are some challenges in composite fabrication using nanoparticles: (1) introduction of good chemical bonds between polymer and nano filler, and (2) homogeneous dispersion of nano fillers due to their affinity towards

agglomeration [29, 30]. These challenges can be resolved using chemically engineered (functionalized) nano- particles [28–30].

These recent studies clearly demonstrate that nearly all raw nanomaterials need to be surface functionalized prior to incorporation into matrices. While a vast amount of energy has been spent on extraction of nanomaterials from ash, no one seem to have addressed functionalization. Our group is mainly concerned about the feasibility of combining extraction and functionalization with existing processes to generate nanoparticles. The process proposed to chemically transform the material is usually by sol-gel techniques, which seem hardly scalable due to significant use of acidic solutions and subsequent wastewater control [17, 18, 27]. Our group previously identified photo-initiated chemical vapor deposition (PICVD) as a potential affordable and scalable technology for the surface functionalization of nanoparticles [36]. This technique had been applied in our research group for the functionalization of copper (Cu) coupons using syngas and UVC lamps [37]. Subsequently, by considering the applications where composition is less crucial, such as nanofluids, our group investigated to see if such a surface treatment could be sufficient to recover ready-to-use nanoparticles from fly ash. This study proposes a novel method for the single-step extraction and functionalization of nanoparticles from a low-value raw source, municipal solid waste (MSW) incineration fly ash, using PICVD for functionalization.

4.2 Materials And Methods

MSW fly ash was provided by the Quebec City MSW incinerator. This waste residue is selected in order to verify the effectiveness of our process for what we consider to be the most difficult class of fly ash to treat, as it has the widest range of particle sizes and materials composition. Thus, it will demonstrate the range and versatility of our process. Ash powder was sieved using meshes with 300 µm, 150 µm, and 75 µm size. Then, 1 g of ash powder from the less than 75 µm fraction was used for the experiments. The PICVD technique was then applied for functionalization of particles in ash samples.

4.2.1 PICVD experimental apparatus

Figure 4-1. shows the schematic of the experimental apparatus. The PICVD unit consisted of: two 254 nm UVC mercury or germicidal lamps as an initiation source (Cole-Parmer) and a 45 cm long quartz reactor using standard 24/40 taper joints (Technical Glass Products). The UVC lamps had a

main peak at a wavelength of 254 nm. Syngas (CO and H_2) was used as the functionalization precursor (CO: Pur T-44 and H_2: UHP T-30 - Air Liquide). Although, these reactants are not in the peak absorption of UVC lamps (254 nm), they can be activated at 254 nm and produce active compounds for the formation of functionalized polymeric films [37]. Argon gas (HPT - Air Liquide) was used to purge the reactor before experiments to remove oxygen. For some experiments, H_2O_2 (50% aqueous solution- Fischer Scientific) was added as a photoinitiator to accelerate reaction kinetics and enhance the polymerization rate [37, 38], this was done using a syringe pump at a rate of 0.02 mL/min. Experiments were performed either under slight vacuum (-10 kPa) or at near atmospheric pressure (+10 kPa) regulated by a T-valve at the end of reactor. The irradiance of the UVC lamps was measured at 3.5 cm away from the lamp (in the same distance of reactor from the lamps) using an ILT1700 radiometer/photometer coupled with a SED240/QNDS2/W254 nm sensor (International Light Technologies). The average irradiance at this distance was 0.007 W/cm^2.
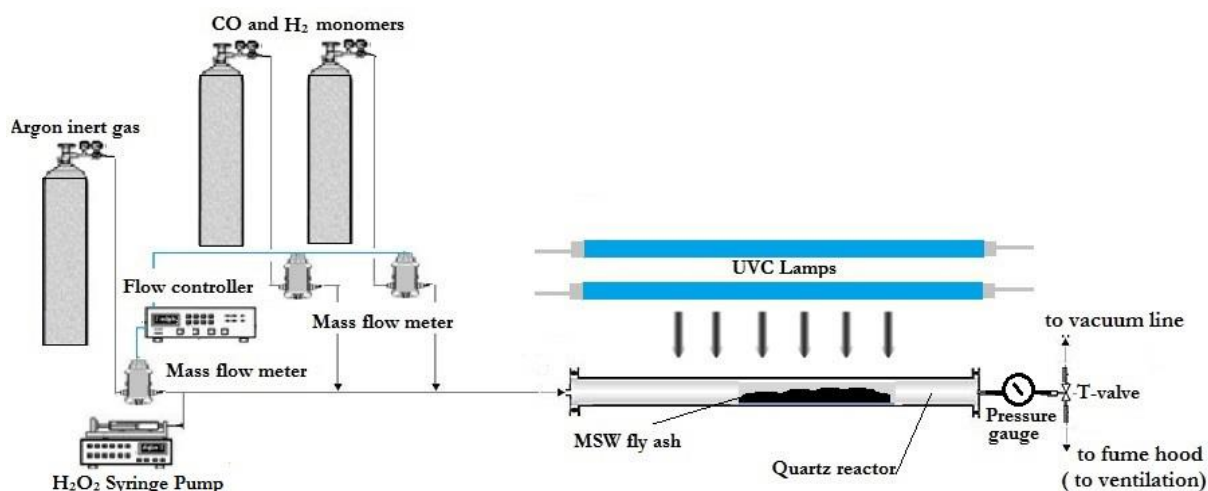
Figure 4-1: Experimental apparatus and injection set-up.

4.2.2 Extraction and functional encapsulation of nanoparticles from ash powder

At first, 1 g of ash powder was loaded in a metal holder and inserted to the reactor. Oxygen molecules are strong electron scavengers; thus, their presence will result in termination of

reactions. To avoid this, reactor was purged using argon gas for 5 minutes. Then, the mixture of CO: 390.1 mL/min and H_2: 48.7 mL/min was injected into the reactor (H_2/CO ratio of 12.5%) [37]. Experiments were performed either while (1) UVC lamps were turned on, or (2) they were turned off (control experiments - syngas was flowing in the reactor). Duration of experiments was fixed to 1h. Temperature inside the reactor was monitored during experiments using an infrared temperature sensor. The measured temperature was 30 ± 7 °C. Table 4-1. summarizes the details of all experiments. Treated ash powders were then dispersed in deionized water or acetone and the resulting samples were loaded in an ultrasonic bath for 2h in order to disperse the particles. The large particulates are then allowed to settle for 24 hours before the liquid supernatant was collected for analysis.

Table 4-1: Experimental details

Experiment Number	H_2O_2 injection	UVC Lamps	Dispersion medium	Pressure
#1	No	Off	Water	Near atmospheric (+10 kPa)
#2	No	On	Water	Near atmospheric (+10 kPa)
#3	Yes	On	Water	Near atmospheric (+10 kPa)
#4	No	On	Water	Slight vacuum (-10 kPa)
#5	Yes	On	Water	Slight vacuum (-10 kPa)
#6	No	On	Acetone	Near atmospheric (+10 kPa)

4.2.3 Characterization and analytical procedures

Dispersed solids remaining in the supernatant were analyzed using Transmission Electron Microscopy (TEM, model JEM 2100F-JEOL Company) in combination with energy-dispersive X-ray spectroscopy (EDS). TEM was operated at 200 kV to acquire bright field images of samples. Morphology and elemental analyses for extracted nanoparticles were conducted using copper (Cu) and nickel (Ni) TEM grids coated with a lacey carbon film (D20040 Grids with formvar substrates

mesh 400, metal Cu; D20045 Grids with formvar substrates mesh 400, metal Ni-SOQUELEC International). The grids were first soaked in the liquid samples and then in the deionized water for few seconds in order to avoid salt contamination on the grids. Then, samples were dried at the room temperature 22 ± 2.5 °C and analyzed. All experimental conditions were repeated at least twice and analyzed using both types of TEM grids in all cases. Moreover, field emission scanning electron microscopy (FESEM) (JEOL JSM7600F) were used to investigate the morphology of untreated ash powder, and its elemental analysis had been performed using Inductively Coupled Plasma Atomic Emission Spectroscopy (ICP-AES, Thermo Scientific iCAP 6500).

After sampling, the remaining supernatant was dried overnight at 55 °C and analyzed by Diffuse Reflectance Fourier Transform Infrared Spectroscopy (DRIFTS, Thermo Scientific Nicolet 6700) to obtain chemical information about the coating and functional organic groups. OMNIC software was used to identify the corresponding peaks. Each sample was scanned 32 times with a resolution of 4.0 cm $^{-1}$. No addition of KBr was necessary for the analysis – samples were directly analyzed in the DRIFTS apparatus to obtain FTIR spectra of solid samples.

4.3 Result And Discussion

4.3.1 Physical characterization

Figure. 4-2 shows FESEM micrographs, along with accompanying EDS spectra, of MSW ash powder before any experiments. This shows that ash samples contains mainly the following elements: Si, Al, O, Ca, Na, Cl, K, P, Mg, S, Ti and Fe. The SEM micrographs serve to illustrate the wide size distribution of the untreated ash.
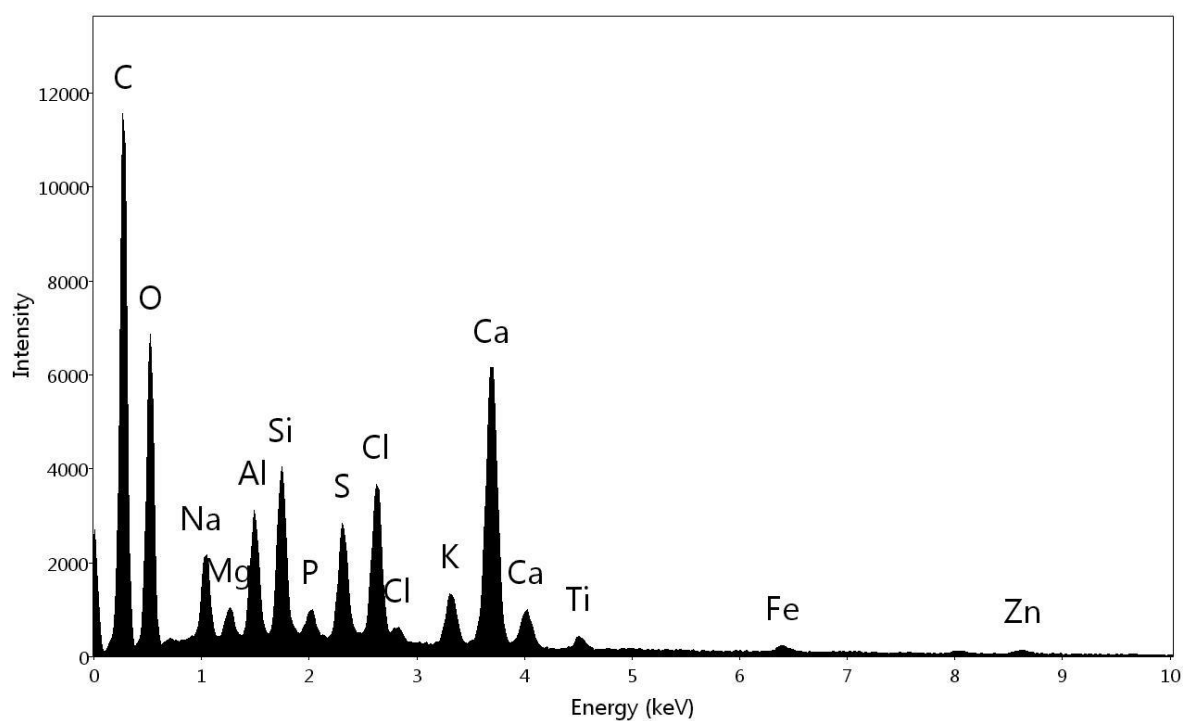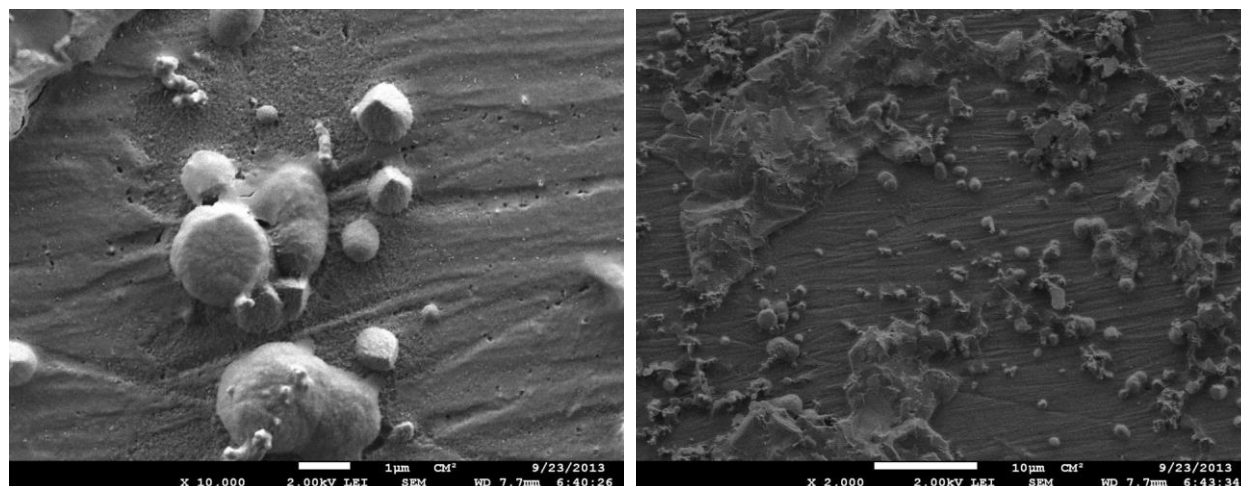
Figure 4-2: SEM and EDS micrographs of untreated ash powder.

Table 4-2 shows the elemental concentration of untreated MSW ash powder. The rest of ash powder is carbon (C) and water (H_2O).

Table 4-2: Elemental concentration of ash powder using ICP-AES analysis.

Element	Ag	Al	As	B	Be
Wavelength	328.06	396.15	189.04	249.77	313.04
concentration (ppm)	0.26	37.41	1.09	0.21	0.00
Std Dev:	0.00	0.19	0.00	0.00	0.00
Element	Ca	Cd	Co	Cr	Cu
Wavelength	393.30	214.43	228.61	206.55	221.81
concentration (ppm)	1495.55	1.59	0.20	1.70	8.45
Std Dev:	0.15	0.00	0.00	0.00	0.01
Element	Fe	K	Mg	Mn	Mo
Wavelength	259.94	766.49	279.55	257.61	202.03
concentration (ppm)	191.63	7.27	84.51	9.41	0.21
Std Dev:	0.01	0.04	0.77	0.06	0.00
Element	Na	Ni	Pb	Sb	Se
Wavelength	589.59	231.60	220.35	217.58	196.09
concentration (ppm)	7.66	1.11	19.71	11.52	0.11
Std Dev:	0.03	0.00	0.01	0.03	0.00
Element	Si	Ti	Tl	V	Zn
Wavelength	251.61	334.94	351.92	292.40	213.85
concentration (ppm)	0.07	6.24	0.00	0.45	48.00
Std Dev:	0.00	0.03	0.08	0.00	0.14

XRD results of crystalline phase of MSW ash powder before any experiments can be found in Figure 4-3.
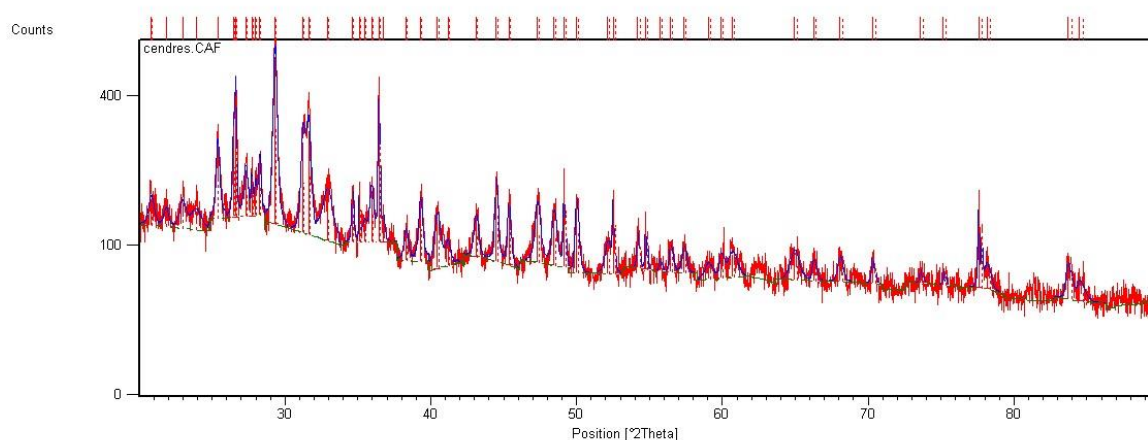
Figure 4-3: XRD pattern of ash powder before any experiments.

This result shows that MSW ash sample contains a large number of phases, which makes the XRD analysis quite uncertain. The large number of peaks makes it possible for many reference patterns (phases) to show a high score of fit with the XRD measurement, even if they are not necessarily present. By using the EDS results shown in Figure 4-2, we can refine the search in the database to find reference patterns that match the measurement. Taking this into account, the samples contains SiO_2, $CaCO_3$ and $NaCl$ and may contain one or more of these phases: $KFeO_2$, $KAlSi_3O_8$, $CaAl_2Si_2O_8$, $Al_2(PO_4)(OH)_3$ and $(Na,Ca)Al(Si,Al)_3O_8$. It is possible and quite probable that other phases are present in this sample, but were either not detected by XRD or were not identified by searching the database.

Figure 4-4; Figure 4-5 show, respectively, the TEM/EDS results of PICVD-untreated and treated ash samples. Results for control experiment (#1, Table 4-1) in Figure 4-4 indicate that there are little or no metal nanoparticles present, except Ca in oxidized form, demonstrating that there is limited potential to extract useful nanoparticles without a functionalization treatment. The TEM micrograph also illustrates the presence of salt (lower-contrast particulates). This by-product is contained in the ash samples, both natively or as a result of the gas cleaning steps applied during the waste incineration process.
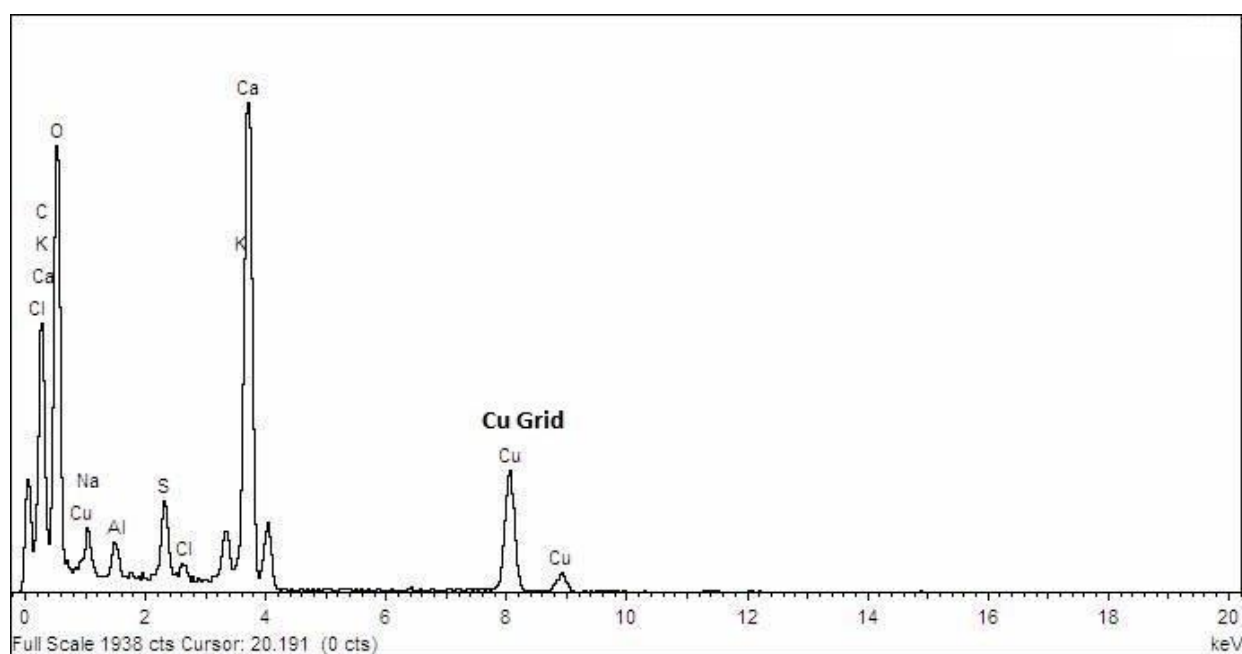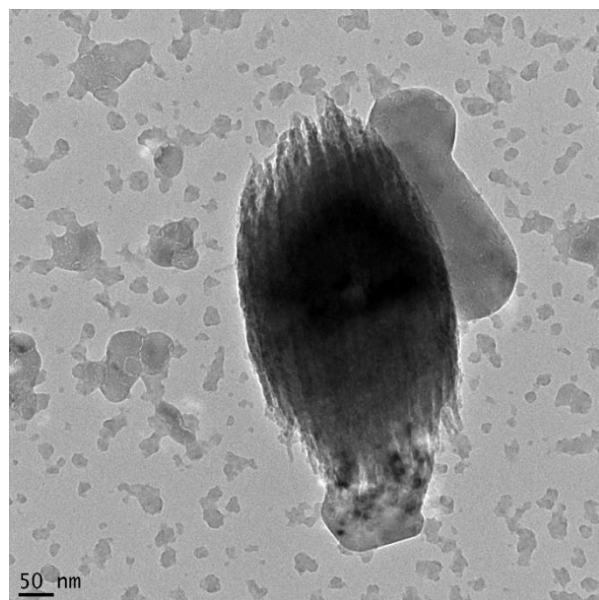
Figure 4-4: (a) A single particle identified on a TEM grid from control experiments; (b) The corresponding EDS spectrum shows its composition is mainly Ca.
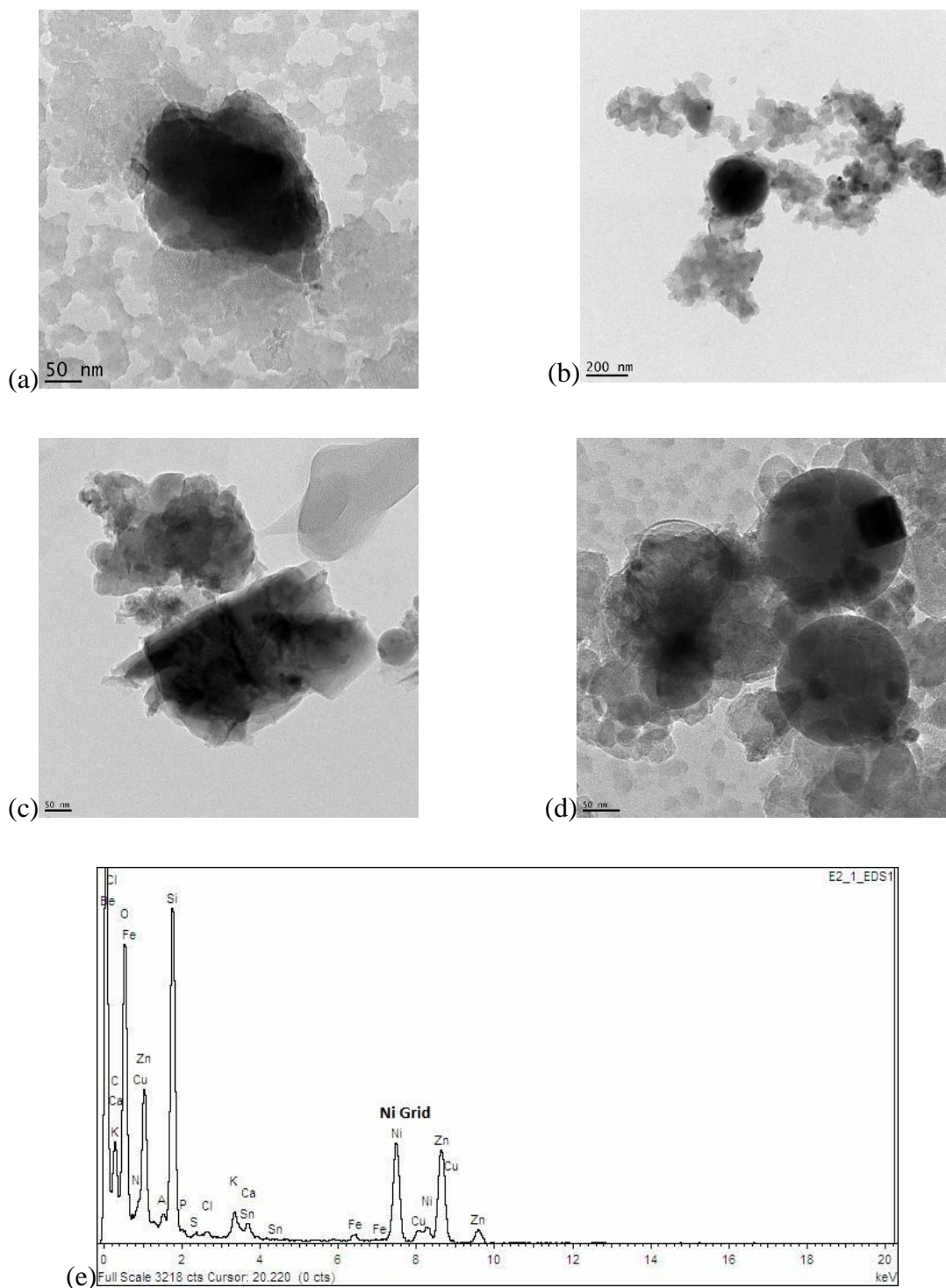
Figure 4-5: TEM micrographs of treated samples (a) Experiment #2, (b) Experiment #3, (c) Experiment #4, (d) Experiment #5, (e) Representative of EDS spectrum taken from experiment #3.

The TEM/EDS results of experiments–2#5 (Table 4-1) in Figure 4-5 demonstrate the presence of nanosize particles in the supernatant of treated ash samples. The nanoparticles found in these samples vary based on the composition of the primary ash sample. Two types of grids were used in order to identify possible Cu and Ni nanoparticles in the samples. EDS analysis was performed on different sections of the grids, confirming the presence of Si, Al, Zn, and Fe as dominant nanoparticles in all of the samples, as well as Cu, Sn, Pb, and Mg.

Lower-contrast salt particulates were also visible for these experiments. These can be removed through successive rinsing steps with water. These results show that extraction of nanoparticles either in the presence or in the absence of H_2O_2 is possible. From treatment to treatment, the same type of nanoparticles can be extracted. However, at this time, only a qualitative study was performed, further quantitative study is warranted.

Several nanofillers like copper oxide (CuO and Cu_2O) [29], iron oxide (FeO, Fe_2O_3 or Fe_3O_4) [39], zinc oxide (ZnO) [40], $CaCO_3$ [28, 30], silica or silicon carbide [35, 41], and aluminum oxide (Al_2O_3) [42] have been applied for in situ polymerization, as previously discussed. These nanoparticles can increase electrical conductivity, photovoltaic properties, thermal conductivity and thermal stability of composites. Almost all of these compounds can be found in the MSW ash samples treated by our method.

While nanoparticles were found generally in agglomerated form, the treated agglomerates remain of interest. Moreover, the facile extraction technique presents other advantages: (1) it can more readily be implemented compared to other functionalization techniques [36], (2) it allows for the extraction of useful nanoparticles allowing clean and closed industrial scale production cycles and (3), it nonetheless allows for stable dispersion of nano-sized particulates because of their functional coating.

As presented, our method allows for the extraction of nanoparticles with multiple components. Other works have focused on the selective extraction of specific materials either by targeted acidic attack or flocculants [17, 18, 27]; through further work, these techniques could be combined with our method. Nonetheless, the low-grade particles we can extract may find applications in various fields.

In order to extend the range of applications, dispersion in other solvents was briefly studied. To do so, treated ash samples were dispersed in a less polar solvent – acetone (polarity index of 5.1,

compared to water at 9.0 [43]). TEM/EDS results (Figure 4-6) showed identical nanoparticles, which demonstrates that either polar (water) or semi-polar (acetone) solvents can be applied for extraction of nanoparticles for this specific set of treatment conditions.
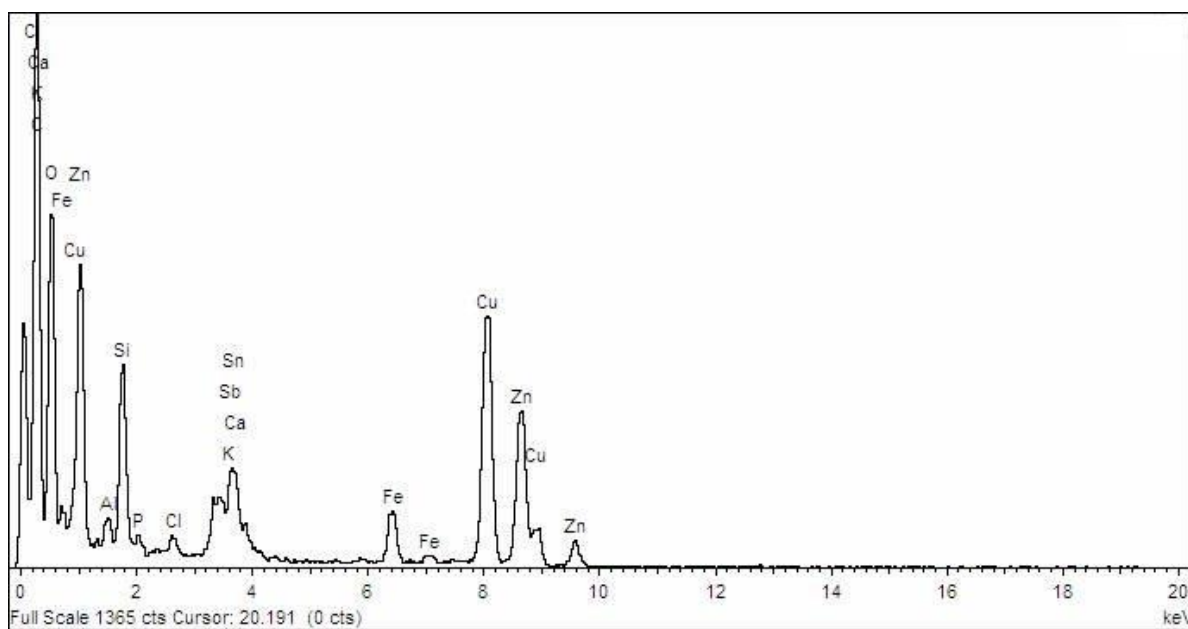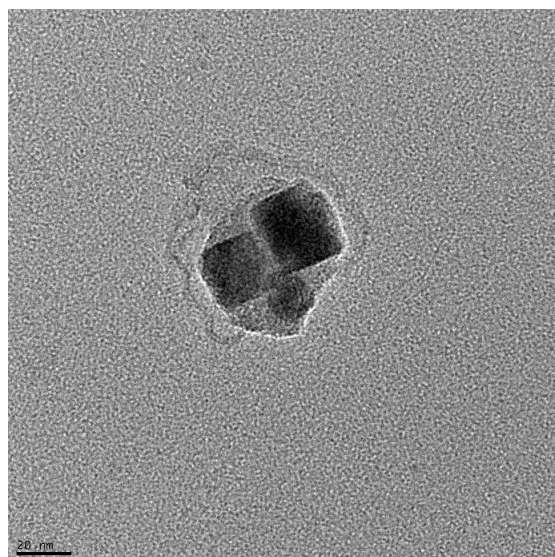
Figure 4-6: TEM micrographs of treated samples (a) Experiment #6, (b) Representative of EDS spectrum.

Syngas (CO and H_2) is one of the common products of gasification processes. It can be used for hydrocarbon formation through the Fischer–Tropsch Synthesis (FTS) pathway. In our case, rather

than target recombination of long hydrocarbon chains, we aim to deposit the radicals produced in the presence of UVC lamps onto substrates – the proposed reaction pathway has been discussed in our previous work [37].

4.3.2 Chemical characterization

DRIFTS analysis was performed to study the organic coating and identify functional groups deposited. Figure 4-7; Figure 4-8 show the DRIFTS spectra taken from experiments 1–6. Table 4-3 represents the likely assignments of the identified peaks in the DRIFTS spectra.
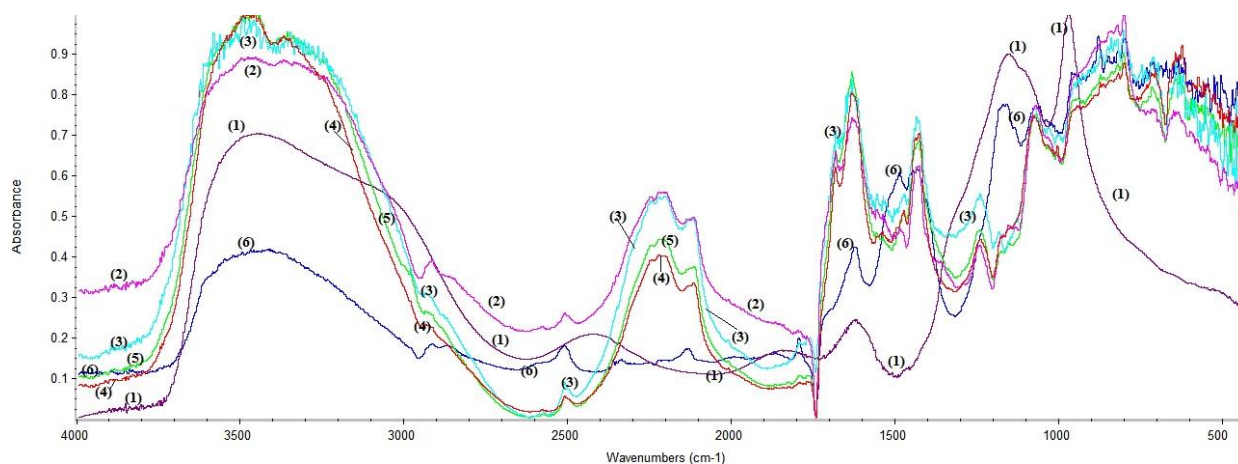
Figure 4-7: DRIFTS spectra comparison for PICVD process: (1) Experiment #1, (2) Experiment #2, (3) Experiment #3, (4) Experiment #4, (5) Experiment #5, (6) Experiment #6.
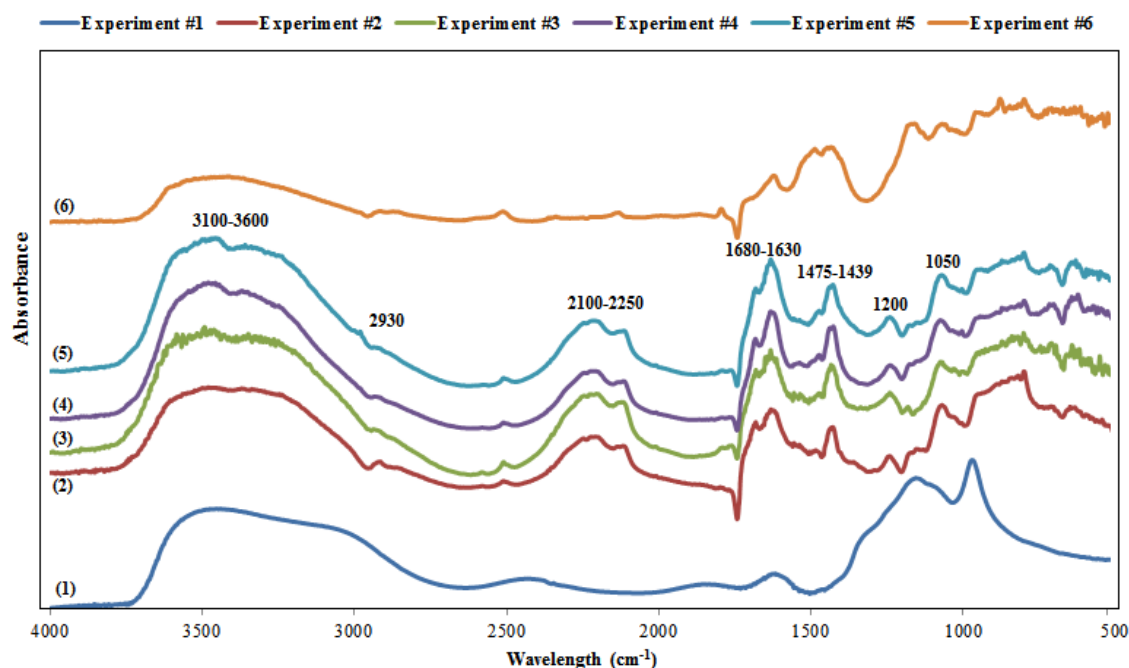
Figure 4-8: DRIFTS spectra for PICVD process along with peaks identifications: (1) Experiment #1, (2) Experiment #2, (3) Experiment #3, (4) Experiment #4, (5) Experiment #5, (6) Experiment #6.

Spectra for the control experiment (experiment 1) shows only –OH functionality due to the adsorption of humidity in 3600–3100 cm^{-1}. In the case of experiments 2–5, which were dispersed in water, clearly, these spectra shows almost similar features and organic coating functionalities. However, the intensity of functional groups is different. The very broad peaks in the 3600–3100 cm^{-1} range strongly indicate presence of hydroxyl groups (single bond OH stretch from both covalently bonded hydroxyl groups and absorbed moisture). This peak overlaps the C–H stretch around 2930 cm^{-1}. There is also a C–O single bond band near 1100–1300 cm^{-1} specifically in the 1000–1070 cm^{-1} and 1240 cm^{-1} ranges, which demonstrate formation of primary alcoholic functional groups as well as phenol groups respectively. In the case of experiment 3, the presence of peaks around 1240 cm^{-1} shows the formation of higher amounts of phenol groups. This means a more aromatic structure was formed in this case compared to the other experimental conditions. Amounts of hydroxyl groups are almost identical in the case of experiments 3, 4, and 5 and they are greater in these experimental conditions compared to experiments 2 and 6.

Table 4-3: Peak assignment in the infrared spectra of dried samples under PICVD coating process.

Peak absorption band (cm^{-1})	Peak assignment
3600-3100	Hydroxyl group, hydrogen-bonded, O-H stretch in aliphatic alcohol
1350-1260	Primary or secondary alcohol, O-H in plane bend
~ 1050	Primary alcohol, C-O stretch
~ 1200	Phenol, C-O stretch
3000-2800	Asymmetric and symmetric methyl ($-CH_3$) and methylene ($-CH_2-$) stretch
2250-2100	$C \equiv C$ stretch in alkynes
1680-1630	C=O stretch in ketones
1475-1430	$-CH_3$ asymmetric and $-CH_3$ asymmetric methyl bending in aliphatic compounds

In experiments 3 and 5, H_2O_2 was used as a photoinitiator, as it can form hydroxyl groups under UVC (254 nm) irradiation due to photolysis. Hydroxyl groups can act as reactive compounds and participate in chain reactions either with CO or H_2 molecules or their radicals [22, 38, 44, 45]. Subsequently, more hydroxyl functionality produces in the presence of H_2O_2 which leads to a more hydrophilic coating (Eqs. (1)–(6)).

$$H_2O_2 + hv\,(254\,nm) \rightarrow 2\,OH^{\bullet} \qquad (1)$$

$$H_2O_2 + OH^{\bullet} \rightarrow H_2O + O_2^{-} + H^{+} \qquad (2)$$

$$H_2O_2 + H^{\bullet} \rightarrow H_2O + OH^{\bullet} \qquad (3)$$

$$H_2O_2 + H^{\bullet} \rightarrow HO_2 + H_2 \qquad (4)$$

$$H_2 + OH^{\bullet} \rightarrow H_2O + H^{\bullet} \qquad (5)$$

$$CO + OH^\bullet \leftrightharpoons HOCO^+ \rightarrow H + CO_2 \qquad\qquad (6)$$

$$\downarrow$$

$$HOCO$$
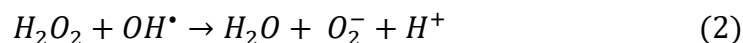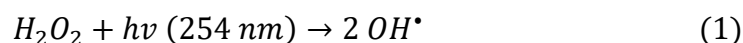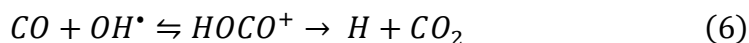
However, the DRIFTS results show that even slight vacuum conditions (experiments 4 and 5) can lead to a similar intensity of the hydroxyl bands to that which was observed for experiments with H_2O_2.

The medium width peak at 1630-1680 cm^{-1} represents ketonic functionality (C=O stretch). This peak is slightly lower in the case of experiments 2 compared to 3, 4, and 5 which means either in the presence of H_2O_2 or vacuum pressure more polar functionalities were formed. On the other hand, peaks around 1475-1430 cm^{-1} are related to the formation of aliphatic groups (-CH$_3$ and -CH$_2$-). Figure 4-7 and 4-8 suggests almost identical amounts of aliphatic groups are produced in the case of experiments under slight vacuum pressure (experiments 4 and 5). However, in the case of near atmospheric pressure experiments (experiments 2 and 3), more aliphatic chain forms in the presence of H_2O_2 (experiment 3) than its absence (experiment 2). The C≡C stretch bands at 2260-2100 cm^{-1} shows the unsaturated functional groups in the coating film. As Figure 4-7 and 4-8 shows, the amounts of unsaturated C≡C functionality is greater in the case of experiments 2 and 3 (near atmospheric pressure) compared to the experiments 4 and 5 (slight vacuum pressure). Thus, it is possible to deduce that longer aliphatic chains with more ketone (C=O stretch) and unsaturated alkyne groups (C≡C stretch) are produced in the presence of H_2O_2 and at atmospheric pressure (experiment 3), while at near atmospheric pressure more aliphatic groups are formed. Unsaturated coatings have the possibility of undergoing further reactions to add more functionality to the coating, if desired. On the other hand, slight vacuum pressure can lead to results comparable to H_2O_2 injection, at least in terms of the presence of hydroxyl groups. The process economics remain to be analyzed to compare the cost of peroxide to the cost of maintaining a slight vacuum at an industrial scale.

In the case of experiment 6, all observed peaks are of lower intensity. This is attributed to the fact that the acetone solvent was not as efficient in extracting functionalized nanoparticles, given its lower polarity. In fact, qualitative inspection during TEM indicated that fewer nanoparticles were extracted.

4.4 Conclusion

Industrial waste is becoming a real challenge for today's world. Worldwatch Institute projects that the amounts of MSW in the word will increase from today's 1.3 billion tons/year to 2.6 billion tons by 2025 due to urbanization and growing prosperity [46]. On the other hand, the high demand for the production of nanomaterials is estimated to lead to a global market value of \$3.3 trillion by 2018 [47]. Conservative market estimates indicate that only for metal oxide nanoparticles, consumption is expected to rise from 270,000 tons in 2012 to 1,660,000 tons by 2020 [48, 49]. In this work, we investigated the effectiveness of a PICVD-based technique for direct extraction and functional encapsulation of nanoparticles from MSW fly ash powder. Syngas was used as a precursor for polymeric film deposition in the presence of UVC lamps. In some of the experiments, H_2O_2 was injected to accelerate photochemical reactions. TEM/EDS results indicate extraction of functionalized nanoparticles, thus demonstrating the performance of PICVD. DRIFTS analysis demonstrated formation of a polymeric coating on the particles with –OH, –CH_2, –CH_3, C–O, C=O, and C≡C. Moreover, results showed more unsaturated polymeric film forms at atmospheric pressure compared to the vacuum.

Given the massive production scale of ash and syngas as by-products of several processes, the practical implementation of these two materials for extraction of precious materials like coated functionalized nanoparticles may have a profound impact in several industries such as waste water treatment and construction materials. Subsequent research will focus on treating ash in a fluidized bed reactor, in order to apply higher quantities of ash samples from different sources (coal, cane, oil shale and MSW) under PICVD treatment.

4.5 References

[1]   F. Peng, K. Liang, and A. Hu, "Nano-crystal glass ceramics obtained from high alumina coal fly ash," *Fuel,* vol. 84, pp. 341-346, 2005.

[2]   S. M. Kulkarni and Kishore, "Effects of surface treatments and size of fly ash particles on the compressive properties of epoxy based particulate composites," *Journal of Materials Science,* vol. 37, pp. 4321-4326, 2002.

[3]   R. W. Styron, "Fly ash composition for use in concrete mix," ed: Google Patents, 2003.

[4]   F. H. Gustin, H. P. Shannonhouse, and R. W. Styron, "Fixation and utilization of ash residue from the incineration of municipal solid waste," ed: Google Patents, 1994.

[5]   G.-M. Gao, H.-F. Zou, S.-C. Gan, Z.-J. Liu, B.-C. An, J.-J. Xu*, et al.*, "Preparation and properties of silica nanoparticles from oil shale ash," *Powder Technology,* vol. 191, pp. 47-51, 2009.

[6]   N. R. C. Fernandes Machado and D. M. Malachini Miotto, "Synthesis of Na–A and –X zeolites from oil shale ash," *Fuel,* vol. 84, pp. 2289-2294, 2005.

[7]   S. N. Azizi, S. Ghasemi, and H. Yazdani-Sheldarrei, "Synthesis of mesoporous silica (SBA-16) nanoparticles using silica extracted from stem cane ash and its application in electrocatalytic oxidation of methanol," *International Journal of Hydrogen Energy,* vol. 38, pp. 12774-12785, 2013.

[8]   R. Shawabkeh, A. Al-Harahsheh, M. Hami, and A. Khlaifat, "Conversion of oil shale ash into zeolite for cadmium and lead removal from wastewater," *Fuel,* vol. 83, pp. 981-985, 2004.

[9]   M. L. Oliveira, F. Marostega, S. R. Taffarel, B. K. Saikia, F. B. Waanders, K. DaBoit*, et al.*, "Nano-mineralogical investigation of coal and fly ashes from coal-based captive power plant (India): an introduction of occupational health hazards," *Science of the Total Environment,* vol. 468-469, pp. 1128-37, 2014.

[10]   L. F. Silva, T. Moreno, and X. Querol, "An introductory TEM study of Fe-nanominerals within coal fly ash," *Science of the Total Environment,* vol. 407, pp. 4972-4, 2009.

[11]   S. Sadasivan, D. H. Rasmussen, F. P. Chen, and R. K. Kannabiran, "Preparation and characterization of ultrafine silica," *Colloids and Surfaces A: Physicochemical and Engineering Aspects,* vol. 132, pp. 45-52, 1998.

[12]   N. Mahmood, M. S. Khan, A. U. Khan, K. W. Stöckelhuber, and G. Heinrich, "Purification, surface modification of coal ash silica and its potential application in rubber composites," *Journal of Applied Polymer Science,* pp. 1493-1501, 2010.

[13] N. Sombatsompop, S. Thongsang, T. Markpin, and E. Wimolmala, "Fly ash particles and precipitated silica as fillers in rubbers. I. Untreated fillers in natural rubber and styrene-butadiene rubber compounds," *Journal of Applied Polymer Science,* vol. 93, pp. 2119-2130, 2004.

[14] A. D'Anna, "Combustion-formed nanoparticles," *Proceedings of the Combustion Institute,* vol. 32, pp. 593-613, 2009.

[15] H. Cheng, Y. Hu, "Municipal solid waste (MSW) as a renewable source of energy: current and future practices in China", *Bioresource Technology*, vol. 101, pp. 3816–3824, 2010.

[16] C. C. Wiles, "Municipal solid waste combustion ash: State-of-the-knowledge," *Journal of Hazardous Materials,* vol. 47, pp. 325-344, 1996.

[17] H.-Y. Wu and Y.-P. Ting, "Metal extraction from municipal solid waste (MSW) incinerator fly ash—Chemical leaching and fungal bioleaching," *Enzyme and Microbial Technology,* vol. 38, pp. 839-847, 2006.

[18] F. S. Zhang and H. Itoh, "Extraction of metals from municipal solid waste incinerator fly ash by hydrothermal process," *Journal of Hazardous Materials,* vol. 136, pp. 663-70, 2006.

[19] K. BeruBe, D. Balharry, K. Sexton, L. Koshy, and T. Jones, "Combustion-derived nanoparticles: mechanisms of pulmonary toxicity," *Clinical and Experimental Pharmacology and Physiology,* vol. 34, pp. 1044-50, 2007.

[20] K. Donaldson, L. Tran, L. A. Jimenez, R. Duffin, D. E. Newby, N. Mills*, et al.*, "Combustion-derived nanoparticles: a review of their toxicology following inhalation exposure," *Particle and Fibre Toxicology,* vol. 2, p. 10, 2005.

[21] R.D. Hooton, J.A. Bickley, "Prescriptive versus performance approaches for durability design – the end of innocence?," *Materials and Corrosion*, vol. 63, pp. 1097–1101, 2012.

[22] B. Lothenbach, K. Scrivener, R.D. Hooton, "Supplementary cementitious materials", *Cement and Concrete Research,* vol. 41, pp. 1244–1256, 2011.

[23] A.M. Ramezanianpour, R.D. Hooton, "A study on hydration, compressive strength, and porosity of Portland-limestone cement mixes containing SCMs", C*ement and Concrete Composites*, vol. 51, pp. 1–13, 2014.

[24] M.D.A. Thomas, R.D. Hooton, A. Scott, H. Zibara, "The effect of supplementary cementitious materials on chloride binding in hardened cement paste", *Cement and Concrete Research*, vol. 42, pp. 1–7, 2012.

[25] A. Ansarifar, A. Azhar, N. Ibrahim, S. F. Shiah, and J. M. D. Lawton, "The use of a silanised silica filler to reinforce and crosslink natural rubber," *International Journal of Adhesion and Adhesives,* vol. 25, pp. 77-86, 2005.

[26]   T. Sabbas, A. Polettini, R. Pomi, T. Astrup, O. Hjelmar, P. Mostbauer, *et al.*, "Management of municipal solid waste incineration residues," *Waste Management,* vol. 23, pp. 61-88, 2003.

[27]   T. Van Gerven, H. Cooreman, K. Imbrechts, K. Hindrix, and C. Vandecasteele, "Extraction of heavy metals from municipal solid waste incinerator (MSWI) bottom ash with organic solutions," *Journal of Hazardous Materials,* vol. 140, pp. 376-81, 2007.

[28]   N. Chen, C. Wan, Y. Zhang, and Y. Zhang, "Effect of nano-$CaCO_3$ on mechanical properties of PVC and PVC/Blendex blend," *Polymer Testing,* vol. 23, pp. 169-174, 2004.

[29]   Z. Guo, X. Liang, T. Pereira, R. Scaffaro, and H. Thomas Hahn, "CuO nanoparticle filled vinyl-ester resin nanocomposites: Fabrication, characterization and property analysis," *Composites Science and Technology,* vol. 67, pp. 2036-2044, 2007.

[30]   X.-L. Xie, Q.-X. Liu, R. K.-Y. Li, X.-P. Zhou, Q.-X. Zhang, Z.-Z. Yu, *et al.*, "Rheological and mechanical properties of PVC/CaCO3 nanocomposites prepared by in situ polymerization," *Polymer,* vol. 45, pp. 6665-6673, 2004.

[31]   J. Buongiorno, D. C. Venerus, N. Prabhat, T. McKrell, J. Townsend, R. Christianson, *et al.*, "A benchmark study on the thermal conductivity of nanofluids," *Journal of Applied Physics,* vol. 106, p. 094312, 2009.

[32]   R. Taylor, S. Coulombe, T. Otanicar, P. Phelan, A. Gunawan, W. Lv, *et al.*, "Small particles, big impacts: A review of the diverse applications of nanofluids," *Journal of Applied Physics,* vol. 113, p. 011301, 2013.

[33]   L. S. Sundar, M. H. Farooky, S. N. Sarada, and M. K. Singh, "Experimental thermal conductivity of ethylene glycol and water mixture based low volume concentration of Al2O3 and CuO nanofluids," *International Communications in Heat and Mass Transfer,* vol. 41, pp. 41-46, 2013.

[34]   S.-Y. Fu, X.-Q. Feng, B. Lauke, and Y.-W. Mai, "Effects of particle size, particle/matrix interface adhesion and particle loading on mechanical properties of particulate–polymer composites," *Composites Part B: Engineering,* vol. 39, pp. 933-961, 2008.

[35]   R. Hashemi-Nasab and S. M. Mirabedini, "Effect of silica nanoparticles surface treatment on in situ polymerization of styrene–butyl acrylate latex," *Progress in Organic Coatings,* vol. 76, pp. 1016-1023, 2013.

[36]   C. A. Dorval Dion and J. R. Tavares, "Photo-initiated chemical vapor deposition as a scalable particle functionalization technology (a practical review)," *Powder Technology,* vol. 239, pp. 484-491, 2013.

[37]   C. A. Dorval Dion, W. Raphael, E. Tong, and J. R. Tavares, "Photo-initiated chemical vapor deposition of thin films using syngas for the functionalization of surfaces at room

temperature and near-atmospheric pressure," *Surface and Coatings Technology,* vol. 244, pp. 98-108, 2014.

[38]   T. A. Egerton and H. Purnama, "Does hydrogen peroxide really accelerate TiO2 UV-C photocatalyzed decolouration of azo-dyes such as Reactive Orange 16?," *Dyes and Pigments,* vol. 101, pp. 280-285, 2014.

[39]   S. Gyergyek, M. Huskić, D. Makovec, and M. Drofenik, "Superparamagnetic nanocomposites of iron oxide in a polymethyl methacrylate matrix synthesized by in situ polymerization," *Colloids and Surfaces A: Physicochemical and Engineering Aspects,* vol. 317, pp. 49-55, 2008.

[40]   M. Montazer and M. Maali Amiri, "ZnO nano reactor on textiles and polymers: ex situ and in situ synthesis, application, and characterization," *The Journal of Physical Chemistry B,* vol. 118, pp. 1453-70, 2014.

[41]   Z. Guo, T. Y. Kim, K. Lei, T. Pereira, J. G. Sugar, and H. T. Hahn, "Strengthening and thermal stabilization of polyurethane nanocomposites with silicon carbide nanoparticles by a surface-initiated-polymerization approach," *Composites Science and Technology,* vol. 68, pp. 164-170, 2008.

[42]   Y. M. Cao, J. Sun, and D. H. Yu, "Preparation and properties of nano-Al2O3 particles/polyester/epoxy resin ternary composites," *Journal of Applied Polymer Science,* vol. 83, pp. 70-77, 2002.

[43]   P. C. Sadek, *The HPLC solvent guide*. New York :: John Wiley, 1996.

[44]   K. L. Feilberg, S. R. Sellev??g, C. J. Nielsen, D. W. T. Griffith, and M. S. Johnson, "CO+OH⟶ CO2+H: The relative reaction rate of five CO isotopologues," *Physical Chemistry Chemical Physics,* vol. 4, pp. 4687-4693, 2002.

[45]   M. J. Frost, P. Sharkey, and I. W. M. Smith, "Reaction between hydroxyl (deuteroxyl) radicals and carbon monoxide at temperatures down to 80 K: experiment and theory," *The Journal of Physical Chemistry,* vol. 97, pp. 12254-12259, 1993.

[46]   W. E. Wilson, "A Critical Review of the Gas-Phase Reaction Kinetics of the Hydroxyl Radical," *Journal of Physical and Chemical Reference Data,* vol. 1, pp. 535-573, 1972.

[47]   http://www.worldwatch.org/global-municipal-solid-waste-continues-grow, 2014.

[48]   http://www.prnewswire.com/news-releases/global-market-for-nanotechnol-ogy-to-reach-33-trillion-by-2018-181915881, 2014.

[49]   http://www.researchandmarkets.com/reports/2488811/the_global_market_-for_metal_oxide_nanoparticles, 2014.

CHAPTER 5: ARTICLE 2: KINETICS, CHEMISTRY, AND MORPHOLOGY OF SYNGAS PHOTOINITIATED CHEMICAL VAPOR DEPOSITION

Donya Farhanian, Gregory De Crescenzo, and Jason R. Tavares

CREPEC, Department of Chemical Engineering, École Polytechnique de Montréal, P.O. Box 6079, Station Centre-Ville, Montreal, Quebec H3C 3A7, Canada

KEYWORDS:

Photo-initiated chemical vapor deposition (PICVD), Syngas, Photo-polymerization, Deposition rate, Coating.

Abstract
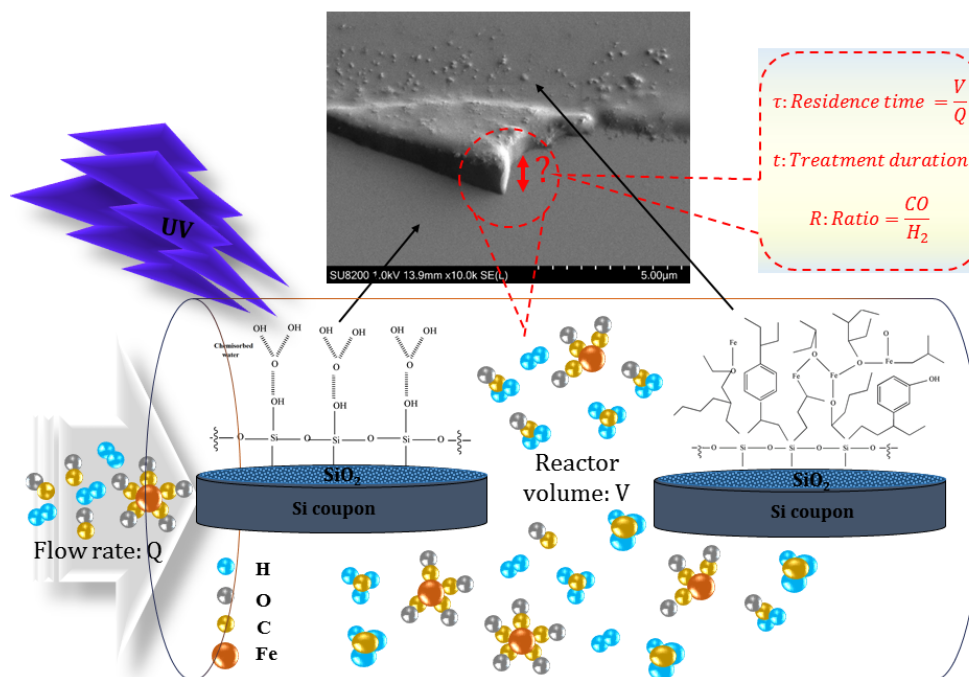
Figure 5-1: Graphical abstract.

Syngas is the product of gasification processes and is used for the production of petrochemicals. Little attention has been paid to its use in the production of oligomeric thin films under ambient conditions. Herein, the nature of the photoinitiated chemical vapor deposition of films made from syngas using high-wavelength ultraviolet light is discussed, including an exploration of the oligomeric films' structure, synthesis mechanism, and growth kinetics. Specifically, X-ray photoelectron spectroscopy and time-of- flight secondary ion mass spectrometry analyses provide insight into the chemical structure, illustrating the effect of photogenerated radicals in the formation of aliphatic, anhydride, and cyclic structures. The films are covalently bonded to the substrate and chemically uniform. Electron and atomic force microscopy identify an island like morphology for the deposit. These insights into the mechanism and structure are linked to processing parameters through a study on the effect of residence time and treatment duration on the deposition rate, as determined through profilometry.

5.1 Introduction

Surface modification techniques have gained a lot of interest due to their ability to tailor surface properties without altering the bulk of the material. Hybrid organic-inorganic coatings are of interest in various fields such as optics, environmental sciences, energy, mechanics, catalysis and sensors, because they can tailor surface wettability as well as the chemical specifications of materials [1-5]. Several techniques such as chemical vapor deposition (including plasma enhanced and thermally activated), atomic layer deposition and sol-gel techniques have been used for thin film synthesis [2,6]. Among these techniques, photo-initiated chemical vapor deposition (PICVD) has considerable superiority given its simple reactor design, ease of use and control, scalability, versatility, affordability and low environmental footprint. The solvent-free deposition nature, as well as the ability to work without any high vacuum or high temperatures make this process an attractive alternative to other gas phase surface modification approaches [7-10].

Most studies in this field use vacuum ultraviolet (VUV) lamps emitting at wavelengths shorter than 200 nm as initiation sources [11-19]. However, despite the ability of light at these wavelengths to cleave most chemical bonds due to their high energy photons (5-15 eV) [20], light transmission becomes prohibitive (i.e. specialized reactor windows, such as MgF_2 and LiF, or designs are compulsory) [2, 21]. Given these limitations, UVC light (200-280 nm) [22], which can be transmitted through affordable quartz windows and generated via commercially ubiquitous germicidal lamps, merits investigation. Its application to PICVD requires the selection of appropriate precursors containing chemical bonds reactive at the wavelength of the UV source.

In general, precursor selection depends on (1) the modification technique, (2) the reactor type and (3) the required chemical and physical bulk properties corresponding to the application. In PICVD, precursors should either absorb UV or, in the case of precursor mixtures, react with the radical/excited species produced upon UV absorption of other monomers. Thus, absorption cross section, absorption coefficient and ionization potential drive precursor selection [2, 23]. Window composition is one of the main features of reactor design. In PICVD processing with UVC lamps, there is no need for special materials and quartz windows are applicable. Many chemical compounds have been investigated for PICVD process such as methyl methacrylate, polyethyleneglycol diacrylate, trimethylolpropane tris (mercaptopropionate), ethylene, styrene,

butadiene, etc [1, 24-29]. However, these need to be excited either in the presence of photoinitiators or photosensitizers, or with high energy UV lamps; this makes the process very expensive.

To overcome these issues, we looked to Fischer-Tropsh synthesis. In this process, catalysts are used to combine the binary mixture of CO and H_2, known as synthesis gas or syngas, into hydrocarbons. Catalysts deactivate during this process, due to the formation of lightly polymerized carbon species [30-34]. This surface fouling can be reimagined as surface engineering - this triggered us to consider syngas as an alternative reactive precursor in PICVD. Very few researchers have attempted to study the photo-polymerization of syngas components [9, 35], and most have focused on carbon monoxide photochemical reactions in the early Earth's atmosphere or with low wavelength VUV lamps [35-37]. Previously, our group demonstrated that syngas PICVD could be used to deposit thin films with various functionalities on copper substrates [9] and nanomaterials [38-41], but the deposition mechanism and kinetics remain elusive. Herein, we report on the photochemical reaction of CO and H_2 molecules to bring new insights into the mechanism and structure of the deposited film, and relate these features to key processing parameters. We present in terms of (i) chemical groups, (ii) density of generated products, (iii) morphology and topography of the deposited thin film, as well as (iv) film growth with respect to the irradiation time (and conversely, reagent residence time). These findings allow us to derive a reaction mechanism for the deposition process and a scheme for the chemical structure of the film, as well as kinetics to explain the deposition rate of the oligomeric film.

5.2 Experimental

5.2.1 Sample preparation

Substrates were type N, orientation 110 silicon wafers with silicon oxide on the top surface (University Wafer), cut into 1 cm × 1 cm coupons. Before experiments, the coupons were cleaned by soaking in isopropanol (Fisher, 99.9% purity) in an ultrasonic bath for 10 minutes, and dried with compressed air.

5.2.2 Experimental methodology

Before mounting onto a sample holder, we masked one side of the silicon coupon with Kapton tape to serve as a reference (Kapton® Polyimide for soldering and splicing; 7648A73 McMaster-Carr).

The sample was inserted into the PICVD reactor (Figure A-1), which consists of a 225 cm^3 plug flow quartz tube reactor with standard 24/40 taper joints (Montreal Glassblowing Inc.), surrounded by 28 UVC mercury (germicidal) lamps mounted in a UV-cabinet (custom made by Daavlin Co.). The UVC lamps have a main emission peak at a wavelength of 253.7 nm (measured via Ocean Optics Spectrometer/USB4000-XR1-ES), with a light intensity of 0.012 W/cm^2 at the reactor distance of 33 cm (measured via ILT1700 Research Radiometer coupled with a SED240/QNDS2/W254 nm sensor, International Light Technologies).

Before experiments, the reactor was purged for 5 minutes with 0.4 L/min of argon (Air Liquide, 99.99%). The prescribed amount of syngas (CO and H$_2$, Air Liquide, 99.99%) was then fed to the reactor at an inlet pressure of 40 psi pressure. The reactor was maintained at atmospheric pressure. The UV cabinet was then turned on and treatment duration time was set according to the experimental plan (Table A-1). Experiments were initiated at room temperature (~22 °C). However, over the course of treatment (2h), the temperature increased to 48 °C as a result of the heat given off by the UV lamps. Each experiment was repeated 3 times to ensure reproducibility.

5.3 Characterization Techniques

Elemental analysis of deposited films was done via a VG ESCALAB 3 MKII X-ray photoelectron spectroscope (XPS) equipped with a non-monochromatic Mg-Kα radiation source, operated at 300 W (15 kV, 20 mA). Survey scans were conducted at an X-ray incident angle of 15° with a penetration depths of ∼10 nm. The pass energy was 100 eV for survey scans and 20 eV for high-resolution scans in 1.00 eV and 0.05 eV increments, respectively. Pressure during analysis was kept under 5×10^{-9} Torr and the analyzed surface was 2 mm × 3 mm. Samples were stored under vacuum overnight prior to analysis. The XPS spectra were acquired normal to the sample surface and analyzed via the Avantage XPS software package. The elemental distribution of the samples was determined based on the peak area comparison (C1s, O1s, etc.), normalized to their corresponding sensitivity factors, after removal of the scattered electrons background. In the case of high-resolution spectra, binding energies were referenced to the C1s peak at 285.0 eV to adjust for possible charging effects, and the Shirley method was applied for background noise subtraction. According to the data trend for each distribution of binding energy, the baseline was manually placed. Each curve is represented by its maximum BE in this discussion. Species elemental distribution is obtained via Gaussian/Lorentzian curve fitting on the original curve. The number of

sub-curves and thus the corresponding species of those sub curves were obtained with full width at half maximum (FWHM) = 1.6, 1.8, 2.2, 2.7 eV for C, O, Si, Fe respectively. These are the most frequent FWHM that we observed with this machine for each elements and normally have been used for all samples.

Static time-of-flight secondary ion mass spectrometry (TOF-SIMS) analysis was carried out with a ION-TOF SIMS IV (from ION-TOF GmbH, Germany) equipped with a 25 keV Bi_3 liquid metal ion source as the primary ion beam source, in high current bunched mode. A bunching system gives pulse durations of 21.9 ns with a mass resolution M/ΔM better than 8,000 around m/z 100 in positive and negative SIMS modes. Depth profiling (10 Å maximum) was performed in non-interlaced mode, where the analysis and sputtering occurred with a 50 μm × 50 μm analysis area confined within a 500 μm × 500 μm sputter area, keeping the total dose below 5×10^{12} ions cm^{-2} (so called static conditions). Imaging of the samples was also performed in high mass resolution mode over an area of 500 μm × 500 μm with an imaging pixel density of 128 pixels × 128 pixels. Three measurements at adjacent spots were performed on the samples and positive and negative ion spectra were compared to confirm uniformity. Ion spectra were internally calibrated using H^+, H_2^+, CH_3^+, $C_2H_2^+$, $C_3H_5^+$ and H^-, C^-, CH^-, C_2H^-, and C_4H^- peaks, respectively.

Surface morphology of the deposited film was examined with a Hitachi ultrahigh-resolution cold field emission scanning electron microscope (Hitachi SU8230), equipped with an X-ray energy-dispersive spectroscope (EDS) (Bruker® Quad detector-Bruker® 4SD Argus system) operated at an accelerating voltage of 1-2.5 kV. Samples were mounted on metal stubs using conductive double-sided carbon tape.

Topography was investigated via a Multi-Mode 3 Atomic Force Microscope (Bruker AS-130) (AFM) operated in tapping mode. Microfabricated V-shaped silicon cantilevers (Applied Nano Inc.) with a theoretical spring constant of 37 N/m, a resonance frequency of ~300 kHz and a silicon conical tip (radius = 6 nm) were used. Squares of 5 μm in size were scanned in air under constant applied force conditions at a 0.8-1 Hz scan rate. Nanoscope analysis software was used for image processing and data analysis; images with 512 × 512 pixel resolution were obtained.

The film thicknesses were measured using stylus profilometry with a Veeco Dektak 150 surface profiler. In order to confirm the profilometry measurements, a few samples were measured by an ex situ M44 variable angle spectroscopic ellipsometer at angles of 65°, 70°, 75° in the wavelength

range of 200-1000 nm. The applied optical model consisted of three components: the silicon substrate, the native SiO_2 layer and the film bulk layer. The Cauchy function with Urbach tail was incorporated for bulk components modulation. The model also took into account possible thickness inhomogeneity within the sampled area.

5.4 Results And Discussion

5.4.1 Chemical characterization of deposited films

High resolution X-ray photoelectron spectroscopy (XPS) and time-of-flight secondary ion mass spectrometry (TOF-SIMS) analyses provided insight into the chemical composition of the deposited films. In order to gain information on the chemical bonding states and structure of the film, the XPS peaks for bare and coated silicon samples were deconvoluted (Figure 5-2). A summary of the high-resolution spectral deconvolutions along with their possible structure assignment and At % is presented in Table 5-1.

Before treatment, the silicon wafer surface was mainly composed of silicon, oxygen and contained a small amount of carbon, most likely due to contaminants [42,43] (~7.6%, Table 5-1). These contaminants (Figure 5-2a') exhibited a high-resolution Cls peak at binding energy BE $\cong$ 285.0 eV and 286.9, which were assigned to C–C and C–H bonds (such as –CH, –CH$_2$, –CH$_3$ and C$_2$H$_2$, C$_2$H$_5$,...) and C–O–C bonds, respectively. Silicon sub-oxides such as SiO (Si^{2+}), Si$_2$O$_3$ (Si^{3+}) and SiO$_2$ (Si^{4+}) were assigned to BE of 101.4-102.0, 102.1-102.7 and 103.5-104.1 eV within the Si2p peak, respectively [45, 46]. Thus, the broad distribution of Si2p spectra at 102.2–104.2 eV was attributed to the various Si–O$_x$ species (Figure 5-2b'). The oxygen peak at BE $\cong$ 533.3 eV represented oxygen in the oxide form (Figure 5-2c'). High-resolution spectral deconvolution of Si2p and O shows that the atomic percentage of oxygen, and silicon did not match. Indeed, in terms of stoichiometry, the Si/O ratio should be ½, but the amount of oxygen was determined to be higher (for 28.3 At % Si, the corresponding atomic percentage for oxygen should be 56.6% (Table 5-1). The observed higher oxygen amount (+7.5%, Table 5-1) was attributed to surface hydroxyl groups (Si-OH) [45, 47].
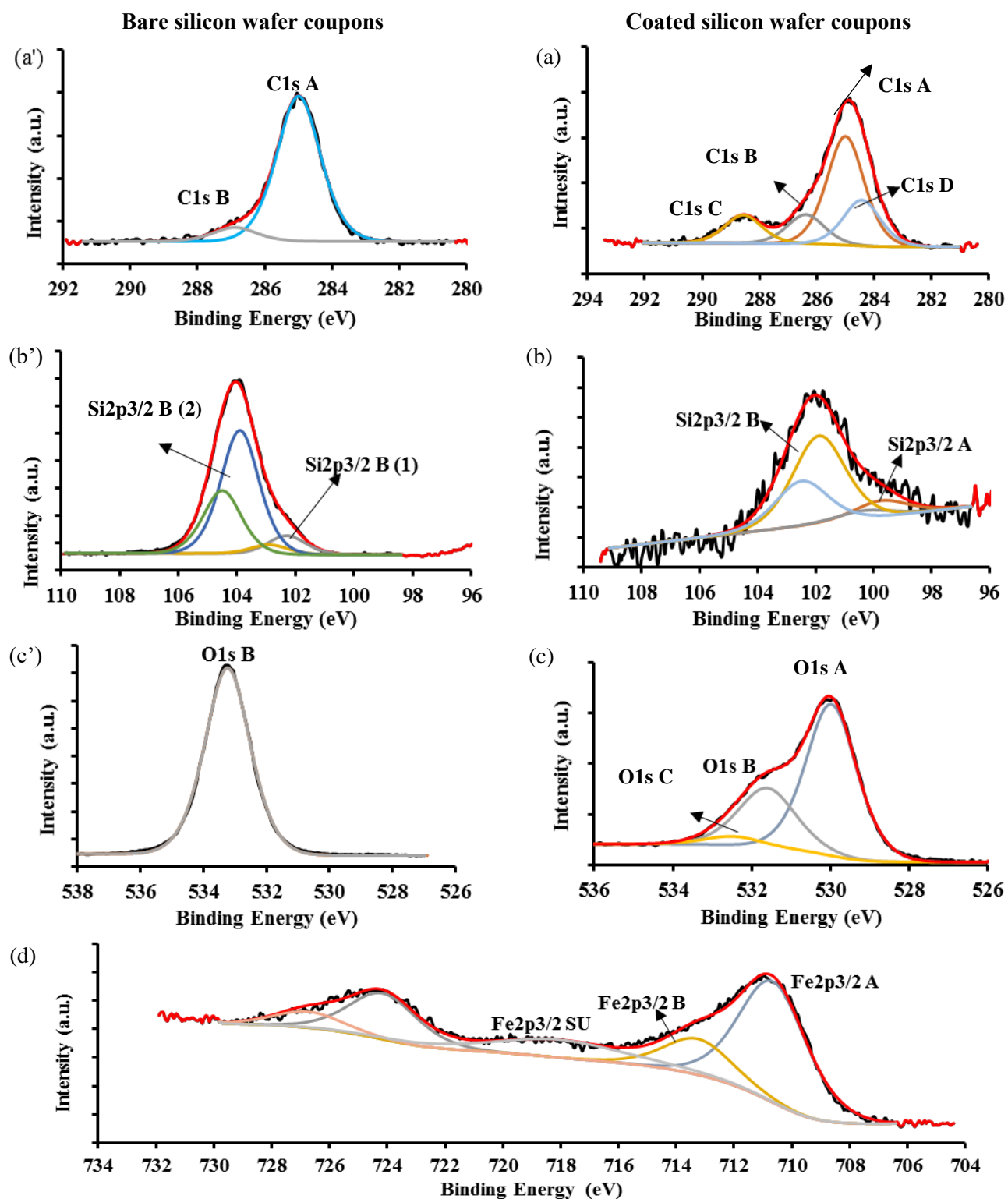
Figure 5-2: Deconvoluted XPS spectra of bare and coated silicon wafer coupons in experiment#1 (Table A-1).

Table 5-1: XPS high-resolution spectral deconvolution peaks and their origins.

Peak Name	Centered Binding Energy [eV]	Possible Structure [1]	Elemental atomic % Area	
			Bare sample	Coated sample[2]
C1s A	285.0	*C–*C,* C–H,*C=*C, etc.	6.4	15.0
C1s B	286.4	*C–O–*C,*C–O–Fe,	1.2	2.4
C1s C	288.6	O–*C–O, O=*C–O,O=*C–O–Fe	-	3.0
C1s D	284.4	Si–*C	-	1.9
O1s A	530.0	Fe–*O	-	36.7
O1s B	531.6	Fe–*O–H, C=*O, Si–*O–H	64.1	8.6
O1s C	532.5	C–*O–Fe, *O=C–*O–Fe	-	6.4
Si2p3/2 A	99.8	*Si–*Si, *Si–Fe	-	1.1
Si2p3/2 B	101.9	H_3C–*Si(O)–CH_3	-	2.0
Si2p3/2 B (1)	102.4	Si^{+2} Polycrystalline Si in Si-O_x	4.5	-
Si2p3/2 B (2)	103.9	Si^{+4} Polycrystalline Si in Si-O_x	23.8	-
Fe2p3/2 A	710.7	*Fe–O, O=C–O–*Fe	-	13.5
Fe2p3/2 B	713.3	C–O–*Fe	-	4.8
Fe2p3/2 SU	718.0	C–O–*Fe, O=C–O–*Fe	-	4.6

(1) *shows the elements correspond to that binding energy.

(2) Elemental atomic % correspond to the experiment #1 (Table A-1).

After PICVD treatment, the C1s peak increased significantly, and the Si2p peak was attenuated, which was in agreement with survey results (Figure A-2 and Figure A-3). The C1s spectrum (Figure 5-2a) showed a group of overlapping peaks with BE from 282 to 292 eV, attributed to four significantly different surface carbon phases (identified as A, B, C and D). The dominant Phase A peak (C1s A, BE $\cong$ 285.0 eV) was attributed to aliphatic carbon (e.g. –CH, –CH_2, –CH_3), as well as polymerized C_nH_m chains (e.g. C≡C, C=C, C–C). Phase B (C1s B, BE $\cong$ 286.4 eV) contained

C=CO–C and C–O–C, though it also could be assigned to C–O–Fe. Phase C (C1s C, BE $\cong$ 288.6 eV) could correspond to O=C–C, O–C–C, and also O=C–O–Fe [6]. This range of BE (286.0–289.0 eV) is generally attributed to carbonates. Phase D (C1s D, BE $\cong$ 284.4 eV) was designated as a carbide carbon layer, in the form of Si–C bonds. This means that the organic films we deposited had bonded with the silicon substrate covalently. Since there is no C1s peak on the untreated sample at BE $\leq$ 284.4 (Figure 5-2a'), this covalent bond was formed during the PICVD process, which was confirmed by the Si2p spectrum: in Figure 5-2b, the attenuation of the doublet Si2p$_{3/2}$ and Si2p$_{1/2}$ in Si-O$_x$ (102-104 eV) was observed after the organic grafting. In grafted silicon samples, the Si2p spectrum consisted of two main peaks and their doublet (A, B) located at BE $\cong$ 99.7 eV, and BE $\cong$ 101.8 eV. The first peak and its corresponding doublet exhibited the characteristic of Si2p$_{3/2}$ with BE $\cong$ 99.7–99.9 eV and Si2p$_{1/2}$ with BE $\cong$ 100.2–100.7 eV. This corresponded to elemental silicon in the form of Si–Si or even Fe–Si bond in the structure of the deposited film [46,48]. The second peak was more alike to the binding energy in organic silicon ~102 eV (Si2p$_{3/2}$ and Si2p$_{1/2}$ of 101.7 eV and 102.4 eV respectively) [46]. Based on the elemental atomic percentage (Table 5-1), we propose the H$_3$C–Si(–O)–CH$_3$ structure for this peak. Other researchers have shown that such covalent bonding is possible through plasma polymerization under low pressure conditions [49]. Here, we demonstrate the formation of a strong covalent bond under gentler, atmospheric PICVD processing conditions.

Using Gaussian fitting and literature reports [46,50], the O1s spectrum (Figure 5-2c) can be divided into three peak areas: A, B and C. A (BE $\cong$ 530 eV) is attributed to oxide species. B (BE $\cong$ 531.6 eV) is assigned to hydroxyl groups such as H–O–Fe, H–O–Si, –O=C, and C–O–O agents in ether and alcohol. C (BE $\cong$ 532.5 eV) corresponds to C–O–Fe, O=C–O–Fe species.

Peaks in the BE range of 705 to 740 eV have been attributed to iron [46]. In syngas PICVD, Fe can come from carbon monoxide cylinders, in the form of iron pentacarbonyl (Fe (CO)$_5$). This compound is generated in small concentrations over extended periods in CO cylinders [51, 52] and happens to be photo-active in the UVC range [53]. The peak deconvolution of the Fe2p spectrum (Figure 5-2d) showed two main phases. Phase A was composed of Fe2p$_{3/2}$ (BE $\cong$ 710.2 eV) and Fe2p1/2 (BE $\cong$ 724.5 eV); these were assigned to iron oxide, either in the free state or in chemical bonds with the organic film (e.g. O–Fe, and O=C–O–Fe), with satellite peaks at BE $\cong$ 718.3 eV (Fe2p$_{3/2}$ satellite) and BE $\cong$ 732.5 eV (Fe2p$_{1/2}$ satellite). Based on the literature [46, 54-57], for

iron sub-oxides such as FeO (Fe^{2+}), Fe_2O_3 (Fe^{3+}) and Fe_3O_4 ($Fe^{8/3+}$), binding energy of Fe2p3/2 spectra are 709.1-710.7, 710.6-711.5 and 707.90-710.7 eV, respectively. Thus, the binding energies in phase A corresponded to either Fe^{3+} in Fe_2O_3 or $Fe^{8/3+}$ in Fe_3O_4. Phase B corresponded to the $Fe2p_{3/2}$ and $Fe2p_{1/2}$ peaks located at BE $\cong$ 713.4 and 726.3 eV, which can be assigned to Fe–O–C and Fe–$(OH)_3$. This indicates that $Fe(CO)_5$ is fully decomposed and converted to iron oxide which had been incorporated in the chemical structure of deposited film.

A complementary characterization of chemical bonds between the silicon wafer and the carbon film was then performed by TOF-SIMS analysis. The latter provided more chemical information on the deposited film and further supported our XPS results (Figure 5-3).

(a)

(b)
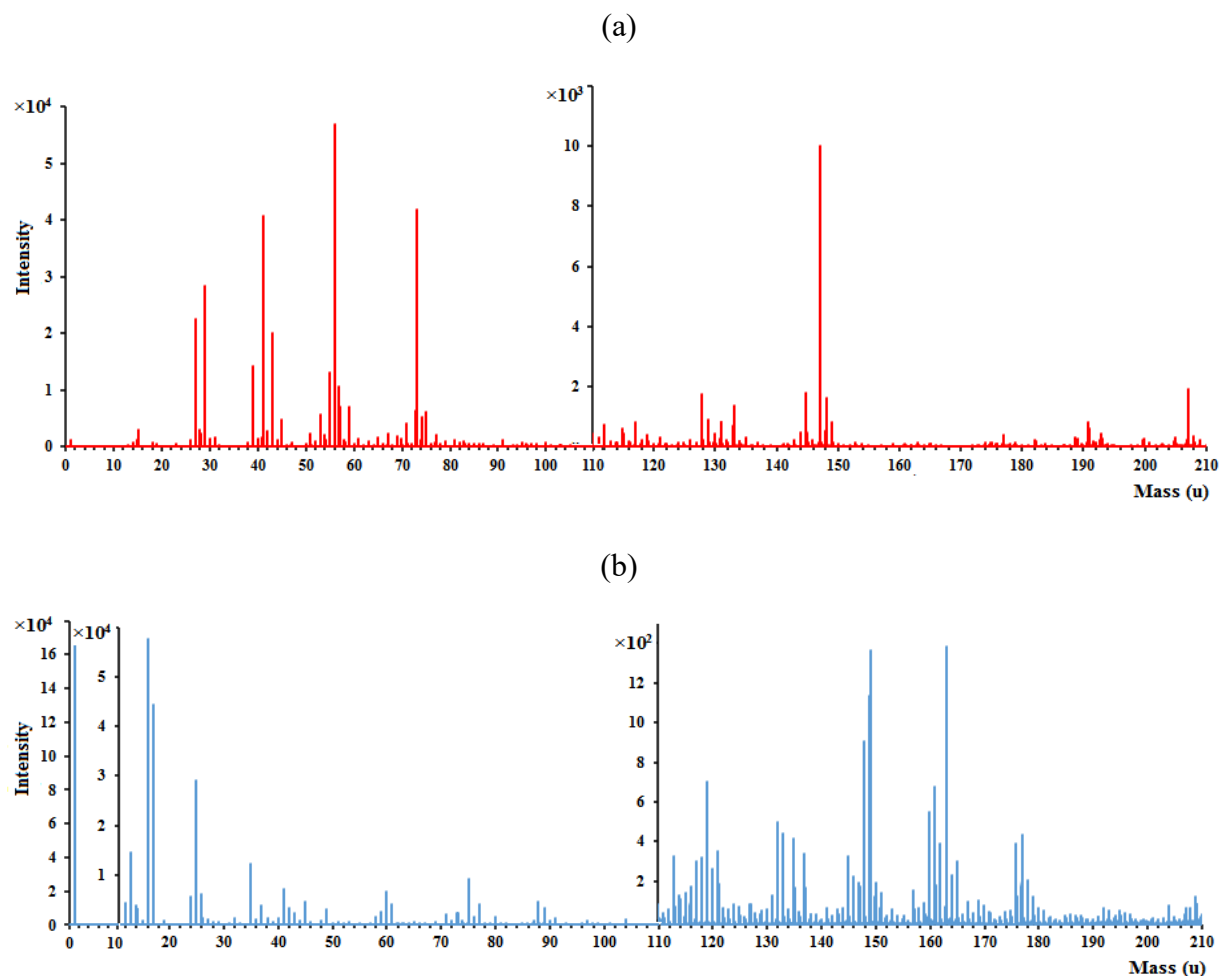
Figure 5-3: TOF-SIMS spectra for coated coupons in experiment #1 (Table A-1): (a) Positive ion and (b) negative ion.

TOF-SIMS results can be divided into three main categories:

(1) Hydrocarbons: Both in the acquired positive and negative spectra, the expected C_nH_m fragments of light polymer-like species were detected. Positive ion spectra suggested that a great number of $C_2H_2^+$, $C_2H_3^+$, $C_2H_5^+$, $C_3H_3^+$, $C_3H_7^+$, $C_4H_9^+$, $C_5H_9^+$, $C_6H_5^+$, $C_6H_6^+$, $C_7H_7^+$, $C_8H_7^+$, $C_8H_{13}^+$, $C_9H_7^+$, $C_9H_{15}^+$, $C_{10}H_8^+$, $C_{11}H_9^+$, up to $C_{12}H_8^+$ ions at m/z = 26, 27, 29, 39, 43, 57, 69, 77, 78, 91, 103, 109, 115, 123, 128, 141, and 152, respectively, were generated by the PICVD treatment. These fragments could be either linear or cyclical. Similar observations have been made in the negative iron spectrum at m/z = 24, 37, 48, 49, 51, 60, 61, 64, 65, 72, 78, 83, and 96 corresponding to C_2^-, C_3H^-, C_4^-, C_4H^-, $C_4H_3^-$, C_5^-, C_5H^-, $C_5H_4^-$, $C_5H_5^-$, C_6^-, $C_6H_6^-$, C_7^-, and C_8^- ions, respectively. Moreover, some fragments with O in $C_nH_mO_y$ formula like $COOH^-$, $C_3H_3O_2^-$, $C_5H_5O^-$, $C_6H_5O^-$, and $C_7H_6O^-$ were detected at m/z = 44, 71, 81, 93, and 106, respectively. These species were related to the carboxylic acid, anhydride and ketone (Figure A-4).

(2) Iron: The spectrum obtained from the positive ions was dominated by peaks representing iron ions. The strongest peaks at m/z = 56 corresponded to Fe^+; whereas, the other peaks at m/z = 57, 68, 69, 70, 71, 72, 73, 80, 84, 85, 86, 89, 96, 101, 112, 124, 128, 132, and 136 in the positive ion spectrum corresponded to different species in the form Fe^+, FeH^+, and $Fe_xO_yH_mC_n^+$, e.g., FeH^+, CFe^+, $FeCH^+$, CH_2Fe^+, $FeCH_3^+$, FeO^+, $FeOH^+$, C_2Fe^+, $COFe^+$, $FeCOH^+$, CH_2OFe^+, $FeCOH_3^+$, C_2OFe^+, $FeCOOH^+$, Fe_2^+, CFe_2^+, Fe_2O^+, C_5OFe^+, and $C_2Fe_2^+$, respectively. Despite these peaks, there was no peak related to the $Fe(CO)_5$ in the negative/positive ion spectra of TOF-SIMS confirming our XPS results indicating this compound was fully decomposed. Several combinations of iron oxide species (e.g. $Fe_2O_2^+$, Fe_3O^+, $Fe_3O_2^+$, $Fe_4O_2^+$) were also found at m/z ranging from 148 to 503. These fragments were also observed in the negative ion mode, as well as fragments in the form of $FeOH^-$, $Fe_xO_yH_mC_n^-$ and OH^- species.

(3) Silicon: The relevant negative and positive ions spectra for silicon showed the presence of Si^+, SiC^+, $SiHO^+$, $SiOCH_3^+$, $SiOC_2H_6^+$ (m/z = 28, 44, 45, 59, 74, respectively) and their relevant negative ions such as $SiCO^-$, SiC_2O^-, SiC_2OH^- (at m/z = 56, 68, 69, respectively). These results corroborated the suspected structure obtained from XPS.

In addition, to confirm the chemical structure of the thin film, TOF-SIMS helped us to investigate the abundance and homogeneity of deposited chemical moieties. Thus, ion imaging was carried out on a deposited film (experiment #1, Table A-1) to identify the ion fragments in the film and their micro-scale spatial distribution (Figure 5-4). We have applied a pixel-by-pixel normalization with respect to the total ion counts. Integrated mass spectrum at each pixel (Figure 5-4a) for all images has been performed. This removed any effect of preferential sputtering and secondary ion yield effects due to topography.

Figure 5-4b-d show the spatial distribution of some light hydrocarbons. $C_2H_2^+$, $C_2H_5^+$, $C_3H_3^+$, … $C_{12}H_8^+$ were observed with dominant distribution of $C_2 > C_3 > C_4$ aliphatic branches. The maximum number of carbon in the polymer reached C_{12}. Also, aromatic structures were detected in the deposited film, most likely phenol, which is in agreements with previous results [9]. Results from these images and TOF-SIMS ion spectra showed formation of acid anhydride, aldehyde, ketones, carboxylic, and hydroxyl groups as well.

Figure 4-4e-h are representative of the spatial distribution of Si ions at the interface between the deposited film and substrate. The SiC distribution images corroborated the formation of covalent bonds between the oligomeric film and the substrate, previously identified by XPS. Moreover, the structures of these covalent bonds are mainly in the form of $SiOCH_3$ and $SiO(CH_3)_2$ at the silicon wafer/deposited film interface. Considering the presence of $SiHO^+$ but not SiO_2 in the sample, the interface consisted mainly of SiOH groups.

Figure 5-4i-l represent some of the iron fragments in the deposited film. Most of the iron in the film was in the form of iron oxide (especially Fe^+) and iron hydroxyl (FeOH). Moreover, some iron was in the form of $COFe^+$, C_3OFe^+, C_5OFe^+, etc. while the ion spectra detected Fe bonding to carbon (FeC^+ and CH_2Fe^+, etc.).
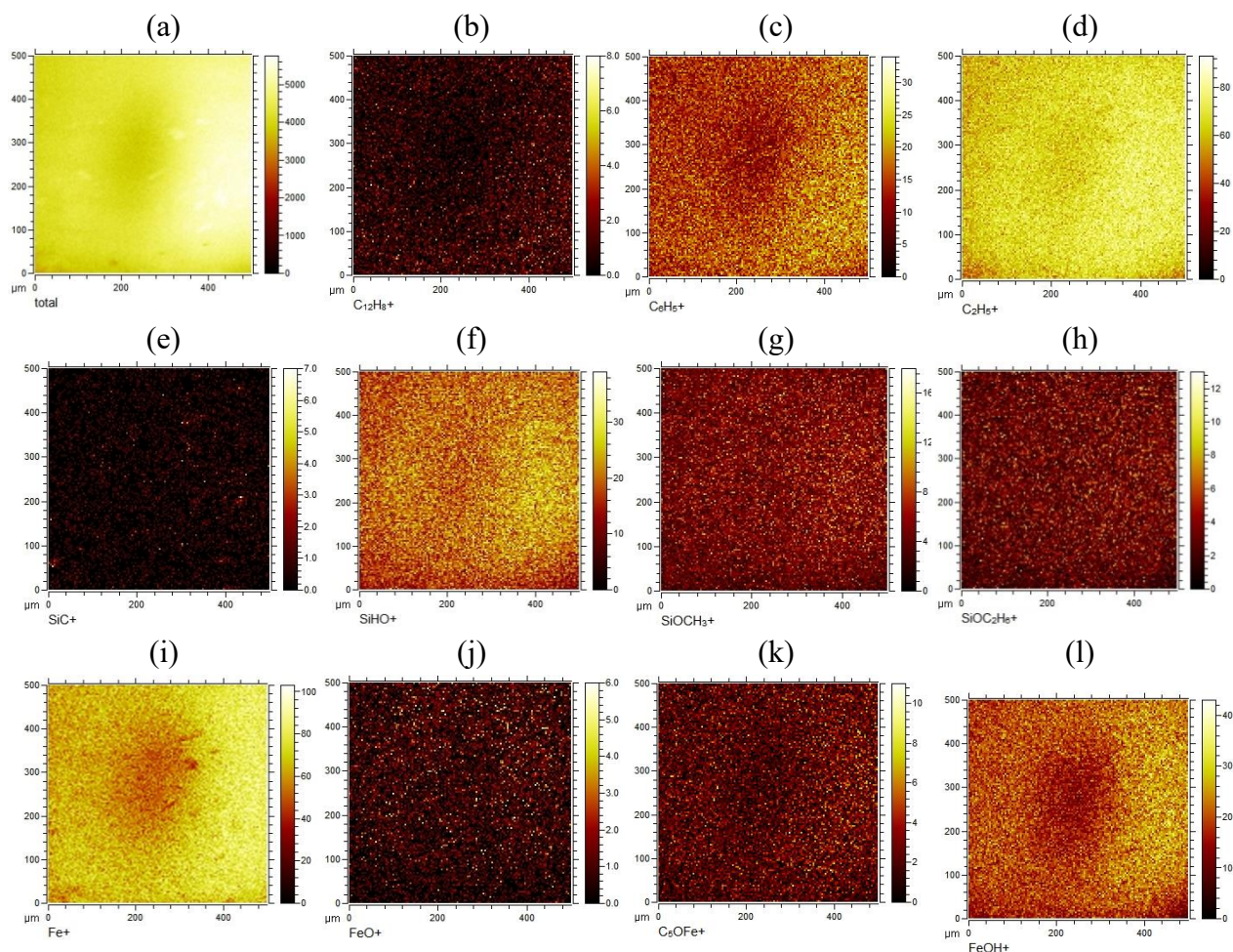
Figure 5-4: A series of positive ion spatially maps showing a 250 μm × 250 μm area of the coated surface normalized pixel by pixel with respect to the total counts images (a) (experiment #1- Table A-1). (a) total counts, (b) $C_{12}H_8^+$, (c) $C_6H_5^+$, (d) $C_2H_5^+$, (e) SiC^+, (f) $SiHO^+$, (g) $SiOCH_3^+$, (h) $SiOC_2H_6^+$, (i) Fe^+, (j) FeO^+, (k) C_5OFe^+, (l) $FeOH^+$.

5.4.2 Proposed mechanism

Based on the in-depth characterization of the chemical structure of the deposited films, we can shed a light on their growth mechanism. Based on the chemical characterization, C, O, H, Fe, Si are the elements existing in the samples. Si and partial O are from the substrate, while the other elements C, H, Fe and partial O are mainly coming from the reactive species. Figure 5-5a shows the chemical structure of the outmost layer of the silicon wafer substrate, which mainly consists of SiO_2 and SiOH, and chemisorbed water. Since the reaction depends on the UV lamps, the absorption cross sections of the participating reactive species are investigated.

Hydrogen (H_2) has an ionization potential of 15.42 eV and a dissociation energy of 4.52 eV [37,58]. Thus, photons at wavelengths below 80.4 nm and 274.3 nm are capable of ionizing and dissociating H_2, provided they can be absorbed. However, H_2 does not absorb light above 110.8 nm [37]. Given that the UVC lamps used in this study emit at 253.7 nm (secondary peak at 185 nm), there will be no energy absorption. In other words, hydrogen cannot participate in the reaction, unless excited by other molecules and radicals.

Carbon monoxide has an ionization potential of 14.01 eV [59] and a dissociation energy of 11.14 eV [58]. This corresponds to a potential for ionization and dissociation at wavelengths below 88.5 nm and 112.3 nm, respectively. CO can absorb light at wavelengths shorter than 200 nm [37], which means that the secondary emission peak at 185 nm can transmit 6.7 eV of energy to the molecule. While this is insufficient for ionization or full dissociation, it is enough to dissociate a constituent π bond (3.7 eV) in CO or cause CO to activate through vibrational excitation [35].

Iron pentacarbonyl ($Fe(CO)_5$) fed concurrently with the CO gas [51, 52], has an ionization potential of 8.35 eV and dissociation energy of 0.37 eV [60,61], corresponding to wavelengths of 148.5 nm and 3350.5 nm, respectively. $Fe(CO)_5$ has strong absorption at 253.7 nm wavelength. It is therefore able to dissociate, resulting in the formation of extra radicals [53, 62].

Thus, the main reactive components following UV irradiation are vibrationally excited CO (CO*), or CO radicals (CO•) with dissociated π bonds and CO• stemming from $Fe(CO)_5$ dissociation. Based on these postulations, two colliding CO* molecules will form a highly unstable unit. Once excess energy has been dissipated via collisions of the nascent cluster with H_2 molecules, lightly polymerized carbon species (mostly consisting of aliphatic chains with $C_2>C_3>C_4$) will be formed

[35, 36, 63]. Iron pentacarbonyl can also play a catalytic role for isomerization of olefins and can increase the formation of alcohols on the film instead of carboxylic groups [64].

Based on the previously identified chemical bonds, as well as the existing Fisher-Tropsch literature [35, 36, 53, 64], we present a series of possible chemical reactions. Initiation mechanisms are based on the absorption cross section, while propagation and termination are based on the structure we obtained and known syngas chemical reactions (see section 7.2):

Initiation

$$CO(\pi - bond\ dissociation) + H_2 \leftrightarrow HCO^{\bullet} + H^{\bullet} \tag{1}$$

$$CO(\pi - bond\ dissociation) + H_2 \leftrightarrow H_2CO^{\bullet} \tag{2}$$

$$2CO^* + H_2 \leftrightarrow CH_2^{\bullet} + CO_2 \tag{3}$$

$$H^{\bullet} + CO^* \leftrightarrow HCO^{\bullet} \tag{4}$$

$$Fe(CO)_5 + hv \leftrightarrow Fe + 5CO^{\bullet} \tag{5}$$

$$Fe(CO)_5 + hv \leftrightarrow Fe(CO)_4^{\bullet} + CO^{\bullet} \tag{6}$$

$$Fe(CO)_4^{\bullet} + hv \leftrightarrow Fe(CO)_3^{\bullet} + CO^{\bullet} \tag{7}$$

Propagation

$$HCO^{\bullet} + H_2 \rightarrow H_2CO^{\bullet} + H^{\bullet} \tag{8}$$

$$CH_2^{\bullet} + H_2 \leftrightarrow CH_3^{\bullet} + H^{\bullet} \tag{9}$$

$$CH_3^{\bullet} + 2CO \leftrightarrow CH_3O^{\bullet} + CO^{\bullet} \tag{10}$$

$$CH_3O^{\bullet} + HCO^{\bullet} \rightarrow CH_3OH + CO^{\bullet} \tag{11}$$

$$CH_3O^{\bullet} + H_2CO^{\bullet} \rightarrow CH_3OH + HCO^{\bullet} \tag{12}$$

$$2CH_2^{\bullet} + H_2 \rightarrow C_2H_2 + 2H^{\bullet} \tag{13}$$

$$H_2CO^{\bullet} + CO \leftrightarrow CO^* + H_2CO^{\bullet} \tag{14}$$

Termination

$$2CH_3O^{\bullet} + 2H_2 \rightarrow C_2H_5 + 2H_2O + HO^{\bullet} \tag{15}$$

$$CO^{\bullet} + HCO^{\bullet} + CH_3O^{\bullet} \rightarrow CH_3OOH \tag{16}$$

$$Fe(CO)_2^{\bullet} + HO^{\bullet} \rightarrow FeOH + 2CO^{\bullet} \tag{17}$$

$$CO^{\bullet} + 2HO^{\bullet} \rightarrow CO_2 + H_2 \tag{18}$$

$$nCO + (2n+1)H_2 \rightarrow C_nH_{2n+1} + nH_2O \qquad \text{Paraffins} \tag{19}$$

$$nCO + (2n)H_2 \rightarrow C_nH_{2n} + nH_2O \qquad \text{Olefins} \tag{20}$$

$$CO + H_2O \rightarrow H_2 + CO_2 \qquad \text{Water-gas shift} \tag{21}$$

Reaction (8) is endothermic (16.4 kcal mol-1), which makes this reaction most likely irreversible. It needs 20 kcal mol-1 activation energy, provided mostly through exothermic reactions (such as (4), which gives off 17 kcal mol-1) [35]. On the other hand, for most free-radical polymeric chain reactions, vibrational excitation is key to provide the driving force for propagation step. As such, reaction (14) must maintain this driving force by transferring vibrational energy to CO, otherwise the reaction would move towards termination [35]. These pathways are based on observations by Roussel and Back, who had conducted research on the photochemistry of CO/H_2 mixtures irradiated with light at 193.3 nm (similar to the secondary emission peak of our Hg lamps).

This proposed series of reactions leads to the formation of light paraffins, olefins and iron oxide on the surface of the Si substrate (with water as an expelled by-product) (Figure 5-5b). Most reactive species are bonded to iron and also can react with either hydroxyl groups on the Si surface or directly with Si to bond covalently.
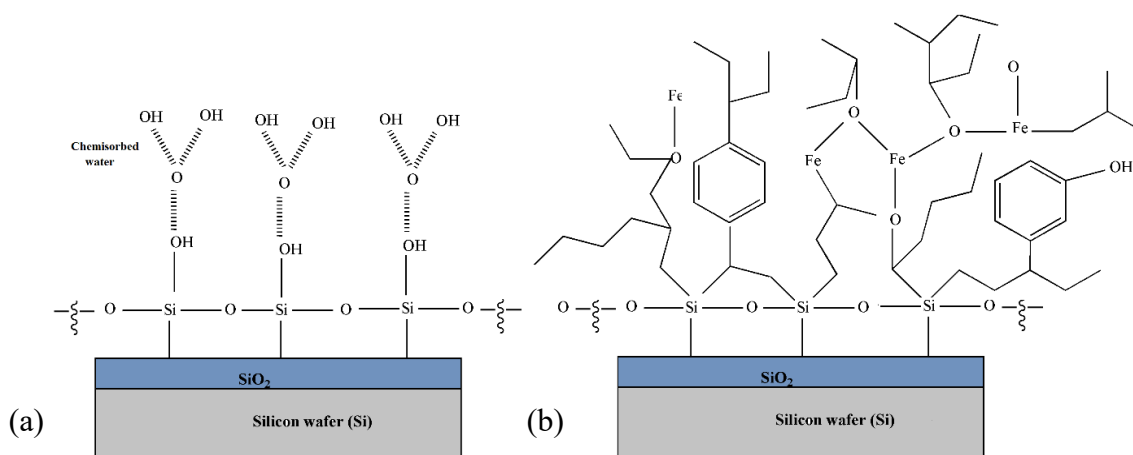
Figure 5-5: Schematic of (a) bare silicon wafer (b) deposited oligomeric film on silicon wafer.

Chemical characterization results showed uniform distribution of chemical bonds in the deposited film. These observations triggered us to explore if we have same uniformity in the morphology and texture of the deposited film.

5.4.3 Surface morphology and topography

The electron micrographs of a coated silicon substrate (Figure 5-6b, c) reveal the formation of a textured, particle-like morphology with many micro patterns and trenches along the deposited film. This surface morphology is corroborated by AFM (Figure 5-6d), showing that the features have a trench size on the order of 40 nm. Such island-like deposition is consistent with previous investigations on PICVD [9]. This textured morphology is observed even for very low film thickness (treatment duration t = 30min). The trenches are filled in as treatment duration increases, leading to a more uniform film (see Supplementary Figure A-5 profilometry results).

This kind of trench morphology of film formation is common especially in the case of transient metals [65], and can be explained in our case by the involvement of iron and iron oxide in the deposition reaction. Film deposition in this case follows the Volmer–Weber (VW) growth mode (3D morphology, island growth) and allows us to gain information on the surface tension of the film through Bauer's criterion ($\gamma_{film} \gg \gamma_{substrate}$, $\gamma_{substrate} = 44.16$ mJ/m^2, Figure 5-6e) [66]. Control of the film morphology (and therefore macroscopic properties such as wettability) is the focus of on-going work, namely through the action of treatment pressure.

Through energy-dispersive X-ray spectroscopy (EDS), SEM measurements allowed us to further confirm the uniform elemental distribution and composition of the films (Figure A-6). Bare silicon substrates show mainly Si and O, with some C (Figure A-6a) – C attributable to contamination [42,43], while the coated sample (Figure A-6b) exhibits an increase in the C peak and the presence of a Fe peak in the deposited film. The mapping analyses of bare and coated samples in Figure A-6c-f confirm the formation of a film (clear contrast with the reference area covered with Kapton tape during treatment). As we move further to the right-hand side, the amounts of Fe and C increase.

The film also exhibits stability to solvent attacks, resisting immersion for 1 h in chloroform (Table A-2), in agreement with previous work showing stability with respect to solvents.
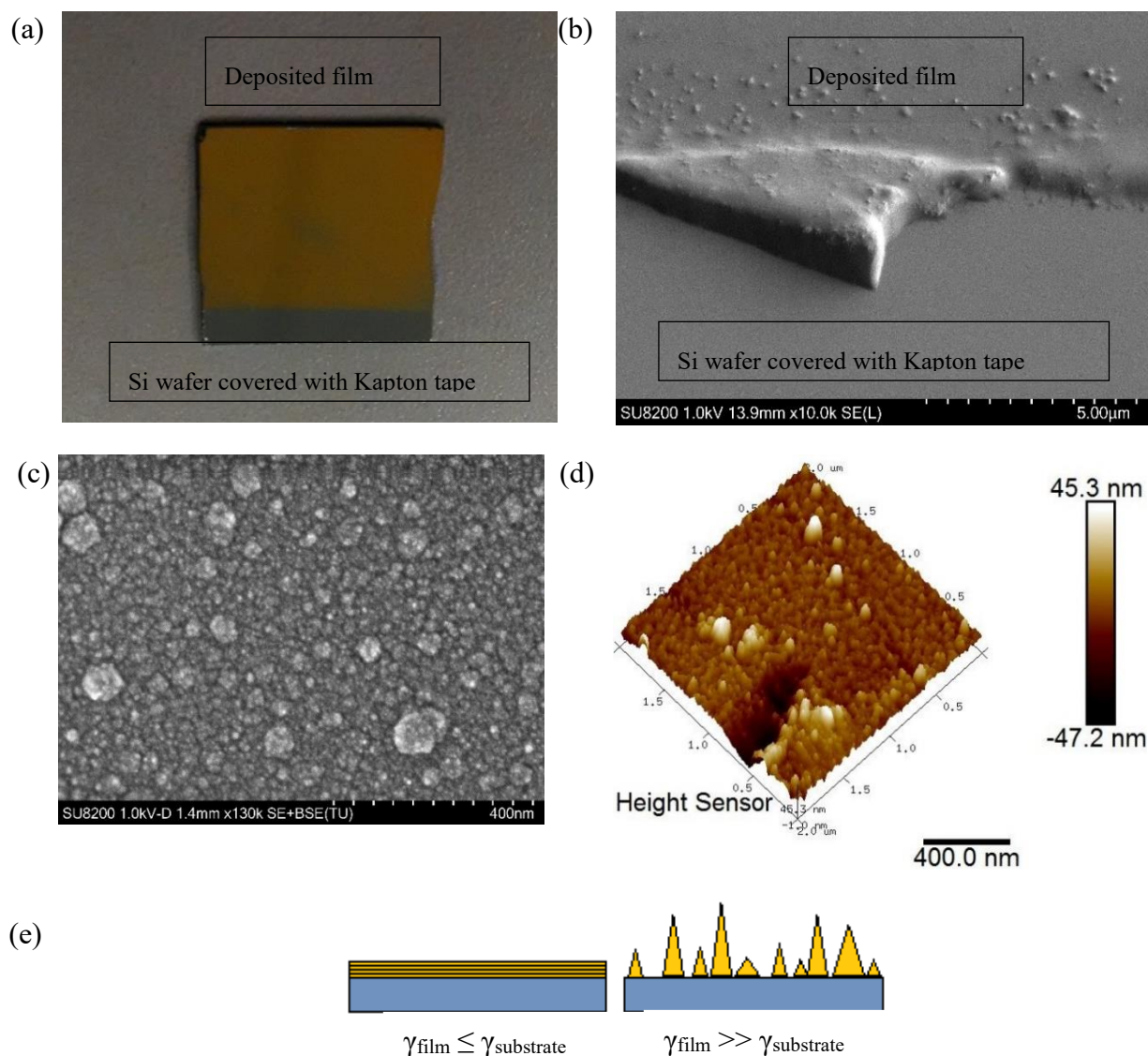
Figure 5-6: (a) Coated silicon coupon, (b) and (c) FESEM images of deposited film, (d) 3D AFM image of deposited thin film in experiment #1, (e) Bauer's thermodynamic film growth study with respect to surface tensions.

5.4.4 Processing parameters

In an effort to control the thickness of the films deposited through syngas PICVD, we conducted a series of experiments focusing on two main parameters (i) residence time and (ii) treatment duration of experiments.

The time during which the interactions between the UV light and the gas precursors occur, resulting in the production of reactive species, depends on the gas residence time (τ). It can be calculated from Equation 5-1, in which V stands for the reactor volume and Q for the gas precursors volumetric flow rate. For a constant reactor volume, decreasing the flow rate leads to longer precursor residence time and saves consumption of gas precursors, which can be important from an operational point of view.

$$\tau = \frac{V}{Q}$$
<div align="right">Equation 5-1</div>

Using a constant gas feed pressure (40 psi), a volumetric precursor ratio (CO/H_2) of 1 and a total gas flow rate varying from 0.4 to 1 L/min for a 120 min treatment duration, we varied the reactor residence times from 0.6 to 0.2 min (Table A-1). Film thickness (assessed through profilometry) and elemental distribution (determined from XPS measurements) are given as a function of residence time in Figure 5-7a and Figure A-2.

As deduced from Figure 5-7a, the film thickness increased with residence time. Linear regression ($R^2 = 0.95$) indicates accumulation at a rate of approximately 165 nm of film per minute of residence time (note that $\tau = 0$ corresponds to an untreated, bare substrate), though the shape of the curve more closely resembles a sigmoid (indicating diminishing returns at longer residence times). The bare substrate was composed primarily of Si and O, along with some C attributable to contaminants [42, 43] (Figure A-2). For coated substrates ($\tau = 0.2 - 0.6$ min), the C atomic percentage increased to a uniform value of approximately 30%, while Si decreases significantly, indicating that the substrate was masked. The elemental distribution did not vary as a function of τ, indicating that film composition and thickness were independent. Also, despite XPS' shallow probing depth (~10 nm), Si remained visible on the thicker films which is explained by the morphology of the film (see section 3.3).

In order to increase the thickness of the deposited films while decreasing precursor consumption (i.e. at longer residence time), we increased the treatment duration. Figure 5-7b shows the effect of treatment duration (30 to 180 min treatment duration, at a fixed residence time of $\tau = 0.6$ min) on film thickness. Full thickness profiles are available in Supplementary Figure A-5. As expected, film thickness increased linearly with treatment duration [18, 44], at a rate of 0.7 nm/min for $\tau = 0.6$ min.

As already noted for residence time experiments, the amount of Si significantly decreased in the treated samples compared to the bare one. Furthermore, the Si At % decreased with increasing deposition time until 120 min, where it reached a plateau (Figure A-3). This would warrant that by increasing the treatment duration, trenches are masked in the deposited film and a more uniform film is achieved, which is confirmed by profilometry analyses (Supplementary results, Figure A-5).

These findings are important in two respects: first, both the residence time and treatment duration affect the film growth and thickness. Second, lower treatment duration or residence times lead to a less homogeneous film texture (Si visible at low t and low τ). Finally, combining longer residence time and varying treatment duration allows for control over the thickness of the film while limiting gas precursor consumption. After 60 min of treatment, there is no statistically significant evolution in the elemental composition of the film (Figure A-3). We suspect that, before 60 min, the observed difference is attributed to the fact that the substrate is not completely covered (trenches in the film).
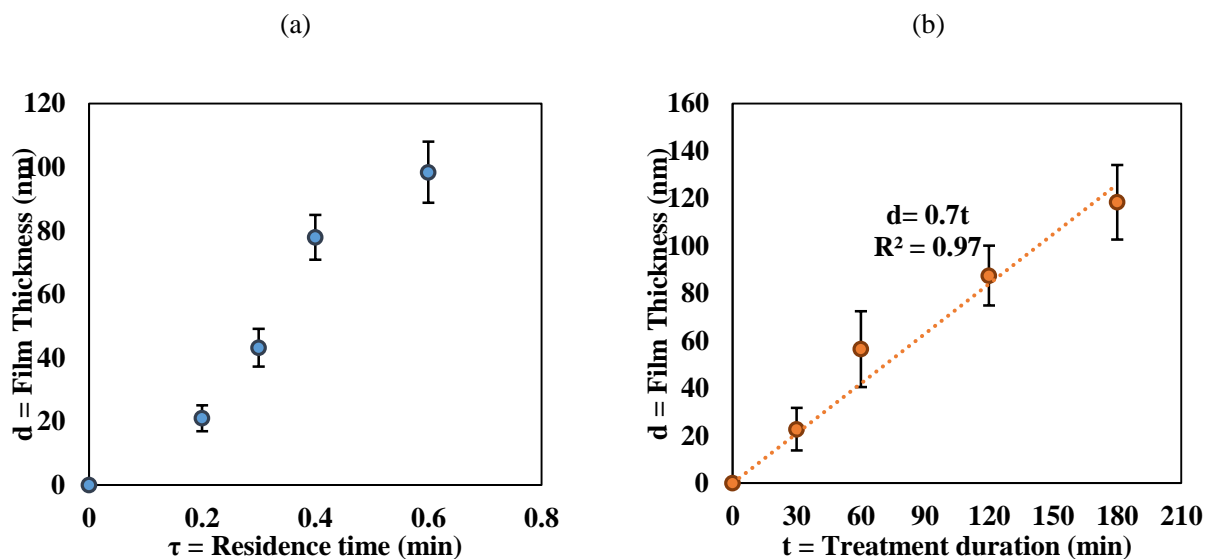
Figure 5-7: (a) Profilometry film growth results vs. residence time (experiments # 1 to # 4, Table A-1; error bars indicate the 95% confidence interval (95%CI)); (b) Variation of film thickness as a function of treatment duration (Data correspond to experiments # 5 to # 8, Table A-1; error bars indicate the 95%CI).

We have shown that film composition is independent of residence time and treatment duration, at a fixed precursor ratio. Given the insights gained from the reaction mechanism, there is reason to believe that varying the precursor ratio may alter the composition and/or growth of the organic film. To investigate this, the gas ratio (CO/H_2) was varied from 0.3 to 3, while the residence time and treatment duration were kept constant at 0.3 min and 2h respectively (Table A-1). Figure A-7 and 8 show that the variation of gas ratio does not have a significant effect both in terms of film growth and chemical composition. The absence of a measurable chemical change after changing the precursor ratio is intriguing, as our previous work had indicated changes in macro-level properties (wettability) as a function of ratio [9]. To confirm, we tested three samples with CO/H_2 ratio = 0.3, 1 and 3 (minimum, middle, and maximum) with TOF-SIMS. Three spots were analyzed on each sample and their spectra were compared to ensure they were representative of the whole sample (Figures A-9 and A-10); these corroborate the high resolution XPS results. Based on these findings, we can conclude that any wettability change previously observed is not likely to be a result of a chemical change, but rather a morphology change on the surface.

5.5 Conclusions

Through this work:

We have gained insight into the growth mechanism of a novel deposition approach (syngas PICVD) and proposed a reaction scheme. Temperature increases over the course of UV treatment would decrease adsorption of reactants and subsequent products to the substrate, considering the constant rate of deposition despite this decrease, one may suggest the reaction limited deposition for PICVD process. Both, XPS and TOF-SIMS reveal the formation of covalently bonded oligomeric film with aliphatic branches and aromatic structure (most likely phenol), as well as acid anhydride, ketones, carboxylic, and hydroxyl moieties. Moreover, we have shown that film thickness can be controlled through treatment duration (as expected), but also through residence time (a feature specific to atmospheric pressure deposition processes). This gives us an ability to control thickness while minimizing precursor consumption. Interestingly, altering the precursor gas ratio does not affect the final composition of the film. However, equal parts seem best suited to provide a slightly thicker film.

Despite these significant findings, a number of potential challenges still exist and are the focus of on-going work, including: (i) the control over Fe contaminants, (ii) understanding the effect of

operating pressure, (iii) relating macroscopic surface properties (wettability) to the observed microstructure, and (v) enhancing functional moieties through additives (H_2O_2, NH_3, etc.). Overall, the development of syngas PICVD with textured oligomeric film shows promise for application in the coatings industry.

5.6 References

[1]   J. P. Deng, L. F. Wang, L. Y. Liu, and W. T. Yang, "Developments and new applications of UV-induced surface graft polymerizations," *Progress in Polymer Science,* vol. 34, pp. 156-193, 2009.

[2]   J. L. Vossen and W. Kern, "Thin Film Processes II," ed: Elsevier, 2012.

[3]   S. B. Herner, "11 - Application of Thin Films in Semiconductor Memories A2 - Seshan, Krishna," in *Handbook of Thin Film Deposition (Third Edition)*, ed Oxford: William Andrew Publishing, 2012, pp. 361-381.

[4]   A. Macleod, "9 - Optical Thin Films A2 - Seshan, Krishna," in *Handbook of Thin Film Deposition (Third Edition)*, ed Oxford: William Andrew Publishing, pp. 271-311, 2012.

[5]   C. J. Petti, M. M. Hilali, and G. Prabhu, "10 - Thin Films in Photovoltaics A2 - Seshan, Krishna," in *Handbook of Thin Film Deposition (Third Edition)*, ed Oxford: William Andrew Publishing, 2012, pp. 313-359.

[6]   S. Kango, S. Kalia, A. Celli, J. Njuguna, Y. Habibi, and R. Kumar, "Surface modification of inorganic nanoparticles for development of organic-inorganic nanocomposites-A review," *Progress in Polymer Science,* vol. 38, pp. 1232-1261, 2013.

[7]   D. J. Broer, G. N. Mol, and G. Challa, "Temperature effects on the kinetics of photoinitiated polymerization of dimethacrylates," *Polymer,* vol. 32, pp. 690-695, 1991.

[8]   K. Chan and K. K. Gleason, "Photoinitiated chemical vapor deposition of polymeric thin films using a volatile photoinitiator," *Langmuir,* vol. 21, pp. 11773-11779, 2005.

[9]   C. A. Dorval Dion, W. Raphael, E. Tong, and J. R. Tavares, "Photo-initiated chemical vapor deposition of thin films using syngas for the functionalization of surfaces at room temperature and near-atmospheric pressure," *Surface and Coatings Technology,* vol. 244, pp. 98-108, 2014.

[10]   K. K. S. Lau and K. K. Gleason, "Initiated chemical vapor deposition (iCVD) of copolymer thin films," *Thin Solid Films,* vol. 516, pp. 678-680, 2008.

[11]   C. Elsner, S. Naumov, J. Zajadacz, and M. R. Buchmeiser, "172 nm excimer VUV-triggered photodegradation and micropatterning of aminosilane films," *Thin Solid Films,* vol. 517, pp. 6772-6776, 2009.

[12]   L. Prager, L. Wennrich, R. Heller, W. Knolle, S. Naumov, A. Prager*, et al.*, "Vacuum-UV irradiation-based formation of methyl-Si-O-Si networks from poly(1,1-dimethylsilazane-co-1-methylsilazane)," *Chemistry,* vol. 15, pp. 675-83, 2009.

[13]   J.-C. Ruiz, P.-L. Girard-Lauriault, F. Truica-Marasescu, and M. R. Wertheimer, "Plasma- and vacuum-ultraviolet (VUV) photo-polymerisation of N- and O-rich thin films," *Radiation Physics and Chemistry,* vol. 79, pp. 310-314, 2010.

[14]   T. Scherzer, "VUV-Induced Photopolymerization of Acrylates," *Macromolecular Chemistry and Physics,* vol. 213, pp. 324-334, 2012.

[15]   V. Skurat, "Vacuum ultraviolet photochemistry of polymers," *Nuclear Instruments and Methods in Physics Research Section B: Beam Interactions with Materials and Atoms,* vol. 208, pp. 27-34, 2003.

[16]   F. Truica-Marasescu, S. Guimond, and M. R. Wertheimer, "VUV-induced nitriding of polymer surfaces: Comparison with plasma treatments in nitrogen," *Nuclear Instruments and Methods in Physics Research Section B: Beam Interactions with Materials and Atoms,* vol. 208, pp. 294-299, 2003.

[17]   F. Truica-Marasescu, S. Pham, and M. R. Wertheimer, "VUV processing of polymers: Surface modification and deposition of organic thin films," *Nuclear Instruments and Methods in Physics Research Section B: Beam Interactions with Materials and Atoms,* vol. 265, pp. 31-36, 2007.

[18]   F. Truica-Marasescu, J.-C. Ruiz, and M. R. Wertheimer, "Vacuum-ultraviolet (VUV) Photo-polymerization of Amine-rich Thin Films from Ammonia-Hydrocarbon Gas Mixtures," *Plasma Processes and Polymers,* vol. 9, pp. 473-484, 2012.

[19]   F. Truica-Marasescu and M. R. Wertheimer, "Vacuum-Ultraviolet Photopolymerisation of Amine-Rich Thin Films," *Macromolecular Chemistry and Physics,* vol. 209, pp. 1043-1049, 2008.

[20]   U. Kogelschatz, H. Esrom, J. Y. Zhang, and I. W. Boyd, "High-intensity sources of incoherent UV and VUV excimer radiation for low-temperature materials processing," *Applied Surface Science,* vol. 168, pp. 29-36, 2000.

[21]   C. Elsner, M. Lenk, L. Prager, and R. Mehnert, "Windowless argon excimer source for surface modification," *Applied Surface Science,* vol. 252, pp. 3616-3624, 2006.

[22]   W. Kowalski, *Ultraviolet Germicidal Irradiation Handbook: UVGI for Air and Surface Disinfection*: Springer Berlin Heidelberg, 2010.

[23]   H. Okabe, *Photochemistry of small molecules*: Wiley: New York, vol. 431, pp 37−58, 1978.

[24]   P. Douglas, H. D. Burrows, and R. C. Evans, "Foundations of Photochemistry: A Background on the Interaction Between Light and Molecules," pp. 1-88, 2013.

[25]   H. Wang, S. Xu, and W. Shi, "Photopolymerization behaviors of hyperbranched polyphosphonate acrylate and properties of the UV cured film," *Progress in Organic Coatings,* vol. 65, pp. 417-424, 2009.

[26]   Y. Yagci, "New photoinitiating systems designed for polymer/inorganic hybrid nanocoatings," *Journal of Coatings Technology and Research,* vol. 9, pp. 125-134, 2009.

[27]   N. S. Allen, "Photoinitiators for UV and visible curing of coatings: Mechanisms and properties," *Journal of Photochemistry and Photobiology A: Chemistry,* vol. 100, p. 101, 1996.

[28]   C. DECKER, "Photoinitiated crosslinking polymerisation," *Progress in polymer science,* vol. 21.4, pp. 593-650, 1996.

[29]   E. Kasparek, J. R. Tavares, M. R. Wertheimer, and P.-L. Girard-Lauriault, "Sulfur-Rich Organic Films Deposited by Plasma- and Vacuum-Ultraviolet (VUV) Photo-Polymerization," *Plasma Processes and Polymers,* 2016.

[30]   E. van Steen and H. Schulz, "Polymerisation kinetics of the Fischer–Tropsch CO hydrogenation using iron and cobalt based catalysts," *Applied Catalysis A: General,* vol. 186, pp. 309-320, 1999.

[31]   A. C. Vosloo, "Fischer–Tropsch: a futuristic view," *Fuel processing technology,* vol. 71, pp. 149-155, 2001.

[32]   Y. Yao, X. Liu, D. Hildebrandt, and D. Glasser, "Fischer–Tropsch synthesis using $H_2/CO/CO_2$ syngas mixtures: A comparison of paraffin to olefin ratios for iron and cobalt based catalysts," *Applied Catalysis A: General,* vol. 433-434, pp. 58-68, 2012.

[33]   C. Zhang, G. Zhao, K. Liu, Y. Yang, H. Xiang, and Y. Li, "Adsorption and reaction of CO and hydrogen on iron-based Fischer–Tropsch synthesis catalysts," *Journal of Molecular Catalysis A: Chemical,* vol. 328, pp. 35-43, 2010.

[34]   Y. Zhang, G. Jacobs, D. E. Sparks, M. E. Dry, and B. H. Davis, "CO and CO_2 hydrogenation study on supported cobalt Fischer–Tropsch synthesis catalysts," *Catalysis Today,* vol. 71, pp. 411-418, 2002.

[35]   P. B. Roussel and R. A. Back, "Photochemistry of $CO-H_2$ mixtures irradiated at 193.3 nm," *Journal of Photochemistry and Photobiology A: Chemistry,* vol. 52, pp. 235-239, 1990.

[36]   J.-S. Wen, J. P. Pinto, and Y. L. Yung, "Photochemistry of CO and H2O: Analysis of laboratory experiments and applications to the prebiotic Earth's atmosphere," *Journal of Geophysical Research: Atmospheres,* vol. 94, pp. 14957-14970, 1989.

[37]   Y. L. Yung and W. B. DeMore, *Photochemistry of Planetary Atmospheres*: Oxford University Press, 1999.

[38]   D. Farhanian, C. A. Dorval Dion, W. Raphael, G. De Crescenzo, and J. R. Tavares, "Combined extraction and functionalization of low-cost nanoparticles from municipal solid waste fly ash through PICVD," *Journal of Environmental Chemical Engineering,* vol. 2, pp. 2242-2251, 2014.

[39]   T. Javanbakht, W. Raphael, and J. R. Tavares, "Physicochemical properties of cellulose nanocrystals treated by photo-initiated chemical vapour deposition (PICVD)," *The Canadian Journal of Chemical Engineering,* vol. 94, pp. 1135-1139, 2016.

[40]   T. Javanbakht, S. Laurent, D. Stanicki, W. Raphael, and J. R. Tavares, "Charge effect of superparamagnetic iron oxide nanoparticles on their surface functionalization by photo-initiated chemical vapour deposition," *Journal of Nanoparticle Research,* vol. 17, p. 462, 2015.

[41]   V. Labonté, A. Marion, N. Virgilio, and J. R. Tavares, "Gas-Phase Surface Engineering of Polystyrene Beads Used to Challenge Automated Particle Inspection Systems," *Industrial & Engineering Chemistry Research,* 2016.

[42]   R. E. Robinson, R. L. Sandberg, D. D. Allred, A. L. Jackson, J. E. Johnson, W. Evans*, et al.*, *Removing Surface Contaminants from Silicon Wafers to Facilitate EUV Optical Characterization*: Society of Vacuum Coaters, 2004.

[43]   R. Robinson, "Removing contaminants from silicon wafers to facilitate EUV optical characterization," degree of Bachelor of Science Department of Physics and Astronomy in partial fulfillment of graduation requirements, Brigham Young University Brigham Young University.

[44]   T. B. Stewart, G. S. Arnold, D. F. Hall, and H. D. Marten, "Absolute rates of vacuum-ultraviolet photochemical deposition of organic films," *The Journal of Physical Chemistry,* vol. 93, pp. 2393-2400, 1989.

[45]   B. E. Deal and C. R. Helms, *The Physics and Chemistry of SiO2 and the Si-SiO2 Interface*: Springer US, 2013.

[46]   D. Briggs, "Handbook of X-ray Photoelectron Spectroscopy C. D. Wanger, W. M. Riggs, L. E. Davis, J. F. Moulder and G. E.Muilenberg Perkin-Elmer Corp., Physical Electronics Division, Eden Prairie, Minnesota, USA" *Surface and Interface Analysis,* vol. 3, 1981.

[47]   M. Yoshimizu, R. Kobayashi, M. Saegusa, T. Takashima, H. Funakubo, K. Akiyama*, et al.*, "Photocatalytic hydrogen evolution over β-iron silicide under infrared-light irradiation," *Chemical Communications,* vol. 51, pp. 2818-2820, 2015.

[48]   K. Rügner, R. Reuter, D. Ellerweg, T. de los Arcos, A. von Keudell, and J. Benedikt, "Insight into the Reaction Scheme of SiO2 Film Deposition at Atmospheric Pressure," *Plasma Processes and Polymers,* vol. 10, pp. 1061-1073, 2013.

[49]   Q. Cao and C. Sylvain, "Organic layer-coated metal nanoparticles prepared by a combined arc evaporation/condensation and plasma polymerization process," *Plasma Sources Science and Technology,* vol. 16, p. 240, 2007.

[50]   G. P. López, D. G. Castner, and B. D. Ratner, "XPS O 1s binding energies for polymers containing hydroxyl, ether, ketone and ester groups," *Surface and Interface Analysis,* vol. 17, pp. 267-272, 1991.

[51]   R. K. Tepe, D. Vassallo, T. Jacksier, and R. M. Barnes, "Iron pentacarbonyl determination in carbon monoxide," *Spectrochimica Acta Part B: Atomic Spectroscopy,* vol. 54, pp. 1861-1868, 1999.

[52]   T. C. Williams and C. R. Shaddix, "Contamination of carbon monoxide with metal carbonyls: implications for combustion research," *Combustion Science and Technology,* vol. 179, pp. 1225-1230, 2007.

[53]   M. Kotzian, N. Roesch, H. Schroeder, and M. C. Zerner, "Optical spectra of transition-metal carbonyls: chromium hexacarbonyl, iron pentacarbonyl, and nickel tetracarbonyl," *Journal of the American Chemical Society,* vol. 111, pp. 7687-7696, 1989.

[54] M. Descostes, F. Mercier, N. Thromat, C. Beaucaire, and M. Gautier-Soyer, "Use of XPS in the determination of chemical environment and oxidation state of iron and sulfur samples: constitution of a data basis in binding energies for Fe and S reference compounds and applications to the evidence of surface species of an oxidized pyrite in a carbonate medium," *Applied Surface Science,* vol. 165, pp. 288-302, 2000.

[55] A. P. Grosvenor, B. A. Kobe, M. C. Biesinger, and N. S. McIntyre, "Investigation of multiplet splitting of Fe 2p XPS spectra and bonding in iron compounds," *Surface and Interface Analysis,* vol. 36, pp. 1564-1574, 2004.

[56] T. Fujii, F. M. F. de Groot, G. A. Sawatzky, F. C. Voogt, T. Hibma, and K. Okada, "\textit{In situ} XPS analysis of various iron oxide films grown by ${\mathrm{NO}}_{2}$-assisted molecular-beam epitaxy," *Physical review B,* vol. 59, pp. 3195-3202, 1999.

[57] T. Yamashita and P. Hayes, "Analysis of XPS spectra of Fe^{2+} and Fe^{3+} ions in oxide materials," *Applied Surface Science,* vol. 254, pp. 2441-2449, 2008.

[58] B. d. Darwent, *Bond dissociation energies in simple molecules [electronic resource] / B. deB. Darwent.* [Washington, D.C.]: U.S. Dept. of Commerce, National Bureau of Standards, 1970.

[59] P. Erman, A. Karawajczyk, E. Rachlewkallne, C. Stromholm, J. Larsson, A. Persson, *et al.*, "Direct Determination of the Ionization-Potential of Co by Resonantly Enhanced Multiphoton Ionization Mass-Spectroscopy," *Chemical Physics Letters,* vol. 215, pp. 173-178, 1993.

[60] A. Junk Gregor and J. Svec Harry, "Energetics of the Ionization and Dissociation of $Ni(CO)_4$, $Fe(CO)_5$, $Cr(CO)_6$, $Mo(CO)_6$ and $W(CO)_6$," in *Zeitschrift für Naturforschung B* vol. 23, ed, p. 1, 1968.

[61] G. Distefano, "Photoionization Study of Fe $(CO)_5$ and Ni $(CO)_4$," *J. Res. Natl. Bur. Stand., Sect. A,* vol. 74, pp. 233-239, 1970.

[62] J. N. Harvey and M. Aschi, "Modelling spin-forbidden reactions: recombination of carbon monoxide with iron tetracarbonyl," *Faraday Discuss,* vol. 124, pp. 129-43; discussion 145-53, 453-5, 2003.

[63] S. V. Filseth, "Vapor Phase Photochemistry of the Neutral Oxides and Sulfides of Carbon," in *Advances in Photochemistry*, ed: John Wiley & Sons, Inc., 2007, pp. 1-57.

[64] R. Kummer, "New Synthesis with Carbon Monoxide. Herausgegeben von J. Falbe. Springer-Verlag, Berlin 1980. XIV, 465 S., geb. DM 244.00," *Angewandte Chemie,* vol. 94, pp. 156-156, 2006.

[65]   S. A. Chambers, "Epitaxial growth and properties of thin film oxides," *Surface Science Reports,* vol. 39, pp. 105-180, 2000.

[66]   H. Brune, "Epitaxial Growth of Thin Films," in *Surface and Interface Science*, ed: Wiley-VCH Verlag GmbH & Co. KGaA, 2013, pp. 421-492.

CHAPTER 6: ARTICLE 3: LARGE-SCALE ENCAPSULATION OF MAGNETIC IRON OXIDE NANOPARTICLES VIA SYNGAS PHOTO-INITIATED CHEMICAL VAPOR DEPOSITION

Donya Farhanian, Gregory De Crescenzo, and Jason R. Tavares

CREPEC, Department of Chemical Engineering, École Polytechnique de Montréal, P.O. Box 6079, Station Centre-Ville, Montreal, Quebec H3C 3A7, Canada
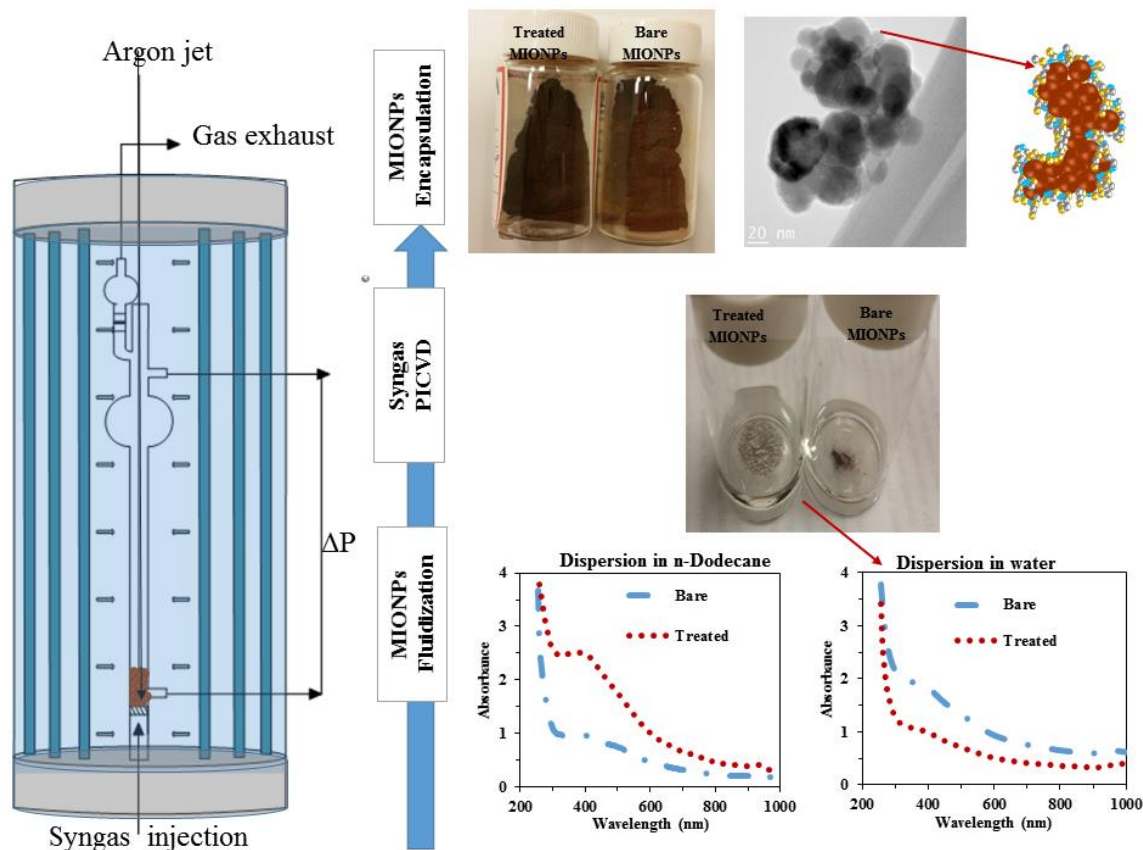
Abstract:

Figure 6-1: Graphical abstract.

Photo-initiated chemical vapor deposition (PICVD) has been adapted for use in a jet-assisted fluidized bed configuration, allowing for the encapsulation of magnetic iron oxide nanoparticles on a larger scale than ever reported (5 g). This new methodology leads to a functional coating with a thickness of 1.4 – 10 nm, confirmed by HRTEM and TGA. XPS characterization confirm that the coating is composed of both linear aliphatic and polymerized carbon chains, with incorporated organometallic bonds and oxygen-containing moieties. UV-Vis absorbance spectra showed that the coating improved dispersion in non-polar solvents, such as n-dodecane. This process represents

a first step towards the large-scale, solvent-free post-synthesis processing of nanoparticles to impart a functional coating.

6.1 Introduction

Magnetic iron oxide nanoparticles (MIONPs) are attractive materials for many industrial applications due to their high surface-to-volume ratio, their morphology, their chemical composition and magnetic properties [1-5]. For example, they have been used as (photo-) catalysts to foster chemical reactions [6-10] and separation processes [11-13]. They have also been employed to improve the mechanical properties of composite materials and produce electrically conductive materials [14-19]. Of interest, in the biopharmaceutical field, these nanoparticles have been successfully applied to drug delivery, high-contrast magnetic resonance imaging (MRI), stem cell labeling/separation and DNA detection [20-24].

Organic encapsulation may further improve the use of iron oxide nanoparticles in these applications, by addressing key points [1, 25-28]: It may (1) limit their agglomeration; (2) enhance stable particle dispersion via anchor groups with high affinity for the desired dispersion matrix and (3) ease the (bio)conjugation of chemicals/drugs via suitable functional anchor moieties.

Many technical approaches for organic encapsulation have been developed through recent advances in surface engineering. Aqueous co-precipitation of chemical reagents via click chemistry, sol-gel, [17, 28-30] as well as plasma [31-34] and thermal chemical vapor deposition [35] are the most common encapsulation techniques. However, in the case of solvent-based reactions, separating coated nanoparticles from solutions often affects process yields drastically (especially if the protocol involves several solvents). This shortcoming is generally dodged in the literature [8, 12, 28]. Plasma and thermal deposition have also important drawbacks, such as high energy consumption, limited scale-up potential (owing to reactor design and low pressure requirements) and compatibility with heat-sensitive substrates [36-38]. In most cases, quantities of coated nanoparticles are limited to micro- or milligrams. Thus, there is an unmet need to develop an industrially viable technique for the encapsulation of nanoparticles. Photo-initiated chemical vapor deposition (PICVD) is well-suited to address this need, as it is a gentle process capable of operating at room temperature and pressure, has a relatively simple reactor design, is capable of

using simple precursors (e.g. syngas), consumes low amounts of energy and provides good control over the thin film deposition process [38-41].

Gas-solid reactors are a popular approach for particles treatment in industry [42-44]. Specifically, fluidized bed reactors are often retained, given that they provide excellent mass and heat transfer (in many cases, this configuration allows for the "stirred-tank" hypothesis to be applied). However, because most nanoparticles belong to the highly-cohesive "Geldart C" group [45, 46], meaning they are not readily fluidized. Indeed, fluidized nanoparticle beds exhibit channeling and form large nano-agglomerates remaining at the bottom of the bed, in turn curtailing bubbling and bed expansion [42, 43, 46]. The implementation of micro jets, sound waves, impactors and vibrations has been assessed to mitigate/eliminate agglomeration [42, 43, 47].

There have been a very limited number of studies involving both particle fluidization and organic encapsulation in a single process [44, 48], and nearly all focused on thermally-based deposition. Zhong et al. have been identified as using a photochemical process (photo-initiated cationic polymerization) for encapsulation of potassium chloride (KCl) micro-particles (40–200 mesh) in a fluidized bed [49]. Later on, Pfeffer's group applied jet-assisted fluidized bed to enhance fluidization of nanoparticles including magnetic iron oxide ones [50].

Previously, our group studied the chemistry of syngas photo-initiated chemical vapor deposition (PICVD) on flat surfaces [39, 40, 51] and on particulates in a plug-flow configuration [41, 52-54]. Herein, we adapt this process for use in a sub-pilot scale jet-assisted fluidization reactor to coat large quantities of MIONPs (grams) in order to improve their dispersion and stability in non-polar (hydrophobic) media.

6.2 Experimental

6.2.1 Materials

Spherical magnetic iron oxide nanoparticles (MIONPs) with 20-30 nm diameter primary particle size (Fe_2O_3, gamma with 98% purity and density = 5.24 g/cm³ at 20 °C) were purchased from NanoAmor Inc. Argon gas with a purity of 99.998%, carbon monoxide and hydrogen gases (the components of syngas) with a purity of 99.8% were purchased from Air Liquide Canada. Solvents such as ethanol, n-dodecane, and acetone with 99.9% purity were purchased from Fisher Scientific Co.

6.2.2 Experimental set-up

The fluidized bed photo-initiated chemical vapor deposition (FB-PICVD) process was carried out in a custom-made fluidized bed reactor (Montreal glass blowing) which consisted of a quartz column with a 25-mm internal diameter, a 28.8-mm external diameter and 1.8-m height (Figure 6-2). The length of column was modular and connections were 24/40 male/female taper joints. A fritted disc with a pore size of 15-40 microns was mounted at the bottom of the column as a gas distributor. An expansion section as well as a pre-filter (i.e., another fritted disc with the same pore size) were installed at the outlet of the reactor to retain the particles. The outlet gas flow then passed through a HEPA filter to remove any entrained small particles before going to the ventilation system.

There were two pressure measurement ports; one was located right above the distributor and the other just before the pre-filter at the top of the column. These pressure ports were connected to a digital manometer (Series 475 Mark III, Dwyer Instruments, 0 to 50 kPa). The reactor column was also equipped with a 1/8" stainless steel tube compressed to form a 100-µm nozzle, to be used as a micro-jet to promote fluidization and provide secondary flow. This micro-jet nozzle was located at the center of the column pointing downwards at about 0.5 cm above the gas distributor. Elastomer-sealed thermal mass flow controllers (SLA5850S Brooks, Polycontrols) connected to a 4-channel electronic control module and power supply were used to supply the inert and reactive precursor gas streams to the system. Secondary flow through the micro-jet nozzle was controlled via a calibrated low flow rotameter (McMaster-Carr. Co.).

The fluidized bed was housed in a custom-made UV cabinet (Daavlin Co.) consisting of 28 UVC lamps. These lamps had a main emission peak at a wavelength of 253.7 nm and a light intensity of 0.012 W/cm^2 at the reactor distance of 33 cm. The wavelength and light intensity were measured via an Ocean Optics Spectrometer/USB4000-XR1-ES and an ILT1700 Research Radiometer coupled with a SED240/QNDS2/ W254 nm sensor (International Light Technologies), respectively.
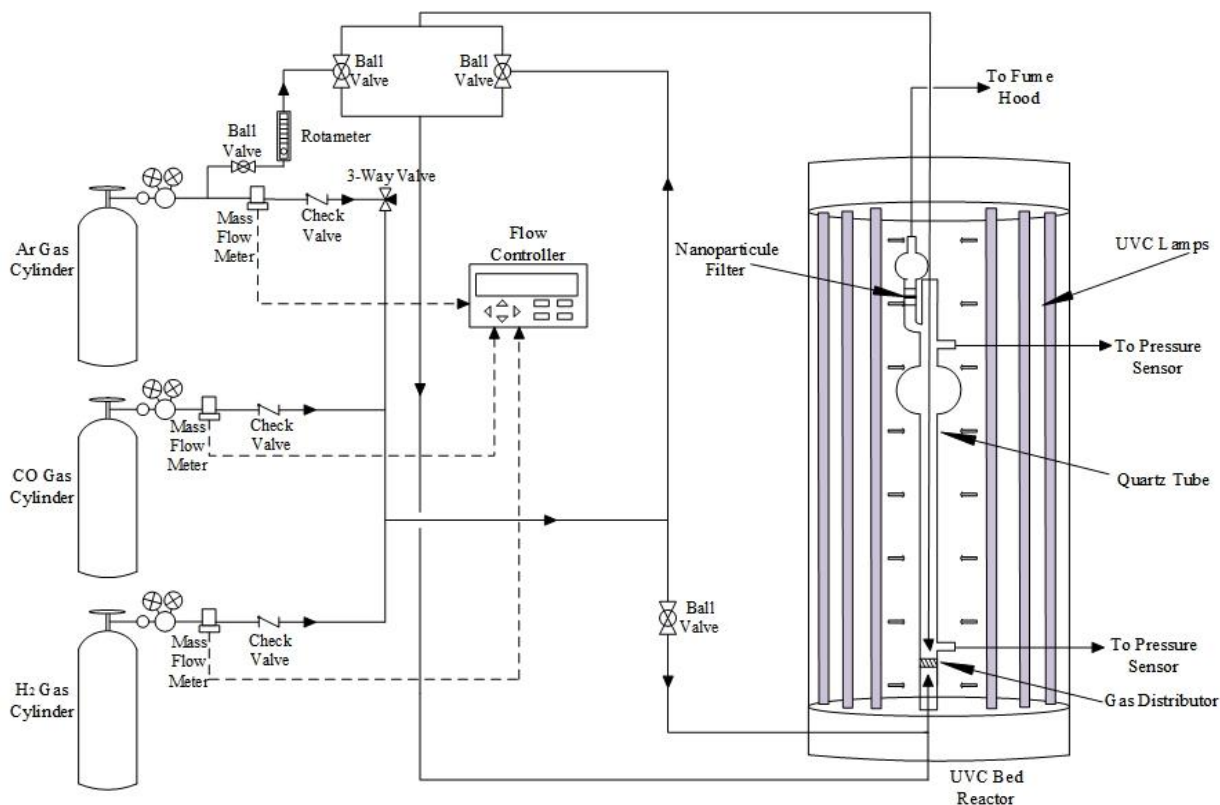
Figure 6-2: Schematic diagram of the FB-PICVD experimental setup.

6.2.3 Fluidization and encapsulation process

5.0 g of vacuum-stored MIONPs were loaded into the reactor. The UVC lamps were turned on for 30 min prior the experiments. Then, 2.4 L/min argon gas (Ar) was injected gradually to fluidize the particles, and facilitate the fluidization of particles by removing adsorbed humidity while evacuating the oxygen from the reactor.

To launch the encapsulation process, hydrogen (H_2) and carbon monoxide (CO) were fed through the reactor distributor gradually, decreasing the Ar flow rate proportionally to maintain particle fluidization. Once the syngas (CO + H_2) flow reached its set point, the Ar micro-jet was activated and adjusted to 0.4 L/min. The minimum fluidization velocity (U_{mf}) was determined by measuring the pressure drop across the particle bed as a function of the syngas superficial gas velocity (U). Figure B-1 shows this differential pressure drop as well as non-dimensional bed expansion as a function of superficial gas velocity during micro-jet assisted fluidization. Considering these curves,

U_{mf} was 5.8 cm/s; however, to improve flowability of particles and increase bed expansion we targeted U = 8.5 cm/s (CO and H_2 flows set to 1.2 L/min – limit of the system), with a micro-jet flow of 0.4 L/min. The micro-jet Ar flow rate was intentionally kept low to avoid dilution of the reactive precursors and avoid excessive gas consumption. The UVC lamps provided sufficient energy to excite the precursors, which would lead to the formation of an oligomeric film on the particles [39, 40]. Total treatment time was 6h, and the film generation reaction was terminated by turning off the UVC lamps and switching the gas flow back to inert gas in order to flush the reactor. Over the course of a typical deposition experiment, the temperature increased from room temperature (~20 °C) to approximately 63 °C; the outlet pressure was atmospheric.

6.2.4 Characterization

To assess the impact of PICVD treatment, if any, on the crystalline phases present in the MIONPs, the particles were analyzed using X-ray diffraction (Philipps X'Pert XRD system) with a Cu anode (K = 0.15406 nm) at a voltage of 50 kV and a current of 40 mA, at room temperature. Scans were conducted from 20.01° to 89.99° at a step size of 0.02° 2Ө/min. Particles phases were identified using the Joint Committee on Powder Diffraction Standards (JCPDS) and ICDD-powder diffraction data system (File 39-1346) [55].

A UV-Visible spectrometer (OceanOptics USB4000-UV-VIS) was used to define the state of aggregation of the nanoparticles in various solvents. The absorption spectrum of the suspensions was obtained from 200 to 1000 nm.

The amount of grafted oligomeric film was determined using thermogravimetric analysis (TGA-METTLER TOLEDO apparatus) operating from 25 to 800 °C at a heating rate of 10 °C/min under nitrogen gas flow. The analyses were conducted on pellets (14.0 ± 2.5 mg) of both bare and treated particles, to ensure that any mass difference recorded was due to thermal decomposition and not loss of particles in the machine.

Transmission electron microscopy (TEM-JEOL JEM-2100F) was applied to determine the thickness of the particles coatings. The TEM was operated at 200 kV to acquire bright field images of the samples. To prepare samples for TEM analysis, particles were dispersed and sonicated in a solvent (methanol, ethanol or n-dodecane). The TEM grids (D20040 grids with formvar lacey carbon, mesh 400, Cu metal SOQUELEC International) were soaked in these suspensions for a

few seconds and dried at room temperature. This was done to improve the uniformity of dispersion on the TEM grids (as opposed to simply depositing the particles onto the grids).

X-ray photoelectron spectroscopy (XPS) characterization was carried out using a VG ESCALAB 3 MKII system equipped with a non-monochromatic Mg-Kα radiation source, operated at 300 W (15 kV, 20 mA). The pass energy of the analyzer was fixed to 100 eV for survey scans and 20 eV for high-resolution scans in 1.00 eV and 0.05 eV increments, respectively. An X-ray incident angle of 15° with a corresponding penetration depth of ∼10 nm was used for survey scans. The binding energy scale of the system and charging of the samples was corrected and calibrated using C1s at 285.0 eV for both high resolution and survey analyses. The analyzed surface was 2 mm × 3 mm and the base pressure of the UHV analysis chamber was kept under 5×10^{-9} Torr. For all spectra, a Shirley background was used before fitting the peaks with a symmetric Gauss-Lorentz sum function. For metallic elements, in this case Fe, a Smart background was selected instead of classic Shirley background. For all peaks, a full width at half-maximum (FWHM) of 1.6, 1.8 and 2.7 eV for C, O, and Fe were used respectively and a Gauss-Lorentz ratio of 50% (0%: pure Gauss, 100%: pure Lorentz) was applied. These are the most frequent FWHM observed with this machine for each element and are normally used for all samples. Moreover, the atomic ratios of elements in the samples were calculated according to the corresponding fitted peak area and corrected by the instrument sensitivity factors (SF). The Scofield sensitivity factors modified for the instrument were 0.25, 0.66 and 2 for C, O and Fe respectively. In this manuscript, all peaks are reported by their centered binding energy (BE). Avantage XPS analysis software was used to deconvolute the peaks in the high-resolution spectra and calculate the peak area.

6.3 Results And Discussion

6.3.1 Physical characterization

6.3.1.1 Structure and nature of MIONPs

MIONPs were treated according to the methodology detailed in section 2.3. Upon particle treatment, we observed a visible color change from light red-brown before treatment to dark black-brown after treatment (Figure 6-3(a)). Such a color change in iron oxide could (though unlikely)

indicate a crystalline phase change. For further investigation, we conducted X-ray diffraction (XRD) and selected area electron diffraction (SAED) analyses (Figures 6-3(b), (c) and (d)).
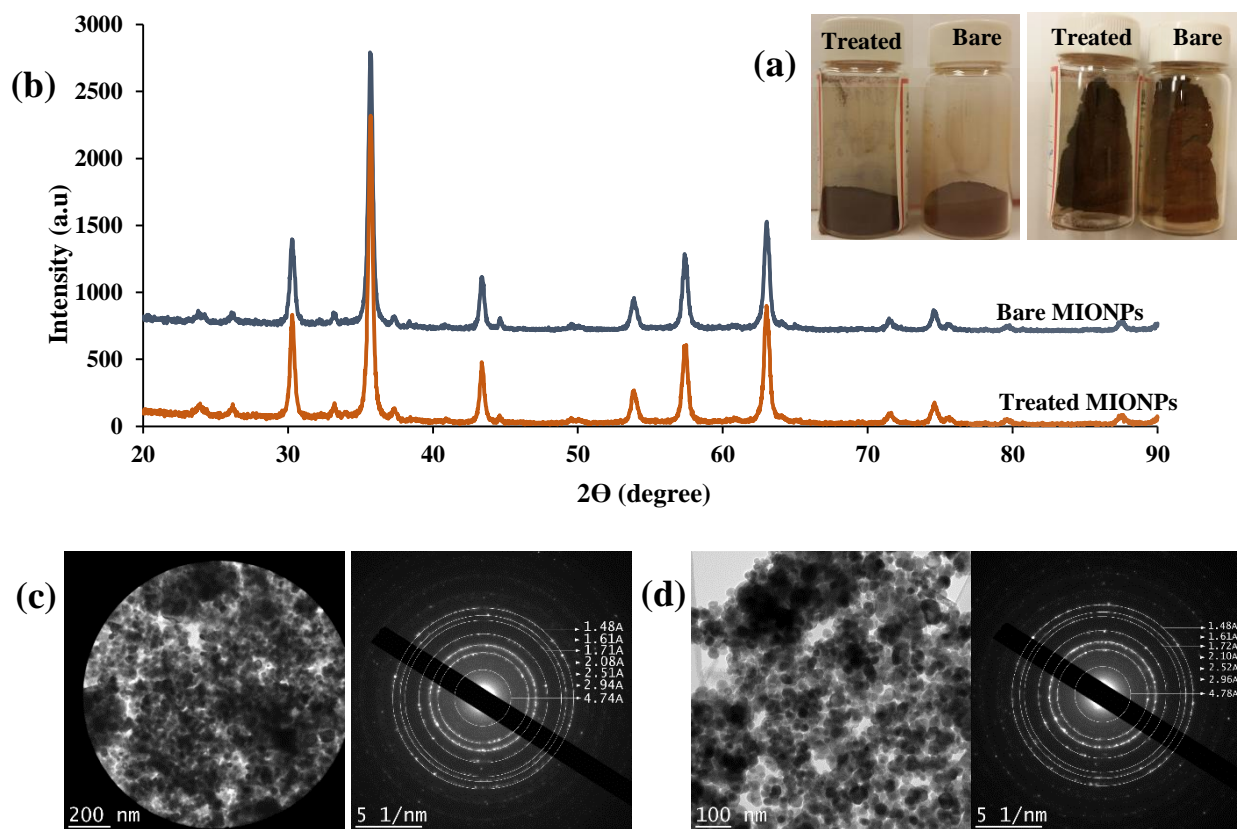
Figure 6-3: (a) MIONPs color before and after treatment, (b) X-ray powder diffraction patterns of bare and treated MIONPs, Selected area electron diffraction pattern (SAED) from bare(c) and treated (d) MIONPs.

For both bare and treated MIONPs, main peaks at 30.25°, 35.75°, 43.37°, 53.95°, 57.45°, and 63.09° were observed in the XRD patterns, indicating that the nanoparticles were single phase and there was no alteration in the crystalline structure after treatment. These peaks corresponded to the diffraction patterns of either γ-Fe_2O_3 or Fe_3O_4 [55-58]. Considering that both magnetite Fe_3O_4 and maghemite γ-Fe_2O_3 have a spinel-type crystal structure, it is difficult to distinguish these phases via XRD. SAED analysis confirmed these results: the shape and diameter of the SAED rings in both bare and treated MIONPS indicated that the particles were similar and there was no change in the crystalline structure. The SAED pattern rings can be associate to four compounds: Fe_3O_4-

magnetite, FeOOH-iron(III) hydroxide, γ-Fe_2O_3 -maghemite and α-Fe_2O_3 –hematite (least likely) [59]. The nanoparticles retained their magnetic properties after PICVD treatment.

As negative controls, we have performed two series of experiments with the same mass of MIONPs in the FB-PICVD reactor. For the first negative experiments (Negative #1), MIONPs were fluidized with only Ar at 2.4 L/min, with 0.4 L/min of secondary Ar from the micro-jet, in the presence of UVC irradiation (without injection of syngas) for 6h (i.e. identical to the genuine PICVD treatments). Our second negative control (Negative #2) corresponded to the fluidization of particles with 1.2 L/min of CO and 1.2 L/min of H_2 (syngas precursor), with 0.4 L/min of secondary Ar, this time without exposure to UVC light. These negative controls were used to independently investigate the effect of UVC lights or syngas on the MIONPs. Figure B-2 and Table B-1 compares bare particles to their negative control counterparts: no color change or coating were observed for either negative control.

6.3.1.2 Coating thickness and thermogravimetric analysis

We collected particles dispersed in n-dodecane for TEM analysis (Figure 6-4). Bare MIONPs mainly consisted of spherical particles in agglomerated form with a 20-50 nm size distribution; the outermost layer of the particles possessed sharp edges with no other observable phase (Figure 6-4(a)). In contrast, the treated particles show a 1.4-10 nm thickness encapsulating layer (Figure 6-4 (b)). However, fluidization does not appear to impact the agglomeration state of the particles significantly – the coated MIONPs tended to remain in an agglomerated state.
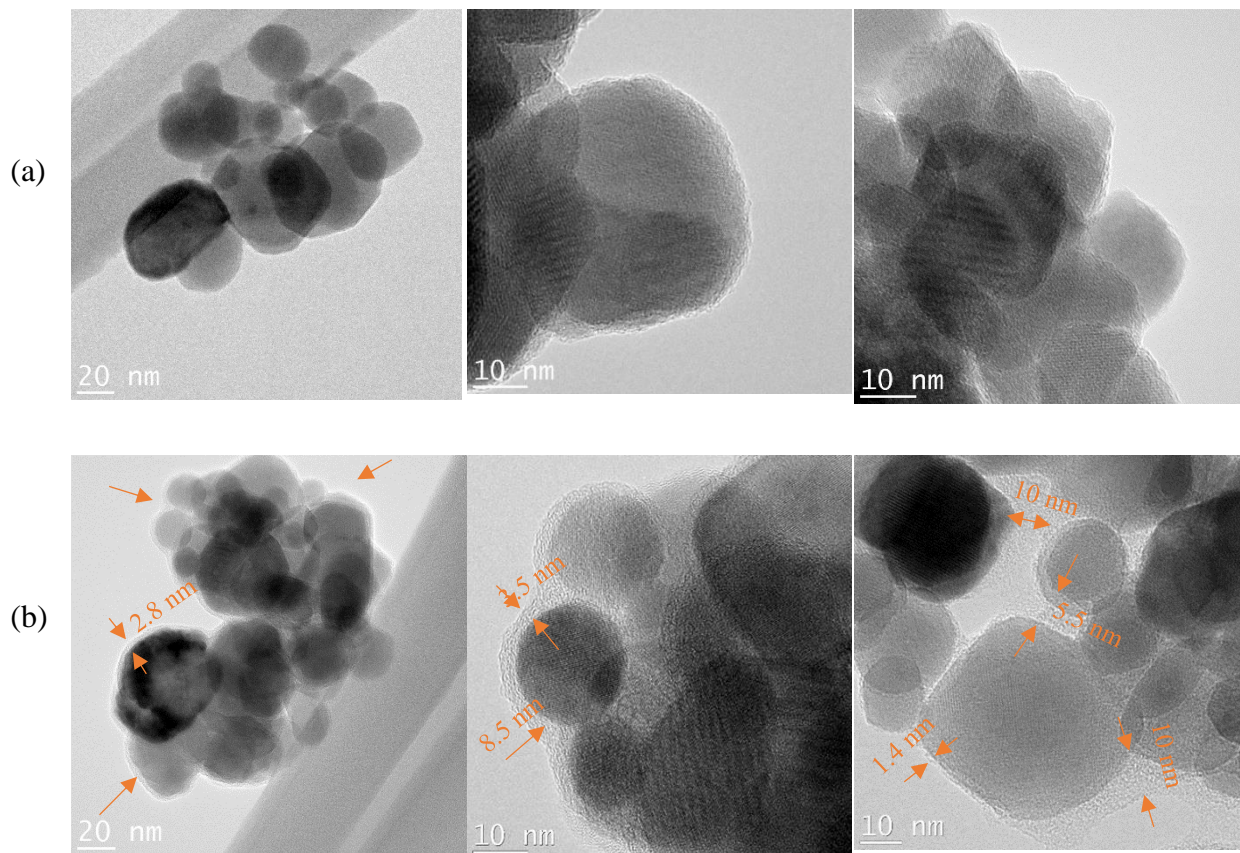
Figure 6-4: Representative TEM images of (a) bare MIONPs and (b) treated MIONPs. Red arrows point to coating.

To define the mass content of organic ligands on the surface of MIONPs, thermo gravimetric analysis (TGA) was performed on both bare and treated particles (Figure 6-5), showing four phases of weight loss:

(1) 0-100 °C: Both bare and treated MIONPs showed ~1% weight loss. This was attributed to adsorbed humidity;

(2) 100-200 °C: Both bare and treated MIONPs showed ~0.5% weight loss, which was attributed to chemisorbed humidity;
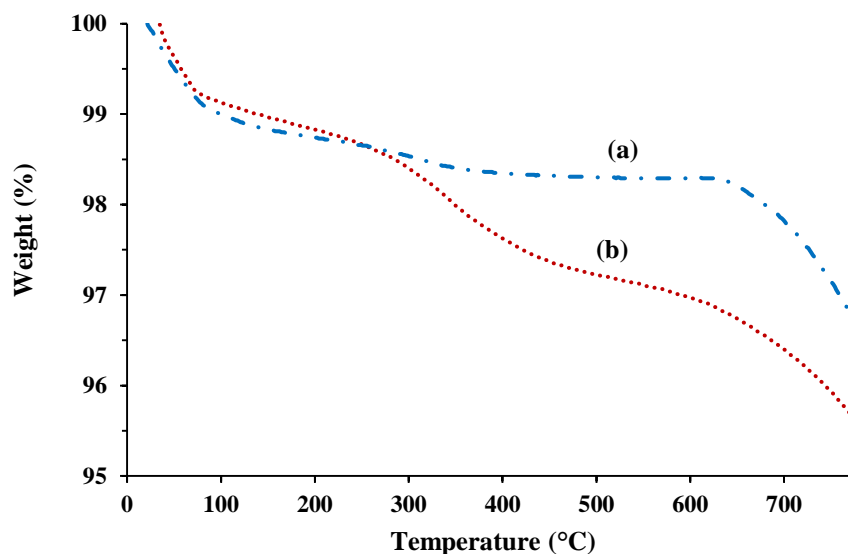
Figure 6-5: TGA (right) curves of (a) bare MIONPs, (b) treated MIONPs.

(3) 200-600 °C: Treated particles showed a weight loss of ~2%, bare particles only lost ~0.5%. This corresponded to the pyrolysis of organic content, with a carbon content 4-times higher in the treated MIONPs compared to the bare particles, which can therefore be attributed to PICVD treatment. Note that bare MIONPs do contain a small amount of carbon attributed to their production process (organic phase thermal decomposition of Fe(acetylacetonate) or iron pentacarbonyl Fe(CO)$_5$, followed by oxidation [5, 60]).

(4) 600-800 °C: Both bare and treated MIONPs showed ~1.7% and ~1.5% weight loss, respectively. This is attributed to the organic content from the MIONPs production process 5, 60 (i.e. not associated with PICVD treatment).

We used ImageJ software to determine the average thickness of the coating from the TEM images. We observed an average thickness of 4.5 nm for a 6h treatment; which corresponds to roughly 0.75 nm coating per hour of treatment. On the other hand, the total weight loss corresponding to the treatment process (TGA decomposition from 200 to 600 °C) corresponds to 0.18 mg for the 6h treatment. Thus, the mass deposition rate would be 0.03 mg/h.

6.3.2 Chemical characterization

With the encapsulation of MIONPs by PICVD confirmed, we wanted to know if the deposited film possessed the same chemistry as the thin films deposited on flat silicon wafers from our previous work [40]. XPS characterization provided further information on the deposited oligomeric film (Figure 6-6) for MIONPs treated with PICVD process. The survey spectrum for treated particles (Figure 6-6 (a')) showed an increase in carbon content, as deduced from the C1s peak compared to bare particles (Figure 5-6 (a)). This is in agreement with the TEM micrographs and TGA analysis demonstrating the formation of an organic film on MIONPs due to the syngas PICVD process. Deconvolution of the C1s, O1s and Fe2p3 high-resolution spectra allowed for a more detailed characterization of MIONPs (Table 6-1) [61].

Table 6-1: Deconvolutions of high-resolution spectral and their respective atomic % (source of BE obtained by comparison to ref [61]).

Peak Name	Centered Binding Energy [eV]	Possible Structure (1)	Atomic % of MIONPs	
			Bare	Treated
C1s A	283.4	Fe–*C	2.1	2.1
C1s B	285.0	*C–*C,* C–H,*C=*C, etc.	6.8	11.1
C1s C	286.4	*C–O–*C,*C–O–Fe, *C–O–H	2.7	3.5
C1s D	287.8	O=*C–C, O–C–O	1.2	1.4
C1s E	289.6	O=*C–O,O=*C–O–Fe	0.7	1.3
Fe2p3/2 A	709.0	C–Fe(O) –C, C–Fe(O)–O	2.2	1.4
Fe2p3/2 B	711.3		19.0	13.6
Fe2p3/2C	714.6	Fe $^{+3}$ in Iron oxide	6.1	5.4
Fe2p3/2SU	718.8		8.6	3.4
O1s A	529.6	Fe–*O	14.8	12.8
O1s B	530.7	H–*O–Fe, *O=C	28.9	36.5
O1s C	532.3	C–O–*Fe, *O=C–*O–Fe	6.9	7.5
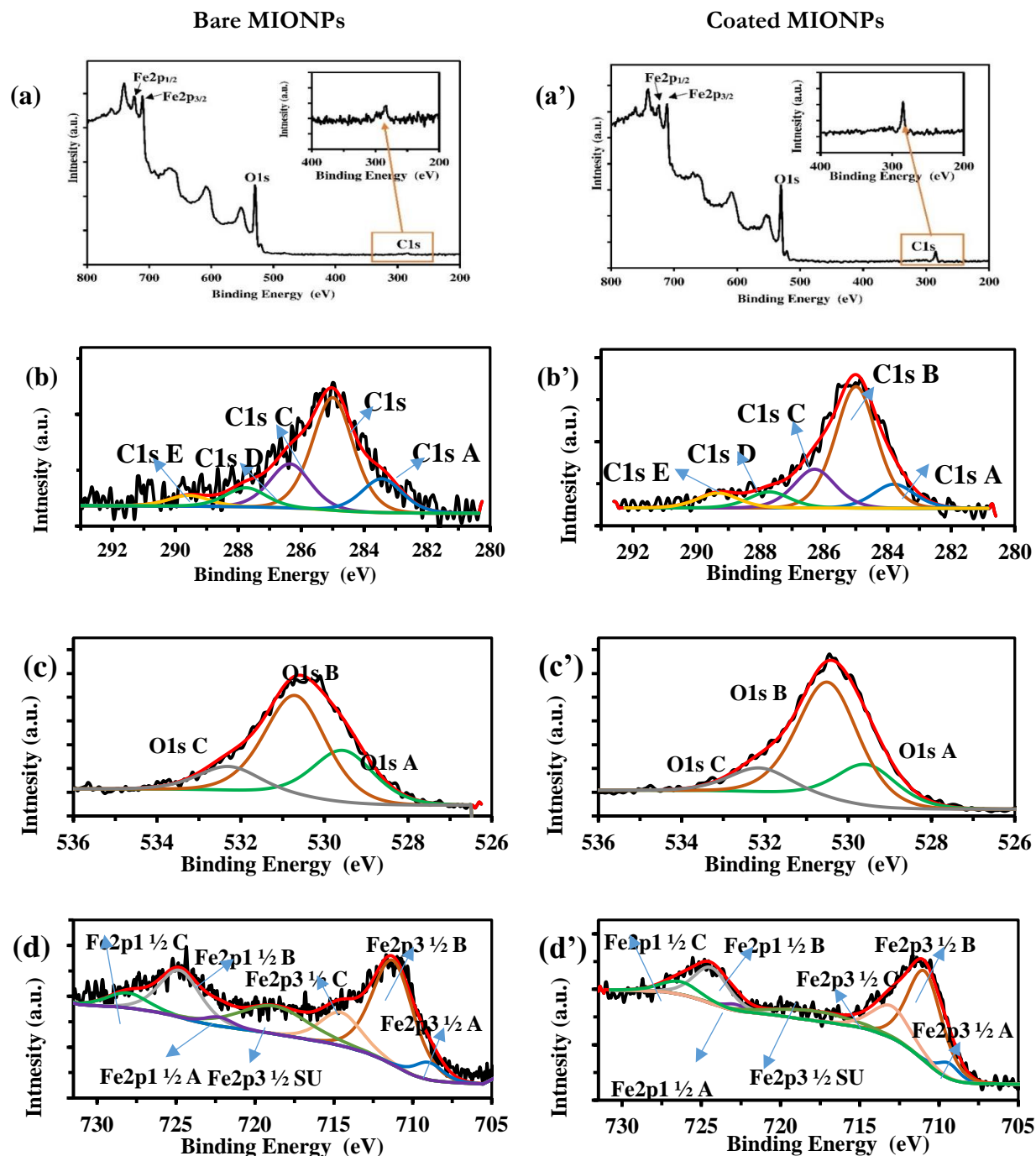
Figure 6-6: XPS Surveys spectra (a) bare MIONPs, (a') treated MIONPs; deconvolutions of high-resolution spectral of C1s for (b) bare MIONPs, (b') treated MIONPs; High resolution oxygen peak deconvolution for (c) bare MIONPs and (c') treated MIONPS; High resolution iron peak deconvolution for (d) bare MIONPs and (d') treated MIONPS.

Bare MIONPs consisted mainly of iron and oxygen, though high-resolution spectra also showed carbon - C1s (Figure 6-6 (b)). A sub peak at BE $\cong$ 283.4 eV indicated covalent bonding between Fe and C (~2%At., Table 6-1), with a correspond sub peak in the Fe2p3/2 spectrum (A, BE $\cong$ 709.0 eV, in Figure 6-6 (d)). Most of the carbon present in the C1s spectrum was BE $\cong$ 285.0 eV and 286.4 eV (Figure 6-6 (b), C1s B and C1s C), assigned to C–C and C–H bonds and C–O–C bonds, respectively. The remaining carbon content is in the form of O=*C–C, O–C–O or O=*C–O–Fe as deduced from sub peaks at BE $\cong$ 287.8 eV and 289.6 eV (Figure 6-6 (b), C1s D and C1s E). As stated previously, the presence of carbon in bare MIONPs is attributable to their production process [5, 60]. The iron spectrum sub peaks at BE $\cong$ 711.3 eV, 714.6v and 718.8 eV (B, C, SU, respectively) as well as their corresponding Fe2p1/2 sub peaks correspond to Fe^{+3} in iron oxide (Figure 6-6 (d)). These sub peaks are consistent with the oxygen bonds indicated as O1s A, O1s B and O1s C at BE $\cong$ 529.6 eV, 530.7 eV and 532.3 eV (Figure 6-6 (c)).

Treated MIONPs were characterized by a 6.2%At. and 5.9%At. increase in the O1s and C1s peaks, respectively, and a 12.1% decrease in Fe. This observation is consistent with the MIONPs being covered by an oligomeric film composed of C and O – also leading to a Fe peak attenuation. C1s high resolution peak deconvolution indicated that most of the carbon deposition is in the form of linear C–C, C=C and C–H bonds at BE $\cong$ 285.0 eV and 286.4 eV (Figure 6-6 (b'), C1s B and C1s C), with slight differences for other types of carbon content. O1s peak deconvolution indicated that the main increase of O sub peaks was in the form of H–*O–Fe and *O=C (Figure 6-6 (c'), O1s B). This agrees with our previously published reports where we demonstrated that syngas PICVD deposition on flat silicon formed a film of aliphatic hydrocarbons bonded to oxygen. However, we also previously showed that films deposited through syngas PICVD consist of C, O and Fe, owing to the presence of $Fe(CO)_5$ in the CO gas stream [40]. This Fe content in the coating is difficult to distinguish here from the Fe in the substrate (Fe_2O_3). To confirm its presence, we can use the Beer-Lambert law:

$$I_z = I_0 \, e^{-\frac{z}{\lambda cos\theta}}$$

Which tells us that the XPS signal intensity from a layer of atoms at distance z (I_z) is less than the signal intensity obtained from the layer at the original surface I_0 by a factor of $e^{-\frac{z}{\lambda cos\theta}}$ (λ is the photoelectron attenuation length and θ is the photoemission angle). If we consider a minimum

coating thickness z of 3 nm and assume an attenuation length of λ of 3.9 nm (calculated by the XPS software), and $\Theta = 0°$ I_z / I_0 should $\cong 0.46$. However, in our case, we have (based on Table 6-1):

$$\frac{I_z}{I_0} = \frac{At\% \text{ of "Fe" in treated MIONPs}}{At\% \text{ of "Fe" in bare MIONPs}} = \frac{23.8}{35.9} = 0.66$$

which is higher than expected, highly suggesting that there is also some iron deposition coming from the PICVD process itself, in agreement with previous reports. These XPS analyses have demonstrated that the oligomeric films deposited on nanoparticles is similar in composition to the film deposited on previously studied flat substrates [40]. Specifically, both oligomeric films consist of organometallic moieties and light hydrocarbons, with similar distribution as a function of BE (for example, 0.8 %At at 286.4eV for nanoparticles, compared to 1.2%At for flat substrates).

6.3.3 Processing considerations

Knowing that the coating chemistry is comparable to that of syngas PICVD coatings generated on flat substrates, it is possible to compare the present results with our previous studies in order to gain processing insight. In Farhanian et al. [40], we showed that film thickness varies both as a function of treatment time and gas residence time within the reactor. Residence time (τ) is defined as the reactor volume divided by the volumetric flow rate. For the range of residence time of interest, in the same system (for a 2 hour treatment), we can consider a linear relation between residence time and film thickness (d) based on previous data [40]: d = 165τ. Considering the dimensions of the FB-PICVD reactor (D = 2.5 cm, h = 1.8m) and the total gas flow rate (Q = 2.8L/min), the residence time is 0.3 min. By applying the linear relation, we therefore expect a film thickness of 49.5 nm after 2 h (i.e. a deposition rate of 0.41 nm/min). However, after 6 h, the film thickness on nanoparticles is only 4.5 nm (section 6.3.1.2), corresponding to a deposition rate is 0.01 nm/min. This difference can be attributed to the masking effect caused by the nanoparticles during fluidization: only particles near the quartz wall are exposed to UVC irradiation. Interestingly, based on the expected deposition rate (0.41 nm/min), 11 min would be required to reach the observed coating thickness of 4.5 nm: in other words, each particle was in proximity to the quartz wall during treatment only 3% of the time.

This indicates that the dimensions and fluidization parameters of the FB-PICVD reactor are not optimal. To improve the efficiency of the process (and therefore decrease treatment time), various methods should be considered: decreasing the reactor diameter, increasing precursor residence

time, improving particle circulation through other assisted fluidization techniques (beyond a single micro-jet) [43, 62]. The FB- PICVD reactor design could be further improved through the use of a jet-impactor system [47] to reduce the formation of agglomerates. These process improvements are the focus of on-going work.

6.3.4 Dispersion

Despite the processing limitations, the functional coating deposited had a significant effect on the dispersion of MIONPs in many solvents. Before any treatment, bare particles tended to settle in water (Figure 6-7(a)-right). In stark contrast, after treatment, the particles remained at the water surface (Figure 6-7(a)-left). When sonicated, treated particles tended to move back to the surface after several hours. To quantify the dispersion of coated MIONPs in various solvents, we used UV-Vis spectroscopy. Indeed, the peak absorption wavelength (λ_{max}) of the particles is highly dependent on their dispersion media [63, 64]. Any shift in λ_{max} or change in absorbance at a fixed λ can thus be used to detect changes in the surface composition of the nanoparticles [63, 64]. Figure 6-7(b) shows UV-Vis absorbance of bare and treated MIONPs dispersed and sonicated in water. For treated particles, we observed decreased absorbance, highly suggesting that the coating of our MIONPs is hydrophobic. That is, the coated MIONPs did not remain in suspension – they accumulated at the surface in order to minimize their interaction with water molecules.

To gain additional insight into the MIONP surface composition, we dispersed and sonicated both bare and treated MIONPs in different solvents such as ethanol (polar-protic with polarity index = 0.66), acetone (polar-aprotic with polarity index = 0.35), and n-dodecane (non-polar) (Figure 6-7(c), (d) and (e), respectively).

In ethanol, there was no change in absorbance, while there was a slight change in the case of acetone. In both polar solvents, no shifts in the peak wavelength (λ_{max}) occurred. On the other hand, dispersion of our coated particles in non-polar n-dodecane not only increased absorbance (indicating that coated particles dispersed more readily), but λ_{max} shifted from roughly 430 nm to 400 nm [63, 64]. Considering the fact that the optical properties of metal nanoparticles depend strongly on their shape, size, absorbed species on their surface as well as interactions between the particles [65], this shift in λ_{max} can be attributed to (1) shape and size changes due to coating or (2) different UV absorption properties of conjugated thin films [66, 67]. Upon addition of a thin layer at the surface of MIONPs, the outer layer of bare nanoparticle is masked. Thus, due to a chemistry

change of the outer layer, interaction between the MIONPs and the oligomeric film may change the refractive index, which in turn explains the shift in λ_{max}. Moreover, encapsulation of nanoparticles can change their surface plasmon resonance (SPR) and contribute to in-plane dipole resonance (longitudinal) or out-of-plane dipole resonance (transverse), which can also lead to a shift in λ_{max} (namely, in the case of encapsulated silver nanoparticles [65]).
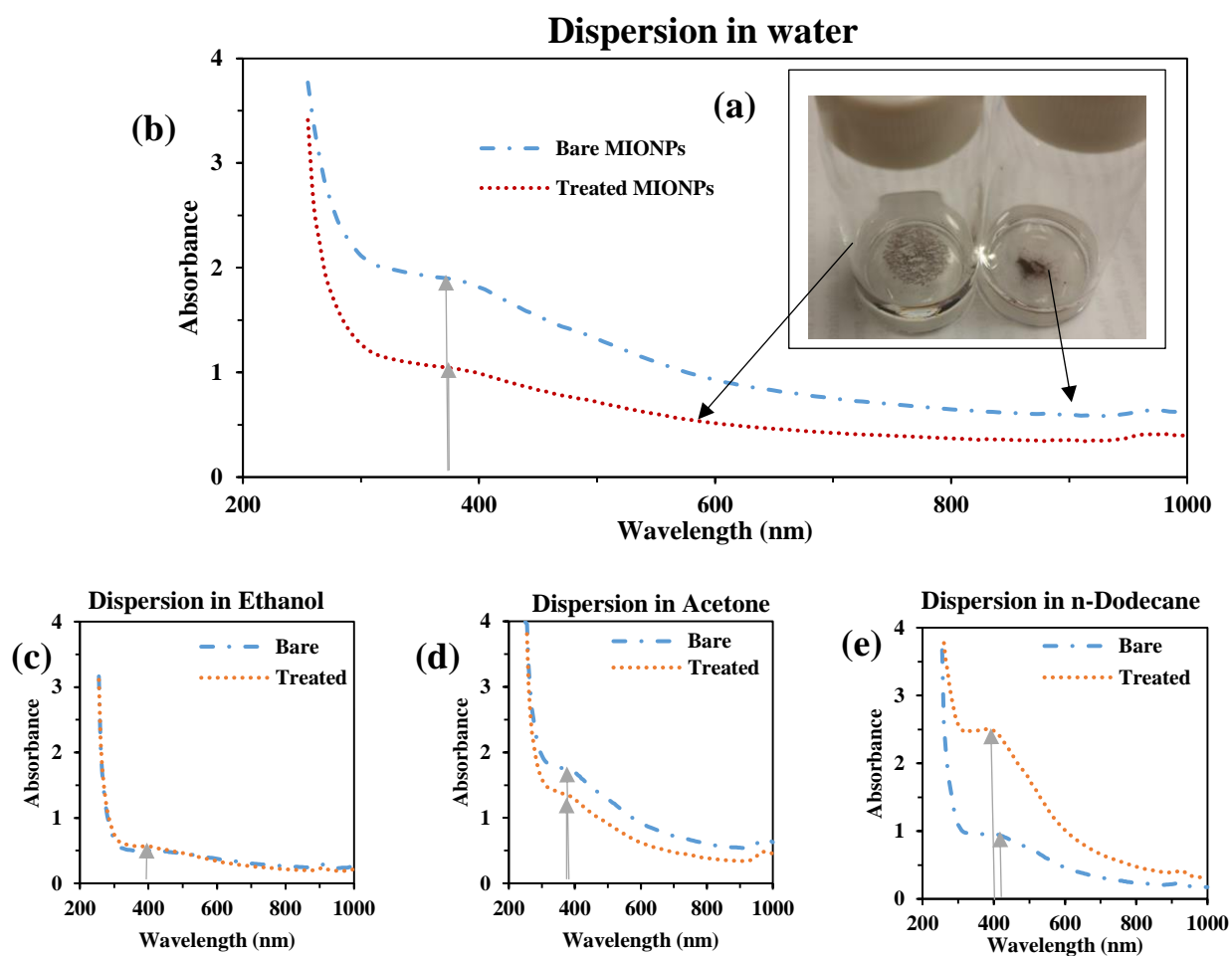
Figure 6-7: (a) Photograph of bare and treated MIONPs dispersed in DI water, UV-Vis absorbance spectrum of bare (blue line) and treated (red dot) MIONPs in (b) Water, (c) Ethanol, (d) Acetone, (e) n-Dodecane.

6.4 Conclusions

FB-PICVD, a scalable process for the encapsulation of nanoparticles, has been demonstrated, using syngas as a functionalization precursor. Magnetic iron oxide nanoparticles (MIONPs) were selected as encapsulation substrates, given their wide range of applications that could benefit from an organic coating. Despite some minor processing limitations, 5 g of nanoparticles were treated, far beyond the typical amount of particles treated (micrograms or milligrams). The syngas PICVD leads to a color change of the MIONPs, demonstrated to be directly attributable to the functional coating (no change in crystallinity). TEM micrographs confirmed the presence of a coating on the nanoparticles (and their agglomerates), on the order of 1.4 to 10 nm, corroborated by an increased amount of carbon observed by TGA. XPS analysis demonstrated that the chemistry of the coating is not dissimilar to films deposited on a flat substrate, showing a 6% increase in carbon content of particles after PICVD treatment, and a functional coating consisting mainly of linear aliphatic hydrocarbons (e.g. $-CH$, $-CH_2$, $-CH_3$) and polymerized chains (e.g. $C\equiv C$, $C=C$, $C-C$) (4.3 %), as well as ketones, esters and carbonates (0.2-0.8%). The functional film had an impact on dispersion properties, with UV-Vis spectroscopy showing evidence of a hydrophobic deposit that enhanced dispersion in non-polar solvents like n-dodecane. On-going work will focus on improving the treatment process' efficiency, while increasing the range and versatility of particles treated through tailored functionalization [39].

6.5 References

[1]   B. I. Kharisov, H. V. Rasika Dias, O. V. Kharissova, V. Manuel Jiménez-Pérez, B. Olvera Pérez, and B. Muñoz Flores, "Iron-containing nanomaterials: synthesis, properties, and environmental applications," *RSC Advances,* vol. 2, p. 9325, 2012.

[2]   A. Figuerola, R. Di Corato, L. Manna, and T. Pellegrino, "From iron oxide nanoparticles towards advanced iron-based inorganic materials designed for biomedical applications," *Pharmacological Research,* vol. 62, pp. 126-43, 2010.

[3]   L. Laconte, N. Nitin, and G. Bao, "Magnetic nanoparticle probes," *Materials Today,* vol. 8, pp. 32-38, 2005.

[4]   A. H. Lu, E. L. Salabas, and F. Schuth, "Magnetic nanoparticles: synthesis, protection, functionalization, and application," *Angewandte Chemie International Edition in English,* vol. 46, pp. 1222-44, 2007.

[5]   W. Wu, Q. He, and C. Jiang, "Magnetic Iron Oxide Nanoparticles: Synthesis and Surface Functionalization Strategies," *Nanoscale Research Letters,* vol. 3, pp. 397-415, 2008.

[6]   S. Ding, Y. Xing, M. Radosz, and Y. Shen, "Magnetic Nanoparticle Supported Catalyst for Atom Transfer Radical Polymerization," *Macromolecules,* vol. 39, pp. 6399-6405, 2006.

[7]   C. Jin, Y. Wang, H. Wei, H. Tang, X. Liu, T. Lu, *et al.*, "Magnetic iron oxide nanoparticles coated by hierarchically structured silica: a highly stable nanocomposite system and ideal catalyst support," *Journal of Materials Chemistry A,* vol. 2, pp. 11202-11208, 2014.

[8]   L. Zhou, B. He, and J. Huang, "One-step synthesis of robust amine- and vinyl-capped magnetic iron oxide nanoparticles for polymer grafting, dye adsorption, and catalysis," *ACS Applied Materials & Interfaces,* vol. 5, pp. 8678-85, 2013.

[9]   H. Yao, M. Fan, Y. Wang, G. Luo, and W. Fei, "Magnetic titanium dioxide based nanomaterials: synthesis, characteristics, and photocatalytic application in pollutant degradation," *Journal of Materials Chemistry A,* vol. 3, pp. 17511-17524, 2015.

[10]   W. Wu, J. Changzhong, and V. A. Roy, "Recent progress in magnetic iron oxide-semiconductor composite nanomaterials as promising photocatalysts," *Nanoscale,* vol. 7, pp. 38-58, 2015.

[11]   L. Upadhyaya, M. Semsarilar, S. Nehache, D. Cot, R. Fernández-Pacheco, G. Martinez, *et al.*, "Nanostructured Mixed Matrix Membranes from Supramolecular Assembly of Block Copolymer Nanoparticles and Iron Oxide Nanoparticles," *Macromolecules,* vol. 49, pp. 7908-7916, 2016.

[12]   S. Palchoudhury and J. R. Lead, "A facile and cost-effective method for separation of oil-water mixtures using polymer-coated iron oxide nanoparticles," *Environmental Science & Technology,* vol. 48, pp. 14558-63, 2014.

[13]   L. M. Rossi, N. J. S. Costa, F. P. Silva, and R. Wojcieszak, "Magnetic nanomaterials in catalysis: advanced catalysts for magnetic separation and beyond," *Green Chemistry,* vol. 16, p. 2906, 2014.

[14]   K. R. Reddy, W. Park, B. C. Sin, J. Noh, and Y. Lee, "Synthesis of electrically conductive and superparamagnetic monodispersed iron oxide-conjugated polymer composite nanoparticles by in situ chemical oxidative polymerization," *Journal of Colloid and Interface Science,* vol. 335, pp. 34-9, 2009.

[15]   J. Koo, H. Kim, K.-Y. Kim, Y. R. Jang, J.-S. Lee, S. W. Yoon*, et al.*, "Controlling the magnetic properties of polymer–iron oxide nanoparticle composite thin films via spatial particle orientation," *RSC Advances,* vol. 6, pp. 55842-55847, 2016.

[16]   C. Baker, S. Ismat Shah, and S. K. Hasanain, "Magnetic behavior of iron and iron-oxide nanoparticle/polymer composites," *Journal of Magnetism and Magnetic Materials,* vol. 280, pp. 412-418, 2004.

[17]   J. Sommertune, A. Sugunan, A. Ahniyaz, R. S. Bejhed, A. Sarwe, C. Johansson*, et al.*, "Polymer/Iron Oxide Nanoparticle Composites--A Straight Forward and Scalable Synthesis Approach," *International Journal of Molecular Sciences,* vol. 16, pp. 19752-68, 2015.

[18]   H. Liang, B. Liu, Q. Yuan, and J. Liu, "Magnetic Iron Oxide Nanoparticle Seeded Growth of Nucleotide Coordinated Polymers," *ACS Applied Materials & Interfaces,* vol. 8, pp. 15615-15622, 2016.

[19]   L. Upadhyaya, M. Semsarilar, R. Fernández-Pacheco, G. Martinez, R. Mallada, I. M. Coelhoso*, et al.*, "Nano-structured magneto-responsive membranes from block copolymers and iron oxide nanoparticles," *Polymer Chemistry,* vol. 8, pp. 605-614, 2017.

[20]   C. C. Berry, "Progress in functionalization of magnetic nanoparticles for applications in biomedicine," *Journal of Physics D: Applied Physics,* vol. 42, p. 224003, 2009.

[21]   Y. Cohen and S. Y. Shoushan, "Magnetic nanoparticles-based diagnostics and theranostics," *Current Opinion in Biotechnology,* vol. 24, pp. 672-81, 2013.

[22]   J. Gao, H. Gu, and B. Xu, "Multifunctional magnetic nanoparticles: design, synthesis, and biomedical applications," *Accounts of Chemical Research,* vol. 42, pp. 1097-107, 2009.

[23]   G. Huang, C. Zhang, S. Li, C. Khemtong, S. G. Yang, R. Tian*, et al.*, "A Novel Strategy for Surface Modification of Superparamagnetic Iron Oxide Nanoparticles for Lung Cancer Imaging," *Journal of Materials Chemistry,* vol. 19, pp. 6367-6372, 2009.

[24]   D. Horak, M. Babic, P. Jendelova, V. Herynek, M. Trchova, Z. Pientka*, et al.*, "D-mannose-modified iron oxide nanoparticles for stem cell labeling," *Bioconjugate Chemistry,* vol. 18, pp. 635-44, 2007.

[25]   Y. Yang, J. Zhang, S. Wang, X. Xu, Z. Zhang, P. Wang, *et al.*, "Facile and generalized encapsulations of inorganic nanocrystals with nitrogen-doped carbonaceous coating for multifunctionality," *Nanoscale,* vol. 7, pp. 3254-62, 2015.

[26]   W. Wu, C. Z. Jiang, and V. A. Roy, "Designed synthesis and surface engineering strategies of magnetic iron oxide nanoparticles for biomedical applications," *Nanoscale,* vol. 8, pp. 19421-19474, 2016.

[27]   Y. Si and Z. Guo, "Superhydrophobic nanocoatings: from materials to fabrications and to applications," *Nanoscale,* vol. 7, pp. 5922-46, 2015.

[28]   B. I. Kharisov, H. V. R. Dias, O. V. Kharissova, A. Vázquez, Y. Peña, and I. Gómez, "Solubilization, dispersion and stabilization of magnetic nanoparticles in water and non-aqueous solvents: recent trends," *RSC Advances.,* vol. 4, pp. 45354-45381, 2014.

[29]   F. Herranz, M. P. Morales, A. G. Roca, R. Vilar, and J. Ruiz-Cabello, "A new method for the aqueous functionalization of superparamagnetic Fe_2O_3 nanoparticles," *Contrast Media & Molecular Imaging,* vol. 3, pp. 215-222, 2008.

[30]   Y. Jiao and P. Akcora, "Assembly of Polymer-Grafted Magnetic Nanoparticles in Polymer Melts," *Macromolecules,* vol. 45, pp. 3463-3470, 2012.

[31]   M. I. Boulos, U. Kogelschatz, and C. Nessim, "Plasma surface treatment using dielectric barrier discharges," ed: Google Patents, 2008.

[32]   S. D. Lazarovich, A. Rosenberg, J. Shiloh, J. Statlender, and E. Wurzberg, "Plasma treatment of processing gases," ed: Google Patents, 2003.

[33]   D. Shi, P. He, J. Lian, L. Wang, and W. J. van Ooij, "Plasma deposition and characterization of acrylic acid thin film on ZnO nanoparticles," *Journal of materials research,* vol. 17, pp. 2555-2560, 2002.

[34]   D. Shi, S. X. Wang, W. J. van Ooij, L. M. Wang, J. Zhao, and Z. Yu, "Uniform deposition of ultrathin polymer films on the surfaces of Al_2O_3 nanoparticles by a plasma treatment," *Applied Physics Letters,* vol. 78, pp. 1243-1245, 2001.

[35]   B. M. Kumfer, K. Shinoda, B. Jeyadevan, and I. M. Kennedy, "Gas-Phase Flame Synthesis And Properties Of Magnetic Iron Oxide Nanoparticles With Reduced Oxidation State," *Journal of aerosol science,* vol. 41, pp. 257-265, 2010.

[36]   W. Kern and J. L. Vossen, *Thin Film Processes II*: Elsevier Science, 2012.

[37]   J. L. Vossen, *Thin Film Processes*: Elsevier Science, 2012.

[38]   C. A. Dorval Dion and J. R. Tavares, "Photo-initiated chemical vapor deposition as a scalable particle functionalization technology (a practical review)," *Powder Technology,* vol. 239, pp. 484-491, 2013.

[39]   C. A. Dorval Dion, W. Raphael, E. Tong, and J. R. Tavares, "Photo-initiated chemical vapor deposition of thin films using syngas for the functionalization of surfaces at room temperature and near-atmospheric pressure," *Surface and Coatings Technology,* vol. 244, pp. 98-108, 2014.

[40]   D. Farhanian, G. De Crescenzo, and J. R. Tavares, "Kinetics, Chemistry, and Morphology of Syngas Photoinitiated Chemical Vapor Deposition," *Langmuir,* 2017.

[41]   D. Farhanian, C. A. Dorval Dion, W. Raphael, G. De Crescenzo, and J. R. Tavares, "Combined extraction and functionalization of low-cost nanoparticles from municipal solid waste fly ash through PICVD," *Journal of Environmental Chemical Engineering,* vol. 2, pp. 2242-2251, 2014.

[42]   J. R. van Ommen, J. M. Valverde, and R. Pfeffer, "Fluidization of nanopowders: a review," *J Nanopart Res,* vol. 14, p. 737, 2012.

[43]   J. Shabanian, R. Jafari, and J. Chaouki, "Fluidization of ultrafine powders," *International review of chemical engineering,* vol. 4, pp. 16-50, 2012.

[44]   B. Esmaeili, J. Chaouki, and C. Dubois, "Encapsulation of nanoparticles by polymerization compounding in a gas/solid fluidized bed reactor," *AIChE Journal,* vol. 55, pp. 2271-2278, 2009.

[45]   D. Geldart, "Types of gas fluidization," *Powder Technology,* vol. 7, pp. 285-292, 1973.

[46]   D. Geldart, N. Harnby, and A. C. Wong, "Fluidization of cohesive powders," *Powder Technology,* vol. 37, pp. 25-37, 1984.

[47]   H. Nasri Lari, J. Chaouki, and J. R. Tavares, "De-agglomeration of nanoparticles in a jet impactor-assisted fluidized bed," *Powder Technology*, 2017.

[48]   B. Esmaeili, J. Chaouki, and C. Dubois, "Nanoparticle encapsulation by a polymer via in situ polymerization in supercritical conditions," *Polymer Engineering & Science,* vol. 52, pp. 637-642, 2012.

[49]   J. Feng, L. Zhu, C. Lu, S. Teng, M.-W. Young, and C. G. Gogos, "A new fluidized bed coating process via photo-initiated cationic polymerization," *Polymer Engineering & Science,* vol. 49, pp. 1107-1116, 2009.

[50]   J. A. Quevedo, A. Omosebi, and R. Pfeffer, "Fluidization enhancement of agglomerates of metal oxide nanopowders by microjets," *AIChE Journal,* 2009.

[51]   A. Bérard, G. S. Patience, G. Chouinard, and J. R. Tavares, "Photo Initiated Chemical Vapour Deposition To Increase Polymer Hydrophobicity," *Scientific Reports,* vol. 6, p. 31574, 2016.

[52] V. Labonté, A. Marion, N. Virgilio, and J. R. Tavares, "Gas-Phase Surface Engineering of Polystyrene Beads Used to Challenge Automated Particle Inspection Systems," *Industrial & Engineering Chemistry Research,* vol. 55, pp. 7362-7372, 2016.

[53] T. Javanbakht, W. Raphael, and J. R. Tavares, "Physicochemical properties of cellulose nanocrystals treated by photo-initiated chemical vapour deposition (PICVD)," *The Canadian Journal of Chemical Engineering,* vol. 94, pp. 1135-1139, 2016.

[54] T. Javanbakht, S. Laurent, D. Stanicki, W. Raphael, and J. R. Tavares, "Charge effect of superparamagnetic iron oxide nanoparticles on their surface functionalization by photo-initiated chemical vapour deposition," *Journal of Nanoparticle Research,* vol. 17, p. 462, 2015.

[55] F. H. Gustin, H. P. Shannonhouse, and R. W. Styron, "Fixation and utilization of ash residue from the incineration of municipal solid waste," ed: Google Patents, 1994.

[56] L. Wang, Y. Shi, H. Zhang, X. Bai, Y. Wang, and T. Ma, "Iron oxide nanostructures as highly efficient heterogeneous catalysts for mesoscopic photovoltaics," *Journal of Materials Chemistry A,* vol. 2, pp. 15279-15283, 2014.

[57] S. Grimm, M. Schultz, S. Barth, and R. Muller, "Flame pyrolysis – a preparation route for ultrafine pure γ-Fe2O3 powders and the control of their particle size and properties," *Journal of Materials Science,* vol. 32, pp. 1083-1092, 1997.

[58] T. Yamashita and P. Hayes, "Analysis of XPS spectra of Fe2+ and Fe3+ ions in oxide materials," *Applied Surface Science,* vol. 254, pp. 2441-2449, 2008.

[59] I. S. Lyubutin, S. S. Starchikov, T. V. Bukreeva, I. A. Lysenko, S. N. Sulyanov, N. Y. Korotkov, *et al.*, "In situ synthesis and characterization of magnetic nanoparticles in shells of biodegradable polyelectrolyte microcapsules," *Materials Science and Engineering C: Materials for Biological Applications,* vol. 45, pp. 225-33, 2014.

[60] W. Wu, Z. Wu, T. Yu, C. Jiang, and W. S. Kim, "Recent progress on magnetic iron oxide nanoparticles: synthesis, surface functional strategies and biomedical applications," *Science and Technology of Advanced Materials,* vol. 16, p. 023501, 2015.

[61] D. Briggs, "Handbook of X-ray Photoelectron Spectroscopy C. D. Wanger, W. M. Riggs, L. E. Davis, J. F. Moulder and G. E.Muilenberg Perkin-Elmer Corp., Physical Electronics Division, Eden Prairie, Minnesota, USA, pp. 195," *Surface and Interface Analysis,* vol. 3, 1981.

[62] B. Esmaeili, J. Chaouki, and C. Dubois, "An evaluation of the solid hold-up distribution in a fluidized bed of nanoparticles using radioactive densitometry and fibre optics," *The Canadian Journal of Chemical Engineering,* vol. 86, pp. 543-552, 2008.

[63]   P. Christian and M. Bromfield, "Preparation of small silver, gold and copper nanoparticles which disperse in both polar and non-polar solvents," *Journal of Materials Chemistry,* vol. 20, pp. 1135-1139, 2010.

[64]   J. A. Creighton and D. G. Eadon, "Ultraviolet-visible absorption spectra of the colloidal metallic elements," *Journal of the Chemical Society, Faraday Transactions,* vol. 87, pp. 3881-3891, 1991.

[65]   P. Sarkar, D. K. Bhui, H. Bar, G. P. Sahoo, S. Samanta, S. Pyne*, et al.*, "Aqueous-Phase Synthesis of Silver Nanodiscs and Nanorods in Methyl Cellulose Matrix: Photophysical Study and Simulation of UV–Vis Extinction Spectra Using DDA Method," *Nanoscale Research Letters,* vol. 5, p. 1611, 2010.

[66]   S. Thobhani, S. Attree, R. Boyd, N. Kumarswami, J. Noble, M. Szymanski*, et al.*, "Bioconjugation and characterisation of gold colloid-labelled proteins," *Journal of Immunological Methods,* vol. 356, pp. 60-69, 2010.

[67]   S. Zhou, L. Wu, M. Xiong, Q. He, and G. Chen, "Dispersion and UV-VIS Properties of Nanoparticles in Coatings," *Journal of Dispersion Science and Technology,* vol. 25, pp. 417-433, 2005.

CHAPTER 7: GENERAL DISCUSSION

Based on the extensive literature review, it was obvious that there is a demand for new gas-phase processes to avoid the complications of wet processing, while overcoming the problems associated with existing gas-phase techniques. Considering the environmentally friendly nature of PICVD processes as well as its affordability and scalability, it was selected as the surface modification tool of choice. In this thesis, we sought to study the parameters, kinetics and mechanism of syngas PICVD in depth and evaluate its application for coating of both micro and nano surfaces.

Thus, the first objective was to investigate the applicability of the process (article 1, Chapter 3), by targeting a specific case study involving low-cost nanoparticles derived from ash. From there, the second objective emphasized on understanding the mechanisms responsible for syngas PICVD (article 2, Chapter 4). Such information is essential to improve our knowledge of the process, and determine the key parameters and their relative importance in controlling the chemical and physical properties of deposited film. Once these aspects were established, for the third objective, we sought to leverage this knowledge and scale-up the process for more valuable and demanding materials. Thus, considering the extensive demand for the large-scale treatment of valuable NPs (such as magnetic iron oxide nanoparticles), we developed a homemade experimental set-up and encapsulated particles in large quantity (article 3, Chapter 5). This thesis provides crucial information for the establishment of operating guidelines of syngas PICVD.

7.1 Proof Of Concept: Applicability And Feasibility Of The Process To Treat NPs

Today, due to urbanization and industrialization, the amount of municipal solid waste ash (MSW) has been increasing rapidly and its disposal is becoming a worldwide concern. Just in Canada, from 2002 to 2008, the disposal of these materials increased from 769 kg to 777 kg per capita and their diversion (garbage which reused, recycled, composted or used for gas production via anaerobic digestion) increased from 212 kg to 254 kg per capita. To manage this amount of waste in 2008, 31,344 full-time workers were employed and total expenditures on solid waste management by local Canadian governments reached $2.6 billion, a $1.1 billion increase over 2002 [227]. Considering the spiraling costs of operating landfills, valorization of these materials has become an attractive alternative to disposal. Given that MSW fly ash contains a significant proportion of

NPs, the first specific objective of this research project focused on investigating the applicability of syngas PICVD to extract these low-grade (but low-cost) valuable materials that could then be used by other industries (namely for heat transfer). While serving as a proof-of-concept to treat NPs by PICVD, this work also begins to study the effect of some operational parameters such as reactor pressure and role of H_2O_2 as a photo-initiator on the chemistry, selectivity and extent of nanoparticles extraction.

The methodology developed consists of two stages: (1) treatment of MSWs ash powders and (2) secondary extraction of functional nanoparticles via polar solvent dispersion. This lab-scale treatment and extraction method was highly reproducible. However, the nanoparticles extracted had (as expected) multiple compositions, including derivatives of Cu, Al and Zn, to name a few. Indeed, varying reactor pressure and H_2O_2 input did not affect the selectivity of NP extraction. This limits the applicability of the extracted NPs to industries where filler composition is not crucial, but where colloidal stability is important, such as nanofluids [31–33] or composites [28– 30] to increase the overall thermal conductivity or to improve mechanical properties in the case of rubber matrices [13, 25]. On the other hand, for applications more sensitive to particle size distribution or chemical composition, the methodology could be improved by size segregation [2,32,34] before treatment or combining it with more selective chemical extraction methods (such as acid washing) [2,29,30,35]. Fly is now used as an additive in concrete mix and cements to increase their mechanical stability[205, 228] or is added in soil to adjust pH and soil salinity[229].

We also studied the impact of reactor pressure (atmospheric and slight vacuum) combined with H_2O_2 injection as a photo-initiator (which add –OH radicals to the process) in terms of produced functional groups. Experimental results showed no significant change in terms of produced chemical moieties. However, H_2O_2/near atmospheric pressure conditions showed higher amounts of phenol groups at 1240 cm^{-1}. Also, H_2O_2 can increase the rate of reaction due to the photolysis and formation of more hydroxyl groups under UVC (254 nm) irradiation. Thus, experiments with H_2O_2 leads to a more hydrophilic coating. Moreover, the C=O peak is slightly higher in H_2O_2 or slight vacuum pressure conditions indicating formation of more polar functionalities. Furthermore, presence of H_2O_2 and operation at atmospheric pressure leads to longer aliphatic chains with more ketone (C=O stretch); while near atmospheric pressure condition without H_2O_2 is more favoured the formation of aliphatic groups. Thus, slight vacuum pressure can lead to comparable results to H_2O_2 injection, at least in terms of hydroxyl group formation. These results gave encouraging

results regarding the operational parameters involving reactor pressure and –OH source photoinitiator.

Moreover, at the time of writing the first paper (Chapter 3), we had no idea about the presence of iron pentacarbonyl in the CO cylinder. Thus, we interpreted the FTIR results without considering this issue. In our first article, we mentioned that unsaturated $C\equiv C$ functionality is greater in near atmospheric pressure condition compared to treatment under slight vacuum pressure. Also, the presence of H_2O_2 and operation at atmospheric pressure was theorized to lead to increased production of unsaturated alkyne groups ($C\equiv C$ stretch). Alkyne stretching does not normally exhibit a strong dipole moment that would result in such an intense band. Revisiting the FTIR spectra (from Figure 4-7 and 4-8), we realized that the peaks at wavenumber 2100-2250 cm^{-1} could best be associated with iron-derived species, such as compounds with $Fe_n(CO)_m$ structures, or even trapped CO and CO_2 gas in the coating [230-232].In this article, we investigated the process in semi-plug flow reactor for nanoparticle extraction and we realized this reactor configuration is not the best, since reactive precursors cannot penetrate to all layers of the MSW ash powders; only a few % of these powders can be coated in this configuration, thus most of them remained untreated. This is compounded by the fact that we sieved ash powders and used only a select fraction (less than 75 µm) for treatment. Under a different reactor configuration (e.g. fluidized bed), there could be a possibility of treatment of larger quantities of ash powders without any need for sieving. However, still there is a need for an economic study of the large-scale treatment of ash in such a reactor to investigate the feasibility of the whole process. We even tested the process in TiO_2 micro-size particles to encapsulate these particles for photocatalytic application. Results, demonstrate the partial coating of particles which suggested the necessity of new reactor design for micro-nano size particle treatment.

7.2 Understanding The Kinetics And Processing Parameters

Previously, the mechanism of syngas PICVD using UVC lamps was completely unknown. One of the key outcomes of this research was the investigation of growth mechanism and kinetics based on the products deposited on a simplified, ideal substrate, silicon (without the geometric complexity of nanomaterials). This allowed us to identify (i) probable radicals formed and their subsequent impact on product formation; (ii) the role of each precursor on the rate of reaction to better control reaction parameters.

These analyses relied heavily on two complementary analytical techniques, namely high-resolution XPS and TOF-SIMS. A key finding from these analyses is that there is a covalent bond formed between silicon and the deposited film. Si-C bonding is observable because the coated film in some parts is thinner; thus, XPS analysis allows us to observe this bond. It is further confirmed by TOF-SIMS analysis. The coating structure is due to the fact that film mostly follows the Volmer-Weber deposition model, with mountain and valley structures. As can clearly be observed in the cross section of the deposited film (Figure 7-1), the deposition area consists of three regions: (1) silicon wafer, which consists of "Si", (2) outmost layer of silicon wafer, which consists of "SiO_2" and (3) coating layer, which consists of a polymeric layer with trenches. The trenches reach all the way to the substrate and there is a small distance between them; thus, during analysis, we detect a "Si" peak and can use its XPS/TOF-SIMS spectra to identify Si-C bonds. Such covalent bonding was previously observed in the case of plasma polymerization (PECVD); thus, this shows that PICVD can provide comparable properties to PECVD without many of the processing limitations [233].
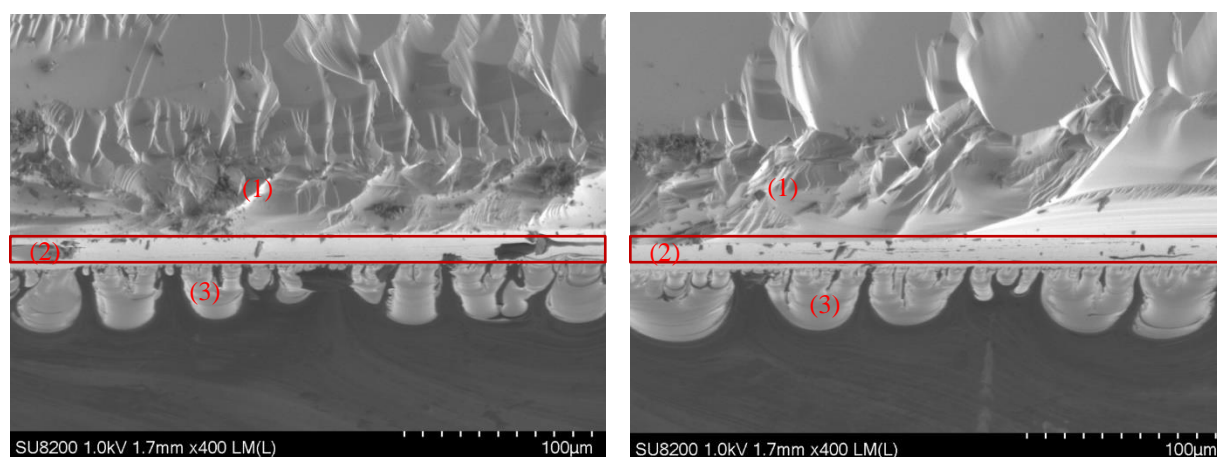
Figure 7-1: SEM micrographs representing the cross section of coated silicon wafer.

The XPS and TOF-SIMS analyses demonstrated the presence of an oligomeric structure consisting of light aliphatic hydrocarbons, aromatic structures (most likely phenol) as well as acid anhydride, ketones, carboxylic and hydroxyl moieties. More in-depth qualification of the functional groups would be possible through derivatization techniques, coupled TGA/FTIR or TGA/GC/MS analyses to help better understand the reaction mechanism. Derivatization can be done via colorimetry method using Toluidine [234, 235] as well as primary derivatization via carbonyl-containing volatile precursors and secondary XPS analysis to investigate the presence of – COOH groups in

the coated film [236]. These analyses also identified the key role played by iron in the system. Indeed, chemical composition studies demonstrated the presence of iron in the deposited film - this was unexpected since there was no known source for iron in the precursors or the substrate. However, individual analysis of each precursor stream (namely, via FTIR spectroscopy of products collected in a liquid nitrogen as well as analysis by GC-MS) determined that iron comes from the CO cylinder. A literature review showed that high-pressure CO stored over extended period reacts with the steel cylinder to produce $Fe(CO)_5$ at ppm levels. Given the impact of this compound on the process, and its potential impact on many syngas processes, we detailed this part of our study as a joint communication article entitled "Shedding Light on Iron Pentacarbonyl Photochemistry Through A CVD Case Study", published in Catalysis Communications.

Essentially, $Fe(CO)_5$ plays a photocatalytic role in the PICVD process that had never been identified in a coating process. We employ the term "photocatalytic" for this compound since it has a high absorption cross-section at 253.7 nm, it accelerates the reaction due to its unstable structure and reacts with CO and H_2 gas streams to produce $Fe_xO_yH_mC_n$ species in the deposited film. In the vocabulary of photopolymerization, $Fe(CO)_5$ can be best described as a photo-initiator, since it actively participates in the reaction. Indeed, its dissociation can provide additional CO radicals that combine with those produced by the irradiation of CO and further stimulate film growth. In spite of identification of $Fe(CO)_5$'s key role in syngas PICVD, we still did not have control over the production and concentration of this compound. $Fe(CO)_5$ is a highly toxic compound with a high vapor pressure at room temperature (2.8 kPa at 20 °C) - it is thus very volatile and if inhaled may cause lung irritation, toxic pneumonitis, or pulmonary edema and subsequently causes dead [237].

The National Institute for Occupational Safety and Health (NIOSH) has set a recommended eight-hour time-weighted average exposure limit to 0.1 ppm (0.23 mg/m^3), with a short-term limit at 0.2 ppm (0.45 mg/m^3) for occupational exposures [237]. Working with such a toxic compound requires operation at low temperatures at vacuum pressure to have controlled injection. The control of this compound's formation is one of the main open areas of research that warrant further investigation.

As previously discussed in the literature review several operational parameters like precursor concentration, residence time and treatment duration, etc. would affect the growth rate. We aimed to study (1) the effect of residence time (which is related to reactor design and has close relation

with gas streams flow rate), (2) treatment duration and (3) gas ratio (which deals with different concentrations of gas streams). Chemical investigation of the deposited film showed almost no difference in terms of chemical functionality despite variation of these parameters. However, both residence time and treatment duration have great impact on the thickness of film. Higher residence time, obtained by decreasing the flow rate of gas precursors while maintaining the concentration constant, resulted in higher film thickness. This is due to increased collisions and formation of radicals, due to longer UVC exposure. Unfortunately, due to the operational limitations of the system, it was not possible to try lower flow rates (i.e. higher residence times) or even operate the coating process in a batch reactor. Further investigation of extended residence time or batch processing could benefit the process and reduce the consumption of precursors. On the other hand, since $Fe(CO)_5$ has a critical role in syngas PICVD, its depletion over long residence times may negatively impact necessary radical formation for chain reaction.

We found that increasing treatment duration is comparable to decreasing the residence time since in both cases precursor contact time increases. However, the economical investigation is amenable to higher residence time since it results to less consumption of gas precursors.

Given the insights gained from the reaction mechanism, there is reason to believe that varying the precursor ratio may alter the composition. It is noteworthy that alteration of gas ratio or gas concentration (while the residence time and treatment duration were kept constant at 0.3 min and 2h respectively) did not impact the thickness of deposit nor its chemistry. This was contradictory to what we observed in our previous investigation [78, 238, 239]. Thus, we realized that wettability change, previously observed is not likely to be a result of a chemical change, but rather a morphology change on the surface.

We proposed schematic for the structure of the deposited film in Figure 5-5. This structure is illustrative and not completely representative of the atomic % of each elements – it serves mainly to highlight the key functionalities present in the coating. However, it is clear that the coating consists of organic and inorganic portions, which are bonded internally. This explains why we observe a hard, hybrid organic-inorganic coating which is difficult to scratch or remove, with very good chemical stability as mentioned and tested in section 5.4.3 and Table A-2. On the other hand, both XPS and TF-SIMS confirm formation of long chain hydrocarbons up to 12 carbons in the

chain. In the propagation steps of syngas Section 2-5; Figure 2-24 and 2-25 we extensively discussed the mechanism that leads to formation of long chain hydrocarbons.

One of the main engineering questions in this part of study was whether the reaction is mass transfer or reaction limited. This questions merits additional discussion beyond what is presented in Chapter 5, based on the impact of operational parameters, especially given that temperature is increasing during reaction due to UV irradiation (future work will aim to adapt the experimental setup to allow for experiments at constant temperature). Figure 7-2 shows the theoretical CVD deposition rate dependency on temperature. Thus, there are three regimes in CVD processes: (1) precursor depletion, (2) mass transport limitation and (3) surface reaction limitation.
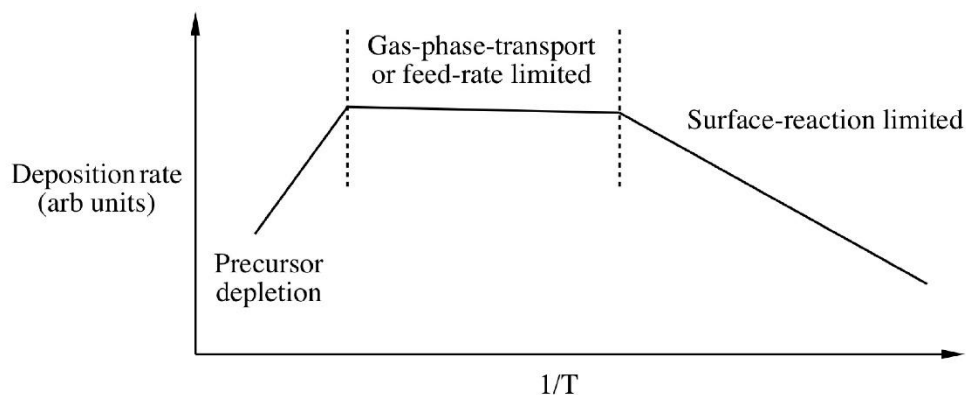
Figure 7-2: Dependence of CVD deposition rate on temperature [19].

Considering this Figure, we replotted our data from Figure 5-7 (b) and obtained the curve shown in Figure 7-3, which shows constant growth as a function of time (and therefore temperature in our system).
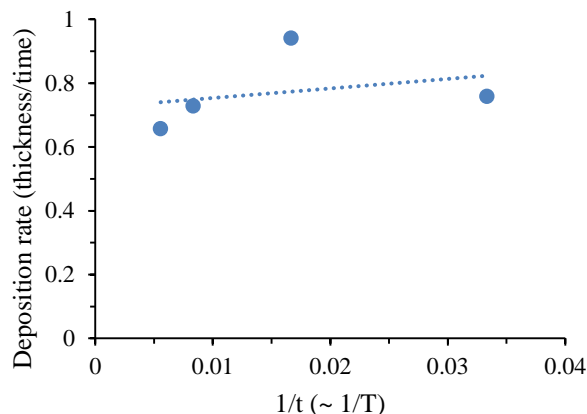
Figure 7-3: Deposition rate vs. treatment duration or temperature.

Considering the linear increase of temperature from 22 to 48 °C after 2h, we can consider that 1/t is almost same trend as 1/T. The growth rate did not change with 1/t (~ 1/T), and we currently observe a linear deposition rate, meaning that the growth trend is very similar to the "Gas phase transport or feed-rate limited (mass transfer limited) region" of Figure 7-2. Moreover, we have suggestive evidence that mass transport limitation may be in play since:

- One of the key reagents identified in our mechanism (iron pentacarbonyl) is present at ppm levels in our process;

- This same compound is a liquid at room temperature (boiling point of 103 °C). If the reaction is entirely surface-based, surface adsorption will be dominated by condensation and the dynamics of vapor-liquid equilibrium can be slow.

7.3 Scaling-Up Of PICVD Process

In the last part of this project, we investigated the applicability of the syngas PICVD process for functional encapsulation of magnetic iron oxide nanoparticles (MIONPs) in large quantity using jet-assisted fluidized bed reactor. Most of the encapsulation processes performed on these particles were in small quantity (milligram) via wet processing, specifically sol-gel techniques. This makes the particles expensive for biological applications such as dual imaging and drug delivery agents. On the other hand, these particles have wide range of applications in other industries like catalysts and separation (catalytic membrane), conductive composites, etc. Thus, it is crucial to find a cheap, industrially scalable process for functional coating of these particles. TEM results showed the

positive effect of syngas PICVD process towards non-polar hydrophobic encapsulation of these particles over the course of treatment while preserving their magnetic properties and also there was no change in their cristalinity, structure and chemical phase. Moreover, syngas PICVD is easily transferable to other nanoparticles and substrates like quantum dots, silver, gold or silica nanoparticles, which can be investigated in the near future. In this part of thesis, we successfully encapsulate nanoparticles, but most of the particles coated were in the agglomerated form (<150 nm). Therefore, still there is room for improvement of nanoparticles fluidization to obtain single encapsulated particles by homogeneous exposure of particles to UVC lamps, while decreasing the consumption of syngas. This will ensure the efficacy of the process while maintaining the desired thickness of deposited film as well as chemical properties over lower treatment time. Given the fact that the main product is not individually coated particles, the treated MIONPs are not ready for biological applications.

The greatest challenge faced during adapting results obtained from previous studies (article 2) for fluidized bed reactor was to maintain the low flow rate and thus the higher residence time for NPs encapsulation. In this reactor, since there was a need for fluidization of NPs in order to overcome the agglomeration, we had to increase the flow rate and thus decrease the effective residence time. To resolve this issue treatment duration was increasing significantly. A more appropriate way to design FB-PICVD reactor to resolve such interferences would be decreasing the diameter of FB-PICVD reactor or adding some other assisted fluidization techniques.

In order to calculate the density of deposit, we used TGA results (mass loss represents the mass of coating) and TEM images (shows the volume of coating). Calculated density is based on the assumption that each particle is encapsulated completely.

Using ImageJ analysis of TEM pictures, the average film thickness of coated particles is 4.5 nm for 6h treatment. Also TGA analysis showed 0.18 mg of deposit for 6h treatment. On the other hand the average particle size is $d_p = 25$ nm for MIONPs with density $\rho_p = 5.24$ g/cm^3. Using this information we can calculate the volume of each particle (V_p) (Equation 7-1)

$$V_p = \frac{4}{3}\pi\frac{d_p{}^2}{4}$$

Equation 7-1

Moreover, considering the mass loss via TGA analysis which represents the mass of coating, total mass of bare particles can be obtained by subtracting the mass inserted into the machine from this mass ($M_{bare\ particles}$ = Mass in TGA – Mass loss : 14 mg- 0.18 mg = 13.82 mg). Having this mass and also the density of MIONPs, the total volume of particles inserted into the TGA machine can be calculated via Equation 7-2.

$$V_t = \frac{M_{bare\ paricles}}{\rho_p}$$

Equation 7-2

Subsequently, the number of particles (N_p) inserted in TGA machine can be calculated by dividing the total volume (V_t) of MIONPs to the volume of one particle (V_p) (Equation 7-3).

$$N_p = \frac{V_t}{V_p}$$

Equation 7-3

Assuming each particle is coated uniformly, mass of coating (mass loss via TGA) can be divided to the number of particles (N_p) to obtain mass of coating surrounding each particle (M_c) (Equation 7-4)

$$M_c = \frac{Mass\ loss\ in\ TGA}{N_p}$$

Equation 7-4

On the other hand, knowing the film thickness of encapsulated particle (ImageJ shows 4.5 nm average film thickness) the volume of coating can be calculated via Equation 7-5 and Figure 7-4.

$$V_p = \frac{4}{3}\pi[\frac{d_2^2}{4} - \frac{d_p^2}{4}]$$

Equation 7-5
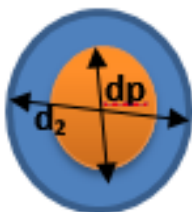
Figure 7-4: Representing figure of coated single particle (orange: particle, blue: coating layer)

Thus, density of coating can be calculated using the mass and voulme of coating obtained from Equation 7-4 and Equation 7-5 using Equation 7-6.

$$\rho_c = \frac{M_c}{V_c}$$

<div align="right">Equation 7-6</div>

However, this calculation leads to very low density (0.045 g/cm^3), which is not logical. This can be explained based on the fact that not all of the particles used for TGA analysis are coated. Part of the particles are not coated and have been separated through dispersion in the solvents. However, in these calculations we considered all particles are coated completely.

Moreover, despite the fact that we treated 5g of MIONPs in the jet-assisted fluidized bed reactor, this is not the limiting mass for treatment and the amount of bare particles could be increased. Even by changing the reactor configuration to a semi-continuous jet assisted FB and connecting the reactor to a powder feeder, the mass of treated particles could be increased.

Also, we applied derivatization techniques on both bare and coated MIONPs. These techniques did not show any increase of –COOH groups due to PICVD coating process. This once again confirmed the presence of hydrophobic coating resulting in better dispersion of MIONPs in n-dodecane

7.4 Discussion: Gaps and Suggestions

Through the 3 articles presented in this thesis, we investigated more than one type of substrate in order to fully demonstrate the flexibility of the process. In the first part, fly ash was used as a substrate to show the efficacy of the process for extraction of functional nanoparticles through hydrophilic coating, while the second and third parts, the focus was mainly on obtaining a greated understanding of the process using a substrate with a simpler geometry (silicon wafer) or a single composition (Fe_2O_3).

Aside from these surfaces, other substrates such as steel plates, and ZnO, SiO_2 and TiO_2 nanoparticles were coated and encapsulated with syngas PICVD – these works are not discussed in detail in this research manuscript. Moreover, coatings with secondary injection of CH_3COOH and NH_3 precursors were also produced - preliminary results confirmed the possibility of additional functionalization (-COOH and –NH_2) by using these compounds.

In the first part, since the target was the extraction of functional nanoparticles through polar solvents, we injected H_2O_2 to favor the production of a hydrophilic coating. Subsequent work focused on the study of syngas PICVD under more simplified conditions, thus the secondary injection of H_2O_2 was omitted. The injection of H_2O_2 in a fluidized bed reactor along with NPs fluidization would have increased the chance of agglomeration; thus, even if hydrophilic coatings are of interest, it would be more logical to use gas precursors with hydrophilic functionalities rather than water-based liquid H_2O_2.

Finally, the deposition rate via UVC stimulated syngas PICVD is quite low (0.7 nm/min) compared to traditional CVD approaches, such as plasma and VUV methods. However, as mentioned previously, for functionalization, thickness is not the first required parameter. Applying plasma for syngas CVD would certainly lead to higher deposition rate and, possibly different functionalities and mechanisms. However, the complexity of the reactor design in PECVD may still keep PICVD as a more interesting approach for scalable surface functionalization.

CHAPTER 8:   CONCLUSIONS AND RECOMMENDATIONS

8.1 Summary And Conclusions

Over the course of this research, syngas photo-initiated chemical vapor deposition was investigated for surface treatment of various type of materials. This work emphasizes the importance of critical thinking for production of new materials and processes that benefit society while maintaining focus on energy consumption, scalability, versatility, affordability and low environmental footprint. Based on our results, an important conclusion to draw from this work is that syngas PICVD is an inexpensive and environmental friendly process for the modification of various surfaces. In this chapter, we explain the main findings we made during this thesis according to our three major articles. This is followed by bullet points, outlining a few of the several commendable contributions of this research and generalize the discoveries to show how they affect and broaden scientific knowledge as a whole.

The first part of the thesis was devoted to the investigation of "proof of concept and feasibility of PICVD process through a waste management case study". Results clearly showed the applicability of this process for the extraction of valuable nanoparticles using municipal solid waste (MSW) as a cost-effective source of nanoparticles through their functional coating and secondary extraction via PICVD. Moreover, the impact of (1) reactor pressure, (2) injection of hydrogen peroxide as a photoinitiator and (3) hydrophilic functional reagent on the chemistry of deposit were investigated. Other important results related to this section can be summarized as the followings:

1. TEM/EDS results of syngas PICVD treatment on treated MSW ash confirm nano-size particles in the supernatant including Si, Al, Zn, and Fe as dominant nanoparticles in all samples, as well as Cu, Sn, Pb, and Mg.

2. DRIFTS analysis on treated MSW ash indicated presence of hydroxyl, primary alcoholic, aliphatic hydrocarbon, ketonic and unsaturated alkyne groups.

3. Longer aliphatic chains with more ketone (C=O stretch) and unsaturated alkyne groups (C≡C stretch) were produced in the presence of H_2O_2 and at atmospheric pressure; while near-atmospheric pressure conditions without H_2O_2 favoured the formation of aliphatic groups. Moreover, H_2O_2 as a photoinitiator can increase the rate of reaction due to the photolysis and

formation of more hydroxyl groups under UVC (254 nm) irradiation. Thus, experiments with H_2O_2 lead to a more hydrophilic coating. This is demonstrated by experimental results.

The second part of this research focused on "understanding the kinetic and chemistry of the deposited film via syngas PICVD on flat microchip silicon substrates to propose a mechanism for the process". In this section, a methodology was provided to control the thickness and chemistry of deposited thin film through operational parameters. Results clearly demonstrated the importance of treatment duration and residence time to tune the thickness of deposit. Moreover, the kinetic study revealed the critical role of $Fe(CO)_5$ as a photocatalyst in the film production and its leading role in the mechanism of film generation and radical formation, subsequently kinetics and amounts of chemical functional groups. In addition, contrary to what was expected, variations of the gas ratio did not affect the surface chemistry (the hypothesis put forth to explain previous wettability results); but this is more related to the morphology and topography of deposited film. Other key results obtained from this section include:

1. Investigation of syngas PICVD mechanism showed formation of an oligomeric structure consisting of light aliphatic hydrocarbons, aromatic structure (most likely phenol) as well as acid anhydride, ketones, and carboxylic and hydroxyl moieties.

2. Both XPS high resolution and TOF-SIMS results confirmed the formation of covalent bonding between deposited thin film and the silicon substrates.

3. Deposited film showed very good chemical stability after soaking in chloroform over the course of 1h. XPS elemental analysis showed no change in the composition of the film before and after soaking in this solvent.

In the last section of this thesis, we demonstrated the "scalability of syngas PICVD for large quantity functional encapsulation of valuable magnetic iron oxide nanoparticles (MIONP)". This benefits the industrialization of the process with economic and environmental sustainability. In this study, a micro-jet assisted fluidized bed reactor was designed to overcome the gap between small-scale and large-scale encapsulation process. Once again, the chemistry of the deposit was investigated via XPS high-resolution analysis and compared with results of flat microchip silicon

substrates. Results revealed identical film chemistry for both cases despite different reactor designs. Other mains results are:

1. TEM analysis of treated MIONPs showed formation of 1.4-10 nm polymeric encapsulating layer.

2. Comparison of TGA analysis of bare and coated particles indicated more weight loss at 200-600°C for treated versus bare particles. This corresponded to the pyrolysis of organic content, hence confirming the presence of organic coating.

3. UV-Vis absorbance analysis indicated that the functional film had an impact on the dispersion properties of treated particles compared to the bare ones. Furthermore, treated MIONPs had more tendency for dispersion in non-polar n-dodecane. This means that the functional deposited thin film has non-polar properties.

4. PICVD treated nanoparticles could find applications in separation, composites and the catalyst industry. Encapsulation of NPs also opens routes for biological application, by possibly imparting a barrier to the potential cytotoxic NPs surface and forming a reactive platform for subsequent chemical functionalization, while maintaining certain bulk properties (e.g. optical or magnetic).

8.2 Original Contributions

This thesis was designed to contribute to the scientific knowledge by:

(1) Demonstrating the efficacy of syngas PICVD using UVC lamps for synthesis and extraction of functional nanomaterials through a case study for waste management. This has never been done before.

(2) Explaining the process mechanism and kinetics, not to mention the role of iron in PICVD coating process and substantiating the formation of a covalent bond between the coating and substrate, which had never been studied before.

(3) Describing the impact of operational parameters on both thickness and chemistry of the deposits, important points for scalability of the process, wettability of the deposited film and subsequently the desired applications.

(4) Large scale functional encapsulation of valuable high-grade magnetic iron oxide nanoparticles (5 g) in a gas-phase reactor at normal conditions using syngas PICVD, which is quite novel. Previous studies could either encapsulate small quantities (i.e., mg or μg levels) or used wet

chemistry or harsh conditions in the gas phase. This is the first steps in developing a technology for economic, industrially viable nanoparticle functional encapsulation.

8.3 Recommendations

The following subjects are recommended for future work:

1. Integrate other chemical precursors to add additional functionality. For example, hydrophilic functionalities like $-NH_2$ and $-COOH$ are desirable for biological applications and can be achieved through ammonia (NH_3) and acetic acid (CH_3COOH) injection, respectively.

2. Study the impact of different concentrations of H_2O_2 as a photo-initiator on the growth rate and the amount of functional moieties produced during the PICVD process.

3. Due to the critical role of iron pentacarbonyl as a photocatalyst in the process, it is vital to have more control over the concentration of this compound. For example, it would be possible to first remove $Fe(CO)_5$ entirely from the CO gas line via zeolite adsorption or thermal decomposition, and then re-produce it through a thermal reaction of Fe and CO at desired levels to control its effect on the reaction.

4. Monitor the thin film deposition on flat substrates via real time ATR-FTIR to obtain a better understanding of the nucleation and growth mode on the surface.

5. Investigate the impact of light intensity on the growth rate and morphology of the deposited film.

6. Systematically investigate the combined effect of operational parameters like residence time, treatment duration, reactor pressure and light intensity on the growth and kinetics of the film deposition.

7. Combine syngas with other gas precursors (e.g. ethylene, acetylene, and butadiene) to produce "copolymers" with different molecular weight, structure or rheological properties.

8. Apply other fluidization assistance techniques such as high-pressure jets, impactors or magnetic fields to improve fluidization, break agglomerates (to treat single nanoparticles) and increase the efficacy of the encapsulation process.

9. Investigate the mechanical properties, tribology and durability of the deposited films.

10. Track the gas reactions by connecting the exhaust of the reactor to an online gas-FTIR or GC/MS, calibrating the concentration of the various products for further kinetic studies of the process.

11. Design a cleaning procedure for the quartz reactor due to the fact that reactor wall would become coated and limit light intensity available over the course of treatment.

12. Design a semi-continuous treatment procedure for the encapsulation of NPs, including a platform for reactor cleaning, unloading the treated particles and uploading a new batch of bare particles for treatment.

13. Perform syngas PICVD treatment on fly ash powders in a fluidized bed reactor for the large quantity extraction of valuable functional encapsulated nanoparticles from waste streams.

14. Study syngas PICVD using other UV sources with different wavelengths. Operation at other wavelengths could lead to alternate functionalization pathways or open the possibility of other chemical precursors with different absorption cross-sections.

15. Design an experimental set-up with constant temperature to decouple the effect of UV and temperature and better assess the limiting reaction step in UVC stimulated syngas PICVD (mass transport limited or reaction limited).

16. Apply UVC stimulated PICVD on industrial syngas to assess the impact of other chemicals present in this gas mixture (e.g. H_2S, CO_2).

LIST OF REFERENCES

[1] C. Lei, H. Zhou, Z. Feng, Y. Zhu, and R. Du, "Liquid phase deposition (LPD) of TiO 2 thin films as photoanodes for cathodic protection of stainless steel," *Journal of Alloys and Compounds,* vol. 513, pp. 552-558, 2012.

[2] T. P. Niesen and M. R. De Guire, "Review: deposition of ceramic thin films at low temperatures from aqueous solutions," *Solid State Ionics,* vol. 151, pp. 61-68, 11// 2002.

[3] H. von Känel, "Handbook of thin-film deposition processes and techniques. Edited by K. K. Schuegraf. Noyes Publications, Park Ridge, N.J., USA 1988. xvii, 413 pp., bound, US $ 72.–ISBN 0-8155-1153-1," *Advanced Materials,* vol. 1, pp. 208-208, 1989.

[4] S. S. Eskildsen, C. Mathiasen, and M. Foss, "Plasma CVD: process capabilities and economic aspects," *Surface & Coatings Technology,* vol. 116, pp. 18-24, Sep 1999.

[5] K. Choy, "Chemical vapour deposition of coatings," *Progress in materials science,* vol. 48, pp. 57-170, 2003.

[6] S. H. Baxamusa, L. Montero, J. M. Dubach, H. A. Clark, S. Borros, and K. K. Gleason, "Protection of Sensors for Biological Applications by Photoinitiated Chemical Vapor Deposition of Hydrogel Thin Films," *Biomacromolecules,* vol. 9, pp. 2857-2862, 2008/10/13 2008.

[7] W. S. O'Shaughnessy, S. Baxamusa, and K. K. Gleason, "Additively patterned polymer thin films by photo-initiated chemical vapor deposition (piCVD)," *Chemistry of Materials,* vol. 19, pp. 5836-5838, 2007.

[8] N. A. Bullett, D. P. Bullett, F.-E. Truica-Marasescu, S. Lerouge, F. Mwale, and M. R. Wertheimer, "Polymer surface micropatterning by plasma and VUV-photochemical modification for controlled cell culture," *Applied Surface Science,* vol. 235, pp. 395-405, 2004.

[9] C. Elsner, S. Naumov, J. Zajadacz, and M. R. Buchmeiser, "172 nm excimer VUV-triggered photodegradation and micropatterning of aminosilane films," *Thin Solid Films,* vol. 517, pp. 6772-6776, 2009.

[10] H. Huang, D. Y. C. Leung, G. Li, M. K. H. Leung, and X. Fu, "Photocatalytic destruction of air pollutants with vacuum ultraviolet (VUV) irradiation," *Catalysis Today,* vol. 175, pp. 310-315, 2011.

[11] E. Kasparek, J. R. Tavares, M. R. Wertheimer, and P.-L. Girard-Lauriault, "Sulfur-Rich Organic Films Deposited by Plasma- and Vacuum-Ultraviolet (VUV) Photo-Polymerization," *Plasma Processes and Polymers,* pp. n/a-n/a, 2016.

[12] U. Kogelschatz, H. Esrom, J. Y. Zhang, and I. W. Boyd, "High-intensity sources of incoherent UV and VUV excimer radiation for low-temperature materials processing," *Applied Surface Science,* vol. 168, pp. 29-36, Dec 15 2000.

[13] J.-C. Ruiz, P.-L. Girard-Lauriault, F. Truica-Marasescu, and M. R. Wertheimer, "Plasma- and vacuum-ultraviolet (VUV) photo-polymerisation of N- and O-rich thin films," *Radiation Physics and Chemistry,* vol. 79, pp. 310-314, 2010.

[14] T. Scherzer, "VUV-Induced Photopolymerization of Acrylates," *Macromolecular Chemistry and Physics,* vol. 213, pp. 324-334, 2012.

[15] F. Truica-Marasescu, S. Guimond, and M. R. Wertheimer, "VUV-induced nitriding of polymer surfaces: Comparison with plasma treatments in nitrogen," *Nuclear Instruments and Methods in Physics Research Section B: Beam Interactions with Materials and Atoms,* vol. 208, pp. 294-299, 2003.

[16] F. Truica-Marasescu, S. Pham, and M. R. Wertheimer, "VUV processing of polymers: Surface modification and deposition of organic thin films," *Nuclear Instruments and Methods in Physics Research Section B: Beam Interactions with Materials and Atoms,* vol. 265, pp. 31-36, 2007.

[17] F. Truica-Marasescu, J.-C. Ruiz, and M. R. Wertheimer, "Vacuum-ultraviolet (VUV) Photo-polymerization of Amine-rich Thin Films from Ammonia-Hydrocarbon Gas Mixtures," *Plasma Processes and Polymers,* vol. 9, pp. 473-484, 2012.

[18] G. Ozaydin-Ince, A. M. Coclite, and K. K. Gleason, "CVD of polymeric thin films: applications in sensors, biotechnology, microelectronics/organic electronics, microfluidics, MEMS, composites and membranes," *Rep Prog Phys,* vol. 75, p. 016501, Jan 2012.

[19] J. L. Vossen and W. Kern, "Thin Film Processes II," ed: Elsevier, 2012.

[20] C. A. Dorval Dion and J. R. Tavares, "Photo-initiated chemical vapor deposition as a scalable particle functionalization technology (a practical review)," *Powder Technology,* vol. 239, pp. 484-491, 2013.

[21] S. Jin, Y. Hu, Z. Gu, L. Liu, and H.-C. Wu, "Application of Quantum Dots in Biological Imaging," *Journal of Nanomaterials,* vol. 2011, pp. 1-13, 2011.

[22] T. Jamieson, R. Bakhshi, D. Petrova, R. Pocock, M. Imani, and A. M. Seifalian, "Biological applications of quantum dots," *Biomaterials,* vol. 28, pp. 4717-32, Nov 2007.

[23] P. Zrazhevskiy, M. Sena, and X. Gao, "Designing multifunctional quantum dots for bioimaging, detection, and drug delivery," *Chem Soc Rev,* vol. 39, pp. 4326-54, Nov 2010.

[24] H. M. Azzazy, M. M. Mansour, and S. C. Kazmierczak, "From diagnostics to therapy: prospects of quantum dots," *Clin Biochem,* vol. 40, pp. 917-27, Sep 2007.

[25] B. Chertok, B. A. Moffat, A. E. David, F. Yu, C. Bergemann, B. D. Ross*, et al.*, "Iron oxide nanoparticles as a drug delivery vehicle for MRI monitored magnetic targeting of brain tumors," *Biomaterials,* vol. 29, pp. 487-96, Feb 2008.

[26] "A novel polyacrylamide magnetic nanoparticle contrast agent for molecular imaging using MRI."

[27] E. D. Smolensky, H.-Y. E. Park, T. S. Berquó, and V. C. Pierre, "Surface functionalization of magnetic iron oxide nanoparticles for MRI applications – effect of anchoring group and ligand exchange protocol," *Contrast Media & Molecular Imaging,* vol. 6, pp. 189-199, 2011.

[28] R. Y. Hong, B. Feng, L. L. Chen, G. H. Liu, H. Z. Li, Y. Zheng*, et al.*, "Synthesis, characterization and MRI application of dextran-coated Fe3O4 magnetic nanoparticles," *Biochemical Engineering Journal,* vol. 42, pp. 290-300, 2008.

[29] W. Wu, Q. He, and C. Jiang, "Magnetic Iron Oxide Nanoparticles: Synthesis and Surface Functionalization Strategies," *Nanoscale Research Letters,* vol. 3, pp. 397-415, 10/02

07/08/received

09/11/accepted 2008.

[30] G. Huang, C. Zhang, S. Li, C. Khemtong, S. G. Yang, R. Tian*, et al.*, "A Novel Strategy for Surface Modification of Superparamagnetic Iron Oxide Nanoparticles for Lung Cancer Imaging," *J Mater Chem,* vol. 19, pp. 6367-6372, 2009.

[31] W. Wu, J. Changzhong, and V. A. Roy, "Recent progress in magnetic iron oxide-semiconductor composite nanomaterials as promising photocatalysts," *Nanoscale,* vol. 7, pp. 38-58, Jan 07 2015.

[32] S. Liang, Y. Wang, J. Yu, C. Zhang, J. Xia, and D. Yin, "Surface modified superparamagnetic iron oxide nanoparticles: as a new carrier for bio-magnetically targeted therapy," *J Mater Sci Mater Med,* vol. 18, pp. 2297-302, Dec 2007.

[33] D. Kennedy, Y. Xue, and M. Mihaylova, "Current and Future Applications of Surface Engineering. ," *The Engineers Journal (Technical),* vol. 59, pp. 287-292, June, 2005. 2005.

[34] J. S. Burnell-Gray, "Foresight in surface engineering," University of Northumbria at Newcastle. 2000.

[35] J. M. Goddard and J. H. Hotchkiss, "Polymer surface modification for the attachment of bioactive compounds," *Progress in Polymer Science,* vol. 32, pp. 698-725, 2007.

[36] O. Savadogo, "Thin-Film Semiconductors Deposited in Nanometric Scales by Electrochemical and Wet Chemical Methods for Photovoltaic Solar Cell Applications," in *Photoelectrochemical Materials and Energy Conversion Processes*, ed: Wiley-VCH Verlag GmbH & Co. KGaA, 2010, pp. 277-350.

[37] L. C. Klein, "III-4 - Sol-Gel Coatings A2 - VOSSEN, JOHN L," in *Thin Film Processes*, W. Kern, Ed., ed San Diego: Academic Press, 1991, pp. 501-522.

[38] P. M. Martin, *Handbook of Deposition Technologies for Films and Coatings: Science, Applications and Technology*: Elsevier Science, 2009.

[39] X.-P. Wang, Y. Yu, X.-F. Hu, and L. Gao, "Hydrophilicity of TiO2 films prepared by liquid phase deposition," *Thin Solid Films,* vol. 371, pp. 148-152, 8/1/ 2000.

[40] K. Tsukuma, T. Akiyama, and H. Imai, "Liquid phase deposition film of tin oxide," *Journal of Non-Crystalline Solids,* vol. 210, pp. 48-54, 2// 1997.

[41] Y. Gao, Y. Masuda, T. Yonezawa, and K. Koumoto, "Site-Selective Deposition and Micropatterning of SrTiO3 Thin Film on Self-Assembled Monolayers by the Liquid Phase Deposition Method," *Chemistry of Materials,* vol. 14, pp. 5006-5014, 2002/12/01 2002.

[42] L. Wang, S. Yu, and J. Cho, "Properties of Liquid-Phase Deposited Silica Films for Low-k Dielectric Applications," *Journal of the American Ceramic Society,* vol. 92, pp. 2388-2391, 2009.

[43] M. Ritala and J. Niinisto, "Chapter 4 Atomic Layer Deposition," in *Chemical Vapour Deposition: Precursors, Processes and Applications*, ed: The Royal Society of Chemistry, 2009, pp. 158-206.

[44] L. F. Hakim, S. M. George, and A. W. Weimer, "Conformal nanocoating of zirconia nanoparticles by atomic layer deposition in a fluidized bed reactor," *Nanotechnology,* vol. 16, pp. S375-81, Jul 2005.

[45] H. Kim, H.-B.-R. Lee, and W. J. Maeng, "Applications of atomic layer deposition to nanofabrication and emerging nanodevices," *Thin Solid Films,* vol. 517, pp. 2563-2580, 2009.

[46] D. M. King, X. Liang, C. S. Carney, L. F. Hakim, P. Li, and A. W. Weimer, "Atomic Layer Deposition of UV-Absorbing ZnO Films on SiO2 and TiO2 Nanoparticles Using a Fluidized Bed Reactor," *Advanced Functional Materials,* vol. 18, pp. 607-615, 2008.

[47] D. M. King, X. Liang, Y. Zhou, C. S. Carney, L. F. Hakim, P. Li*, et al.*, "Atomic layer deposition of TiO2 films on particles in a fluidized bed reactor," *Powder Technology,* vol. 183, pp. 356-363, 2008.

[48] D. M. King, J. A. Spencer, X. Liang, L. F. Hakim, and A. W. Weimer, "Atomic layer deposition on particles using a fluidized bed reactor with in situ mass spectrometry," *Surface and Coatings Technology,* vol. 201, pp. 9163-9171, 2007.

[49]   O. Nilsen, M. Lie, S. Foss, H. Fjellvåg, and A. Kjekshus, "Effect of magnetic field on the growth of α-Fe2O3 thin films by atomic layer deposition," *Applied Surface Science,* vol. 227, pp. 40-47, 2004.

[50]   J. R. Scheffe, A. Francés, D. M. King, X. Liang, B. A. Branch, A. S. Cavanagh*, et al.*, "Atomic layer deposition of iron(III) oxide on zirconia nanoparticles in a fluidized bed reactor using ferrocene and oxygen," *Thin Solid Films,* vol. 517, pp. 1874-1879, 2009.

[51]   D. M. King, X. Liang, P. Li, and A. W. Weimer, "Low-temperature atomic layer deposition of ZnO films on particles in a fluidized bed reactor," *Thin Solid Films,* vol. 516, pp. 8517-8523, 2008.

[52]   J. E. Mahan, *Physical Vapor Deposition of Thin Films*: Wiley, 2000.

[53]   P. K. S. K. S. S. Harsha, *Principles of Vapor Deposition of Thin Films*: Elsevier Science, 2005.

[54]   D. M. Mattox, *Handbook of Physical Vapor Deposition (PVD) Processing*: Elsevier Science, 2014.

[55]   J.-O. Carlsson and P. M. Martin, "Chapter 7 - Chemical Vapor Deposition," in *Handbook of Deposition Technologies for Films and Coatings (Third Edition)*, ed Boston: William Andrew Publishing, 2010, pp. 314-363.

[56]   D. Dobkin and M. K. Zuraw, *Principles of Chemical Vapor Deposition*: Springer Netherlands, 2003.

[57]   R. Sreenivasan and K. K. Gleason, "Overview of Strategies for the CVD of Organic Films and Functional Polymer Layers," *Chemical Vapor Deposition,* vol. 15, pp. 77-90, 2009.

[58]   J. Friedrich, "Mechanisms of Plasma Polymerization - Reviewed from a Chemical Point of View," *Plasma Processes and Polymers,* vol. 8, pp. 783-802, 2011.

[59]   J. Friedrich, G. Kuhn, R. Mix, A. Fritz, and A. Schonhals, "Polymer surface modification with monofunctional groups of variable types and densities," *Journal of Adhesion Science and Technology,* vol. 17, pp. 1591-1617, 2003.

[60]   J. Friedrich, G. Kühn, R. Mix, and W. Unger, "Formation of Plasma Polymer Layers with Functional Groups of Different Type and Density at Polymer Surfaces and their Interaction with Al Atoms," *Plasma Processes and Polymers,* vol. 1, pp. 28-50, 2004.

[61]   I. Retzko, J. F. Friedrich, A. Lippitz, and W. E. S. Unger, "Chemical analysis of plasma-polymerized films: The application of X-ray photoelectron spectroscopy (XPS), X-ray absorption spectroscopy (NEXAFS) and fourier transform infrared spectroscopy (FTIR)," *Journal of Electron Spectroscopy and Related Phenomena,* vol. 121, pp. 111-129, 12// 2001.

[62]   K. S. Siow, L. Britcher, S. Kumar, and H. J. Griesser, "Plasma Methods for the Generation of Chemically Reactive Surfaces for Biomolecule Immobilization and Cell Colonization - A Review," *Plasma Processes and Polymers,* vol. 3, pp. 392-418, 2006.

[63]   Ih-Houng Loh and Sc.D., "plasma surface modification in biomedical applications."

[64]   L. Chu, W. Knoll, and R. Förch, "Biologically Multifunctional Surfaces Using Plasma Polymerization Methods," *Plasma Processes and Polymers,* vol. 3, pp. 498-505, 2006.

[65]   P. K. Chu, J. Y. Chen, L. P. Wang, and N. Huang, "Plasma-surface modification of biomaterials," *Materials Science & Engineering R-Reports,* vol. 36, pp. 143-206, Mar 29 2002.

[66]   J. Pelletier and T. Lagarde, "Chemical vapor deposition in high-density low-pressure plasmas: reactor scale-up and performance," *Thin Solid Films,* vol. 241, pp. 240-246, 1994/04/01 1994.

[67] A. Gatto, E. Bassoli, and M. Fornari, "Plasma Transferred Arc deposition of powdered high performances alloys: process parameters optimisation as a function of alloy and geometrical configuration," *Surface and Coatings Technology,* vol. 187, pp. 265-271, 10/22/ 2004.

[68] M. Kaur and A. K. Srivastava, "Photopolymerization: A Review," *Journal of Macromolecular Science, Part C: Polymer Reviews,* vol. 42, pp. 481-512, 2002.

[69] K. Chan and K. K. Gleason, "Photoinitiated chemical vapor deposition of polymeric thin films using a volatile photoinitiator," *Langmuir,* vol. 21, pp. 11773-11779, Dec 6 2005.

[70] M. Tehfe, F. Louradour, J. Lalevée, and J.-P. Fouassier, "Photopolymerization Reactions: On the Way to a Green and Sustainable Chemistry," *Applied Sciences,* vol. 3, pp. 490-514, 2013.

[71] M. Sangermano, P. Meier, and S. Tzavalas, *Infrared Spectroscopy as a Tool to Monitor Radiation Curing*: INTECH Open Access Publisher, 2012.

[72] F. Truica-Marasescu, "Vacuum ultraviolet photo-physical chemistry of Hydrocarbon polymers," PhD, Physic Engineering, Ecole Polytechnqiue 2005.

[73] W. Kowalski, *Ultraviolet Germicidal Irradiation Handbook: UVGI for Air and Surface Disinfection*: Springer Berlin Heidelberg, 2010.

[74] Y. Taniyasu, M. Kasu, and T. Makimoto, "An aluminium nitride light-emitting diode with a wavelength of 210[thinsp]nanometres," *Nature,* vol. 441, pp. 325-328, 05/18/print 2006.

[75] B. Baroli, "Photopolymerization of biomaterials: issues and potentialities in drug delivery, tissue engineering, and cell encapsulation applications," *Journal of Chemical Technology & Biotechnology,* vol. 81, pp. 491-499, 2006.

[76] J. P. Wesley and P. Marquardt, *Light a Photon Flux, and Other Topics*: B. Wesley, 2006.

[77] *http://www.daviddarling.info/encyclopedia/I/irradiance.html*.

[78] C. A. Dorval Dion, W. Raphael, E. Tong, and J. R. Tavares, "Photo-initiated chemical vapor deposition of thin films using syngas for the functionalization of surfaces at room temperature and near-atmospheric pressure," *Surface and Coatings Technology,* vol. 244, pp. 98-108, 2014.

[79] M. Danno and M. Hanabusa, "Amorphous carbon films prepared by photo-CVD from acetylene," *Materials Letters,* vol. 4, pp. 261-264, 1986/07/01 1986.

[80] N. Chen, C. Wan, Y. Zhang, and Y. Zhang, "Effect of nano-CaCO3 on mechanical properties of PVC and PVC/Blendex blend," *Polymer Testing,* vol. 23, pp. 169-174, 2004.

[81] Q. S. Wu, D. M. Sun, H. J. Liu, and Y. P. Ding, "Abnormal polymorph conversion of calcium carbonate and nano-self-assembly of vaterite by a supported liquid membrane system," *Crystal Growth & Design,* vol. 4, pp. 717-720, Jul-Aug 2004.

[82] B. M. Cheng, H.-C. Lu, H.-K. Chen, M. Bahou, Y. P. Lee, A. M. Mebel*, et al.*, "ABSORPTION CROSS SECTIONS OF NH3, NH2D, NHD2, AND ND3 IN THE SPECTRAL RANGE 140Y220 nm AND IMPLICATIONS FOR PLANETARY ISOTOPIC FRACTIONATION," *The Astrophysical Journal,* vol. 647, pp. 1535-1542, 2006.

[83] A. St-Georges-Robillard, J.-C. Ruiz, A. Petit, H. T. Wang, F. Mwale, B. Elkin*, et al.*, "Adhesion of U-937 Monocytes on Different Amine-functionalised Polymer Surfaces," *Plasma Processes and Polymers,* vol. 9, pp. 243-252, 2012.

[84] F. Truica-Marasescu, P.-L. Girard-Lauriault, A. Lippitz, W. E. S. Unger, and M. R. Wertheimer, "Nitrogen-rich plasma polymers: Comparison of films deposited in atmospheric- and low-pressure plasmas," *Thin Solid Films,* vol. 516, pp. 7406-7417, 2008.

[85] F. Truica-Marasescu and M. R. Wertheimer, "Vacuum-Ultraviolet Photopolymerisation of Amine-Rich Thin Films," *Macromolecular Chemistry and Physics,* vol. 209, pp. 1043-1049, 2008.

[86] *http://www.perkinelmer.com/category/cells-windows*.

[87] P. Nuernberger, D. Wolpert, H. Weiss, and G. Gerber, "Femtosecond laser-assisted catalytic surface reactions of syngas and their optimization by tailored laser pulses," in *Ultrafast Phenomena XV: Proceedings of the 15th International Conference, Pacific Grove, USA, July 30 – August 4, 2006*, P. Corkum, D. M. Jonas, R. J. D. Miller, and A. M. Weiner, Eds., ed Berlin, Heidelberg: Springer Berlin Heidelberg, 2007, pp. 237-239.

[88] W. S. O'Shaughnessy, S. Baxamusa, and K. K. Gleason, "Additively patterned polymer thin films by photo-initiated chemical vapor deposition (piCVD)," *Chemistry of Materials,* vol. 19, pp. 5836-5838, Nov 27 2007.

[89] N. S. Allen, "Photoinitiators for UV and visible curing of coatings: Mechanisms and properties," *Journal of Photochemistry and Photobiology A: Chemistry,* vol. 100, p. 101, 10/25/Number 1-3/October 1996 1996.

[90] W. Chehade, V. Gorshelev, A. Serdyuchenko, J. P. Burrows, and M. Weber, "Revised temperature-dependent ozone absorption cross-section spectra (Bogumil et al.) measured with the SCIAMACHY satellite spectrometer," *Atmospheric Measurement Techniques,* vol. 6, pp. 3055-3065, 2013.

[91] O. J. Nielsen, M. S. Johnson, T. J. Wallington, L. K. Christensen, and J. Platz, "UV absorption spectra of HO2, CH3O2, C2H5O2, and CH3C(O)CH2O2 radicals and mechanism of the reactions of F and Cl atoms with CH3C(O)CH3," *International Journal of Chemical Kinetics,* vol. 34, pp. 283-291, 2002.

[92] J. Orphal, "A critical review of the absorption cross-sections of O3 and NO2 in the ultraviolet and visible," *Journal of Photochemistry and Photobiology A: Chemistry,* vol. 157, pp. 185-209, 2003.

[93] J. Orphal and K. Chance, "Ultraviolet and visible absorption cross-sections for HITRAN," *Journal of Quantitative Spectroscopy and Radiative Transfer,* vol. 82, pp. 491-504, 2003.

[94] X. D. Peng, A. W. Wang, B. A. Toseland, and P. J. A. Tijm, "Single-Step Syngas-to-Dimethyl Ether Processes for Optimal Productivity, Minimal Emissions, and Natural Gas-Derived Syngas," *Industrial & Engineering Chemistry Research,* vol. 38, pp. 4381-4388, 1999/11/01 1999.

[95] C. Decker, "Photoinitiated curing of multifunctional monomers," *Acta Polymerica,* vol. 45, pp. 333-347, 1994.

[96] E. Peris, M.-J. Bañuls, Á. Maquieira, and R. Puchades, "Photopolymerization as a promising method to sense biorecognition events," *TrAC Trends in Analytical Chemistry,* vol. 41, pp. 86-104, 2012.

[97] E. Andrzejewska, "Photopolymerization kinetics of multifunctional monomers," *Progress in Polymer Science,* vol. 26, pp. 605-665, May 2001.

[98] C. Liu, T. Li, J. Zhang, S. Chen, Z. Xu, A. Zhang, *et al.*, "Preparation and properties of phosphorous–nitrogen containing UV-curable polymeric coatings based on thiol–ene click reaction," *Progress in Organic Coatings,* vol. 90, pp. 21-27, 1// 2016.

[99] L. Montero, S. H. Baxamusa, S. Borros, and K. K. Gleason, "Thin Hydrogel Films With Nanoconfined Surface Reactivity by Photoinitiated Chemical Vapor Deposition," *Chemistry of Materials,* vol. 21, pp. 399-403, Jan 27 2009.

[100] V. Jančovičová, J. Kindernay, Z. Jakubíková, and I. Mrlláková, "Influence of photoinitiator and curing conditions on polymerization kinetics and gloss of UV-cured coatings," *Chemical Papers,* vol. 61, pp. 383-390, 2007.

[101] L. Lecamp, B. Youssef, C. Bunel, and P. Lebaudy, "Photoinitiated polymerization of a dimethacrylate oligomer: 1. Influence of photoinitiator concentration, temperature and light intensity," *Polymer,* vol. 38, pp. 6089-6096, 1997/01/01 1997.

[102] L. Liang, P. C. Rieke, G. E. Fryxell, J. Liu, M. H. Engehard, and K. L. Alford, "Temperature-sensitive surfaces prepared by UV photografting reaction of photosensitizer and N-isopropylacrylamide," *Journal of Physical Chemistry B,* vol. 104, pp. 11667-11673, Dec 14 2000.

[103] J. Deng, L. Wang, L. Liu, and W. Yang, "Developments and new applications of UV-induced surface graft polymerizations," *Progress in Polymer Science,* vol. 34, pp. 156-193, 1/1/2009 2009.

[104] C. DECKER, "Photoinitiated crosslinking polymerisation," *Progress in polymer science,* vol. 21.4, pp. 593-650, 1996.

[105] C. Decker, L. Keller, K. Zahouily, and S. Benfarhi, "Synthesis of nanocomposite polymers by UV-radiation curing," *Polymer,* vol. 46, pp. 6640-6648, 2005.

[106] C. Decker and I. Lorinczova, "UV-radiation curing of waterborne acrylate coatings," *Jct Research,* vol. 1, pp. 247-256, Oct 2004.

[107] C. Decker, F. Masson, and R. Schwalm, "How to speed up the UV curing of water-based acrylic coatings," *Jct Research,* vol. 1, pp. 127-136, Apr 2004.

[108] Y. Fuchs, O. Soppera, and K. Haupt, "Photopolymerization and photostructuring of molecularly imprinted polymers for sensor applications--a review," *Anal Chim Acta,* vol. 717, pp. 7-20, Mar 2 2012.

[109] T. Scherzer, R. Mehnert, and H. Lucht, "On-line monitoring of the acrylate conversion in UV photopolymerization by near-infrared reflection spectroscopy," *Macromolecular Symposia,* vol. 205, pp. 151-162, 2004.

[110] H. Okabe, *Photochemistry of small molecules*: Wiley, 1978.

[111] J. Y. Tsao and D. J. Ehrlich, "UV laser photopolymerization of volatile surface-adsorbed methyl methacrylate," *Applied Physics Letters,* vol. 42, pp. 997-999, 1983.

[112] M.-D. Hsieh and E. T. Zellers, "In situ UV-photopolymerization of gas-phase monomers for microanalytical system applications," *Sensors and Actuators B: Chemical,* vol. 82, pp. 287-296, 2/28/ 2002.

[113] A. Mason, S. C. Mukhopadhyay, K. P. Jayasundera, and N. Bhattacharyya, *Sensing Technology: Current Status and Future Trends II*: Springer International Publishing, 2013.

[114] T. Scherzer and U. Decker, "Kinetic investigations on the UV-induced photopolymerization of a diacrylate by time-resolved FTIR spectroscopy: the influence of photoinitiator concentration, light intensity and temperature," *Radiation Physics and Chemistry,* vol. 55, pp. 615-619, 8/1/ 1999.

[115] G. R. Tryson and A. R. Shultz, "A calorimetric study of acrylate photopolymerization," *Journal of Polymer Science: Polymer Physics Edition,* vol. 17, pp. 2059-2075, 1979.

[116] D. J. Broer, G. N. Mol, and G. Challa, "Temperature effects on the kinetics of photoinitiated polymerization of dimethacrylates," *Polymer,* vol. 32, pp. 690-695, 1991/01/01 1991.

[117] T. Scherzer, W. Knolle, S. Naumov, C. Elsner, and M. R. Buchmeiser, "Self-initiation of the UV photopolymerization of brominated acrylates," *Journal of Polymer Science Part A: Polymer Chemistry,* vol. 46, pp. 4905-4916, 2008.

[118] J. Pola, H. Beckers, and H. Bürger, "Single-pulse laser-induced decomposition of trifluoromethylsilane," *Chemical Physics Letters,* vol. 178, pp. 192-196, 1991.

[119] J. A. O'Neill, M. Horsburgh, J. Tann, K. J. Grant, G. L. Paul, and W. Sinclair, "Production of Fine Ceramic Powders from Chloromethylsilanes Using Pulsed Excimer Radiation," *Journal of the American Ceramic Society,* vol. 72, pp. 1130-1135, 1989.

[120] J. Pola, "Laser-generated silenes and their gas-phase polymerization," *Radiation Physics and Chemistry,* vol. 49, pp. 151-154, 1997.

[121] J. Pola, M. Urbanová, Z. Bastl, J. Šubrt, M. Sakuragi, A. Ouchi*, et al.*, "Laser-induced formation of polymers from unsaturated (organyl)trimethylsilanes in the gas phase," *Polymer,* vol. 42, pp. 1311-1318, 2001.

[122] J. Pola, M. Urbanová, V. Dřínek, J. Šubrt, and H. Beckers, "IR laser-induced decomposition of disiloxane for chemical vapour deposition of poly(hydridosiloxane) films," *Applied Organometallic Chemistry,* vol. 13, pp. 655-658, 1999.

[123] J. Pola, J. Vitek, Z. Bastl, M. Urbanova, J. Subrt, and R. Taylor, "IR laser-induced decomposition of prop-2-enylsilane and ethynylsilane for chemical vapour deposition of Si/C phases," *Journal of Materials Chemistry,* vol. 7, pp. 1415-1420, 1997.

[124] K. K. S. Lau and K. K. Gleason, "Initiated Chemical Vapor Deposition (iCVD) of Poly(alkyl acrylates): An Experimental Study," *Macromolecules,* vol. 39, pp. 3688-3694, 2006.

[125] A. Atkinson, "Mercury photosensitized reaction of tetrafluoroethylene," *Nature,* vol. 163, pp. 291-291, 1949.

[126] J. Heicklen, V. Knight, and S. A. Greene, "Mercury-Photosensitized Oxidation of Tetrafluoroethylene," *The Journal of Chemical Physics,* vol. 42, pp. 221-227, 1965.

[127] D. Saunders and J. Heicklen, "The Reaction of Oxygen Atoms with Tetrafluoroethylene1," *Journal of the American Chemical Society,* vol. 87, pp. 2088-2092, 1965/05/01 1965.

[128] F. Gozzo and G. Camaggi, "Oxidation reactions of tetrafluoroethylene and products therefrom—II," *Tetrahedron,* vol. 22, pp. 2181-2190, 1966.

[129] J. Heicklen and V. Knight, "Reaction of Oxygen Atoms with Tetrafluoroethylene in the Presence of Molecular Oxygen1," *The Journal of Physical Chemistry,* vol. 70, pp. 3893-3901, 1966.

[130] A. Asatekin, M. C. Barr, S. H. Baxamusa, K. K. S. Lau, W. Tenhaeff, J. Xu*, et al.*, "Designing polymer surfaces via vapor deposition," *Materials Today,* vol. 13, pp. 26-33, 5// 2010.

[131] W. E. Tenhaeff and K. K. Gleason, "Initiated and Oxidative Chemical Vapor Deposition of Polymeric Thin Films: iCVD and oCVD," *Advanced Functional Materials,* vol. 18, pp. 979-992, 2008.

[132] J. Feng, L. Zhu, C. Lu, S. Teng, M.-W. Young, and C. G. Gogos, "A new fluidized bed coating process via photo-initiated cationic polymerization," *Polymer Engineering & Science,* vol. 49, pp. 1107-1116, 2009.

[133] A. M. Boies, J. T. Roberts, S. L. Girshick, B. Zhang, T. Nakamura, and A. Mochizuki, "SiO2 coating of silver nanoparticles by photoinduced chemical vapor deposition," *Nanotechnology,* vol. 20, p. 295604, Jul 22 2009.

[134] B. Zhang, Y.-C. Liao, S. L. Girshick, and J. T. Roberts, "Growth of coatings on nanoparticles by photoinduced chemical vapor deposition," *Journal of Nanoparticle Research,* vol. 10, pp. 173-178, 2007.

[135] M.-A. Neouze and U. Schubert, "Surface Modification and Functionalization of Metal and Metal Oxide Nanoparticles by Organic Ligands," *Monatshefte für Chemie - Chemical Monthly,* vol. 139, pp. 183-195, 2008.

[136] D. Bäuerle, "Transformation and Functionalization of Organic Materials," pp. 605-621, 2011.

[137] A. G. Osorio, I. C. L. Silveira, V. L. Bueno, and C. P. Bergmann, "H2SO4/HNO3/HCl—Functionalization and its effect on dispersion of carbon nanotubes in aqueous media," *Applied Surface Science,* vol. 255, pp. 2485-2489, 2008.

[138] J. M. Delgado, A. Berná, J. M. Orts, A. Rodes, and J. M. Feliu, "In Situ Infrared Study of the Adsorption and Surface Acid− Base Properties of the Anions of Dicarboxylic Acids at Gold Single Crystal and Thin-Film Electrodes," *The Journal of Physical Chemistry C,* vol. 111, pp. 9943-9952, 2007.

[139] T. R. Sarkar and J. Irudayaraj, "Carboxyl-coated magnetic nanoparticles for mRNA isolation and extraction of supercoiled plasmid DNA," *Anal Biochem,* vol. 379, pp. 130-2, Aug 1 2008.

[140] H. A. Gaballa, L. M. Geever, J. A. Killion, and C. L. Higginbotham, "Synthesis and characterization of physically crosslinked N-vinylcaprolactam, acrylic acid, methacrylic acid, and N,N-dimethylacrylamide hydrogels," *Journal of Polymer Science Part B: Polymer Physics,* vol. 51, pp. 1555-1564, 2013.

[141] J. Y. Lai, "Effect of chemical composition on corneal tissue response to photopolymerized materials comprising 2-hydroxyethyl methacrylate and acrylic acid," *Mater Sci Eng C Mater Biol Appl,* vol. 34, pp. 334-40, Jan 1 2014.

[142] R. Fausto and E. M. S. Macoas, "Photochemical reactivity of matrix-isolated monomeric carboxylic acids," *Journal of Molecular Structure,* vol. 563, pp. 27-40, May 28 2001.

[143] R. A. Sperling and W. J. Parak, "Surface modification, functionalization and bioconjugation of colloidal inorganic nanoparticles," *Philos Trans A Math Phys Eng Sci,* vol. 368, pp. 1333-83, Mar 28 2010.

[144] D. Kisailus, M. Najarian, J. C. Weaver, and D. E. Morse, "Functionalized Gold Nanoparticles Mimic Catalytic Activity of a Polysiloxane-Synthesizing Enzyme," *Advanced Materials,* vol. 17, pp. 1234-1239, 2005.

[145] S. Roux, B. Garcia, J.-L. Bridot, M. Salomé, C. Marquette, L. Lemelle*, et al.*, "Synthesis, Characterization of Dihydrolipoic Acid Capped Gold Nanoparticles, and Functionalization by the Electroluminescent Luminol," *Langmuir,* vol. 21, pp. 2526-2536, 2005/03/01 2005.

[146] M. Zayats, E. Katz, R. Baron, and I. Willner, "Reconstitution of Apo-Glucose Dehydrogenase on Pyrroloquinoline Quinone-Functionalized Au Nanoparticles Yields an Electrically Contacted Biocatalyst," *Journal of the American Chemical Society,* vol. 127, pp. 12400-12406, 2005/09/01 2005.

[147] A. Wolcott, D. Gerion, M. Visconte, J. Sun, A. Schwartzberg, S. Chen*, et al.*, "Silica-Coated CdTe Quantum Dots Functionalized with Thiols for Bioconjugation to IgG Proteins," *The Journal of Physical Chemistry B,* vol. 110, pp. 5779-5789, 2006/03/01 2006.

[148] J. Chomoucka, J. Drbohlavova, V. Adam, R. Kizek, and J. Hubalek, "Synthesis of glutathione-coated quantum dots," in *2009 32nd International Spring Seminar on Electronics Technology*, 2009, pp. 1-5.

[149] S. Mazumder, R. Dey, M. K. Mitra, S. Mukherjee, and G. C. Das, "Review: Biofunctionalized Quantum Dots in Biology and Medicine," *Journal of Nanomaterials,* vol. 2009, 2009.

[150] E. Ramirez, S. Jansat, K. Philippot, P. Lecante, M. Gomez, A. M. Masdeu-Bultó, *et al.*, "Influence of organic ligands on the stabilization of palladium nanoparticles," *Journal of Organometallic Chemistry,* vol. 689, pp. 4601-4610, 2004/11/29/ 2004.

[151] B. Cortese, G. Gigli, G. M. Ingo, G. Padeletti, and D. Caschera, "A brief review of surface-functionalized cotton fabrics," *Surface Innovations,* vol. 1, pp. 140-156, 2013.

[152] J. Drelich, E. Chibowski, D. D. Meng, and K. Terpilowski, "Hydrophilic and superhydrophilic surfaces and materials," *Soft Matter,* vol. 7, p. 9804, 2011.

[153] S. Yamasaki, S. Tanaka, M. Fukuda, Y. Murayama, Y. Kondo, H. Ogasawara, *et al.*, "Development of the organic-inorganic hybrid super-hydrophilic layer," *Fuji film Research & Development,* vol. 55, pp. 29-33, 2010.

[154] A. S. de Dios and M. E. Diaz-Garcia, "Multifunctional nanoparticles: analytical prospects," *Anal Chim Acta,* vol. 666, pp. 1-22, May 7 2010.

[155] "ISO (International Organization for Standardization), Nanotechnologies: terminology and definitions for nano-objects—nanoparticle, nanofibre and nanoplate, ISO/TS 27687,2008, Geneva, Switzerland.," ed.

[156] L. Y. Chou, K. Ming, and W. C. Chan, "Strategies for the intracellular delivery of nanoparticles," *Chem Soc Rev,* vol. 40, pp. 233-45, Jan 2011.

[157] C.-N. Lok, C.-M. Ho, R. Chen, Q.-Y. He, W.-Y. Yu, H. Sun, *et al.*, "Silver nanoparticles: partial oxidation and antibacterial activities," *JBIC Journal of Biological Inorganic Chemistry,* vol. 12, pp. 527-534, 2007// 2007.

[158] L. S. W. a. R. Y. Hong, "Synthesis, Surface Modification and Characterisation of Nanoparticles."

[159] R. J. Byers and E. R. Hitchman, "Quantum dots brighten biological imaging," *Prog Histochem Cytochem,* vol. 45, pp. 201-37, Feb 2011.

[160] M. Geszke-Moritz and M. Moritz, "Quantum dots as versatile probes in medical sciences: synthesis, modification and properties," *Mater Sci Eng C Mater Biol Appl,* vol. 33, pp. 1008-21, Apr 1 2013.

[161] E. Cassette, M. Helle, L. Bezdetnaya, F. Marchal, B. Dubertret, and T. Pons, "Design of new quantum dot materials for deep tissue infrared imaging," *Adv Drug Deliv Rev,* vol. 65, pp. 719-31, May 2013.

[162] G. P. Drummen, "Quantum dots-from synthesis to applications in biomedicine and life sciences," *Int J Mol Sci,* vol. 11, pp. 154-63, 2010.

[163] V. Biju, S. Mundayoor, R. V. Omkumar, A. Anas, and M. Ishikawa, "Bioconjugated quantum dots for cancer research: present status, prospects and remaining issues," *Biotechnol Adv,* vol. 28, pp. 199-213, Mar-Apr 2010.

[164] R. M. Levenson and J. R. Mansfield, "Multispectral imaging in biology and medicine: slices of life," *Cytometry A,* vol. 69, pp. 748-58, Aug 1 2006.

[165] P. Bordes, E. Pollet, and L. Averous, "Nano-biocomposites: Biodegradable polyester/nanoclay systems," *Progress in Polymer Science,* vol. 34, pp. 125-155, 2009.

[166] S. Sinharay and M. Bousmina, "Biodegradable polymers and their layered silicate nanocomposites: In greening the 21st century materials world," *Progress in Materials Science,* vol. 50, pp. 962-1079, 2005.

[167] I. L. Medintz, H. T. Uyeda, E. R. Goldman, and H. Mattoussi, "Quantum dot bioconjugates for imaging, labelling and sensing," *Nat Mater,* vol. 4, pp. 435-46, Jun 2005.

[168] J. R. Mansfield, K. W. Gossage, C. C. Hoyt, and R. M. Levenson, "Autofluorescence removal, multiplexing, and automated analysis methods for in-vivo fluorescence imaging," *J Biomed Opt,* vol. 10, p. 41207, Jul-Aug 2005.

[169] P. Subramaniam, S. J. Lee, S. Shah, S. Patel, V. Starovoytov, and K.-B. Lee, "Generation of a Library of Non-Toxic Quantum Dots for Cellular Imaging and siRNA Delivery," *Advanced Materials,* vol. 24, pp. 4014-4019, 2012.

[170] M. Haase and H. Schafer, "Upconverting nanoparticles," *Angew Chem Int Ed Engl,* vol. 50, pp. 5808-29, Jun 20 2011.

[171] M. Wang, G. Abbineni, A. Clevenger, C. Mao, and S. Xu, "Upconversion nanoparticles: synthesis, surface modification and biological applications," *Nanomedicine,* vol. 7, pp. 710-29, Dec 2011.

[172] O. Ehlert, R. Thomann, M. Darbandi, and T. Nann, "A Four-Color Colloidal Multiplexing Nanoparticle System," *ACS Nano,* vol. 2, pp. 120-124, 2008/01/01 2008.

[173] L. Cheng, C. Wang, and Z. Liu, "Upconversion nanoparticles and their composite nanostructures for biomedical imaging and cancer therapy," *Nanoscale,* vol. 5, pp. 23-37, Jan 7 2013.

[174] F. Wang, D. Banerjee, Y. Liu, X. Chen, and X. Liu, "Upconversion nanoparticles in biological labeling, imaging, and therapy," *Analyst,* vol. 135, pp. 1839-54, Aug 2010.

[175] H. Hu, M. X. Yu, F. Y. Li, Z. G. Chen, X. Gao, L. Q. Xiong*, et al.*, "Facile Epoxidation Strategy for Producing Amphiphilic Up-Converting Rare-Earth Nanophosphors as Biological Labels," *Chemistry of Materials,* vol. 20, pp. 7003-7009, Nov 25 2008.

[176] Z. Li, Y. Zhang, and S. Jiang, "Multicolor Core/Shell-Structured Upconversion Fluorescent Nanoparticles," *Advanced Materials,* vol. 20, pp. 4765-4769, 2008.

[177] F. Vetrone, R. Naccache, V. Mahalingam, C. G. Morgan, and J. A. Capobianco, "The Active-Core/Active-Shell Approach: A Strategy to Enhance the Upconversion Luminescence in Lanthanide-Doped Nanoparticles," *Advanced Functional Materials,* vol. 19, pp. 2924-2929, 2009.

[178] Y. Cohen and S. Y. Shoushan, "Magnetic nanoparticles-based diagnostics and theranostics," *Curr Opin Biotechnol,* vol. 24, pp. 672-81, Aug 2013.

[179] J. Gao, H. Gu, and B. Xu, "Multifunctional magnetic nanoparticles: design, synthesis, and biomedical applications," *Acc Chem Res,* vol. 42, pp. 1097-107, Aug 18 2009.

[180] L. Laconte, N. Nitin, and G. Bao, "Magnetic nanoparticle probes," *Materials Today,* vol. 8, pp. 32-38, 2005.

[181] A.-H. Lu, E. L. Salabas, and F. Schüth, "Magnetic Nanoparticles: Synthesis, Protection, Functionalization, and Application," *Angewandte Chemie International Edition,* vol. 46, pp. 1222-1244, 2007.

[182] Q. Ma, Y. Nakane, Y. Mori, M. Hasegawa, Y. Yoshioka, T. M. Watanabe*, et al.*, "Multilayered, core/shell nanoprobes based on magnetic ferric oxide particles and quantum dots for multimodality imaging of breast cancer tumors," *Biomaterials,* vol. 33, pp. 8486-94, Nov 2012.

[183] C. Sun, J. S. H. Lee, and M. Zhang, "Magnetic nanoparticles in MR imaging and drug delivery," *Advanced Drug Delivery Reviews,* vol. 60, pp. 1252-1265, 2008/08/17/ 2008.

[184] J. R. Howard, *Fluidized Bed Technology: Principles and Applications*: Taylor & Francis, 1989.

[185] W.-c. Yang, *Handbook of fluidization and fluid-particle systems. [electronic resource]*: New York : Marcel Dekker, c2003., 2003.

[186] D. Geldart, N. Harnby, and A. C. Wong, "Fluidization of cohesive powders," *Powder Technology,* vol. 37, pp. 25-37, 1984/01/01 1984.

[187] J. Shabanian, R. Jafari, and J. Chaouki, "Fluidization of ultrafine powders," *International review of chemical engineering,* vol. 4, pp. 16-50, 2012.

[188] J. M. Valverde Millán, "Fluidization of Nanopowders," vol. 18, pp. 65-73, 2013.

[189] J. R. van Ommen, J. M. Valverde, and R. Pfeffer, "Fluidization of nanopowders: a review," *J Nanopart Res,* vol. 14, p. 737, Mar 2012.

[190] D. Geldart, "Types of gas fluidization," *Powder Technology,* vol. 7, pp. 285-292, 1973/05/01 1973.

[191] Ö. Gündoğdu and U. Tüzün, "Gas Fluidisation of Nano-particle Assemblies Modified Geldart classification to account for multiple- scale fluidisation of agglomerates and clusters†."

[192] H. Nasri Lari, J. Chaouki, and J. R. Tavares, "De-agglomeration of nanoparticles in a jet impactor-assisted fluidized bed," *Powder Technology*.

[193] X. Liang, D. M. King, P. Li, S. M. George, and A. W. Weimer, "Nanocoating hybrid polymer films on large quantities of cohesive nanoparticles by molecular layer deposition," *AIChE Journal,* vol. 55, pp. 1030-1039, 2009.

[194] Y. Chen, J. Yang, A. Mujumdar, and R. Dave, "Fluidized bed film coating of cohesive Geldart group C powders," *Powder Technology,* vol. 189, pp. 466-480, 2009.

[195] M. Capece and R. Dave, "Application of fluidized bed film coating for membrane encapsulation of catalysts," *Powder Technology,* vol. 211, pp. 199-206, 2011.

[196] Y. Hao, Z. Qunfeng, W. Fei, Q. Weizhong, and L. Guohua, "Agglomerated CNTs synthesized in a fluidized bed reactor: Agglomerate structure and formation mechanism," *Carbon,* vol. 41, pp. 2855-2863, 2003.

[197] M. Barletta, G. Simone, and V. Tagliaferri, "Advance in fluidized bed coating: An experimental investigation on a performance polymer coating alloy," *Journal of Materials Processing Technology,* vol. 178, pp. 170-180, 2006.

[198] B. Esmaeili, J. Chaouki, and C. Dubois, "Nanoparticle encapsulation by a polymer via in situ polymerization in supercritical conditions," *Polymer Engineering & Science,* vol. 52, pp. 637-642, 2012.

[199] "Kirk-Othmer Encyclopedia of Chemical Technology- FISCHER–TROPSCH PROCESS " in *Kirk-Othmer Encyclopedia of Chemical Technology*, ed: John Wiley & Sons, Inc. , 2007.

[200] C. Franco, F. Pinto, I. Gulyurtlu, and I. Cabrita, "The study of reactions influencing the biomass steam gasification process☆," *Fuel,* vol. 82, pp. 835-842, 2003/05/01/ 2003.

[201] D. Sutton, B. Kelleher, and J. R. H. Ross, "Review of literature on catalysts for biomass gasification," *Fuel Processing Technology,* vol. 73, pp. 155-173, 2001/11/13/ 2001.

[202] L. Devi, K. J. Ptasinski, and F. J. J. G. Janssen, "A review of the primary measures for tar elimination in biomass gasification processes," *Biomass and Bioenergy,* vol. 24, pp. 125-140, 2003/02/01/ 2003.

[203] J. F. González, S. Román, D. Bragado, and M. Calderón, "Investigation on the reactions influencing biomass air and air/steam gasification for hydrogen production," *Fuel Processing Technology,* vol. 89, pp. 764-772, 2008/08/01/ 2008.

[204] "Municipal solid waste combustion ash: State-of-the-knowledge."

[205] R. W. Styron, "Fly ash composition for use in concrete mix," ed: Google Patents, 2003.

[206] H. Cheng and Y. Hu, "Municipal solid waste (MSW) as a renewable source of energy: current and future practices in China," *Bioresour Technol,* vol. 101, pp. 3816-24, Jun 2010.

[207] T. Sabbas, A. Polettini, R. Pomi, T. Astrup, O. Hjelmar, P. Mostbauer*, et al.*, "Management of municipal solid waste incineration residues," *Waste Management,* vol. 23, pp. 61-88, 2003.

[208] T. Van Gerven, H. Cooreman, K. Imbrechts, K. Hindrix, and C. Vandecasteele, "Extraction of heavy metals from municipal solid waste incinerator (MSWI) bottom ash with organic solutions," *J Hazard Mater,* vol. 140, pp. 376-81, Feb 9 2007.

[209] I. Wender, "Reactions of synthesis gas," *Fuel Processing Technology,* vol. 48, pp. 189-297, I 996.

[210] M. Ojeda, R. Nabar, A. U. Nilekar, A. Ishikawa, M. Mavrikakis, and E. Iglesia, "CO activation pathways and the mechanism of Fischer–Tropsch synthesis," *Journal of Catalysis,* vol. 272, pp. 287-297, 2010.

[211] M. E. Dry, "The Fischer–Tropsch process: 1950–2000," *Catalysis Today,* vol. 71, pp. 227-241, 2002/01/15/ 2002.

[212] Z. X. Wang, T. Dong, L. X. Yuan, T. Kan, X. F. Zhu, Y. Torimoto*, et al.*, "Characteristics of Bio-Oil-Syngas and Its Utilization in Fischer−Tropsch Synthesis," *Energy & Fuels,* vol. 21, pp. 2421-2432, 2007/07/01 2007.

[213] T. Riedel, M. Claeys, H. Schulz, G. Schaub, S.-S. Nam, K.-W. Jun*, et al.*, "Comparative study of Fischer–Tropsch synthesis with H2/CO and H2/CO2 syngas using Fe- and Co-based catalysts," *Applied Catalysis A: General,* vol. 186, pp. 201-213, 10/4/ 1999.

[214] B. Liu and S. Ji, "Comparative study of fluidized-bed and fixed-bed reactor for syngas methanation over Ni-W/TiO2-SiO2 catalyst," *Journal of Energy Chemistry,* vol. 22, pp. 740-746, 2013.

[215] Y. Yao, X. Liu, D. Hildebrandt, and D. Glasser, "Fischer–Tropsch synthesis using H2/CO/CO2 syngas mixtures: A comparison of paraffin to olefin ratios for iron and cobalt based catalysts," *Applied Catalysis A: General,* vol. 433-434, pp. 58-68, 2012.

[216] S. Lögdberg, D. Tristantini, Ø. Borg, L. Ilver, B. Gevert, S. Järås*, et al.*, "Hydrocarbon production via Fischer–Tropsch synthesis from H2-poor syngas over different Fe-Co/γ-Al2O3 bimetallic catalysts," *Applied Catalysis B: Environmental,* vol. 89, pp. 167-182, 2009.

[217] T. Y. Park, I.-S. Nam, and Y. G. Kim, "Kinetic Analysis of Mixed Alcohol Synthesis from Syngas over K/MoS2 Catalyst," *Industrial & Engineering Chemistry Research,* vol. 36, pp. 5246-5257, 1997/12/01 1997.

[218] T. Ma, H. Imai, M. Yamawaki, K. Terasaka, and X. Li, "Selective Synthesis of Gasoline-Ranged Hydrocarbons from Syngas over Hybrid Catalyst Consisting of Metal-Loaded ZSM-5 Coupled with Copper-Zinc Oxide," *Catalysts,* vol. 4, pp. 116-128, 2014.

[219] S. Karimipour, R. Gerspacher, R. Gupta, and R. J. Spiteri, "Study of factors affecting syngas quality and their interactions in fluidized bed gasification of lignite coal," *Fuel,* vol. 103, pp. 308-320, 2013.

[220] T. C. Williams and C. R. Shaddix, "Contamination of carbon monoxide with metal carbonyls: implications for combustion research," *Combustion Science and Technology,* vol. 179, pp. 1225-1230, 2007/05/03 2007.

[221] R. K. Tepe, D. Vassallo, T. Jacksier, and R. M. Barnes, "Iron pentacarbonyl determination in carbon monoxide," *Spectrochimica Acta Part B: Atomic Spectroscopy,* vol. 54, pp. 1861-1868, 12/13/ 1999.

[222] J. Falbe, *New Syntheses with Carbon Monoxide*: Springer-Verlag Berlin Heidelberg, 1980.

[223] E. van Steen and H. Schulz, "Polymerisation kinetics of the Fischer–Tropsch CO hydrogenation using iron and cobalt based catalysts," *Applied Catalysis A: General,* vol. 186, pp. 309-320, 10/4/ 1999.

[224] A. C. Vosloo, "Fischer–Tropsch: a futuristic view," *Fuel processing technology,* vol. 71, pp. 149-155, 2001.

[225] C. Zhang, G. Zhao, K. Liu, Y. Yang, H. Xiang, and Y. Li, "Adsorption and reaction of CO and hydrogen on iron-based Fischer–Tropsch synthesis catalysts," *Journal of Molecular Catalysis A: Chemical,* vol. 328, pp. 35-43, 2010.

[226] U. Lassi, *Deactivation Correlations of Pd/Rh Three-way Catalysts Designed for Euro IV Emission Limits: Effect of Ageing Atmosphere, Temperature and Time*: Oulun yliopisto, 2003.

[227] *http://www.statcan.gc.ca/pub/16-201-x/2012000/part-partie3-eng.htm*.

[228] M. D. Jackson, S. R. Mulcahy, H. Chen, Y. Li, Q. Li, P. Cappelletti*, et al.*, "Phillipsite and Al-tobermorite mineral cements produced through low-temperature water-rock reactions in Roman marine concrete," *American Mineralogist,* vol. 102, pp. 1435-1450, 2017.

[229] T. Matsi and V. Z. Keramidas, "Fly ash application on two acid soils and its effect on soil salinity, pH, B, P and on ryegrass growth and composition," *Environmental Pollution,* vol. 104, pp. 107-112, 1999/01/01/ 1999.

[230] R. K. Sheline and K. S. Pitzer, "The Infrared Spectra and Structures of the Iron Carbonyls1," *Journal of the American Chemical Society,* vol. 72, pp. 1107-1112, 1950/03/01 1950.

[231] A. M. Ricks, Z. E. Reed, and M. A. Duncan, "Infrared spectroscopy of mass-selected metal carbonyl cations," *Journal of Molecular Spectroscopy,* vol. 266, pp. 63-74, 2011/04/01/ 2011.

[232] M. G. I. Galinato, C. M. Whaley, and N. Lehnert, "Vibrational Analysis of the Model Complex (μ-edt)[Fe(CO)(3)](2) and Comparison to Iron-only Hydrogenase: The Activation Scale of Hydrogenase Model Systems," *Inorganic chemistry,* vol. 49, pp. 3201-3215, 2010.

[233] Q. Cao and C. Sylvain, "Organic layer-coated metal nanoparticles prepared by a combined arc evaporation/condensation and plasma polymerization process," *Plasma Sources Science and Technology,* vol. 16, p. 240, 2007.

[234] A. Tiraferri and M. Elimelech, "Direct quantification of negatively charged functional groups on membrane surfaces," *Journal of Membrane Science,* vol. 389, pp. 499-508, 2012/02/01/ 2012.

[235] A. Hennig, A. Hoffmann, H. Borcherding, T. Thiele, U. Schedler, and U. Resch-Genger, "Simple Colorimetric Method for Quantification of Surface Carboxy Groups on Polymer Particles," *Analytical Chemistry,* vol. 83, pp. 4970-4974, 2011/06/15 2011.

[236] A. Chilkoti, B. D. Ratner, and D. Briggs, "Plasma-deposited polymeric films prepared from carbonyl-containing volatile precursors: XPS chemical derivatization and static SIMS surface characterization," *Chemistry of Materials,* vol. 3, pp. 51-61, 1991/01/01 1991.

[237] ""Iron pentacarbonyl (as Fe)". NIOSH Pocket Guide to Chemical Hazards. Centers for Disease Control and Prevention. April 4, 2011. Retrieved November 19, 2013.."

[238] V. Labonté, A. Marion, N. Virgilio, and J. R. Tavares, "Gas-Phase Surface Engineering of Polystyrene Beads Used to Challenge Automated Particle Inspection Systems," *Industrial & Engineering Chemistry Research,* 2016/06/20 2016.

[239] A. Bérard, G. S. Patience, G. Chouinard, and J. R. Tavares, "Photo Initiated Chemical Vapour Deposition To Increase Polymer Hydrophobicity," *Scientific Reports,* vol. 6, p. 31574, 08/17/online 2016.

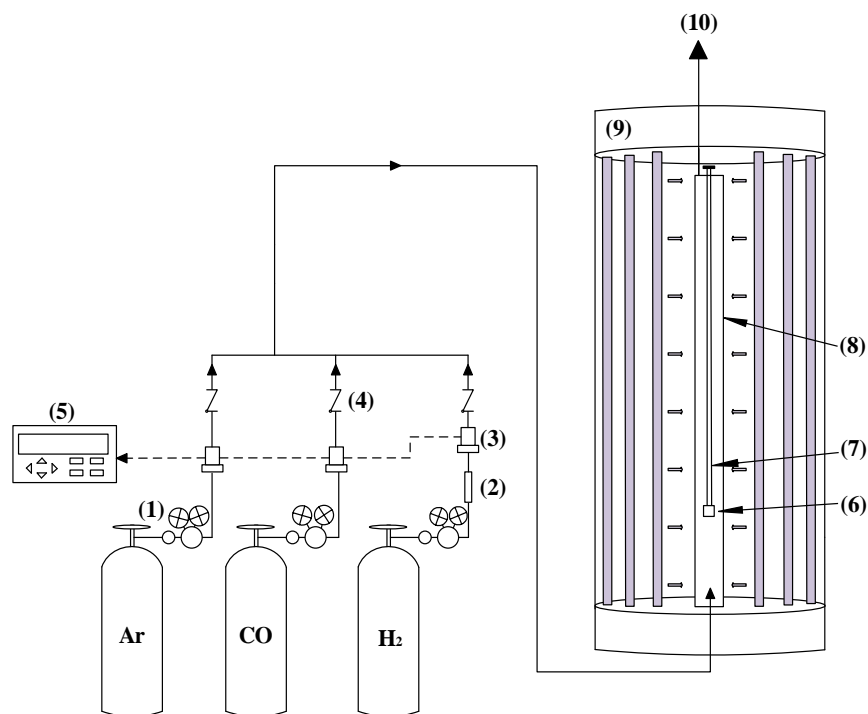# APPENDIX A –ARTICLE 2 SUPPLIMENTARY INFORMATION

Figure A-1: Schematic of experimental set-up: (1) Gas regulator, (2) Flash back arrester, (3) Mass flow meter, (4) Check valve, (5) Mass flow controller box, (6) Silicon wafer coupon, (7) Sample holder, (8) Quartz tube reactor, (9) UVC cabinet, (10) Exhaust gas to the ventilation

Table A-1: Summary of the experimental conditions.

Parameter investigated	Experiment number	Flow rate			Residence time (min)	Gas ratio	Treatment duration (min)
		CO (L/min)	H$_2$ (L/min)	Total (L/min)			
Residence time	#1	0.2	0.2	0.4	0.6	1	120
	#2	0.3	0.3	0.6	0.4	1	120
	#3	0.4	0.4	0.8	0.3	1	120
	#4	0.5	0.5	1	0.2	1	120
Treatment duration	#5	0.2	0.2	0.4	0.6	1	30
	#6	0.2	0.2	0.4	0.6	1	60
	#7	0.2	0.2	0.4	0.6	1	120
	#8	0.2	0.2	0.4	0.6	1	180
Gas ratio	#9	0.2	0.6	0.8	0.3	0.3	120
	#10	0.3	0.5	0.8	0.3	0.6	120
	#11	0.4	0.4	0.8	0.3	1	120
	#12	0.46	0.34	0.8	0.3	1.4	120
	#13	0.5	0.3	0.8	0.3	1.7	120
	#14	0.6	0.2	0.8	0.3	3	120
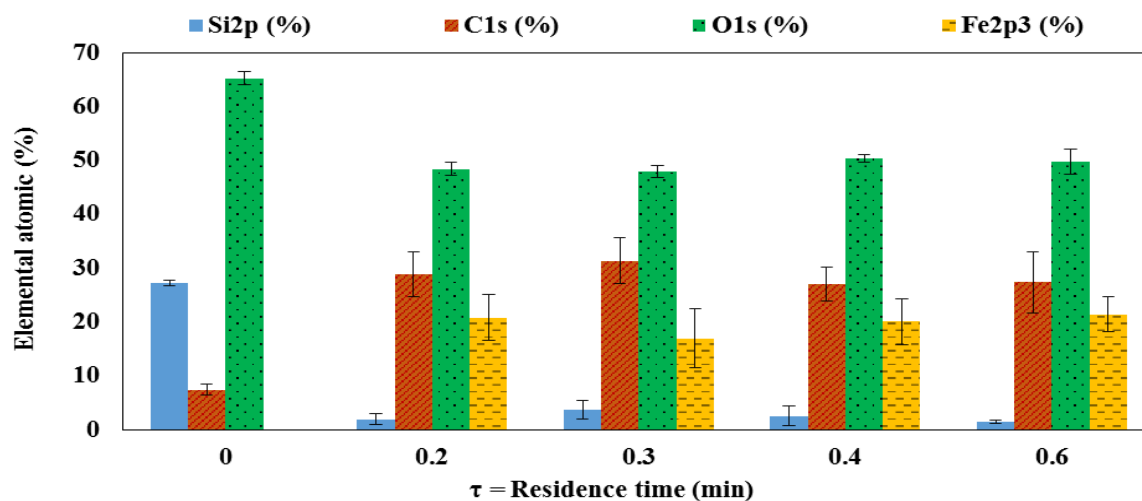
Figure A-2: Elemental atomic % of deposited film measured via XPS analysis vs. residence time (experiments # 1 to # 4, Table A-1; (error bars indicate the 95% confidence interval (95%CI)).
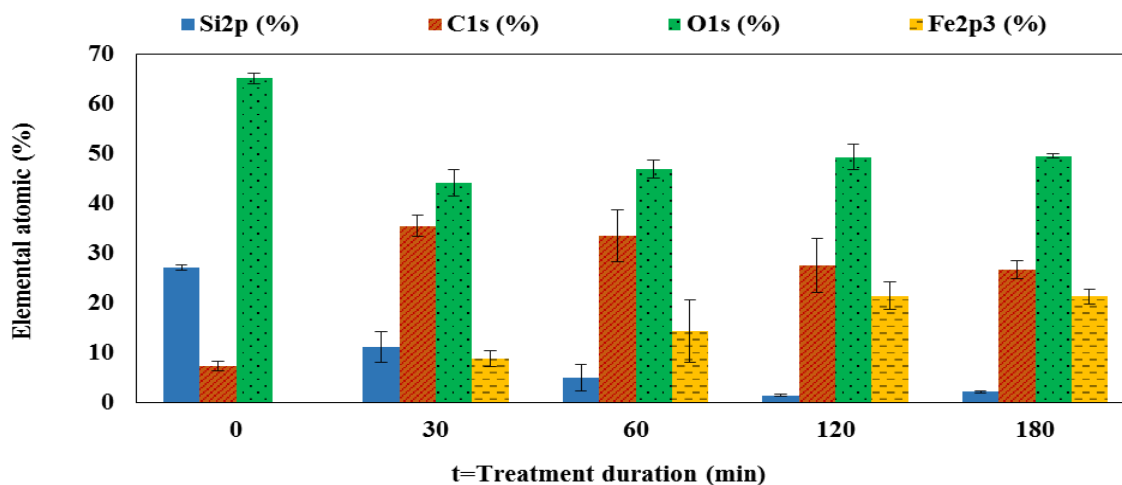
Figure A-3: Elemental atomic % of deposited film measured via XPS analysis vs. treatment duration (experiments # 5 to # 8, Table A-1; (error bars indicate the 95% confidence interval (95%CI)).
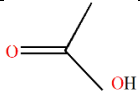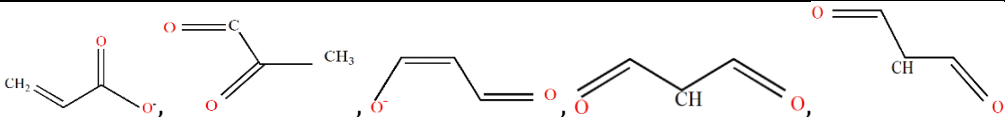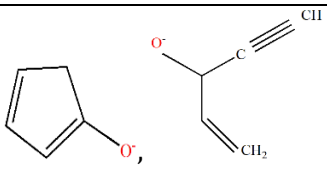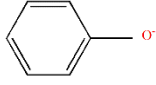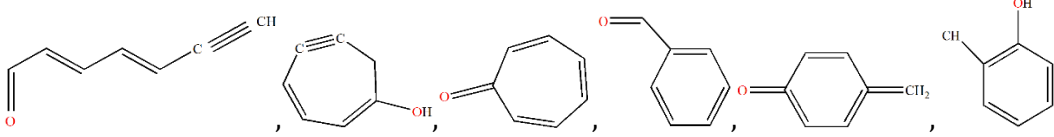
COOH⁻	
C₃H₃O₂⁻	
C₅H₅O⁻	
C₆H₅O⁻	
C₇H₆O⁻	

Figure A-4: Possible structure of chemical formula in the TOF-SIMS ion results.
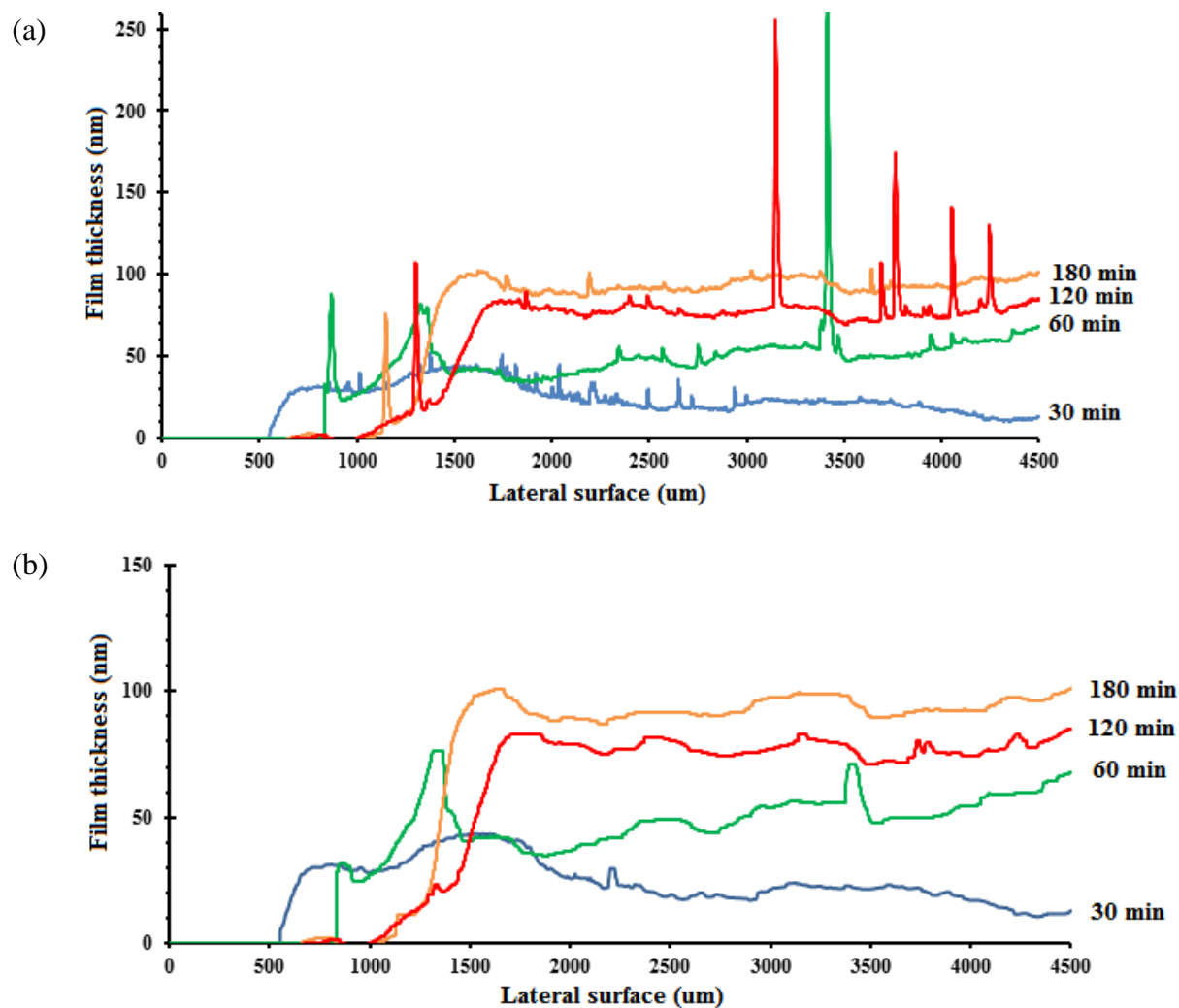
Figure A-5: Profilometry results (a) raw data, (b) curve smoothing data (experiments #5-8, Table A-1).
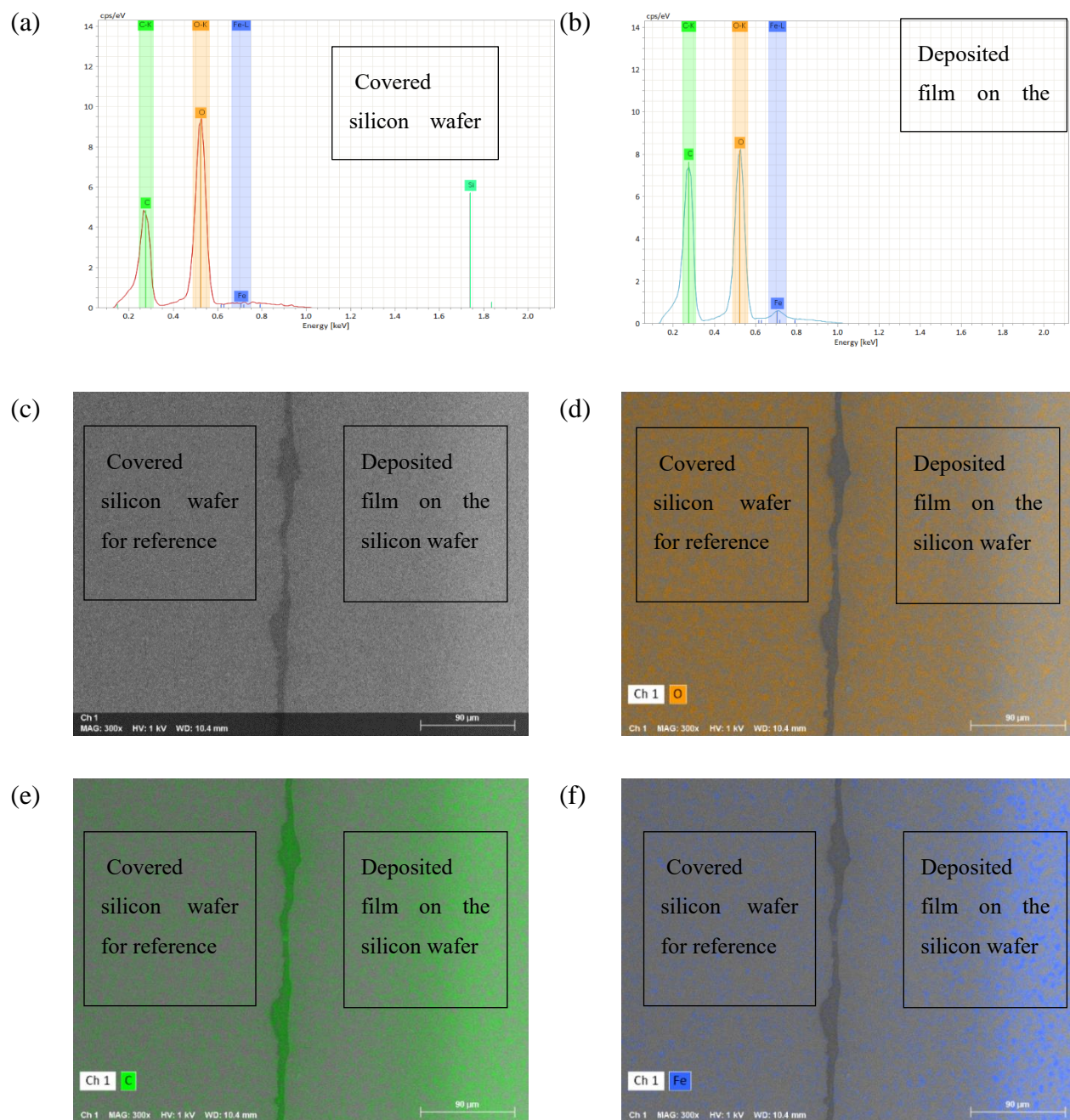
Figure A-6: Top view EDS micrograph and chemical mapping of the sample in experiment #1: (a) EDS micrograph of bare sample, (b) EDS micrograph of coated sample, (c) FESEM image of two side of sample coated and covered with Kapton tape, (d) chemical mapping of oxygen, (e) chemical mapping of carbon, (f) chemical mapping of iron.

Table A-2: Comparison of the elemental distribution (obtained by XPS) before and after soaking in chloroform for 1 hour.

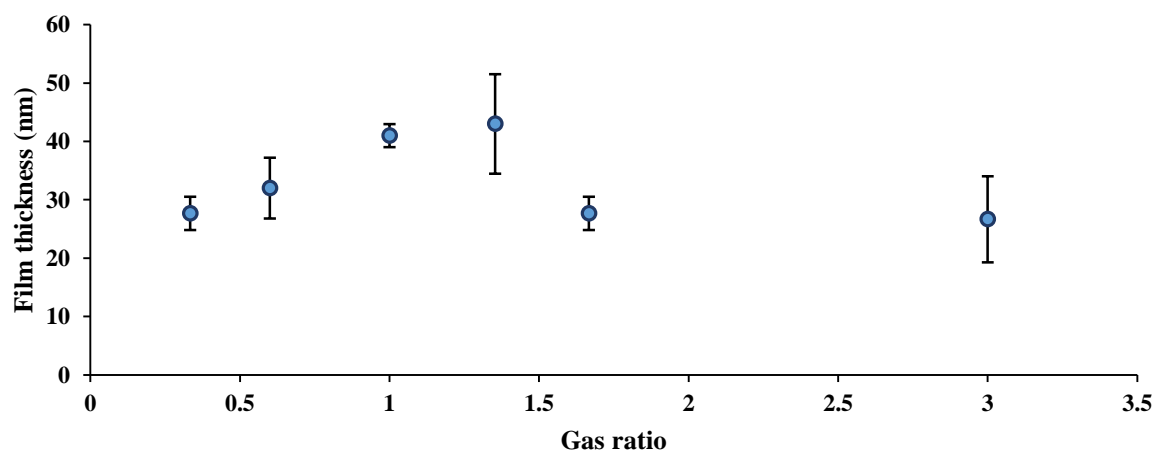| Element	Peak Binding Energy	At. % before soaking	At. % after soaking
Si	Si2s, 153.57 eV	6.4	7.7
C	C1s, 285.00 eV	40.4	46.5
O	O1s, 530.00 eV	46.8	41.1
Fe	Fe2p, 710.95 eV	6.4	4.6

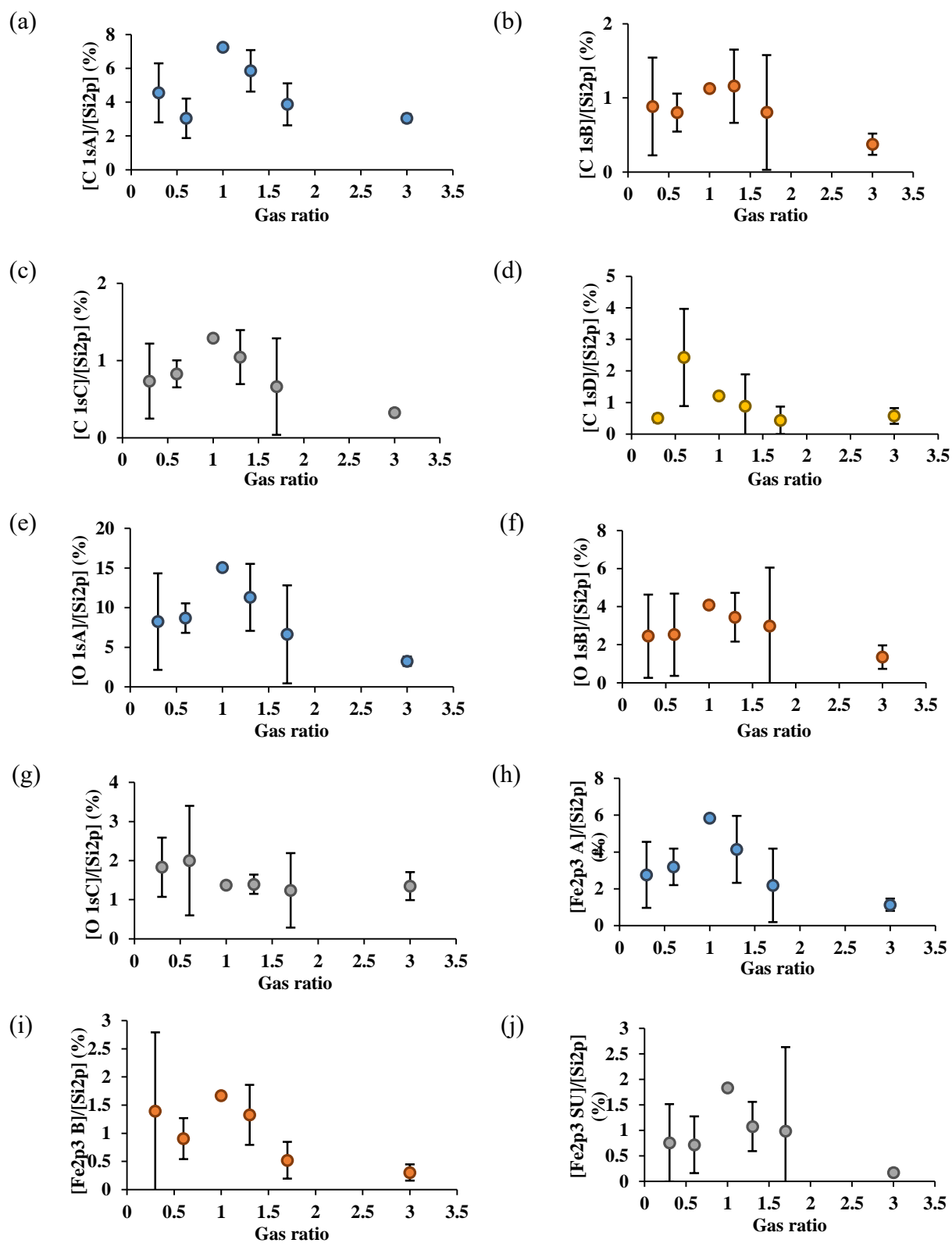Figure A-7: Film thickness as a function of the CO/H_2 gas ratio

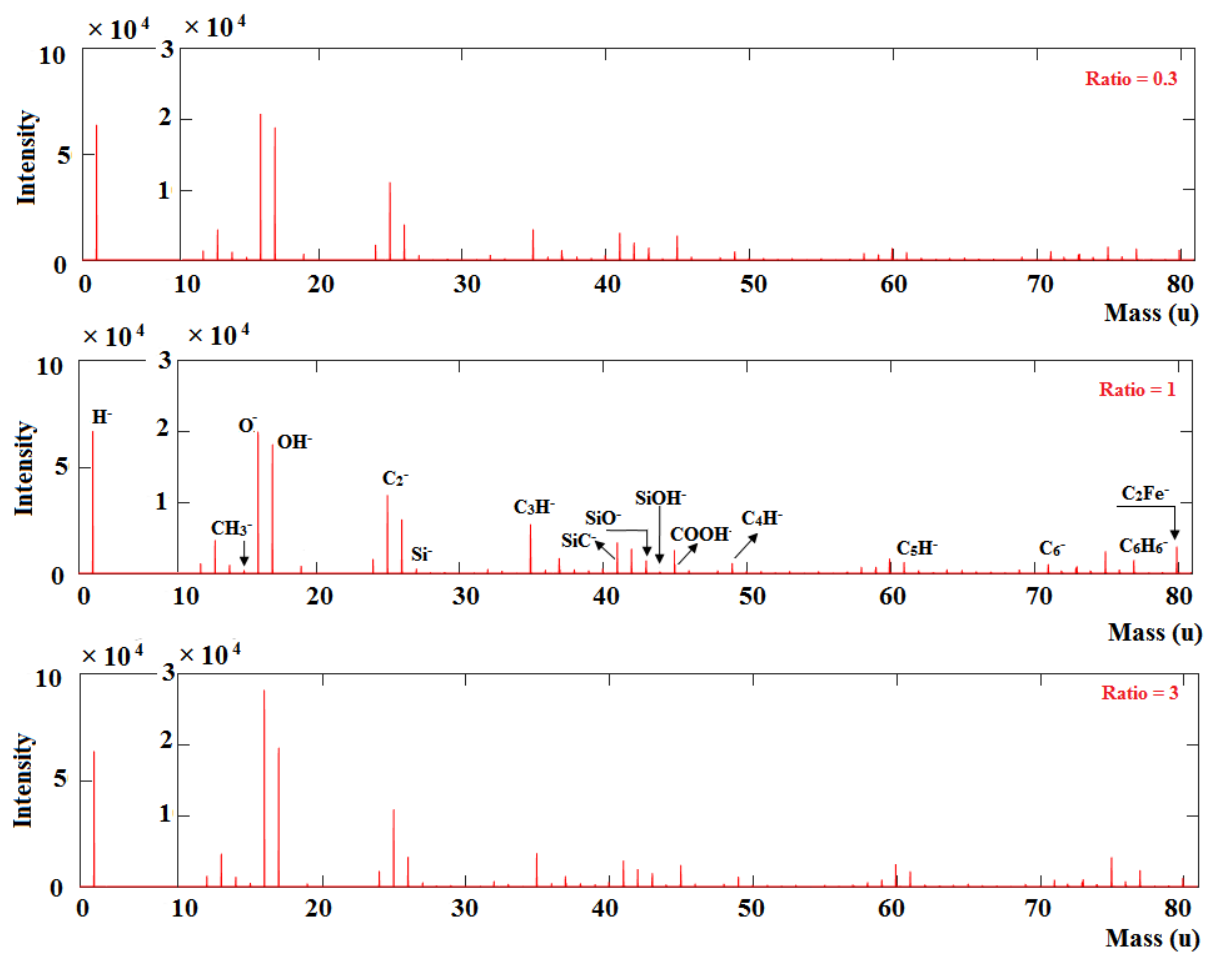Figure A-8: XPS deconvolution peak trends vs. gas ratio variation.

Figure A-9: TOF-SIMS negative ion spectra for ratio = 0.3, 1 and 3 (Experiment #9, #11, and
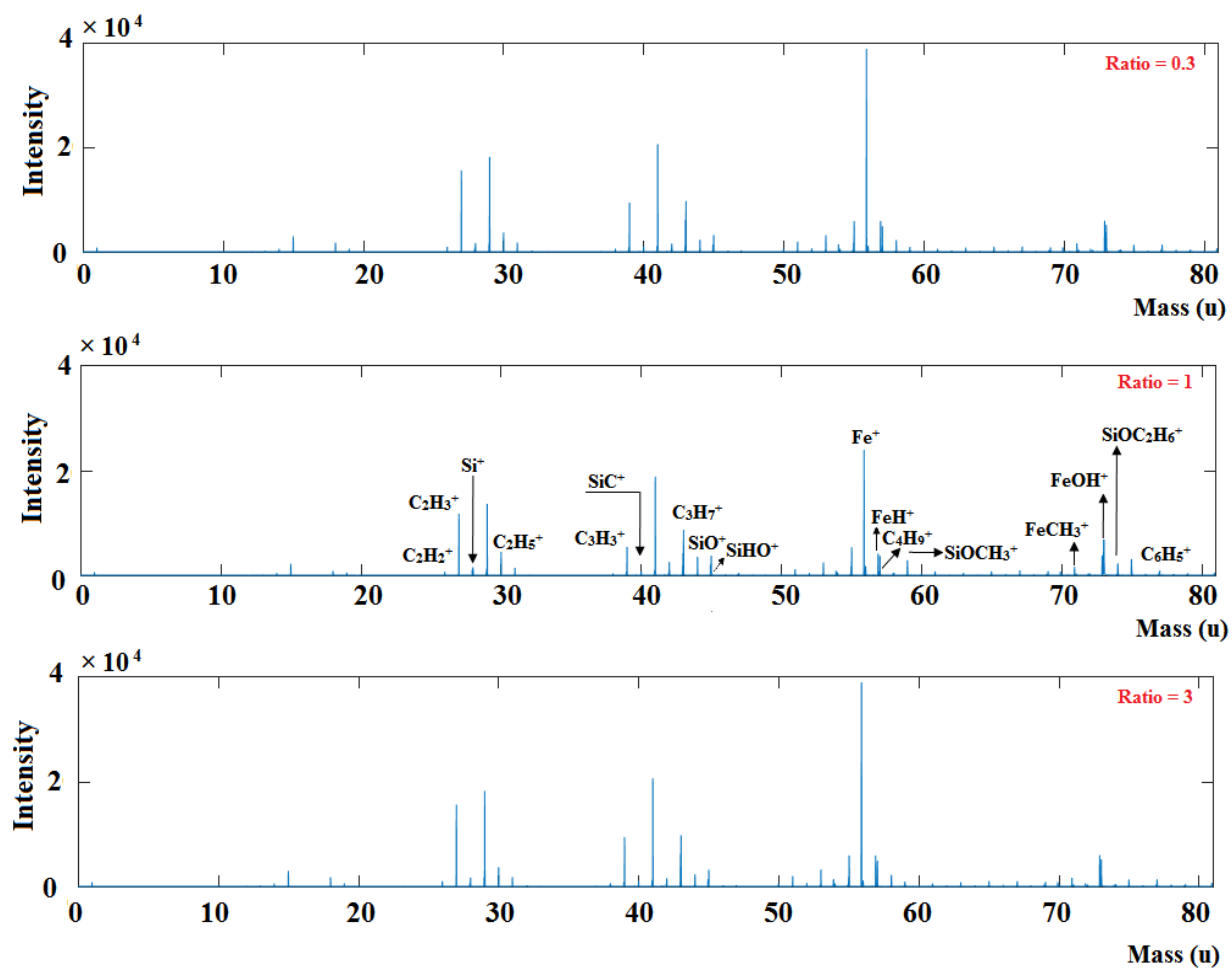
#14 , Table A-1)

Figure A-10: TOF-SIMS positive ion spectra for ratio = 0.3, 1 and 3 (Experiment #9, #11, and

#14 , Table A-1)

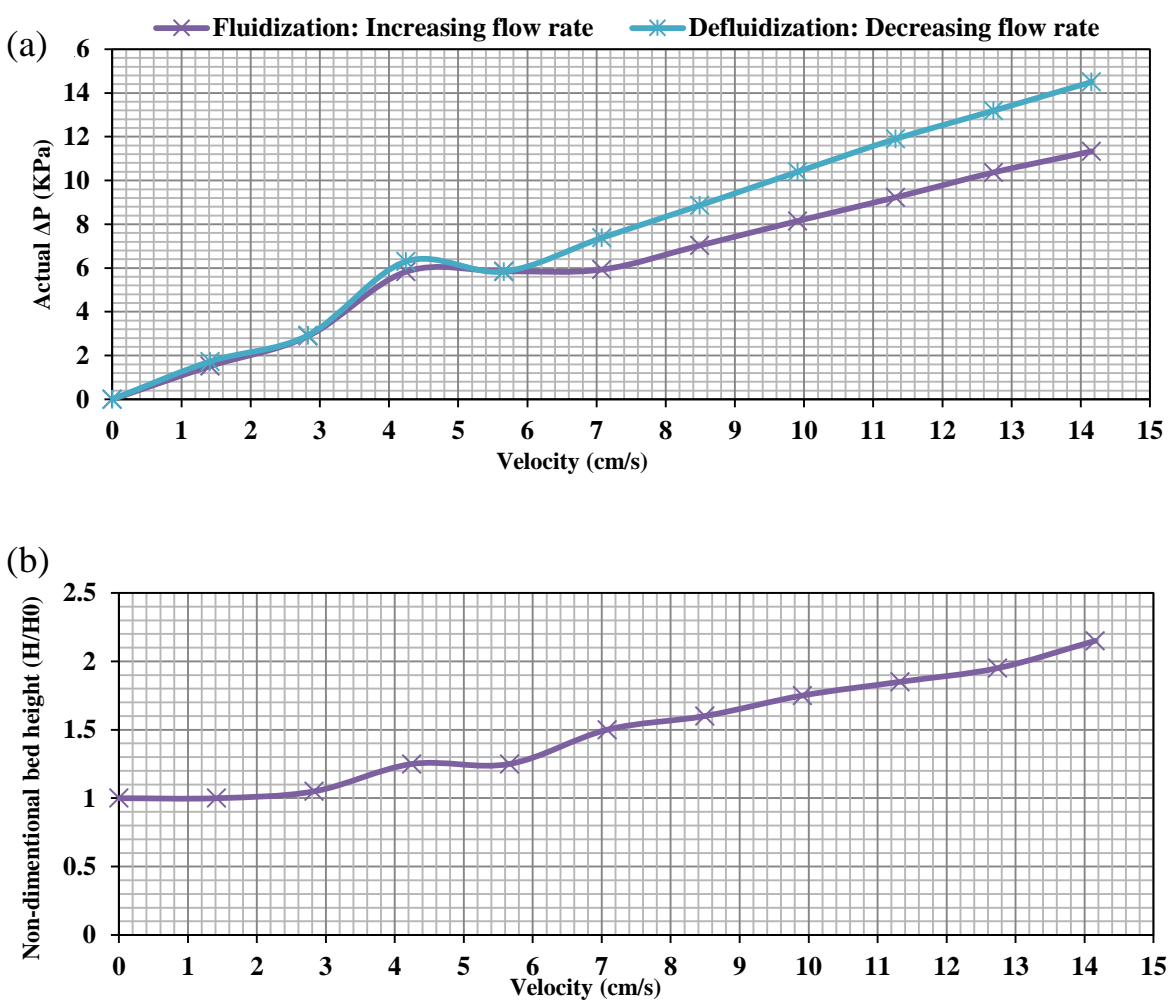# APPENDIX B –ARTICLE 3 SUPPLIMENTARY INFORMATION

Figure B-1: (a) The actual pressure drop as a function of gas velocity during fluidization (increasing flow rate) and defluidization (decreasing flow rate) of MIONPs, (b) The non-dimensional fluidized bed height as a function of gas velocity for MIONPs.
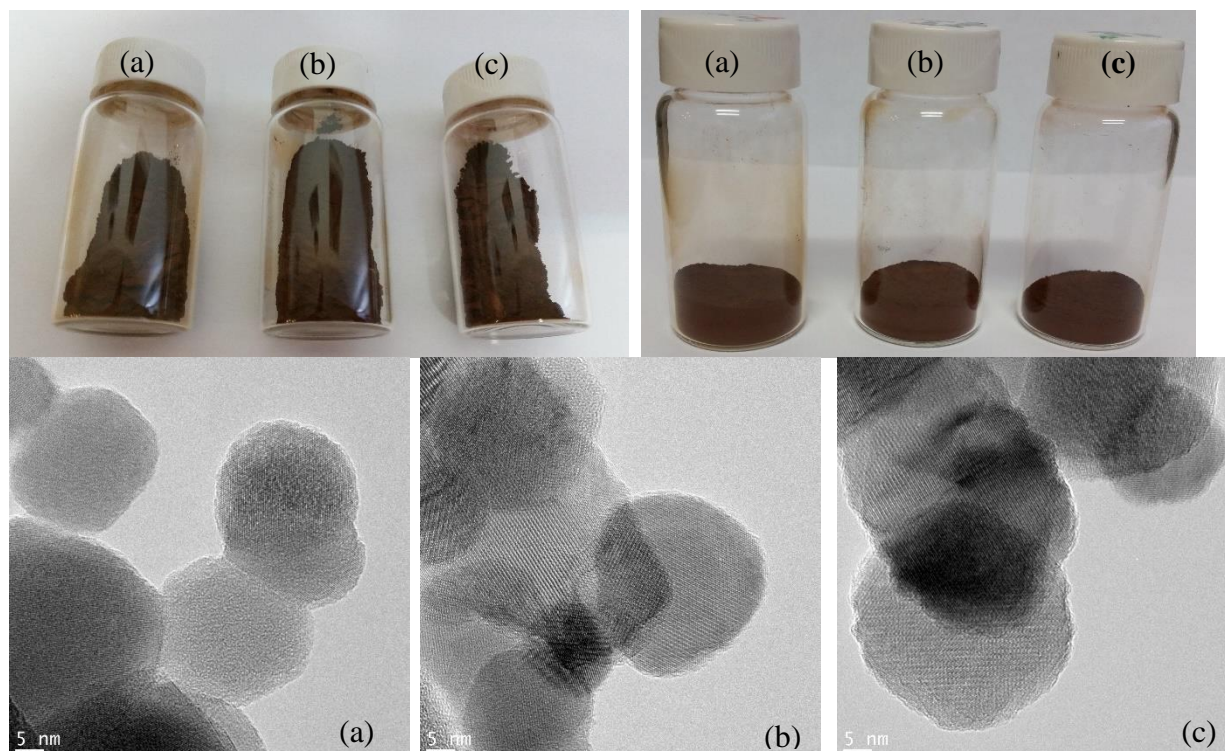
Figure B-2: Representative picture and TEM images of (a) Bare MIONPs, (b) Negative #1: MIONPs under UVC and argon gas treatment, (c) Negative #2: MIONPs under syngas precursors and argon gas treatment.

Table B-1: Elemental At.% of bare and treated MIONPs under Negative experiments.

Name	Peak BE	At. %		
		Bare	Negative #1	Negative #2
C1s	285.0	13.5	13.2	14.4
O1s	530.0	50.6	57.4	55.3
Fe2p3	711.4	35.9	29.4	30.3

LIST OF PUBLICATIONS FROM THIS THESIS:

(a) Articles published or accepted in refereed journals:

[1] Farhanian, D., De Crescenzo, G., Tavares, J.R., (2017), Large-Scale Encapsulation of Magnetic Iron Oxide Nanoparticles via Syngas Photo-Initiated Chemical Vapor Deposition, Submitted to Nanoscale.

[2] Farhanian, D. †, Nasri Lari, H. †, Boffito, D. C., Patience, G. S., De Crescenzo, G., Chaouki, J., Tavares, J.R., (2017), Shedding Light on Iron Pentacarbonyl Photochemistry through a CVD Case Study, Submitted to Catalysis Communications († These authors contributed equally to the study).

[3] Farhanian, D., De Crescenzo, G., Tavares, J.R., (2017), Kinetics, Chemistry, and Morphology of Syngas Photo-initiated Chemical Vapor Deposition, Published in Langmuir Journal.

[4] Farhanian, D., De Crescenzo, G., Tavares, J.R., (2014), Combined Extraction and Functionalization of Low-Cost Nanoparticles from Municipal Solid Waste Fly Ash through PICVD, Published in Journal of Environmental Chemical Engineering.

(b) Articles published or accepted in conference proceedings or non-refereed contributions

[5] Farhanian, D., De Crescenzo, G., Tavares, J.R., Functional Grafting via Syngas Photo-initiated Chemical Vapor Deposition, 8th Symposium - Functional Coatings and Surface Engineering (FCSE-2017), Montreal, Quebec, Canada, 4-7 June, 2017, Oral presentation.

[6] Farhanian, D., De Crescenzo, G., Tavares, J.R., Growth of thin films via atmospheric UVC-driven syngas PICVD, 23rd International Symposium on Plasma Chemistry (ISPC 2017), Montreal, Quebec, Canada, July 30 - August 4, 2017, Poster presentation.

[7] Farhanian, D., De Crescenzo, G., Tavares, J.R., The Kinetics and Chemistry of Syngas Photo-initiated Chemical Vapor Deposition, 66th Canadian Chemical Engineering Conference (CSChE 2016), Quebec, Canada, 16-19 October, 2016, Oral presentation.

[8] Farhanian, D., De Crescenzo, G., Tavares, J.R., Synthesis of Functional Hybrid Magnetic Nanomaterials in Micro jet-assisted Fluidized bed via PICVD, Forth International Conference on Multifunctional, Hybrid and Nanomaterials, Sitges, Spain, 9-13 March, 2015, Oral presentation.

[9] Farhanian, D., De Crescenzo, G., Tavares, J.R., Polymeric Encapsulation of TiO_2 and ZnO particles using PICVD, 64th Canadian Chemical Engineering Conference (CSChE 2014), Niagara Falls, Ontario, Canada, 19-22 October, 2014, Oral presentation.

[10] Farhanian, D., Raphael, W., Dorval Dion, C.A., De Crescenzo, G., Tavares, J.R., Single Step Extraction and Functionalization of Low-Cost Nanoparticles from Municipal Solid Waste Fly Ash through PICVD, Nanotech-Advanced Materials, Washington DC, USA, 16-18 June, 2014, Oral presentation.

[11] Farhanian D., De Crescenzo, G., Tavares, J.R., Combined Extraction and Functionalization of Low-Cost Nanoparticles from Municipal Solid Waste Fly Ash through PICVD, McGill-Polytechnique Chemical Engineering Research Day, Montreal, Canada, 19 March 2014, Oral presentation.

[12] Farhanian, D., De Crescenzo, G., Tavares, J.R., Versatile Functionalization of Surfaces through PICVD – Decoupling the Plasma from the Process, Colloque Plasma-Quebec, Montreal, Canada, 28 March, 2014, Poster presentation.

[13] Farhanian, D., De Crescenzo, G., Tavares, J.R., Polymeric Encapsulation of TiO_2 Powder via PICVD Technique, CREPEC Colloquium, Montreal, Canada, 10 December 2014, Poster presentation.